Investigating Local Structure in Lithium-ion Battery Materials

Christopher William Cook

Lancaster University

Department of Chemistry

This thesis is submitted in partial fulfilment of the requirements for the degree of Doctor of Philosophy

July 2025

Declaration

I hereby declare that this thesis is the product of my own work, and its content does not include work published elsewhere, unless explicitly stated. The content of this thesis has not been submitted, in whole or in part, for the award of any other degree, diploma or qualification at Lancaster University or any other institution. The number of words does not exceed 69000, excluding references.

Chris Cook

July 2025

Abstract

The planned widespread adoption of electric vehicles means increased demand for the batteries to power them. However, the current commercial standard materials are made from a limited range of elements, placing excessive demands on resources. There is therefore a motivation to develop new cathode chemistries, form a more diverse range of materials. A major obstacle to the commercialisation of these new materials is that they suffer from unwanted side reactions. These can occur at the material's surface or within the bulk structure and can negatively impact performance.

This thesis focusses on understanding these unwanted processes, and the performance of different countermeasures, by exploring the material's local structure and how it changes when used in a battery. First, plasma polymerisation was explored as an alternative way of preparing protective coatings, to prevent surface reactions, using X-ray photoelectron spectroscopy (XPS), electron paramagnetic resonance (EPR) spectroscopy and ^{1}H solid-state nuclear magnetic resonance (SSNMR) spectroscopy. Precursor adhesion and substrate damage are shown to be important considerations when preparing coatings using this approach. Then oxyfluoride disordered rocksalt (DRX) materials were explored using a multinuclear SSNMR approach, supported by X-ray diffraction (XRD) and density functional theory (DFT) calculations. This showed that these materials are not truly disordered, with the formation of LiF-like regions potentially being important for stabling the material structure during cycling. Finally, the high-voltage behaviour of vanadium-based DRX materials was investigated, using SSNMR, XRD and EPR as well as pair distribution function (PDF) analysis and resonant inelastic X-ray scattering (RIXS) measurements. These results indicate that structural rearrangements that occur at high voltages may give the appearance of other side reactions.

The work presented in this thesis uses multiple characterisation techniques to provide insight into the structures of potential next-generation cathode materials, that could serve to guide material synthesis.

Acknowledgements

I would first like to thank my long-suffering supervisor, John, who first took a chance on me back in 2019. Since then, he has continued to supervise me with patience and humour, giving me freedom to explore and develop (and giving me a kick when needed). I suppose he has also taught me a thing or two about science, NMR and how to think and write (note the compound adjective in the first line). Thank you also to Nuria, Rob and Xiao who have all contributed their knowledge and support at various stages throughout this project.

As any PhD student with multiple supervisors will probably tell you, handling them all can be… challenging. However, it has meant that I have had the opportunity to work with some truly great people. So I would like to thank all of the group members (actual and honorary) who have taught and supported me throughout this process: Matthew, Kieran, Ryan, Zhenjiang, Shaoquan, Mingqing, Sia, Hannah, Tommy, Sarah, Alexandra, Beth, Jack, Begoña, Lauren, Alex, Valerie, Alessio, Amy, Dom, Abby, Xin and, of course, Trouble (known also as Hekang). I am so grateful to all of you for making the past few years what they have been.

Beyond cTAP C01, I would also like to thank the members of the Chemistry department at Lancaster University, especially Michael, Nathan, Lefteris and Geoff for all their help and discussions. Thank you also to Jasmine for recommending Zotero over Mendeley, greatly expediting the referencing process. I would also like to thank the Faraday Institution, who made all this possible. I am particularly grateful to Dom Grantley-Smith, who has been patient with me even when I probably made his job a little difficult.

The PhD process is known to be inherently stressful, but getting smacked in the mouth or kicked in the ribs is an effective way of forgetting about it, at least for a time. I am therefore especially grateful to my instructor Andrea, "the wee team", Mark, Alex and everyone else at HSD karate club. You guys have been so important in helping me through all of this. I would also like to thank my coaches, Julie and John, the HDKI-GB squad, the broader HDKI and beyond for the opportunities and support (and beatings) you have so willingly provided. A special thank you to Sandra and John, who never fail to make me smile. Osu!

Finally, I would like to thank my family who have supported, encouraged and endured my interest in science from the very beginning.

List of publications

The following works feature contributions from the author that are not included in this thesis:

1. A. R. Haworth, **C. W. Cook** and J. M. Griffin, Solid-state NMR studies of coatings and interfaces in batteries, *Current Opinion in Colloid and Interface Science,* 2022, **62**, 101638
2. K. Griffiths, **C. W. Cook**, V. R. Seymour, R. J. Bragg, N. R. Halcovitch and J. M. Griffin, Chemical lithiation reveals the structures of conjugated tetralithium dicarboxylates, *Chemical Communications*, 2025, DOI: 10.1039/d5cc03043a
3. H. Brough, **C. W. Cook**, J. M. Griffin and M. J. G. Peach, Combining double-hybrid functionals with rSCAN yields solid-state 13C chemical shifts with sub-ppm accuracy, *Physical Chemistry Chemical Physics*, 2025, DOI: 10.1039/D5CP01111F

EPR spectra were also contributed to the following theses:

1. A. Quadrelli, Monolayer Polymers grown on Surfaces via Ullmann Coupling and Plasma Polymerisation, 2023
2. T.-L. Whewell, Structural investigations of organic functional materials using NMR crystallography, 2024

Table of contents

1. Introduction

1.1. Lithium-ion batteries

To combat climate change, the UK seeks to reach net-zero carbon emissions by 2050, with other countries setting similar targets.[1] Batteries are expected to play an important role in this by stabilising the intermittent energy outputs of renewable sources and facilitating the electrification of small vehicles.[1–3] When using batteries in electric vehicles, high gravimetric energy density is important. This is to say that the amount of energy stored per unit mass needs to be as large as possible to allow the greatest distance to be travelled between charges. Lithium-ion batteries (LIBs) are the dominant force in this regard, with the low mass and negative voltage (–3.04 V vs the standard hydrogen electrode (SHE)) of the lithium ion resulting in energy densities of 250 – 300 Wh kg^{-1}.[2,4]

In common with other battery chemistries, (such as sodium- and potassium-ion) LIBs comprise three fundamental components. These are the cathode and anode submerged in a liquid electrolyte. This is illustrated schematically in Figure 1.1. The cathode and anode are typically mounted on current collectors (aluminium and copper respectively), which can be connected to an external circuit.[3]

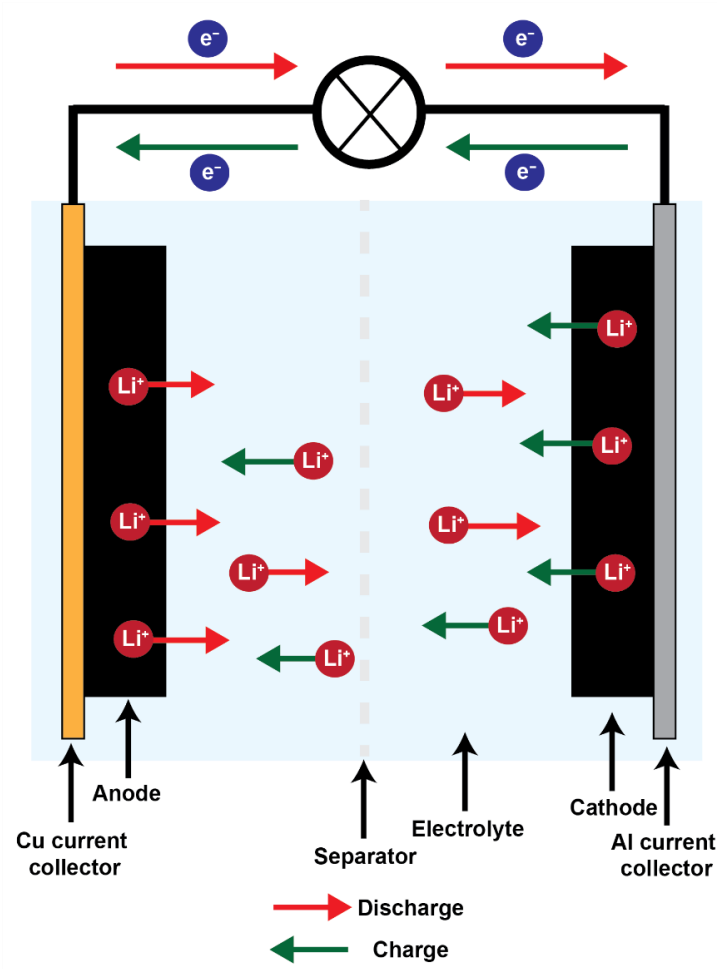

Figure 1.1: The components of a LIB.

Commercial LIBs operate via an intercalation or "rocking chair" mechanism, where lithium ions are inserted into interstitial sites within the electrode structure. This results in no changes to the structure of the electrode materials, aside from changes in interlayer spacing. Charge compensation for the movement of ions is provided by redox processes involving transition metal ions or by π-orbitals in the case of carbonaceous species. On charging, lithium ions are inserted into the graphite anode, and the cathode (normally a transition metal oxide) is oxidised. This is thermodynamically unfavourable, and so on discharging, lithium ions are deintercalated from the anode and reinserted into the cathode (with the transition metal ion being reduced).[4,5]

Energy can also be stored by conversion reactions, instead of intercalation mechanisms. In these reactions, the insertion of lithium ions into the material causes the formation of new phases. These phases change as lithium ions are inserted into the material. As such, the accommodation of lithium ions is not limited to interstitial sites (as in intercalation

materials). This can result in higher capacities for conversion materials, although structural transformations result in lower electrode stability.[6]

1.2. Energy density and capacity

When considering portable applications, such as electric vehicles, the gravimetric energy density of the battery is important to consider, which is the amount of energy stored per unit mass. This is related to the operating voltage of the cell and the specific capacity.[7]

The voltage of a cell is determined by the difference in potentials between the two electrodes as per Equation 1.1.[5]

$$V_{cell} = V_{cathode} - V_{anode} \tag{1.1}$$

Equation 1.1 shows that having a larger difference in potentials between the electrodes leads to a greater cell voltage and by extension, greater energy density. This highlights the first benefit of using LIBs as the very negative potential of the lithium ion (vs the SHE) facilitates high cell voltages.[8]

The specific capacity of a material is how much charge that material can store per unit mass. This is derived from Faraday's law of electrolysis, which states that the mass of material deposited in an electrochemical reaction is proportional to the amount of electricity put through the cell. This can be expressed mathematically by Equation 1.2, where i is the current, t is the time, n is the moles of product formed, z is the number of electrons transferred, and F is Faraday's constant (96485 C mol^{-1}).[9,10]

$$it = nFz \tag{1.2}$$

Equation 1.2 can then be rewritten as Equation 1.3, where Q is the charge, m is the mass of material and M_w is the molar mass of the material.[10]

$$Q = \frac{mFz}{M_w} \tag{1.3}$$

Specific capacity is the amount of charge stored normalised by mass, and so Equation 1.3 can be rearranged to give Equation 1.4. As specific capacity is normally expressed in mA h g^{-1} (rather than A s g^{-1}), a factor of 3.6 is included here (a combination of the two conversion factors for hours and milliamps).

$$\frac{Q}{m} = \frac{Fz}{3.6M_w} \tag{1.4}$$

The relationship in Equation 1.4 highlights the second benefit of using lithium ions, which is that they are light, leading to high specific capacities.[8] It should be noted that in principle, using higher valence cations could also improve capacity as more electrons can be transferred per ion intercalated. However, the higher charge density of these ions means that they experience greater electrostatic interactions with the cathode material, slowing diffusion.[11] Furthermore, the smallest ion with a charge higher than lithium is magnesium. With an atomic mass of 24 g mol^{-1}, magnesium is more than 3 times heavier than lithium, meaning that the improvement in capacity from the higher charge is mitigated somewhat by the heavier ion.

1.3. Testing battery materials

Testing of battery materials on a small scale is normally performed using a coin cell. Figure 1.2 shows the general construction of such a cell, although there are variations in the type of electrode, separator and specific electrolytes used.[12] Swagelok cells can also be used when larger amounts of sample are required for analysis.[13]

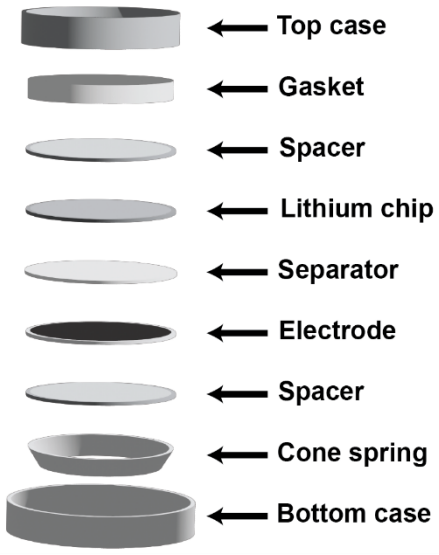

Figure 1.2: Components of a coin cell commonly used to test battery materials.

The most common way to test a material's performance is to use galvanostatic cycling. In this test, a constant current, determined by the mass of active material, is applied. When a specified cutoff voltage is reached, the current is reversed. This is repeated for the desired number of cycles. Currents are often expressed in terms of C-rate. This is an indicator of the time to completely charge or discharge the theoretical capacity of the material at that specific current. For example, a C-rate of 1 C means that the material will be fully charged

or discharged in one hour, whilst a C-rate of C/20 means it will take 20 hours for the same process.[12,14]

The result of galvanostatic cycling is a voltage profile, which is a plot of specific capacity against voltage, and can be used to provide information on the electrochemical properties of a material. Sloped regions indicate the presence of solid solution reactions whereas plateaus suggest the formation of a new phase at a particular potential.[15] Voltage profiles are also used to calculate Coulombic efficiency, which is the ratio of the capacity achieved by a charging or discharging step compared to its preceding step. A Coulombic efficiency that deviates significantly from 100% indicates the presence of parasitic side reactions, that cause a loss of capacity over multiple cycles.[14]

Another useful parameter that can be obtained from galvanostatic cycling is the cycle life of a material. This is defined as the number of cycles before the capacity drops below 80% of the initial capacity. Initial capacity in this case does not always refer to the capacity of the first cycle, as there may be large drops in capacity between the first and second cycles due to side reactions. In these cases, it is more appropriate to calculate cycle life based on later cycles, as these are more representative of the long-term behaviour of the material.[14]

1.3. Anode materials

1.3.1. Lithium metal anodes

The most efficient way to incorporate lithium ions into an electrode is simply to use a lithium metal anode. Metal anodes require no additional materials, to host the lithium ions, improve conductivity or act as a current collector. Thus, lithium metal anodes have high specific capacities. Furthermore, the negative potential of lithium (vs the SHE) would lead to cells with high energy densities.[8] However, lithium ions deposit asymmetrically onto the metal surface, leading to the formation of metallic dendrites. These can detach from the surface, creating so-called dead lithium, that is no longer usable in the cell, impacting performance. Furthermore, dendrites can punch through the separator, causing short circuits.[4,16] The resulting safety concerns mean that lithium metal anodes have never been widely adopted. Efforts have been made to develop strategies to facilitate the use of lithium metal anodes, such as employing metal oxide coatings to supress dendrite formation.[17] Lithium metal batteries are also of interest for batteries using solid-state electrolytes.[16,17] However, as this thesis is primarily concerned with materials for "wet" cells, this will not be discussed further.

It should also be mentioned that lithium metal anodes are routinely used as the anode in laboratory-scale measurements. This is because of its stable potential and high capacity, which means that the reactions being tested are never limited by the anode capacity.[18] Such cells are often referred to as "half cells".

1.3.2. Graphite

Since the first commercial LIBs in 1994, graphite has been the anode of choice for most commercial cells. It is cheap, easy to produce and naturally conductive. Lithium ions can be accommodated between the graphene sheets up to a stoichiometry of LiC_6, resulting in a capacity of 372 mA h g^{-1}. Charge neutrality is preserved by transfer of electrons into the graphite π orbitals.[4] Graphite has a low cell potential of ~0.1 V vs Li/Li^+, resulting in cells with high cell voltages.[19]

There are, however, several issues with graphite anodes. Firstly, the low potential means that there is a risk of dendrite formation and short circuits.[19,20] Poor lithium diffusion limits the accessible capacity, particularly at low temperatures, with only 12% of the capacity being accessible at –20 °C.[19,21] This is potentially an issue when using graphite anodes in environments that may be exposed to low temperatures, such as electric vehicles. The poor diffusion of lithium ions also means that graphite exhibits poor capacity when cycled quickly, as would be required for a fast charging of electric vehicles.[19] During cycling, graphite also undergoes volumetric changes. These changes, combined with the formation of ordered stages, can cause delamination of the electrode from the current collector.[20]

1.3.3. Lithium titanate

The risk of lithium plating for graphite anodes has led to the investigation of other materials with higher redox potentials. Lithium titanium oxide (LTO) has a potential of 1.55 V (vs Li/Li^+), due to the $Ti^{3+/4+}$ redox couple.[22] This removes the risk of lithium plating as well as SEI formation, as this is above the voltages required to reduce the electrolyte. In addition, LTO undergoes very small changes in volume when lithium is inserted/removed, making it more structurally stable. However, it can only store three lithium ions per formula unit, resulting a theoretical capacity of 175 mA h g^{-1}, much lower than the capacity of graphite.[20] Furthermore, its electrical conductivity is poor, and lithium diffusion is slow. There is therefore interest in addressing these challenges using doping or conductive coatings.[23]

1.3.4. Silicon

Another alternative to graphite anodes are silicon anodes. Abundant and environmentally friendly, silicon has a very high capacity of 4200 mA h g^{-1}, when lithiated to $Li_{4.4}Si$. Silicon also has a potential of 0.4 V, reducing the risk of dendrite formation, whilst being much lower than LTO.[24] Despite these advantages, silicon undergoes large volume expansion of over 300% when lithiated (compared to 10% for graphite).[25] It also has poor conductivity and so, whilst still of interest, is not currently a competitor to graphite when used on its own.[26] However, silicon can be used in combination with graphite, with Tesla making use of anodes that contain 10 wt% silicon.[27]

1.4. Cathode materials

The cathode is the heavier and more expensive electrode in a LIB.[28] Furthermore, the capacity is generally lower than the anode, limiting the performance of the whole cell. Therefore, the development and optimisation of cathode materials is of particular interest.

Early attempts at rechargeable LIBs used TiS_2 as a cathode. This is made up of alternating layers of titanium and sulphur, allowing lithium ions to intercalate in between the layers.[28] However, the cell potential of this material is low (< 2.5 V), resulting in low energy density. To improve the cell voltage, oxide cathode materials were investigated by the group of John Goodenough. This is because the O^{2-} 2p band has a lower energy than the S^{2-} 3p band, allowing for much greater cell voltages.[29] Oxide materials used for cathode materials normally belong to one of three material families. These are layered oxides, spinel oxides and polyanion materials.

1.4.1. Layered materials

The first layered oxide investigated was $LiCoO_2$ (LCO). This is made up of octahedral $Co^{3+/4+}$ ions coordinated to six O^{2-} ions. These are arranged in layers, between which lithium ions can insert. In addition to its higher operating voltage (~ 4 V), LCO contains lithium as synthesised, meaning that a lithium metal anode is not required. These qualities made it an ideal replacement for TiS_2, resulting in it being used as the first commercial cathode material in the 1990's. However, when more than 0.5 lithium ions (per formula unit) are extracted, the structure collapses, resulting in poor cycling performance. As a result, the operating voltage of LCO is restricted to below 4.4 V. This limits the practical capacity of LCO to ~140 mA h g^{-1}, around 50% of the theoretical capacity.[29,30]

Different approaches have been used to try and improve the performance of LCO, such as doping the material with titanium or magnesium or applying surface coatings.[30] However, the practical challenges of LCO as well as the cost of cobalt has led to other materials being investigated.[29,31] One such class of materials are $LiNi_{1-x-y}Mn_xCo_yO_2$ (NMC) materials.[32] These materials address the problems of LCO, by using different metal ions. Not only are these metals cheaper, but substitution of cobalt for nickel improves the capacity, whilst the inclusion of manganese stabilises the structure. Cobalt is still used in these materials as it improves the electron transfer properties of the material. To further improve the capacity of the material, the other metal ions in NMC materials are reduced in favour of increasing the nickel content, with capacities of 200 mA h g^{-1} being achieved for NMC811, as against 150 mA h g^{-1} for NMC111.[31]

The obvious extreme end of the NMC series is to only use nickel, resulting in $LiNiO_2$ (LNO). LNO has a high theoretical capacity of 275 mA h g^{-1}. However, it is challenging to synthesise owing to the stability of Ni^{2+} compared to Ni^{3+}. Any Ni^{2+} present can occupy Li^+ sites (due to their similar sizes). Such cation disorder is unfavourable for material performance. Furthermore, LNO is prone to phase transformations on cycling, resulting in poor performance.[31] Despite these challenges, the prospect of such high capacity means that LNO is an active area of research with different countermeasures being investigated.[33,34]

1.4.2. Spinel materials

Another class of oxide materials being investigated are spinel materials, the first example being $LiMn_2O_4$. This is significantly cheaper than LCO, owing to the greater natural abundance of manganese compared to cobalt, whilst offering higher cell voltages. In addition, the spinel structure allows fast lithium-ion diffusion.[35] However, in the presence of trace amounts of H^+, which can be formed from the decomposition of the electrolyte salt (Section 1.5.3.), Mn^{3+} ions can disproportionate to Mn^{2+} and Mn^{4+}. This is problematic for the capacity of the electrode, but also Mn^{2+} dissolves into the electrolyte, poisoning the graphite anode.[36,37]

The compositional space of spinel materials is far more limited than for layered oxides. Of the other first row transition metals only vanadium and titanium can form spinel oxides, owing to the difficulty in stabilising the 3+ oxidation states of the other metals.[29] However, neither of these materials are suitable as cathode materials. As previously discussed, the

$Ti^{3+/4+}$ redox couple has a potential of only ~ 1.5 V. LiV_2O_4 on the other had undergoes structural transformations at 3 V.

An alternative approach to accessing other spinel structures is to substitute other ions into $LiMn_2O_4$. Of these $LiNi_{0.5}Mn_{1.5}O_4$ is perhaps the most successful. In this material, all the manganese is Mn^{4+}, avoiding disproportionation. Instead, the redox activity of the material comes from nickel going between the +2 and +4 oxidation states. This has a high voltage of 4.7 V vs Li/Li^+, which offsets the low capacity of 147 mA h g^{-1}, to achieve high overall energy density (650 W h kg^{-1}). However, the high voltage far exceeds the stability of the electrolyte, resulting in decomposition reactions (Section 1.5.3.).[38,39]

1.4.3. Polyanion materials: lithium iron phosphate

Another cathode material worth briefly discussing is lithium iron phosphate, $LiFePO_4$ (LFP). LFP has a specific capacity of 170 mA h g^{-1}, which is better than the spinel materials already mentioned. In addition, iron is relatively abundant. These reasons combined with higher thermal stabilities means that LFP has found a level of commercial success.[29,38,40]

However, the low conductivities of LFP means that electrodes require large amounts of carbon additives, reducing the energy density the final cells.[29] Furthermore, LFP has a low operating voltage when compared to the materials previously discussed (3.5 V vs Li/Li^+).[41]

1.5. Electrolytes and interphases

1.5.1. Electrolytes

The two electrodes previously described are submerged in an electrolyte solution, which allows lithium ions to migrate between the electrodes. This is normally a lithium salt, such as $LiPF_6$, dissolved in a mixture of carbonate solvents (Figure 1.3).[42]

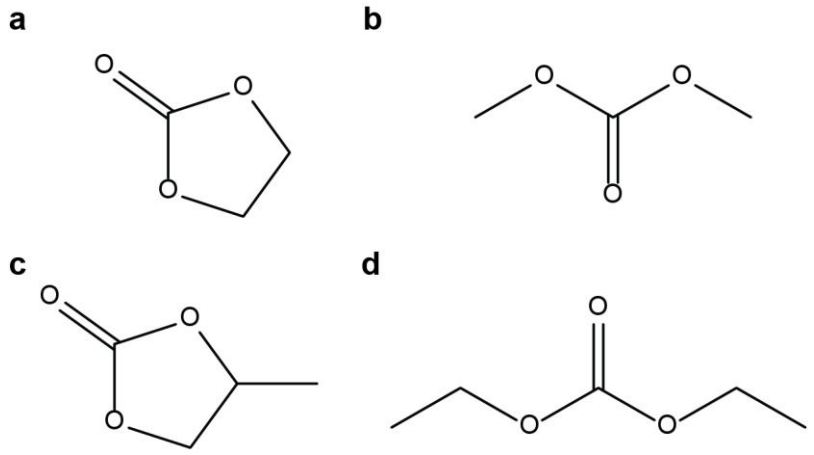

Figure 1.3: Commonly used solvents in LIB electrolytes. (a) ethylene carbonate (EC), (b) dimethyl carbonate (DC), (c) propylene carbonate (PC) and (d) diethyl carbonate (DEC).

1.5.2. Electrode-electrolyte interphases

It would be simple to assume that the electrodes and electrolyte exist as three discrete entities. However, this is not the case. Instead, parasitic reactions between the electrodes and the electrolyte result in the deposition of electrode-electrolyte interphase layers. The layer that forms at the anode is called the solid-electrolyte interphase (SEI) and the layer that forms on the cathode is the cathode-electrolyte interphase (CEI).[43] Whilst thin, these layers have significant impact on the overall lifetime of the battery. A stable interphase layer can mitigate further reactions, facilitating long-term cycling of the battery.[44,45] Indeed, this is the case for graphite, where a stable SEI forms during the first discharge, that is imperative for reversible cycling.[46,47] However, an unstable interphase reduces accessible lithium and may continue to thicken impeding ion diffusion.[48] As a result, there has been interest in understanding the nature of interphase layers and how they form, to improve cell performance.

In the review by Xiao *et al* they argue that highly controlled conditions are needed to test contributions for the CEI, making use of model electrode materials.[47] This is likely useful, but the formation of the CEI is tied to many factors influencing each other, as will be discussed. Therefore, it may not be valid to isolate individual contributing factors when the CEI should perhaps be viewed as something greater than the sum of its parts.

1.5.3. Interphase formation mechanisms

The processes that form interphase layers are a mixture of electrochemical processes and conventional chemical reactions. If the Fermi level of the anode is of higher energy than

the lowest unoccupied molecular orbital (LUMO) of the electrolyte solvent, the solvent molecule will be reduced.[44] This typically starts to occur below 1.5 V, and the decomposition products of these reactions deposit onto the anode surface, forming the SEI.[42] The opposite process, *i.e.*, oxidation of the solvent molecules, can also occur at the cathode if the Fermi level is below the energy of the highest occupied molecular orbital (HOMO) of the solvent molecule. This typically occurs at around 4.5 V and beyond. These kinds of potentials are not normally reached in commercial cells, and so there is normally much less deposition at the cathode than the anode.[47,49]

Another electrochemical process that contributes to CEI formation is "crosstalk" with the SEI. Crosstalk is where species from the SEI migrate across to the CEI during cell discharge.[50] This idea is supported by the fact that the thickness and composition change at different states of charge.[50,51] As such, the formation of the SEI plays an important role in the formation of the CEI.

As mentioned already, there are several chemical reactions that can occur in addition to the electrochemical reactions, contributing to the interphase layers. Oxygen in M-O bonds on the surface can act as nucleophiles causing ring opening of the cyclic solvent molecules.[44] Similarly reactive oxygen species (such as superoxides, O_2^-) evolved at high potentials can also react as nucleophiles.[52]

Another set of possible chemical reactions stem from the decomposition of the $LiPF_6$ salt, shown in Equation 1.5.

$$LiPF_6 \rightarrow LiF + PF_5 \tag{1.5}$$

The LiF formed in this reaction can then deposit onto the electrode surfaces. Furthermore, the PF_5 can react with any residual water in the system, or water formed from the oxidation of solvent molecules to form HF (Equation 1.6). This HF can then react with other species, such as lithium carbonate, to form further LiF.[53]

$$PF_5 \rightarrow 2HF + POF_3 \tag{1.6}$$

The transition metal ions themselves can also be unstable when in high oxidation states.[54] For example Ni^{4+} can be reduced to Ni^{3+} by oxidising the electrolyte.

1.5.4. Composition of interphase layers

There have been many different species identified as being part of the SEI and CEI, formed from the electrolyte salt and solvent by the mechanisms previously described. Consumption of the electrolyte solvent leads to the formation of organic species such as poly(ethylene oxide) fragments and lithium acetate-type species. $LiPF_6$ can form LiF and HF. The HF can then react with the metals at the surface or Li_2CO_3 forming further LiF. LiF is a poor ionic conductor and therefore its presence can negatively impact cell performance.[50] A combination of reactions also lead to the deposition of organophosphate species.[44]

It is also worth noting that species such as Li_2CO_3 can be formed from electrolyte decomposition but may also be "native" to the material. This is to say that they are already present on the surface of the material, as residue from the synthesis, rather than formed during cycling.[55] These species do however contribute to other reactions that occur during cycling, such as the formation of LiF, as mentioned previously.

Crosstalk is an important part of the formation of the CEI. However, it has been reported as being somewhat reversible, with poly(ethylene oxide) (PEO) and lithium acetate species being removed on charging. Such species are thought to solvate to lithium ions, allowing them to migrate back to the anode.[50] Therefore the composition of interphases should not be simply viewed as static.[49]

The composition of the interphase layer also is thought to depend on what part of the electrode it deposits on. Hestenes *et al* report that LiF, Li_2CO_3 and lithium acetate species deposit selectively onto the cathode material. Alkyl carbonates on the other hand, deposit indiscriminately, and may be found on carbon or binder regions of the electrode.[55]

1.6. Thesis summary

Improving energy density requires cells with high voltages and/or specific capacities. However, these materials suffer from deleterious processes, that originate at the level of the material's local structure. The focus of this thesis is investigating the local structure of materials for use with next-generation cathode materials, either as cathode materials themselves or as protective coatings. This chapter has introduced the fundamental operating principles of lithium-ion batteries as well as the types of materials used in their construction, to provide context for the sections that follow.

Chapter 2 will address the theory and literature surrounding the materials of interest, used as surface coatings or cathode materials. Specifically, plasma polymers and disordered rocksalt (DRX) materials will be discussed.

Chapter 3 will introduce the fundamental theory behind solid-state nuclear magnetic resonance (SSNMR) spectroscopy, electron paramagnetic resonance (EPR) spectroscopy, powder X-ray diffraction (PXRD), pair distribution function (PDF) analysis, X-ray photoelectron spectroscopy (XPS) and resonant inelastic X-ray scattering (RIXS).

Chapter 4 presents an investigation into the use of plasma polymers to supress parasitic side reactions and provides insight into the interaction of plasma with various substrates, primarily using XPS and EPR spectroscopy.

Chapter 5 will explore the local structures of a range of oxyfluoride DRX materials and how these evolve on electrochemical cycling, by employing SSNMR spectroscopy and PXRD.

Chapter 6 uses SSNMR spectroscopy, EPR spectroscopy, PXRD, PDF analysis and RIXS to explore the phenomenon of oxygen redox (O-redox) in vanadium-based DRX materials.

2. Surface coatings and disordered rocksalts

2.1. Overview

As discussed in Chapter 1, improving the energy density of lithium-ion batteries (LIBs) can be accomplished either by increasing the operating voltage of the cell or increasing the capacity of the electrodes. As such the work in this thesis is divided in two. Chapter 4 will focus on surface coatings as a means of improving the performance of high-voltage cathodes. Meanwhile, Chapters 5 and 6 will focus on understanding high-capacity cathode materials, specifically disordered rocksalt (DRX) materials. The following sections will outline some of the literature associated with these areas, as well as introduce some of the preparation methods that were used to prepare the materials studied in the results chapters.

2.2. Surface coatings

As discussed in Chapter 1, the stability of the interphase layers in a battery is important to ensure longevity of performance. However, the interphase that forms naturally is not always stable. The obvious solution is to engineer an interphase with desirable properties. This can be achieved by one of two methods, using electrolyte additives or surface coatings.[56] As this thesis is primarily concerned with cathode materials, most of the discussion will be focussed on the cathode electrolyte interphase (CEI).

2.2.1. Electrolyte additives

Interphase layers form because of decomposition of the electrolyte and instability of the electrodes. This can be capitalised upon by including sacrificial additives in the electrolyte. These are less stable than the electrolyte salts/solvents and so are oxidised or reduced first. These then form the interphase, supressing any further parasitic side reactions.[57] The ability to select the additive also allows for a degree of control over the chemistry of the CEI.[43] Only small amounts of additive are required, which can be added to the electrolyte, making this approach simple and cost-effective.[58,59]

Many materials have been tested including both organic compounds and lithium salts such as vinyl carbonate, fluoroethylene carbonate (FEC), lithium bis(oxalato)borate

(LiBOB).[43,59,60] Another approach is to use additives that contain silicon atoms, such as pentafluorophenyltriethoxysilane (TPS).[59] This is because it oxidises at high voltages, forming a silicon-containing CEI. Silicon has a strong affinity for fluorine and so the coating is thought to be able to scavenge HF. Silicon-containing additives can also remove HF from the electrolyte before forming the CEI. This was shown by Han *et al*, who used tris(trimethyl silyl) phosphite as an additive.[61] Whilst in the electrolyte, this molecule reacts with HF, cleaving the Si-O bond. The products of this reaction then go on to form the CEI. This results in a capacity retention of close to 100% after 50 cycles as opposed to around 20% for the cells without an additive. These can act as scavengers of fluoride containing species. This is an idea that is also used in several types of surface coatings.

Multiple additives can be used together. This was demonstrated by Chen *et al.*, who used $LiPO_2F_2$ in combination with FEC.[57] This results in a thin CEI (6.8 nm), that has a high LiF content, which impedes solvent breakdown, whilst still being flexible enough to accommodate volumetric changes, owing to its organic content. This dramatically improved the performance of the NMC111 cathode material, with a capacity retention of 86.4% after 400 cycles as opposed to 38.7%.

A variation on this is to use an additive that reacts with the electrolyte solvent. This was done by Yang *et al*, who used aluminium isopropoxide to facilitate polymerisation of the ethylene carbonate molecules.[58] This results in a coating that contains organic components, as well as Al_2O_3 and AlF_3, based on XPS. The coatings produced do result in better capacity retention for NMC811 and LCO, provided the amount of aluminium isopropoxide is low (< 1 wt%). The coatings produced by this method are also thinner than the natural CEI (7 nm vs 20 nm) but did not crack after cycling unlike the natural CEI. It should however be noted that it is not clear how many cells this analysis was carried out on. Given the variability between coin cells, the differences in performance may be an experimental issue.

Another approach that could be loosely grouped under additives is to use high concentration electrolytes, with concentrations of 4 M. Doing so reduces the availability of reactive solvent molecules.[62] As a result, the interphase layers are largely derived from the decomposition of the electrolyte ions, making them more robust. This is due to a higher inorganic content, *i.e.*, species such as LiF.[63] It should be noted however that as discussed in Chapter 1, LiF has also been linked to poor cell performance. These conflicting results likely stem from poor testing protocols as argued by Xiao *et. al.*[47]

2.2.2. Surface coatings

The second method to control the CEI is to use a surface coating, also known as an artificial CEI (ACEI).[64] In this case, the cathode material is coated prior to cell assembly, with a coating designed to exhibit favourable properties, suppressing side reactions and improving cell performance.

There are several criteria a surface coating should ideally fulfil. Coatings should be thin and homogenous to allow easy and uniform ion mobility. They should also be chemically robust, as well as having some degree of flexibility to accommodate volumetric changes in the cathode without cracking. Scavenging groups, such as the previously mentioned Si-O bond, are also promising for reducing transition metal ion dissolution.[56] It can also be beneficial to use electronically conducting coatings to enhance the charge transfer within the electrode.[36] However, this is separate to improving the performance by replacing CEI formation.

There are many examples of materials that have been investigated as cathode coatings. The following sections will discuss some of the different materials used.

2.2.2.1. Oxide coatings

A popular type of material to use as a protective coating are inorganic oxides such as Al_2O_3, ZrO_2, ZnO and SiO_2.[33,36,65] These can have several beneficial effects such as suppressing ion dissolution and scavenging HF, by reacting to form fluorides. Furthermore, these coatings can also restrict the volume expansion that may occur during phase transitions. This however requires the coating material to be harder than the cathode material, so that it can withstand changes in particle size without breaking. [36] However, oxide materials do not always have high ionic conductivities. [65]

The cations in the oxides used as surface coatings typically only have one valence state, so that they cannot take part in redox processes and act as physical barriers between the electrode and the electrolyte.[56] This is not to say that other oxides have never been tested. For example, Zhang *et al*, used TiO_2-based coatings, which initially showed improved capacity retention.[66] However, TiO_2 can be electrochemically lithiated to form Li_xTiO_2. The resulting Ti^{3+} can catalyse unwanted reactions, leading to poor long-term performance. Another example oxide with multiple valence states is V_2O_5.[67] This can also be lithiated, but the authors kept the voltage to above 3 V, minimising any reduction of vanadium.[68] As such, in this case, V_2O_5 was successful in improving the capacity retention of the material.

Oxide coatings can be prepared by a wide variety of methods, which dictate the properties and effectiveness of the coating. "Wet" methods, such as sol-gel synthesis, are simplest and have been used to prepare Al_2O_3 coatings. These coatings are often homogenous, but it is difficult to control the thickness, and the surface chemistry may be modified.[33,56] Also, as previously mentioned, $LiPF_6$ forms HF even if only very small amounts of water are present.[58] Therefore, if using a wet method, it is imperative that the drying step is completely effective. This is less of an issue if the solvent is volatile. For example, Al_2O_3 coatings can be prepared via a sol-gel method using ethanol as the solvent.[33]

"Dry" coating techniques avoid the need for thorough drying steps. Nisar *et al*, describe the use of "soft" ball milling to coat spinel materials with ZrO_2.[65] This leads to an improvement in long-term capacity retention as well as a small improvement in initial capacity. However, this could be due to the smaller particle size because of the ball milling process. Smaller particle sizes result in better lithium-ion transport, owing to the shorter diffusion lengths.[69] The nominal amounts of ZrO_2 are also likely inaccurate as milling in a ZrO_2 jar will introduce further ZrO_2 as the milling media wear down.[70] It is also not clear whether such a method will cause phase transitions in the material, given that ball mill synthesis is often used to prepare metastable phases (as will be discussed in Section 2.4.6.).

Atomic layer deposition (ALD) is perhaps the most suitable way of preparing thin, uniform surface coatings as it allows for precise control over layer thickness and chemistry and is solvent-free.[71] Furthermore, it can be used to coat whole electrodes, rather than the active material in its powdered form. This allows electronically insulating materials to be used, as the external coating does not impact conduction within the electrode, such as ZnO.[36] However, the precursors required for ALD are often hazardous. It is also slow and expensive and therefore may not be suited to all industrial applications.[71]

2.2.2.2. Solid-state electrolytes

Solid-state electrolyte materials have also been investigated as potential surface coatings. This is because they have high lithium-ion conductivities, facilitating ion movements, but low electronic conductivities, supressing unwanted reactions. An example of this is $Li_{3x}Ln_{2/3-x}TiO_3$ (LLTO), coated onto NMC622 by a sol-gel method.[72] This does improve the capacity retention of the material with 87.2% capacity retention after 200 cycles compared to 56.6% for uncoated NMC622. But perhaps more interestingly, the synthesis uses residual lithium species on the surface (left over from the synthesis) as the lithium

precursor for the LLTO. These species impede lithium-ion transport, so this approach has additional performance benefits beyond simply protecting the cathode.

2.2.2.3. Polymer-based coatings

Conducting polymers such as polypyrroles or polyimides have also been researched.[73,74] These can be ionically and/or electronically conducting and so can improve charge mobility throughout the electrode. In addition, the flexibility of polymer materials may allow them to avoid cracking during cycling, preventing the continued deposition of CEI layers.[56] An example is LNMO coated with a polypyrrole coating.[73] This sees a 92% capacity retention after 300 cycles, compared to 76.7% for uncoated LNMO. However, the electrochemical profile does not seem to change consistently as the weight percentage of the coating is increased. This could suggest that the differences observed are due to variation between coin cells. This is perhaps also due to the inherent flexibility of polymer coatings, allowing them to accommodate volume changes without cracking.

It is worth pointing out that the preparation method for the polypyrrole coatings is relatively simple, which may make it useful industrially, although the aqueous solutions used would require heavy drying. The process is however perhaps simpler than the method for making the polyimide coating described by Cho *et al*, as this requires several consecutive heating steps to prepare the coating.[74]

Aside from the previously mentioned conducting polymers, other polymers have been investigated. Poly(vinyl difluoride) (PVDF) is one such example, as demonstrated by Kang *et al*.[75] Ubiquitous in the battery field as a binder, PVDF undergoes thermal decomposition when heated. This forms reactive fluorine species that can then react with unreacted lithium precursors on the cathode surface, like the previously described LLTO coatings. The result of this is the formation of a protective LiF layer, which resulted in a 97% capacity retention compared to 83.6% for uncoated NMC811, after 100 cycles. This also further suggests that LiF can be of benefit to cell performance.

2.2.2.4. Alkylated lithium silicates

The final class of materials that will be discussed are alkylated lithium silicates ($Li_xSi_yO_z$). These are of interest owing to their open frameworks, allowing for easy lithium-ion diffusion. Also, as mentioned previously, the presence of silicon allows these materials to scavenge HF. Rosy *et al.* report one of these coatings, prepared by ALD with a single precursor.[76] This material, when coated onto $0.35Li_2MnO_3 \cdot 0.65LiNi_{0.35}Mn_{0.45}Co_{0.20}O_2$,

resulted in a 35% capacity increase, compared to the uncoated material. No reason for this capacity increase is given, but perhaps it arises due to lithiation/delithiation of the coating itself. However, this approach would not be suitable for large-scale manufacture in its current form, as the precursor has a lengthy synthesis. The synthesis also requires the use of mercury, which is potentially problematic.

2.3. Plasma polymerisation

The coating materials discussed have been shown to be beneficial for improving battery lifetimes. However, there can be issues with the preparation method, or the precursors used. Therefore, alternative methods for creating coatings should be explored, particularly those that use simple starting materials under mild, dry conditions.

2.3.1. Introduction

The chemical properties of surfaces determine how they interact with their environment. This has led to the development of a range of processes for modifying surfaces. One family of surface modification techniques are plasma-based processes, which have received interest owing to their low process temperature, solvent-free nature and versatility. This section will focus on one such technique, namely plasma polymerisation.

First properly developed by Goodman in the 1960's, plasma polymerisation is a method of depositing thin coatings derived from organic plasmas.[77] They have found use in many areas, from antibiofouling coatings to carbon fibres, owing to the attractive properties of the process and the coatings it creates.[78–81] Plasma polymerisation has a low process temperature and is entirely solvent-free. Unlike conventional polymerisation, there is no requirement for unsaturation, enabling a wide range of traditionally "unpolymerisable" precursors to be used. As a result, plasma polymer coatings can contain a diverse set of functionalities, including -COOH, C-O-C, -SH and -NH_2. The coatings can also be prepared to be ultra-thin, with coatings below 10 nm in thickness being achievable.[82]

The coatings created by plasma polymerisation are often also said to be substrate independent. However, this only refers to the upper most surface of the coating, whilst the chemistry of the coating bulk can vary throughout its depth and can be influenced by interactions with the substrate.[83]

It is important to be clear, that despite being referred to as "polymers", plasma polymer coatings are quite different to conventional polymers. Instead of being composed of a

single repeating monomer unit, a plasma polymer is a random, crosslinked network.[77,84] Therefore, whilst some would term the starting material a monomer, others would call it a precursor to better reflect its relationship to the final deposit.

2.3.2. Overview of the process

Plasma polymerisation is not a widely used method of sample preparation, at least when compared to other forms of polymerisation. Therefore, before looking at the details of the process, it is useful to give an overview of the basic steps involved.

The process starts with introducing the precursor vapour into a chamber at low pressure. Through random processes, a small number of electron-ion pairs are then generated.[85] These would be of no consequence, if it were not for the application of a radiofrequency (RF) field. This accelerates the electrons, resulting in collisions that generate radicals and excited states in addition to further electrons and ions. These electrons are then also accelerated generating further reactive species, which sustain the plasma. The reactive species generated then react and deposit onto the substrate, leading to the generation of a plasma polymer film.[86,87]

2.3.3. Practical considerations: reactor design

Plasma polymerisation is carried out in a plasma reactor, which must fulfil two basic requirements. Firstly, it must have a vacuum chamber with a way of introducing the precursor vapour. Secondly, it must have a way of supplying power to the vapour. This power supply can be a direct current (DC) or an RF source, but RF power is favoured for the generation of organic plasmas. RF is supplied at a frequency of 13.56 MHz as per the allowed frequencies for industrial, scientific and medical (ISM) uses.[88] RF also means that the electrode can be wrapped around the outside of a glass barrel, which is more efficient than containing the electrodes within a steel vessel.[87] Aside from these basic requirements, there are a wide variety of reactor designs, based on the individual requirements of the user. For example, cruciform barrels enable the use of extra sensors, whilst vertical barrels equipped with loudspeakers allow the agitation and uniform coating of powdered substrates.[87,89] Figure 2.1 shows an image of the reactor used for the work carried out in this thesis.

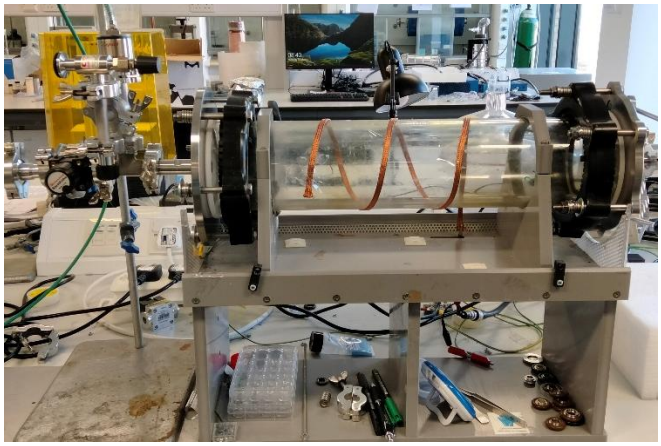

Figure 2.1: An example of a "Clark" reactor.

2.3.4. The plasma phase

2.3.4.1. Equilibrium and non-equilibrium plasmas

As previously alluded to, the plasma phase is a highly complex gaseous phase consisting of electrons, ions, radicals, excited states and neutral gas molecules. If the gas is more than a simple monatomic species (such as argon) the complexity increases further owing to the wide range of fragmented species possible. Regardless of the species, the kinetic energy is an important thermodynamic parameter when describing plasmas. Typically, this is referred to by a temperature, which is expressed in electron volts. The conversion factor is shown in Equation 2.1.[90]

$$1\ eV = \frac{1.6 \times 10^{-19} J}{1.38 \times 10^{-23} JK^{-1}} = 11600\ K \qquad (2.1)$$

When considering the temperature of species, there are two possible situations. Either the temperatures of all species are equivalent, or the electron temperature is much higher than those of neutral species and ions. These are called equilibrium and non-equilibrium plasmas respectively. Equilibrium plasmas require high temperatures (such as in stars), and so most man-made plasmas are non-equilibrium plasmas.[77]

2.3.4.2. Composition of plasmas

Electrons are the most important species in the plasma as they are responsible for generating new reactive species and sustaining the plasma. Electrons are generated in one of two ways. Before plasma ignition, a small number of neutral species are ionised by absorbing cosmic rays and other random processes. When a radio frequency field is

applied, further electrons are generated through collisions with neutral species. These processes are shown in Equations 2.2 and 2.3 for a neutral species X_2.[90]

$$X_2 + h\nu \rightarrow X_2^+ + e^- \quad (2.2)$$

$$X_2 + e^- \rightarrow X_2^+ + 2e^- \quad (2.3)$$

To possess enough energy to ionise molecules or break bonds, electrons must be heated. This is achieved through the application of an RF field (Stochastic heating), which accelerates the electrons. Electrons can also gain energy through collisions (Ohmic heating), but the amount of energy transferred is negligible in comparison to that supplied by the external field.

The amount of energy an electron has determines what kind of species it can generate. The energy of all the electrons in the plasma is described by the electron energy distribution function (EEDF) (Figure 2.2). This follows a Maxwellian distribution with most electrons possessing 3 – 5 eV of energy being capable of generating radicals from organic molecules, and those with > 10 eV being capable of ionisation.[90]

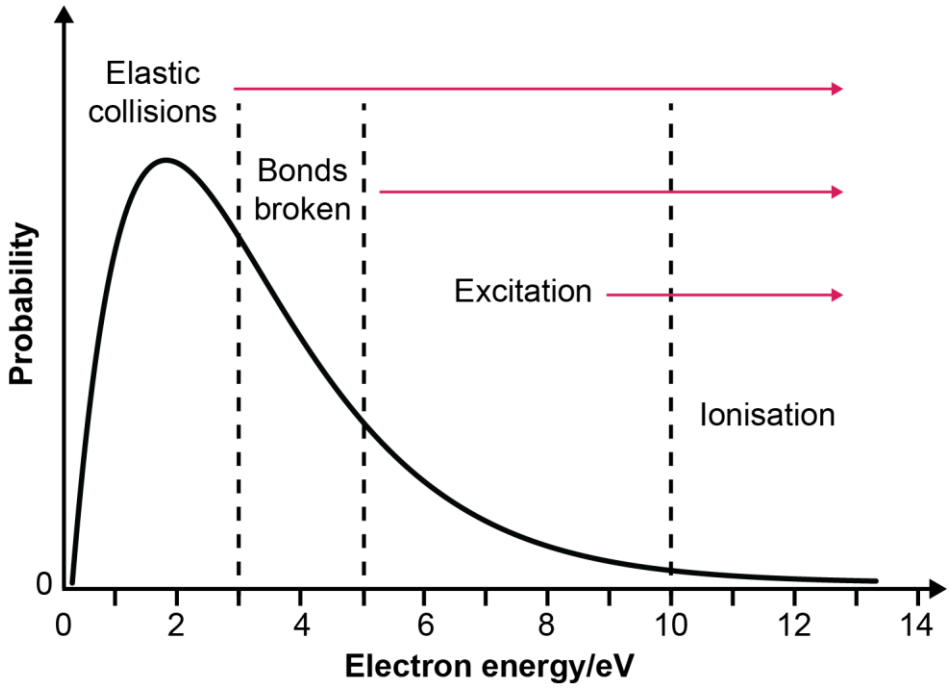

Figure 2.2: The electron energy distribution function, at an arbitrary temperature. The regions are labelled with the processes that can occur at those electron energies. Based on Figure 2 in the review by Michelmore *et al.*[90]

The formation of positive ions through collisions generates electrons and is therefore a necessary step in sustaining the plasma. However, positive ions are not very abundant as

very few electrons have the energy necessary for ionisation, with there being one ion for every 10^4 – 10^6 neutral molecules. As they are relatively large, ions do not get accelerated by the RF field and remain at ambient temperatures and therefore do not assist in sustaining the plasma.[90]

Ions can also be generated in the plasma phase via protonation of neutral species. In this case the protons are supplied by water adsorbed to the walls of the plasma chamber, as per Equation 2.4.[90]

$$H_3O^+ + X_2 \rightarrow X_2H^+ + H_2O \qquad (2.4)$$

In addition, when precursors containing electronegative atoms are used (*e.g.,* CF_4), electron collisions can generate negative ions (Equation 2.5). This process consumes electrons and therefore does not contribute to sustaining the plasma. Negative ions are also thought to not contribute to the coating deposition in the way that positive ions do (this shall be discussed in Section 2.3.5.).[90]

$$X_2 + e^- \rightarrow X_2^- \qquad (2.5)$$

Fragmentation of the precursor molecule generates reactive radical species (Equation 2.6). It should be noted that the two radicals need not be identical, depending on which bond is broken.

$$X_2 + e^- \rightarrow X^{\cdot} + X^{\cdot} + e^- \qquad (2.6)$$

As bond dissociation requires less energy than ionisation, radicals are more abundant in the plasma phase (for every one radical there are 200 neutral gas molecules). Radicals are neutral, and therefore are not affected by the RF field, remaining at ambient temperatures. Radicals can also be generated by abstraction of hydrogen radicals.[91]

If an electron with energy of 5 – 10 eV collides with a neutral species, the collision can result in the formation of an excited state. These excited states are typically short-lived (10 ns), although metastable states can be formed with lifetimes exceeding 1 ms. Regardless, when excited states relax, they can emit photons. Some of these photons are in the UV region, (referred to as vacuum UV or VUV), whilst others are in the visible

range. These visible photons are responsible for the characteristic plasma glow. Equations 2.7 and 2.8 show the generation of an excited state and the subsequent relaxation step.[90]

$$X_2 + e^- \rightarrow X_2^* \quad (2.7)$$

$$X_2^* \rightarrow X_2 + h\upsilon \quad (2.8)$$

2.3.5. Plasma polymer deposition mechanisms

2.3.5.1. Radical-only mechanisms

Radicals are the dominant reactive species in the plasma phase. Therefore, it has been historically assumed, perhaps influenced by conventional polymerisation mechanisms, that coating deposition is solely due to radicals. The first model proposed was the Rapid Step Growth Polymerisation (RSGP) model, put forward by Yasuda in 1985. This is summarised in Figure 2.3.[77]

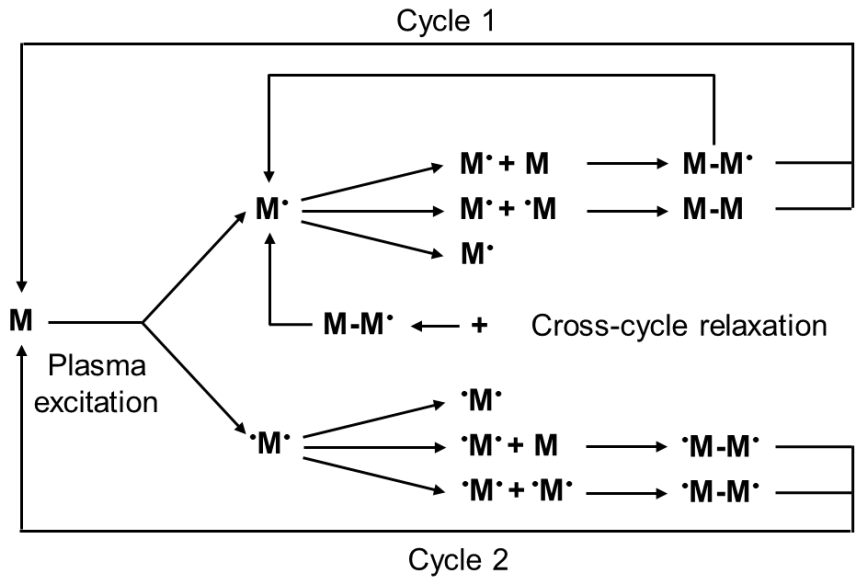

Figure 2.3: Rapid step growth polymerisation. **M** denotes a species undergoing a reaction in the plasma phase.[77]

RSGP starts with an initial excitation of the precursor, to generate monoradicals or diradicals. These then react with uncharged precursor molecules or other radicals in one of two cycles (cycle 1: monoradicals, cycle 2: diradicals). If the product of the reaction has no radicals, it is re-excited by the plasma and the process continues until the product condenses onto the substrate.[77]

2.3.5.2. The role of ions in plasma deposition

In the years since Yasuda's model, many authors have started to reevaluate the role of ions in plasma deposition, despite their low abundance. This is due to the consideration of the physics of placing surfaces into a plasma and the formation of sheath regions. However, the precise role of ions is still a topic of debate.[77,90]

The flux (J) of any species to a surface placed in a plasma is given by Equation 2.9, where n is the number of that species and v is its velocity given by Equation 2.10 (where k is Boltzmann's constant, T is the temperature of the species and m is the mass of the species).[90]

$$J = \frac{1}{4}nv \tag{2.9}$$

$$v = \sqrt{\frac{8kT}{\pi m}} \tag{2.10}$$

Electrons are much lighter than any other species and so move much quicker, resulting in higher electron flux to the surface and a build-up of negative charge at the surface. This negative charge then repels electrons and attracts positive ions creating a region of positive charge adjacent to the surface, called the sheath.[92] The sheath region repels any slow-moving ions, but if an ion is moving sufficiently fast, it can pass through and be accelerated toward the surface. This is called the Bohm velocity and is given by Equation 2.11.[90]

$$v_{Bohm} = \sqrt{\frac{kT_e}{m}} \tag{2.11}$$

As a result of the acceleration ions experience due to the negative charge build up on the surface, they gain a large amount of energy (10 – 30 eV). They can then collide with the surface and generate surface radicals that can react with species in the plasma phase.[93] The presence of these sites has been shown by EPR spectroscopy, specifically for poly(ethylene naphthalate).[94] However, given that this is an organic material it is maybe not a representative example of how all substrates would interact. Regardless, higher incorporation of precursor functionality is observed for ester-containing coatings when surface activation is used.

The concept of surface activation has led to the development of the ion-Activated Growth Model (AGM). In this model, a precursor can be incorporated into the coating through reactions with the surface sites (induced plasma polymerisation), as well as reactions in the plasma phase covered by the RSGP model (plasma-state polymerisation).[77]

Ions are not the only source of surface activation as this can arise due to electron impact and VUV, although the contributions of these processes are smaller than the contribution of ions. This is due to the lower energy of these species when compared to ions that have been accelerated towards the surface.[90]

2.3.5.3. Plasma phase reactions

In addition to simply activating the surface, there are those who believe that ions also contribute significantly to the mass of the final coating. There are several reasons for this. First, plasma polymers have very similar chemistries to hyperthermal films. Hyperthermal films are deposited only from ions. Secondly, ions have higher sticking probabilities. Around 20 – 50% of ions that arrive at the surface will stick as against < 0.1% for neutrals and radicals.[95] This is because ions arrive at the surface with significant energy, whilst other species are reliant on the surface being activated (to provide the chemical energy necessary to facilitate the reaction). Radicals must also collide with the surface in the correct orientation, meaning the rate of deposition can be further slowed by steric effects.[90]

Further to the higher sticking probabilities, there are also more ions at the surface due to the negative charge. In addition, ions are potentially larger than radicals as they are not formed by fragmentation. This means that an ion that arrives at the surface will contribute more mass to the final coating than a given radical.[90]

The sticking probability can be improved if the precursor contains double bonds as these can react with surface species by radical propagation reactions, which greatly increases the rate of deposition as following the AGM.[77]

When accounting for the contribution of ions, there appear several additional reactions with ions not accounted for in the RSGP model and AGM. Considering only two-body collisions in the plasma bulk, there are five chemical reactions possible. These are shown in Equations 2.12 to 2.16, where *N* indicates a neutral species, *I*, an ionic species and *R* a radical species. The reactions are arranged in descending order of probability.[90]

$$N + R^{\cdot} \rightarrow NR^{\cdot} \quad (2.12)$$

$$R^{\cdot} + R^{\cdot} \rightarrow N \; or \cdot RR \cdot \quad (2.13)$$

$$N + I^{+} \rightarrow NI^{+} \quad (2.14)$$

$$I^{+} + R^{\cdot} \rightarrow IR^{+\cdot} \quad (2.15)$$

$$I^{+} + I^{-} \rightarrow N \quad (2.16)$$

2.3.6. Coating chemistry

The chemistry of the final coating is derived from the precursor used. Plasmas can be created from a wide range of precursors and as such a wide range of coating chemistries are possible.[77] Quite often the goal is to incorporate as much of the original precursor functionality into the final coating as possible, imparting the coating with the properties of the precursor. However, this is challenging as there are numerous fragmentation pathways possible, leading to a range of different functional groups in the final coating. For example, using an ether or alcohol precursor containing C-O bonds, will result in a coating with a degree of C=O bonds. In addition, the highly cross-linked structure provides an environment for stable radicals to form. These can be later oxidised, modifying the coating chemistry after it has been prepared.

Several papers describe so-called "soft landing" of precursor molecules onto substrates.[91,96] The idea of this is to deposit the precursor with minimal damage. There are two parts to this. First is to use higher pressures as this reduces the energy of each individual ion through a greater number of collisions, making it more likely that the functional group survives the collision with the surface. The second part is to use lower power. This means less energy is transferred to the precursor molecules in the plasma phase, reducing the amount of fragmentation.

Applying these principles has been reported to improve functional group retention, such as for -COOH groups and even nitroxide radicals.[96,97]

2.3.7. Considerations of coating powders and other non-uniform substrates

Most substrates used for plasma polymerisation are very flat, such as silicon or polytetrafluoroethylene (PTFE) wafers. For a substrate that is not smooth or a powder, the amount of material arriving at different points on the surface will vary resulting in a non-uniform coating. One approach to deal with this as mentioned previously is to agitate a powder sample during deposition, either with a loudspeaker or by rotating the vessel.[89] However, the equipment to do this is not a standard set up.

2.3.8. Precedent for using plasma polymers in batteries

As outlined in the previous section, plasma polymerisation is a solvent-free method of quickly depositing, thin and uniform coatings with a wide variety of surface chemistries. These are all desirable characteristics when choosing a coating method for use in batteries. Furthermore, the fact that the coatings are organic polymers likely endows them with mechanical flexibility, allowing them to avoid cracking during cycling.

Whilst not commonly used, there is some precedent for using plasma polymerisation to prepare coatings for use in batteries. In the 1990's, Takehara *et al.* coated lithium anodes with a plasma polymer derived from 1,1-difluoroethene. This was chosen as it can complex with lithium to allow for a degree of ionic conductivity.[98] It was suggested that these coatings will supress dendrite formation, although they were never tested in a cell and so it is unclear what practical impact they would have.

In 2002, Nakajima *et al.* also used plasma polymerisation, this time to improve the performance of graphite anodes. Described as "plasma-fluorinated graphite", rather than a coating, graphite was exposed to a plasma derived from CF_4.[99] This led to slightly improved capacities, of up to 382 mA h g^{-1}, which slightly exceeds the theoretical capacity of graphite (372 mA h g^{-1}). This is thought to be because the fluorination increases the surface area, improving the kinetics of lithium intercalation. However, the effect of these coating was only tested up to 10 cycles, and so the effect of these coatings on long-term cycling is unknown. More recently fluorinated plasma polymers have been investigated to coat ZnO anodes.[100] Whilst these do improve capacity retention, coating the material results in a different electrochemical profile, with no visible plateaus. The authors do not comment on this difference, so it is unclear why this occurs.

It is worth considering that the highly cross-linked nature of plasma polymers may impede ion migration. This was highlighted in the previously mentioned work by Takehara *et al*, who note that the conductivity of plasma polymerised poly(1,1-difluoroethene) is lower than its conventionally polymerised counterpart (3×10^{-8} S cm^{-1} vs 4×10^{-7} S cm^{-1}).[98] Therefore, it may be necessary to optimise conditions that yield a lower degree of cross-linking.

Another observation is that the cases where plasma polymers have been used, they have been exclusively to coat anodes. Whilst this may be because the SEI has been known about for longer, it raises the question of whether a plasma polymer will be stable at the high voltages that a cathode will experience.

2.3.9. Potential coating chemistries

Central to applying plasma polymerisation to cathode materials will be the identification of coatings that benefit performance, whilst still being possible to prepare with plasma polymerisation. An ideal material would possess all the advantageous properties of the various materials previously discussed. It would be electronically insulating, to suppress reactions, whilst still enabling ion migration. Additionally, it should be electrochemically stable over the voltage range the cell operates, as well as chemically resistant to being dissolved by the electrolyte solvent. The coating ideally would have HF scavenging groups to reduce transition metal dissolution. Finally, it should be flexible to prevent cracking during cycling. Given the control plasma polymerisation enables the user over the final coating, it should be possible to achieve several of these under the right conditions. The following sections will discuss three possible coating families that could be useful in the context of batteries. These are: poly(ethylene oxide)-like films, fluorinated plasma polymers and silicon-containing coatings.

2.3.9.1. Poly(ethylene oxide)

Poly(ethylene oxide) (PEO) is a polymer with a backbone comprised of C-C and C-O bonds. Its structure is shown in Figure 2.4. PEO has been investigated as a solid-state electrolyte, as lithium ions can "hop" through the structure by coordinating to the oxygen atoms in the polymer backbone.[101,102] This ability to conduct lithium ions may mean it is a viable cathode coating.

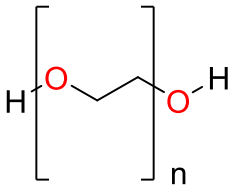

Figure 2.4: The structure of PEO.[101]

PEO-like coatings are also of interest in the field of plasma polymerisation for use as antifouling coatings. As such, there are several different methods for creating these coatings from different precursors containing the -CH_2CH_2O- structural unit.[103] Ethers such as tetraglyme, 12-crown-6 or 15-crown-5 are perhaps most preferable in terms of the structure of the final coating. These precursors have been shown to lead to coatings with high PEO character with over 80% of the carbon environments being C-O bonds.[104] However, all these precursors are hazardous, which is not ideal for industrial applications.[105] An alternative method is to use ethanol. Whilst this results in fewer C-O bonds (around 17%), ethanol is much simpler to create coatings from.[106] This is because no heating elements are required to maintain suitable vapour pressure, unlike the previously mentioned ethers.[104]

A potential issue with the application of these coatings to cathode materials is their electrochemical stability. Conventional PEO is stable up to between 4 – 4.6 V, owing to oxidation of OH groups.[58,101] It would therefore be expected that plasma polymer with PEO-like chemistry would not exceed this upper range. Materials like LNMO operate at voltages just outside this range (4.7 V), and so it is likely that the coatings would break down in this system. This is not to say that the coatings would be useless. PEO fragments are found in natural CEIs so the coating may still benefit the performance to a degree.[50] It could also still be applied to lower voltage materials such as lithium iron phosphate (cell voltage around 3.5 V).[107]

3.3.9.2. Fluoropolymers

Like PEO, fluoropolymers have been investigated as solid-state electrolytes. Figure 2.5 shows an example of such a material as reported by Ma *et al.* This family of materials are stable up to 5.3 V, owing to the strength of the C-F bond, which would make them ideal for coating high-voltage materials.[108]

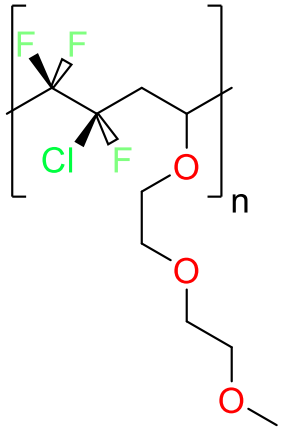

Figure 2.5: Copolymer of chlorotrifluoroethylene and diethylene glycol methyl vinyl ether.[108]

It is also possible to create fluoropolymers by plasma polymerisation of a precursor such as CF_4.[100] However, to achieve a structure like that of Ma *et al*, would require at least two precursors to incorporate the ether sidechain. This is important as removing it would reduce ionic conductivity. One way to achieve this would be to first deposit a coating with a particular chemistry, along with a functional handle, which could be used to attach the sidechain.[109,110] This would however increase the complexity of the preparation procedure. Another possibility would be to use a precursor with both desired functionalities, such as perfluoro-15-crown-5, although this may lead to unforeseen complications due to unexpected interactions between the different groups.

2.3.9.3. Silicon-containing coatings

The previous discussion of different coatings highlights that silicon-containing coatings are advantageous due to the ability of silicon to scavenge HF. Therefore, the final class of materials considered as part of this review are silicon-containing polymers.

A common feature of many of the solutions discussed for extending battery lifetimes is the incorporation of HF scavengers, typically some sort of Si-O group. This is the reason for including this last class of materials, siloxane polymers. These are a very interesting set of polymers that can have extremely diverse structures and functionalities, achieved simply by varying the deposition conditions. These can range from organosilicon films, with a high level of organic character, to films that are predominantly SiO_x.[111]

Siloxane polymers are advantageous over other Si-O containing materials discussed previously, as a result of the precursors used. Typically, this is hexamethyldisiloxane

(HMDSO) (Figure 2.6), due to its low cost and toxicity, which sets it apart from the precursors for ALD.[112]

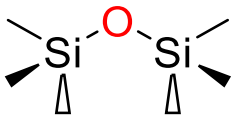

Figure 2.6: Structure of HMDSO.[112]

To maximise HF scavenging capabilities, maximising Si-O groups is perhaps the most important consideration when choosing deposition conditions. This can be achieved by three methods. First, higher power conditions result in a greater degree of fragmentation, favouring the formation of O-Si-O groups in the coating.[113] Second, the precursor vapour can be mixed with a large amount of oxygen (10:1 oxygen:HMDSO), resulting in more oxygen being incorporated into the structure.[114] Third, the frequency of the radiowaves can be increased to microwaves, as this also increases fragmentation.[115]

The Si-O bonds present in these siloxane polymers may have further benefits beyond HF scavenging. It has been shown that O-Si-O groups in these polymers can hydrolyse in the presence of water, to Si-OH.[114] This would be advantageous, because as previously mentioned, residual water is the cause of HF formation. Therefore, these coatings may offer two routes to dealing with HF formation.

2.4. Disordered rocksalts

2.4.1. Introduction

As mentioned in the introduction, one way to improve the energy density of a battery is to use electrode materials with high capacities. One such family of materials being investigated as potential cathode materials are cation-disordered rocksalt (DRX) materials ($LiMO_2$). These materials can access both transition metal and oxygen redox (O-redox), resulting in high capacities, with up to 425 mA h g^{-1} being reported (layered oxides *ca.* 220 mA h g^{-1}).[116]

2.4.2. Cation disorder and structure of DRXs

As the name implies, DRXs are based on the rocksalt structure (space group 225, Fm-3m). This means that they consist of a 1:1 ratio of cations to anions, in a cubic close packed arrangement. What makes a DRX cation-disordered is that the different metal cations do not occupy specific sites in the structure as they would in a layered material. Instead, the cations are randomly mixed across all cation sites.[117] Figure 2.7 shows a diagram of the rocksalt structure.

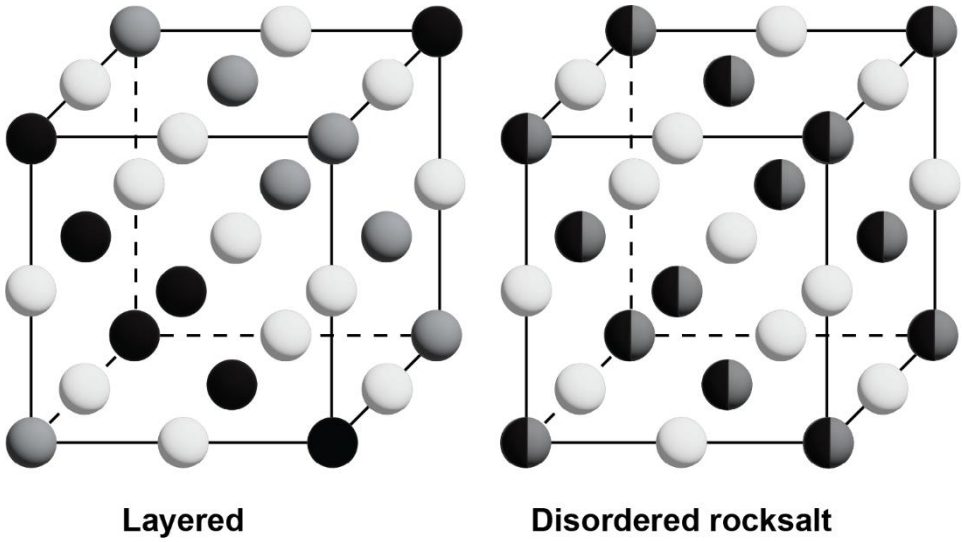

Figure 2.7: The DRX structure compared to a layered rocksalt structure. White, grey and black circles represent oxygen, lithium and transition metal ions respectively. Based on Figure 1 in the review by Clement *et al.*[117]

Cation disorder was generally thought to impact performance. Whilst this is true for some materials, such as $LiTiO_2$, these materials are generally synthesised without an excess of lithium ions and therefore would be expected to have poor electrochemical performance

(see Section 2.4.3.).[118,119] In fact there are several benefits that arise from cation-disordered structures. Firstly, DRX materials have a much larger compositional space that can be utilised compared to layered materials. In layered materials, migration of transition metal ions to lithium sites on delithiation leads to poor reversibility. Therefore, only transition metal ions with high barriers to migration can be used. This limits materials to those primarily prepared from nickel, cobalt and manganese (provided it is redox inactive and remains 4+). The reason for this is that these ions have high barriers to migration from octahedral sites due to their ligand field stabilisation energies.[120] This consideration is unnecessary in DRX materials as all cation sites are the same. It is therefore less of an issue if the ions migrate, although migration to tetrahedral sites (rather than octahedral sites) can still be a problem, due to impeded lithium-ion movement.[121] An additional benefit in terms of cycling performance is that the disordered structure also results in small isotropic volume changes.[117] The disordered arrangement is also what enables O-redox and the resulting high capacities of DRX materials.[122] This will be discussed further in Section 2.4.4.

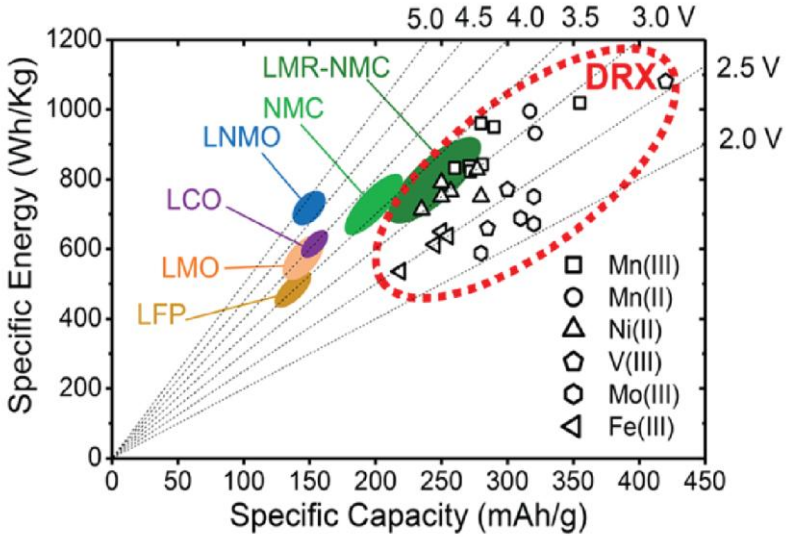

Figure 2.8: Comparison of specific capacity of DRX materials with other known cathode materials. From the review by Chen *et al*, Figure 1a.[123]

Lithium ions are generally much larger than transition metal ions, due to their lower charge. Yet, in a DRX structure, all cations occupy the same sites, resulting in distortions. One way to mitigate these distortions and stabilise the DRX structure is to incorporate d^0 metal ions. This is because in the absence of *d* electrons, the energy of the site depends solely on the oxygen orbitals, which are always occupied. This means that the d^0 ion is less sensitive to site distortions, and therefore able to accommodate the distortions from other ions.[124] As a result, many reported DRX materials contain a d^0 ion, such as Ti^{4+}, V^{5+} or Nb^{5+}.[117,125]

2.4.3. Lithium-ion movement in DRXs

In DRX materials lithium ions move by hopping between adjacent octahedral sites via an intermediate tetrahedral site. This is referred to as o-t-o diffusion and is summarised in Figure 2.9.[126]

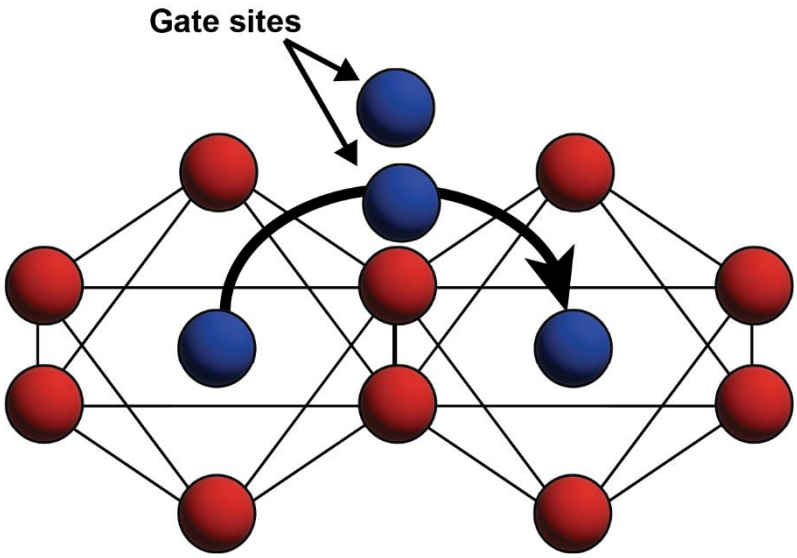

Figure 2.9: Diagram illustrating the o-t-o hops in a DRX. Red circles indicate anions, blue circles indicate metal cations. Based on Figure 2b in the paper by Urban et al.[126]

Figure 2.9 shows that there are four cation sites. The cation disorder present in a DRX means that for the cations shown in Figure 2.9, there are five possible combinations. These are Li_4, Li_3M, Li_2M_2, LiM_3 and M_4 (where M refers to the transition metal cation(s)). For lithium ions to be able to move, the two octahedral sites must be occupied by lithium ions and so LiM_3 and M_4 sites do not contribute to lithium-ion diffusion. The energy barrier associated with lithium ions hopping between octahedral sites depends on the cations either side of the tetrahedral site, which are termed gate sites. If either or both sites are occupied by transition metal ions, the electrostatic repulsion is too great for lithium ions to "hop". Therefore, only sites where all four cations are lithium ions (referred to as 0-TM sites) can take part in lithium diffusion.[126]

Stoichiometric DRXs with a 1:1 ratio of lithium to transition metal cations exhibit poor electrochemical performance.[118] This is because for lithium ions to move throughout the structure, known as percolation, there needs to be networks of connected 0-TM sites.[119] For this to occur, an excess of lithium ions is required. Specifically, an excess of 9% enables percolation to become active, whilst an excess of 25% enables the extraction of one lithium ion per formula unit.[126] This might suggest that the lithium content of a material should be

increased as much as possible. However, this comes at the expense of transition metal ions, reducing the conductivity and increasing the reliance on O-redox which negatively impacts cycling stability.[127]

The minimum thresholds assume a fully random structure from which percolating networks can form. However, the DRX structure is not completely random, with local ordering or short-range order (SRO) being observed, impacting the formation of percolating networks.[125,128] How SRO manifests is a balance between contributions from bonding and electrostatics.[127] Jones *et al* report that ordering occurs so that some level of local electroneutrality is achieved.[129] Analysis of PDF data by Szymanski *et al* also suggests that high valent cations (such as Ti^{4+}) ideally are as far away from each other as possible, to minimise electrostatic repulsion. They also suggest that there are local displacements to minimise strain that occurs because of size differences.[130] In fluorinated DRX materials (see Section 2.4.5.), bonding preferences also play a role. The stronger bonding between lithium and fluorine compared to fluorine and a transition metal, results in fluorine preferentially associating with lithium. This leads to the formation of lithium-rich/transition metal poor regions.[127,131]

The impact that SRO can have on percolating networks, and by extension, the electrochemical performance of a material has led to a number of different ways to attempt to influence it. These can be minor modifications to synthesis procedures, such as rapid quenching to "lock in" the disordered arrangement.[129,132] A more drastic approach is to supress any ordering. This can be achieved by using many different transition metal ions in a single "high entropy" material, such as $Li_{1.3}Mn_{0.1}^{2+}Co_{0.1}^{2+}Mn_{0.1}^{3+}Cr^{3+}Ti_{0.1}Nb_{0.2}O_{1.7}F_{0.3}$.[133] This is not to say that SRO is entirely negative as it can be useful if the formation of lithium-rich regions is promoted.[127] As already discussed, this can be achieved using fluorinated DRXs as the favourable bonding between lithium and fluorine promotes the formation of lithium-rich, transition metal-poor regions.

2.4.4. Oxygen redox

2.4.4.1. Oxygen redox in DRX materials

As mentioned previously, many DRX materials achieve capacities greater than would be expected for solely TM redox. This additional capacity is thought to originate from redox activity of the oxide anions, so-called O-redox.[134]

O-redox is not unique to DRXs, with it being reported for other, layered materials.[135] However, DRX materials are particularly prone to it. This is because Li-rich materials with disordered arrangements favour Li-O-Li bonding configurations (with the Li ions being at 180° to each other). Furthermore, the octahedral coordination of oxygen in a DRX means that multiple such configurations are possible for a single oxide anion. In this Li-O-Li arrangement, there is poor overlap between the oxygen 2p and the lithium 2s orbitals, leading to a low degree of hybridisation.[122] This means that the oxygen 2p orbital is higher in energy and active towards O-redox as it is close in energy to the Fermi level.[122,134]

To be practically useful, the additional capacity accessed through O-redox needs to be reversible. Understanding what makes O-redox requires understanding the nature of the oxidised oxygen species and how they form. This is a topic that has attracted a large amount of debate. Some works suggest molecular oxygen is formed, whilst others suggest peroxide species, with others suggesting both.[136–139]

It should be pointed out however, that the studies cited explore different materials. Therefore, the discrepancies observed may be because the different materials respond differently to O-redox. The work by Yue *et al* provides precedent for this.[138] They observe that $Li_{1.15}Ni_{0.45}Ti_{0.3}Mo_{0.1}O_{1.85}F_{0.15}$ shows greater O_2 evolution than $Li_{1.15}Ni_{0.35}Ti_{0.5}O_{1.85}F_{0.15}$, which they suggest is due to the addition of molybdenum. This being said, the stoichiometries are not perfectly comparable, which highlights part of the challenge of preparing materials for direct comparison.

There is also the possibility that there are other processes occurring within the material that might produce oxidised oxygen species, giving the appearance of O-redox. This is argued by Ogley *et al*, who note that molecular oxygen is observed in different layered materials (NMC811 and LCO) despite their different structural responses to delithiation.[140] Combined with the variation between materials, this means that without performing a systematic study on a range of materials, it is very difficult to draw general conclusions about the nature of the oxidised species.

2.4.4.2. Characterising oxygen redox

As this thesis is concerned with studying local structure, it is worth exploring the different techniques used to explore the structural transformations occurring when O-redox is thought to be active. This will include examples for materials other than DRXs, to understand what has been done to study O-redox in a broader sense. Further information about the fundamental theory of these techniques can be found in Chapter 3.

It is worth mentioning that the first indication of O-redox is usually found in the electrochemistry, with additional capacity being observed beyond what is expected solely for transition metal redox.[141] Whilst this does not give any information about the species formed, it does suggest at what voltages they are formed, which informs what voltages should be explored by other techniques.

Of the techniques used to probe oxygen species, perhaps the most highly regarded is O K-edge resonant inelastic X-ray scattering (RIXS). This is because it can distinguish between molecular oxygen, superoxides and peroxides, based on the vibrational features close to the elastic peak. These features have been observed for Li_2MnO_2F, and were assigned to molecular oxygen over other species, in agreement with DFT results.[136] Beyond DRXs, this method has been used to confirm the presence of molecular oxygen in other materials, including $LiNiO_2$, $Li_{1.2}Ni_{0.13}Co_{0.13}Mn_{0.54}O_2$.[142,143] However, it should be noted that this signature of molecular oxygen is seen for other materials, including NMC811 and LCO, which should not experience the same O-redox processes.[140] This could suggest that the oxygen observed does not come directly from O-redox but is instead formed because of structural changes that occur on cycling, giving the appearance that it is derived directly from the electrochemistry. Gao *et al* have also argued that the molecular oxygen signature observed comes from the dissociation of M-(O-O) species within the structure.[144] This is thought to occur because of the X-ray beam used in the RIXS measurement. Despite this, subsequent works still argue for the presence of electrochemically produced molecular oxygen, on the basis of RIXS.[145]

In addition to the signature from molecular oxygen, it has also been reported that RIXS data shows the formation of -OH groups in $Li_{1.2}Ni_{0.13}Co_{0.13}Mn_{0.54}O_2$.[146] This is because the spacings are like what would be expected for bending modes of transition metal hydroxides. However, at present, this has only been reported once with no evidence from other supporting techniques and so requires further investigation.

Additional O K-edge RIXS features can also be observed at an emission energy of around 525 eV. These have not been attributed to anything more specific than oxidised oxygen species. However, they have been reported for multiple materials.[138,141] As such, the growth and decay of these features on cycling can be used to give some indication into the reversibility of the O-redox processes.

When O K-edge RIXS is unavailable, O K-edge XAS has been employed. This was used by Abulikemu *et al* to confirm stable electronic configurations on cycling and by Jiang *et al* to show oxidation of oxygen occurs.[147,148] However, any conclusions drawn from this are unreliable as the O K-edge pre-edge features (which are of specific interest) can be distorted by transition metal effects.[149]

Another useful technique is Differential Electrochemical Mass Spectrometry (DEMS). This can detect oxygen that forms on cycling, such as in LMNO and Li_2NiO_2F which show formation of oxygen gas on charging above ~4.2 V.[137,150] Equally, it can be used to rule out the presence of molecular oxygen.[147] Whilst this can be used to corroborate RIXS measurements, it also allows the effect of countermeasures (such as fluorination) to be tested.[137] DEMS can also be used to detect CO_2, the presence of which implies the existence of oxidised oxygen species, which react with the electrolyte solvent to form CO_2.[143]

The use of XPS has also been reported, to identify the presence of peroxide species.[139,151,152] The challenge of doing this is the limited sampling depth of XPS (< 10 nm), as CEI formation may confuse interpretation. Whilst the data presented by Sathiya and McCalla contain peaks assigned to the bulk material, implying the CEI is not obscuring the sample completely, it is not possible to probe into the bulk of the material with this technique. It is worth mentioning that the work by McCalla *et al* also uses STEM, supported by neutron diffraction, to visualise O-O dimers, providing further support for peroxide formation.

An alternative way to investigate oxidised oxygen species is to use EPR spectroscopy. O_2^{3-} and O^- are EPR active and therefore can be observed (O_2^{2-} is EPR silent). This approach is not applicable to all materials however, as it relies on the transition metal ion being diamagnetic to avoid dominating any signal from the oxygen species of interest. This is true for the material $Li_2Ru_{0.75}Sn_{0.25}O_3$ at high voltages, allowing oxygen species to be observed.[153]

Another potential technique is ^{17}O NMR as it is sensitive to local environments whilst avoiding the risk of beam damage associated with RIXS. ^{17}O NMR has never been applied to a DRX material (as of the time of writing) but was used by House *et al* to study molecular oxygen in $Li_{1.2}Ni_{0.13}Co_{0.13}Mn_{0.54}O_2$.[142] The spectra recorded show a broad peak, centred at 3000 ppm with spinning sidebands. This is assigned to molecular oxygen on the basis that its chemical shift allegedly matches that of condensed oxygen, with the breadth being because of the paramagnetic nature of oxygen molecules. The signal also appears on charging and reduces in intensity on discharging, suggesting that it is related to electrochemical processes. However, this seems an unlikely assignment for several reasons. First, Bassey *et al* suggest that the chemical shift is incorrect for molecular oxygen. In addition, C_Q for such an environment would be large making any signal difficult to observe. Further broadening would arise due to the rapid relaxation of paramagnetic species.[154] Fermi contact shifts would also likely result in much larger chemical shifts. For example, Clement *et al*, suggest that a fluorine nucleus directly bound to a paramagnetic metal ion, would have a chemical shift of around 5300 ppm.[155] In the case of molecular oxygen, the oxygen atoms are the paramagnetic centres, meaning that it would not be inconceivable that the chemical shift would be even larger. For all these reasons it is highly unlikely that the signal observed comes from molecular oxygen, and that such a signal would be incredibly challenging to observe. A more likely suggestion is that it comes from oxygen bonded to transition metal ions that become more diamagnetic on charging. Alternatively, it could be due to O_2^{2-} species. As previously stated, these are diamagnetic, meaning that out of all the potential oxidised oxygen species, they are most amenable to NMR. In this case the breadth of the signal would be because the surroundings are highly paramagnetic, due to the transition metal ions and any molecular oxygen trapped within the structure.

It is interesting that RIXS has been applied to several different materials, and whilst molecular oxygen is sometimes observed, peroxides and superoxides are never observed. This is despite being observed by other techniques (EPR, STEM and possibly XPS). Based on the literature discussed so far, it does seem that different materials respond differently to O-redox, and therefore it is not surprising that RIXS gives different results. However, the fact that other oxygen species are never observed by RIXS (based on the literature presented here) could suggest that it is a challenge of the technique. For instance, RIXS is a "photon hungry" technique and thus is prone to beam damage. Perhaps the high flux of X-rays destroys any other oxygen species, possibly causing them to decay to molecular oxygen. As mentioned, this has recently been suggested, although it is the subject of

debate.[144] Therefore, whilst RIXS can be a valuable tool in identifying species, it perhaps should not be relied upon to rule out particular species.

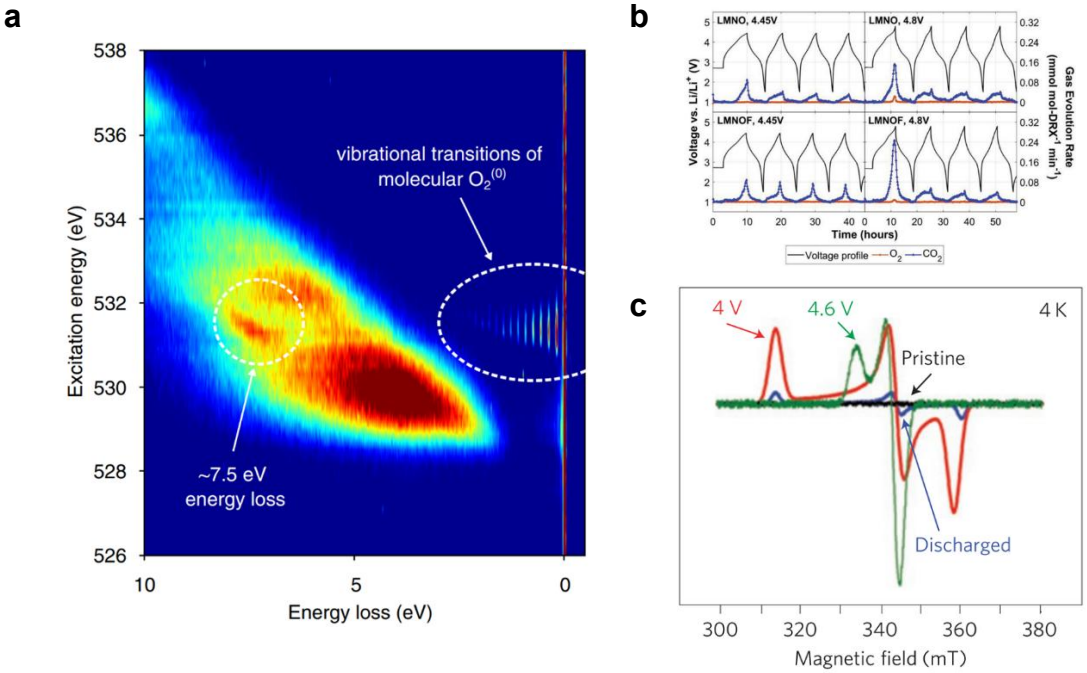

Figure 2.10: Some of the analytical techniques used to study O-redox. (a) High resolution RIXS map of $Li_{2-x}MnO_2F$ recorded at 5 V. From Figure 3b in the paper by McColl *et al.*[136] (b) *In situ* DEMS data collected for multiple cycles at different cut-off voltages for LMNO and LMNOF. From Figure 6 in the paper by Crafton *et al.*[137] (c) X-band EPR spectra of $Li_2Ru_{0.5}Sn_{0.5}O_3$ recorded at different states of charge at 4 K. From Figure 5c from the paper by Sathiya *et al.*[151]

The techniques discussed so far have solely focussed on probing the oxygen species. However, it is useful to support this by probing the redox activity of the transition metal ions. Transition metal L-edge XAS can provide information on whether transition metal redox is active at a particular voltage.[147,148,156] If this is challenging, such as in the case of titanium, L-edge RIXS can be employed instead.[156] EPR can also be used to track whether metal redox has stopped at a particular voltage based on the intensity of the signal.[147]

2.4.5. Fluorinated DRXs

Whilst O-redox offers additional capacity, this capacity is often not reversible. This is due to loss of oxygen from the structure as well as parasitic side reactions caused by reactions of the oxidised species with the electrolyte solvent.[134] There is therefore interest in developing strategies to counter the deleterious effects of O-redox.[117,157] One potential method is to partially substitute oxygen for fluorine. This lowers the total charge of the anions, whilst maintaining the cation to anion ratio required for a DRX. This means that the transition metal ion can be in a lower oxidation state, allowing for more lithium to be

extracted by transition metal redox, even allowing double redox processes (*e.g.*, $V^{3+} \rightarrow V^{5+}$). This reduces the reliance on O-redox.[117,158,159]

2.4.5.1. Structure of fluorinated DRXs

Transition metal - fluorine bonds have high bond energies and are therefore unfavourable. This means that fluorination is not possible in layered materials as each fluoride ion would be bonded to three transition metal ions.[117] In a DRX however, the disordered arrangement imparts greater flexibility in terms of bonding environments. This means that fluoride ions can preferentially associate with lithium ions, which is further assisted by the lithium-rich nature of DRX materials. This allows the fluoride ions to occupy lithium-rich, transition metal poor regions of the material.[117,158,160] Monte Carlo simulations suggest that up to 90% of the fluorine in a material may be coordinated to either six lithium ions or five lithium ions and one transition metal ion.[155]

Whilst the disordered arrangement of DRXs makes fluorination possible, it is not straightforward. This is because the bonding in LiF is stronger than transition metal fluorides. As such there is no thermodynamic driving force for fluorine substitution, limiting the solubility of LiF into the DRX structure.[161] The typical limit for fluorides prepared by solid state synthesis is ~ 10 at.%. This can be improved to around 30 at.%, by using ball mill synthesis, owing to the ability of ball milling to access metastable states.[158] However, a reliance on ball milling limits any industrial application of these materials, as ball milling is highly inefficient.

It is possible that a modest level of fluorination may in principle, be practically useful in supressing O-redox. However, the preference for fluorine to form lithium-rich domains means that at low levels of fluorination, there are isolated lithium domains, negatively impacting percolation. Above a suitable level, the lithium-rich domains connect facilitating percolation.

This means that for a given material, there is a limited compositional space that results in electrochemically viable oxyfluoride DRXs.[117]

2.4.5.2. Effects of fluorination on material performance

The objective of fluorination is to suppress O-redox, and there are examples in literature where oxide DRXs are compared to analogous oxyfluorides, with reduced oxygen evolution being observed. For example, Crafton *et al*, compare $Li_{1.2}Mn_{0.625}Ni_{0.175}O_{1.95}F_{0.05}$ to

LMNO, and observe reduced O_2 production using DEMS.[137] Li *et al* also report that a plateau in the electrochemical data (that is attributed to O-redox) is reduced for an oxyfluoride material compared to an oxide.[160] This would suggest that fluorination can be an effective means of reducing O-redox. However, in both cases, O-redox is not perfectly suppressed and there are other examples where O-redox appears to still be active in oxyfluoride materials. EPR data collected for Li_2VO_2F at 4.1 V indicates the presence of superoxide species, which is supported by DFT calculations, and these are suggested to be responsible for the poor performance of the material.[13] DEMS measurements on Li_2NiO_2F show oxygen evolution, and RIXS measurements performed on Li_2MnO_2F show evolution of molecular oxygen.[136,150] This suggests that it is not possible to fully supress O-redox with the levels of fluorination currently achievable.

It should be noted that the fluorine incorporated into the DRX is not necessarily stable, particularly at high voltages. Crafton *et al* found that approximately 1 – 2% of the fluorine within the structure can dissolve at high voltages.[159] Fluorine loss has also been reported by Yue *et al*.[162] This however can be beneficial as it can form a passivating layer on the surface, reducing further parasitic reactions.

2.4.5.3. Characterising oxyfluorides

As oxyfluoride materials are typically prepared by ball milling, they can be challenging to characterise by diffraction as the small particle size leads to broad peaks. Furthermore, the similar scattering strengths of oxygen and fluorine mean that they cannot be readily distinguished by scattering-based techniques, such as pair distribution function (PDF) analysis.[117] Microscopy has been used to provide some insight, suggesting that oxygen and fluorine do occupy the same lattice sites.[163] Another useful technique is ^{19}F solid-state NMR. Whilst the intrinsic paramagnetism of many systems and overlapping signals from binders or salts can make interpretation challenging, the sensitivity of the ^{19}F nucleus means that this has been used in multiple papers to study oxyfluorides.[150,155,159] This allows the identification of LiF and LiF-like phases.

In theory it could be possible to use F K-edge XAS to probe redox processes, however it is difficult to disentangle multiple contributions to the spectra.

2.4.6. Synthesis methods

2.4.6.1. Solid-state synthesis

One way to synthesise DRX materials is by standard solid-state synthesis. The DRX phase is never the ground state structure, due to the distortions created by disordering. However, above a certain temperature the entropic contribution to the free energy means cation disordering becomes feasible. There are therefore many examples of materials prepared this way, such as $Li_{2-x}VTiO_4$, $Li_{1.2}Mn_{0.4}Ti_{0.4}O_{1.6}F_{0.4}$ and $Li_{1.15}Ni_{0.375}Ti_{0.375}Mo_{0.1}O_2$.[130,164,165] Typical syntheses involve heating between 700 – 1100 °C, under air or argon flow for 10 – 12 hours.[117,165]

There are however several challenges associated with solid-state synthesis of DRX materials. Firstly, not all compositions are experimentally accessible as the disordering temperature is too high. This is because, whilst the entropic contribution is independent of the material (to first approximation), the enthalpy change associated with disordering is not.[117] For example, the high energy penalty associated with having Co^{3+} in distorted octahedra, means that $LiCoO_2$ disorders at ~5000 K. This is experimentally inaccessible as it is beyond the melting point of this material.[166]

Another challenge of solid-state synthesis is achieving high levels of fluorination, with levels of only ~ 7.5 at.% being achieved when using LiF as a precursor. This is due to the strength of the bonding in LiF, which leads to phase segregation at higher fluorination levels.[161] Other fluorides (such as MnF_2) can be used, however LiF still forms during the reaction. Increasing the reaction temperature can improve transition metal ion incorporation, however this leads to LiF evaporation and hence lower fluorination levels.[130] PTFE can also be used as the fluorine source leading to fluorination levels of ~ 10 – 12.5 at.%. This is because of the lower stability of PTFE compared to LiF, leading to a greater thermodynamic driving force for fluorine substitution.[158,161]

Zhang *et al* adopted an alternative approach to fluorinate their material. Instead of incorporating fluorine into the synthesis, $Li_{1.15}Ni_{0.375}Ti_{0.375}Mo_{0.1}O_2$ was prepared and then exposed to fluorine gas, using a fluidised bed reactor.[164] This leads to a lower capacity but better capacity retention. However, this method does not allow access to the other benefits of fluorination (suppressed O-redox, greater transition metal ion capacity, improved SRO) as fluorine incorporation is limited to an LiF layer on the surface.

It is also worth mentioning that DRX materials have been reported being prepared by hydrothermal synthesis, followed by being heated in a tube furnace under oxygen.[121] However, this type of method does not seem to be widely used, possibly because this method involves a number of steps.

2.4.6.2. Ball mill synthesis

Mechanochemical or ball mill synthesis is another method of synthesising DRX materials. It is especially useful for synthesising metastable materials with high fluorine contents (*e.g.*, Li_2VO_2F, Li_2MnO_2F and Li_2NiO_2F), that would otherwise be inaccessible by solid-state synthesis.[136,150,167] The reasons for why ball milling is able to achieve this are not fully understood.[168] Some work suggests that it is a result of shockwaves causing local heating and pressure effects when the balls strike the powder.[169] It has also been suggested that ball milling delivers mechanical energy equivalent to ~1750 ºC on an empirical basis.[168]

In a typical synthesis, metal oxides, LiF and Li_2O are mixed at high speeds (> 500 rpm) for at least 40 hours under inert atmosphere.[167,168] Whilst other precursors are added in stoichiometric amounts, Li_2O is usually added in excess (10%), to account for lithium loss during the synthesis. Precursors may also be mixed at slower speeds (~ 300 rpm) before the main, fast milling step.[168]

Whilst ball milling is useful, allowing access to high fluorine contents, it has several drawbacks. The long milling periods mean that it is energy intensive, despite often being touted as a "green" technique.[127,170] It is also challenging to scale up to an industrial level, owing to the extra infrastructure required, such as cooling systems.[171] This means that whilst the materials made by this approach may perform well, they may never see commercial use. Furthermore, on a material level, ball milled samples are prone to contamination from the milling media, which may influence their performance.[170] Highly fluorinated materials may also result in phase separation.[172]

2.4.6.3. Microwave synthesis

Both methods described previously are time and energy intensive. In addition, ball milling is also difficult to scale. A potential alternative method is microwave synthesis. This was reported by Wu *et al*, who were able to synthesise $Li_{1.2}Mn_{0.4}Ti_{0.4}O_2$ and $Li_{1.3}Mn_{0.4}Nb_{0.3}O_{1-x}F_x$ in less than five minutes.[132] This is made possible by using carbon as a susceptor which allows temperatures of over 1500 °C to be achieved very quickly. Samples are then quenched in water, so that the DRX structure does not have time to relax to a more

favourable structure. Comparing the electrochemical performance to the same materials synthesised by solid-state synthesis suggests that this is a viable approach to preparing DRX materials. However, it is not at present clear what level of fluorination is achieved (due to difficulty dissolving the samples for inductively-coupled plasma (ICP) analysis). This approach will likely also encounter the same problem as solid-state synthesis, in that certain compositions are inaccessible due to their high disordering temperatures.

2.4.6.4. Electrochemical synthesis

DRX materials can also be prepared electrochemically by lithiating a suitable precursor. Perhaps the most widely reported material this is true for is $Li_3V_2O_5$, which is prepared by electrochemical lithiation of V_2O_5.[173] This approach has since been reported for several other materials including Cr_2O_3 and MnO_2.[68] As this is performed on the scale of a single cell, it is not an industrially applicable method. However, it is perhaps a useful way to generate samples at different states of charge for mechanistic studies.

3. Characterisation methods

3.1. Solid-state nuclear magnetic resonance spectroscopy

3.1.1. Introduction

Solid-state nuclear magnetic resonance spectroscopy (SSNMR) is a useful probe of local structure. It is isotope specific, quantitative and non-destructive. SSNMR also has no requirement for long-range order, meaning that it is complementary to X-ray diffraction techniques, that will be discussed later. These qualities make it particularly useful in the characterisation of energy materials.

3.1.2. Nuclear spin

According to quantum mechanics, the state of a system is described by its wavefunction. For instance, the total nuclear wavefunction, Ψ_n, can be written according to Equation 3.1.

$$\Psi_n = \psi_{space}\psi_{spin} \tag{3.1}$$

Here, ψ_{space} is a function depending on the spatial coordinates of the nucleus and ψ_{spin} depends on the spin of the nucleus. The contributions to these functions do not greatly affect each other, and so the spatial component will be ignored as this section is concerned only with spin and its application to NMR spectroscopy.[174]

Spin or spin angular momentum (denoted **I**) is an intrinsic property of the nucleus, much like its charge or mass. It is determined by the number of protons and neutrons present in the nucleus.[175] The magnitude of the spin is given by Equation 3.2.[176]

$$|\mathbf{I}| = \hbar\sqrt{I(I+1)} \tag{3.2}$$

Here ħ is the reduced Planck's constant and I is the spin quantum number. I is quantised and can be zero, or take integer or half-integer values, *i.e.*, $I = 0, 1/2, 1$, *etc.* For a given value of I, there are $2I+1$ allowed spin states. Each of these is given a second quantum number, m_I, which takes values from $-I$ to I, in integer steps. Each of these spin states can therefore be expressed using Dirac notation as follows:

$$|I,m_I\rangle \tag{3.3}$$

It should be noted that in the case of a spin-1/2 nucleus, the two spin states are also denoted as α and β ($m_I = 1/2$ and $-1/2$ respectively).[175] This is also the case when discussing electrons and EPR spectroscopy (Section 3.2.).

The energy of a spin state can be determined using the Schrödinger equation (Equation 3.4), where $\hat{H}$ is the Hamiltonian, or energy operator and E is the energy of the system.[174]

$$\hat{H}|I,m_I\rangle = E|I,m_I\rangle \tag{3.4}$$

The Hamiltonian for a nuclear spin can be expressed using Equation 3.5, where $\hat{\boldsymbol{\mu}}$ is the magnetic moment operator and $\mathbf{B_0}$ is the applied magnetic field. $\hat{\boldsymbol{\mu}}$ is then calculated using Equation 3.6, which can be combined with Equation 3.5 to give Equation 3.7. Here $\hat{\mathbf{I}}$ is the spin operator and γ is the gyromagnetic ratio, a nucleus-specific constant.

$$\hat{H} = -\hat{\boldsymbol{\mu}} \cdot \boldsymbol{B}_0 \tag{3.5}$$

$$\hat{\boldsymbol{\mu}} = \gamma\hbar\hat{\boldsymbol{I}} \tag{3.6}$$

$$\hat{H} = -\gamma\hbar\hat{\boldsymbol{I}}\boldsymbol{B}_0 \tag{3.7}$$

As the field is applied along the z-axis, only $\hat{I}_z$ needs to be considered giving Equation 3.8.

$$\hat{H} = -\gamma\hbar\hat{I}_z B_0 \tag{3.8}$$

The solutions or eigenvalues of $\hat{I}_z$, are the values of m_I, and so substituting the Hamiltonian back into Equation 3.4 results in the energy of a spin state being given by Equation 3.9. Equation 3.10 then gives the energy difference between spin states, ΔE_z.[174]

$$E_{I,m_I} = -\gamma\hbar B_0 m_I \tag{3.9}$$

$$\Delta E_z = \gamma\hbar B_0 \tag{3.10}$$

From Equations 3.9 and 3.10, in the presence of an external field, the energies of the spin states are not degenerate. Instead, they are split by a constant (in the absence of other interactions) energy difference, ΔE_z. This is called the Zeeman splitting and is the interaction that makes NMR possible. The Zeeman splitting can also be expressed as a frequency. This is called the Larmor frequency and is given by Equation 3.11 (in hertz) or Equation 3.12 (in rad s^{-1}).[177]

$$\nu_0 = -\frac{\gamma B_0}{2\pi} \tag{3.11}$$

$$\omega_0 = -\gamma B_0 \tag{3.12}$$

Figure 3.1 shows the energy levels of a spin-1/2 nucleus in the presence of an external field, B_0. The allowed transitions, where $\Delta m_I = \pm 1$, are denoted by arrows.[176,178]

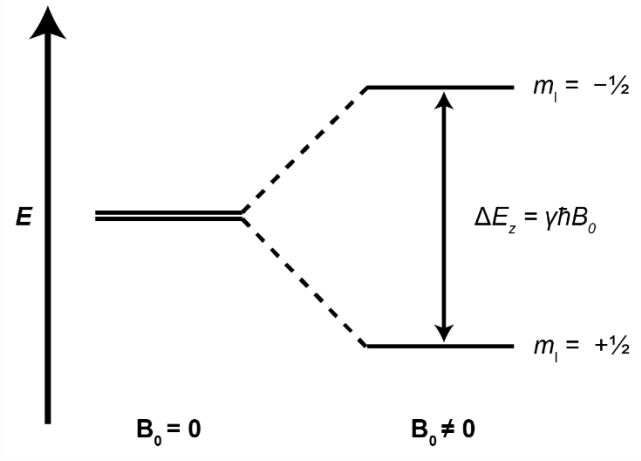

Figure 3.1: The relative energies of the two spin states for a spin-1/2 nucleus in the absence of and in the presence of an external magnetic field, B_0.

For a spin-0 nucleus, there is only one possible spin state (2×0+1), and hence only one energy level. There are therefore no possible transitions like what is shown in Figure 3.1. Therefore, spin-0 nuclei are not observable by NMR and are termed "NMR-silent".

The existence of an energy difference between the spin states means that for an ensemble of spins there is a population difference as per the Boltzmann equation (Equation 3.13). p denotes the population of an energy level, k_B is the Boltzmann constant, and T is the absolute temperature.[176]

$$\frac{p_{upper}}{p_{lower}} = exp\left(\frac{\Delta E_z}{k_B T}\right) \tag{3.13}$$

The population difference is the origin of the NMR signal and so its size is very important. However, the Zeeman energy (Equation 3.10) is very small compared to thermal energy at ambient temperatures. As such the population difference between spin states is also very small. For example, for ^{13}C in a 9.4 T field at room temperature, for every 100000 spins in the β state, there are 100017 in the a state. This means that the magnetisation is also small, and hence NMR is a fundamentally insensitive technique.[179]

From Equations 3.10 and 3.13 the magnetic field used when recording NMR spectra should be as large as possible to maximise the population difference. For this reason, NMR spectrometers generally use superconducting magnets with fields ranging from 4.7 to 28.2 T and beyond.[180] Often the strength of these magnets is described in terms of the ^1H Larmor frequency at that field, using Equation 3.11. For instance, a 9.4 T magnet would

be referred to as a 400 MHz spectrometer. Bulk magnetisation can also be increased by lowering the temperature of the sample. Whilst effective, this can be technically challenging at very low temperatures, at least at the time of writing.[181] Furthermore, relaxation times (Section 3.1.6.) increase, meaning that individual NMR spectra take longer to acquire.[182]

The small population difference means that, in principle, NMR experiments should be performed on as large a sample as possible, although there may be practical limitations imposed upon this by the equipment (see Section 3.1.7.). Most NMR-active nuclei are not 100% naturally abundant. ^{13}C for example, is only 1.1% abundant, which means that even with a large amount of sample, only 1.1% of the carbon atoms present will contribute to the signal. This can be overcome by enriching the sample, but this is expensive and not always straightforward.[179]

In addition, the gyromagnetic ratio depends on the nucleus, and so the sensitivity varies. Of the nuclei commonly encountered, ^{1}H has the highest gyromagnetic ratio, followed by ^{19}F, whilst ^{13}C is about four times lower. Table 3.1 shows some example nuclei, their natural abundance and their gyromagnetic ratios relative to ^{1}H.[179]

Table 3.1: Natural abundance of selected isotopes studied by NMR as well as the size of their gyromagnetic ratios relative to ^{1}H.[179]

Nucleus	Natural abundance/%	γ_x/γ_H
^{1}H	99.99	1
^{19}F	100.0	0.9410
^{31}P	100.0	0.4049
^{7}Li	92.41	0.3887
^{23}Na	100.0	0.2644
^{51}V	99.75	0.2629
^{27}Al	100.0	0.2607
^{13}C	1.07	0.2514
^{93}Nb	100.0	0.2448
^{45}Sc	100.0	0.2429
^{6}Li	7.59	0.1472
^{17}O	0.038	0.1356

Whilst these different gyromagnetic ratios can pose challenges with sensitivity, the fact that each isotope has a unique gyromagnetic ratio means that each isotope has its own Larmor

frequency. This means that when recording an NMR spectrum, generally only one isotope is observed.[179] As a result, NMR can generally be viewed as isotope specific, although it should be noted that this is not always the case. For example, the gyromagnetic ratios of ^{47}Ti and ^{49}Ti are -1.5105×10^{7} and -1.5110×10^{7} rad s^{-1} T^{-1}, respectively. This means that these nuclei are often observed simultaneously.[183]

3.1.3. The vector model and radiofrequency pulses

A wholly accurate description of NMR experiments requires the use of quantum mechanics.[174] However, it is possible to understand some aspects of the theory using a classical approach called the vector model. This provides an intuitive picture of how the radiofrequency (RF) pulses used in an NMR experiment interact with the nuclear spins. Furthermore, much of the language used to describe NMR experiments is based on the vector model.

As described in the previous section, nuclear spins possess a magnetic moment. In the presence of an external magnetic field, the most energetically favourable orientation for this magnetic moment is to be parallel to the direction of the external field (assuming a positive gyromagnetic ratio). Complete ordering of the magnetic moments is disrupted by thermal motion. Under the normal conditions used for an NMR experiment, the energy associated with thermal motion is much larger than the Zeeman interaction and so most magnetic moments do not align with the field. However, given the energetic preference to align with the field, when the vectors of all individual magnetic moments are averaged together, there will be a slight net alignment with the field. The entire sample therefore has a magnetic moment, referred to as the bulk magnetisation or polarisation, aligned along the z-axis, the direction of the external field (Figure 3.2).[177]

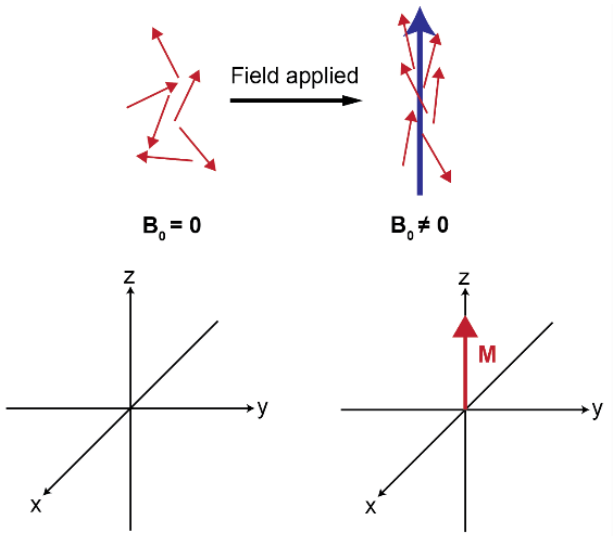

Figure 3.2: Formation of the bulk magnetisation through the application of an external magnetic field along the z-axis. The red arrows represent individual nuclear spins, and the blue arrow represents the applied field, B_0. The arrow labelled M represents the bulk magnetisation.

If the bulk magnetisation moves away from its equilibrium position along the z-axis, it will precess at the Larmor frequency (Figure 3.3). If this motion occurs inside a coil, the movement of the magnetisation will induce a current in the coil that can be detected, resulting in the NMR signal. It should be noted that the nuclear spins do precess about the z-axis, when at equilibrium. However, this is not observed as they do so out of phase with each other.[177]

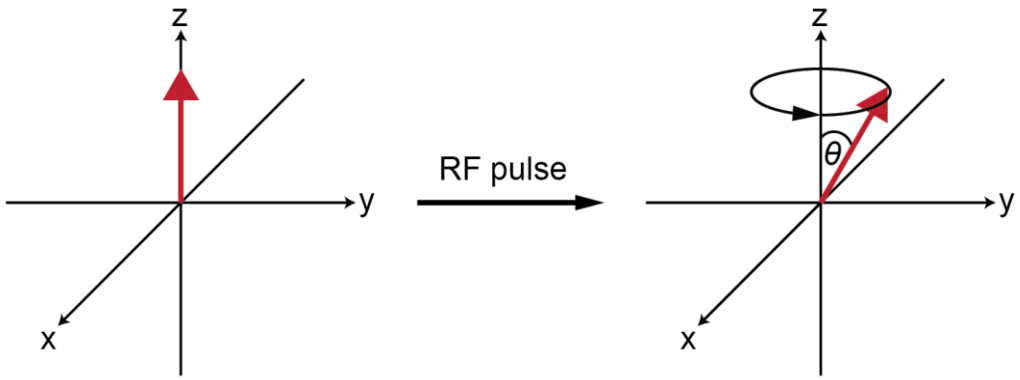

Figure 3.3: Larmor precession of the bulk magnetisation after the application of an RF pulse causing the bulk magnetisation to move away from the z-axis by an angle θ.

The orientation of the bulk magnetisation can be manipulated by the application of RF pulses, applied along a different axis to the external field. This is because the pulse will have a magnetic field component, which the magnetisation can precess around. However, as soon as the magnetisation leaves its equilibrium position, it will start to precess about

B_0, as well as the magnetic field of the RF pulse. The combination of this precession with the motion caused by the oscillating magnetic field of the RF pulse, results in complicated motion, making it difficult to understand the effect of individual pulses. To simplify this, it is common to use a rotating coordinate system, rather than a static one (referred to as the laboratory frame). The frequency at which the magnetisation appears to precess in this rotating frame, is the difference between the Larmor frequency (ω_0) and the frequency of the rotating frame (ω_{rot}). This difference is called the offset, Ω, calculated using by Equation 3.15.[177]

$$\Omega = \omega_0 - \omega_{rot} \tag{3.15}$$

From this, if the frequency of the rotating frame is equal to the Larmor frequency, the offset will be zero and the magnetisation will appear to be stationary. However, if they are not equal, the magnetisation will appear to precess about a much smaller field. This reduced field, ΔB, is given by Equation 3.16, a rearrangement of Equation 3.12.[177]

$$\Delta B = -\frac{\Omega}{\gamma} \tag{3.16}$$

The magnetic field associated with the RF pulse, B_1, will start to influence the magnetisation when is comparable in size to the reduced field. This is the case when the transmitter frequency (and the frequency of the rotating frame) is similar to the Larmor frequency, and the offset is close to zero. In this way, the RF pulse can manipulate the precession of the bulk magnetisation, despite being much weaker than the external field.

The reduced field and B_1 are orthogonal vectors and so add together to give the effective magnetic field, at an angle relative to B_0. The bulk magnetisation then precesses about this effective field. The size of the effective field can be calculated by Equation 3.17, based on Pythagoras' theorem.[177]

$$B_{eff} = \sqrt{B_1^2 + (\Delta B)^2} \tag{3.17}$$

The angle that the effective field makes relative to B_0 is referred to as the tilt angle (Figure 3.4). This is determined by the strength of the pulse as well as its duration, τ_{RF}. It is calculated using Equation 3.18.[174]

$$\theta = \gamma B_1 \tau_{RF} \tag{3.18}$$

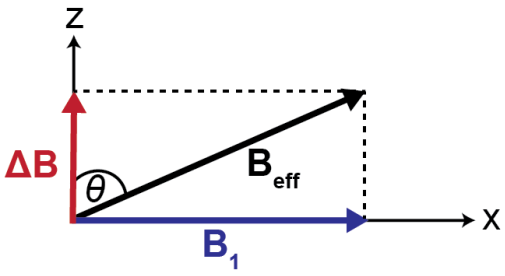

Figure 3.4: The effective magnetic field, B_{eff}, arising from the vector sum of the reduced field and RF field.

Pulses are typically referred to by their tip angle, as well as the axis they are applied along. For example, the most basic pulse-acquire experiment uses a 90° pulse, applied along the x-axis (*i.e.*, a $90_x°$).[179] This pulse moves the bulk magnetisation to align with the –y-axis. When the pulse is switched off, the magnetisation then precesses about the z-axis (B_0), inducing a current in the detector coil. This is shown in Figure 3.5.[177]

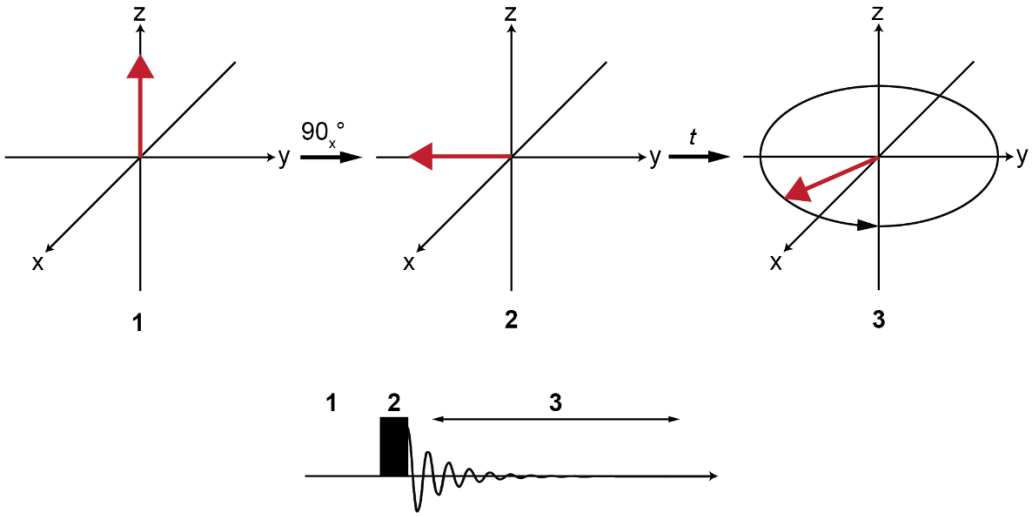

Figure 3.5: The effect of a 90° RF pulse on the bulk magnetisation (top) and a representation of this as a basic pulse sequence diagram (bottom).

Pulses can have any tip angle and be applied along any direction (aside from the z-axis) as required by the experiment (Sections 3.1.9. and 3.1.10.). Another common pulse is the 180° pulse. This inverts the magnetisation to point along the mirror image axis and is used to refocus signals, such as in the spin echo pulse sequence (Figure 3.6).[174,177] The applications of this will be discussed in Section 3.1.8.

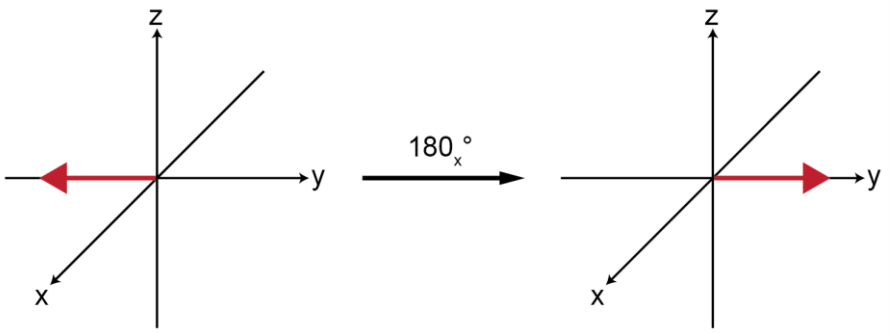

Figure 3.6: The effect of a $180_x°$ RF pulse on the bulk magnetisation.

In addition to their angle, pulses can also be defined as hard or soft, also known as non-selective or selective pulses, respectively. A hard pulse is when the nutation frequency of the pulse, ω_1, is much larger than the resonance offset. In this case, the pulse can affect resonances whose frequency is somewhat different to the transmitter frequency. These pulses can therefore excite wider regions of the spectra. Soft pulses have much lower RF frequencies, closer to that of the offset. These pulses therefore excite a much narrower region and so can be used in certain experiments to excite only specific peaks.[177]

3.1.4. The NMR signal

The signal that is recorded by the spectrometer is called the free-induction decay (FID). This is a plot of intensity as a function of time. However, it is very difficult to extract meaningful information from it. As a result, it is often converted to an NMR spectrum, in terms of frequency. This is done by performing a Fourier transformation, as per Equation 3.19.[175]

$$S(\omega) = \int_0^\infty S(t)\exp(-i\omega t).dt \tag{3.19}$$

This converts the intensity as a function of time to an intensity as a function of frequency. It should be noted that in practice integrating to infinity is not necessary, with the upper limit being some time when the signal has died away. If this time is shorter than the duration of the FID, a Fourier transform of the data will result in sinc "wiggles" in the baseline and an overall loss of resolution. This is called truncation and is avoided by ensuring that the acquisition time is sufficiently long.[179]

To determine the direction of precession, and as a result, the sign of the frequency measured, it is necessary to measure the signal at two points orthogonal to each other (*i.e.*, along the x-and y-axes). This is called quadrature detection. Practically, this is achieved by

passing the output from the probe through two electronic mixers. These have a phase shift of 90° to each other, resulting in two components, referred to as the real and imaginary components. These are then combined to give the NMR spectrum.[177]

3.1.5. Internal interactions

Whilst the Zeeman splitting is normally the dominant interaction that a spin will experience in a magnetic field, there are several other interactions that manifest in an NMR experiment. For a diamagnetic material, these are: chemical shielding, dipolar coupling, J coupling and the quadrupole interaction. Together these are termed internal interactions.[179] Table 3.2 summarises the different sizes of these interactions compared to the Zeeman interaction.

Table 3.2: The interactions that a nuclear spin may experience and their typical magnitudes.[178]

Interaction	Magnitude/Hz
Zeeman	$10^7 – 10^9$
Shielding	$10^2 – 10^5$
Dipolar coupling	$10^3 – 10^5$
J coupling	$1 – 10^3$
Quadrupolar	$10^3 – 10^7$

In the case of paramagnetic materials (those with unpaired electrons), there are additional interactions that will be discussed later (Section 3.1.10.).

3.1.5.1. NMR of solid samples

Before discussing the different internal interactions, it is important to highlight that each of them has an anisotropic component. This means that its size depends on the orientation relative to the magnetic field. In a solution, there is rapid tumbling which averages the anisotropic components to zero. As such, these components do not have any great influence on the spectra recorded for samples in solution. This is not the case in solid materials, where there is minimal motion. As such, the orientations are fixed. Furthermore, in a powdered sample a distribution of crystallite orientations is present. This gives rise to broad peaks, referred to as powder patterns.[174,178,179]

3.1.5.2. Chemical shielding anisotropy

In the previous discussion it has been assumed that the nucleus will experience the full extent of the external field and will precess at the Larmor frequency as defined by Equation 3.11. However, the electrons surrounding the nucleus interact with the magnetic field, producing a secondary field that opposes or augments the applied field. This is called the chemical shielding interaction, which manifests in an NMR spectrum as the chemical shift.[179]

The shielding interaction can be considered as comprising two parts, the diamagnetic and the paramagnetic shielding. Diamagnetic shielding arises due to the circulation of electrons (usually core electrons), which induce a field that opposes the applied field. Paramagnetic shielding arises from distortion of the electronic distribution by the external field. This causes mixing of excited states leading to a small amount of paramagnetic character and a field that supports the applied field.[175]

The size of the shielding field depends on the size of the external field and is given by Equation 3.20. $\boldsymbol{\sigma}$ is the shielding tensor, shown in Equation 3.21. A tensor is required to describe the shielding as the electrons may not be spherically distributed around the nucleus.[179]

$$\boldsymbol{B}_s = -\boldsymbol{\sigma}\boldsymbol{B}_0 \tag{3.20}$$

$$\boldsymbol{\sigma} = \begin{pmatrix} \sigma_{xx} & \sigma_{xy} & \sigma_{xz} \\ \sigma_{yx} & \sigma_{yy} & \sigma_{yz} \\ \sigma_{zx} & \sigma_{zy} & \sigma_{zz} \end{pmatrix} \tag{3.21}$$

If $\mathbf{B_0}$ is applied along the z-axis (Equation 3.22), the components of $\mathbf{B_s}$ are given by Equations 3.23 – 3.25.[179]

$$\boldsymbol{B}_s = -\begin{pmatrix} \sigma_{xx} & \sigma_{xy} & \sigma_{xz} \\ \sigma_{yx} & \sigma_{yy} & \sigma_{yz} \\ \sigma_{zx} & \sigma_{zy} & \sigma_{zz} \end{pmatrix} \cdot \begin{pmatrix} 0 \\ 0 \\ B_0 \end{pmatrix} \tag{3.22}$$

$$\boldsymbol{B_{sx}} = -\boldsymbol{\sigma_{xz}}\boldsymbol{B_0} \tag{3.23}$$

$$\boldsymbol{B_{sy}} = -\boldsymbol{\sigma_{yz}}\boldsymbol{B_0} \tag{3.24}$$

$$\boldsymbol{B_{sz}} = -\boldsymbol{\sigma_{zz}}\boldsymbol{B_0} \tag{3.25}$$

Often tensors are symmetric (*e.g.*, $\sigma_{xy} = \sigma_{yx}$). This means that there are six unique components of the tensor, and a set of axes can be selected, so that the tensor is diagonal (all off-diagonal elements are zero). This is called the principal axis system or principal axis

frame (PAS or PAF). The diagonal terms in this tensor are referred to as the principal components. Equation 3.26 shows $\boldsymbol{\sigma}^{PAS}$.[178]

$$\boldsymbol{\sigma^{PAS}} = \begin{pmatrix} \sigma_{XX} & 0 & 0 \\ 0 & \sigma_{YY} & 0 \\ 0 & 0 & \sigma_{ZZ} \end{pmatrix} \tag{3.26}$$

The principal values can be used to define three parameters which describe the tensor. These are the isotropic shielding, anisotropy and asymmetry (Equations 3.27, 3.28 and 3.29 respectively).[174] Note that the sizes of the tensor components have been determined by the Haeberlen convention, although other conventions may be used.[184]

$$\sigma_{iso} = \frac{1}{3}(\sigma_{XX}^{PAS} + \sigma_{YY}^{PAS} + \sigma_{ZZ}^{PAS}) \tag{3.27}$$

$$\Delta = \sigma_{ZZ}^{PAS} - \sigma_{iso} \tag{3.28}$$

$$\eta = \frac{\sigma_{XX}^{PAS} - \sigma_{YY}^{PAS}}{\Delta} \tag{3.29}$$

Using these quantities, the chemical shielding for any orientation to the external field can be calculated. Equation 3.30 describes the case where all three principal values are not equal. Note that θ and φ are the polar angles shown in Figure 3.7.[174]

$$\omega_{cs}(\theta, \phi) = -\omega_0\sigma_{iso} - \frac{1}{2}\omega_0\Delta(3cos^2\theta - 1 + \eta sin^2\theta cos2\phi) \tag{3.30}$$

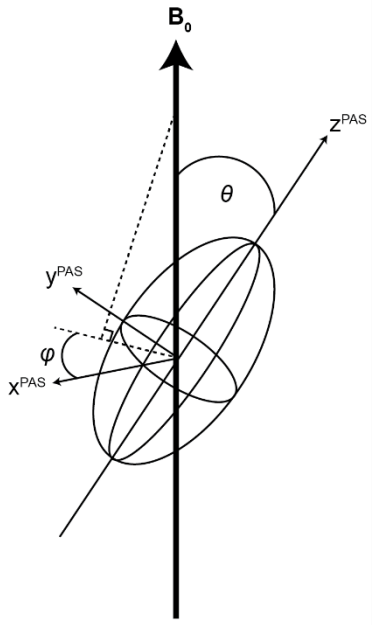

Figure 3.7: Definitions of the polar angles used in Equation 3.30 drawn on an illustration of the chemical shielding tensor.

From this equation, the value of the shielding depends not only on the principal values (or quantities derived from them) but also the orientation of the PAS relative to the external field (Figure 3.7). This means that a different shielding will be observed depending on how a molecule is oriented. In a liquid, tumbling of the molecules averages this to zero, leaving only the isotropic shielding. However, in a powdered sample, where all orientations are present, continuous powder lineshapes are observed. The appearance of these changes depending on the relative magnitudes of the principal components of the tensor as shown in Figure 3.8.[179]

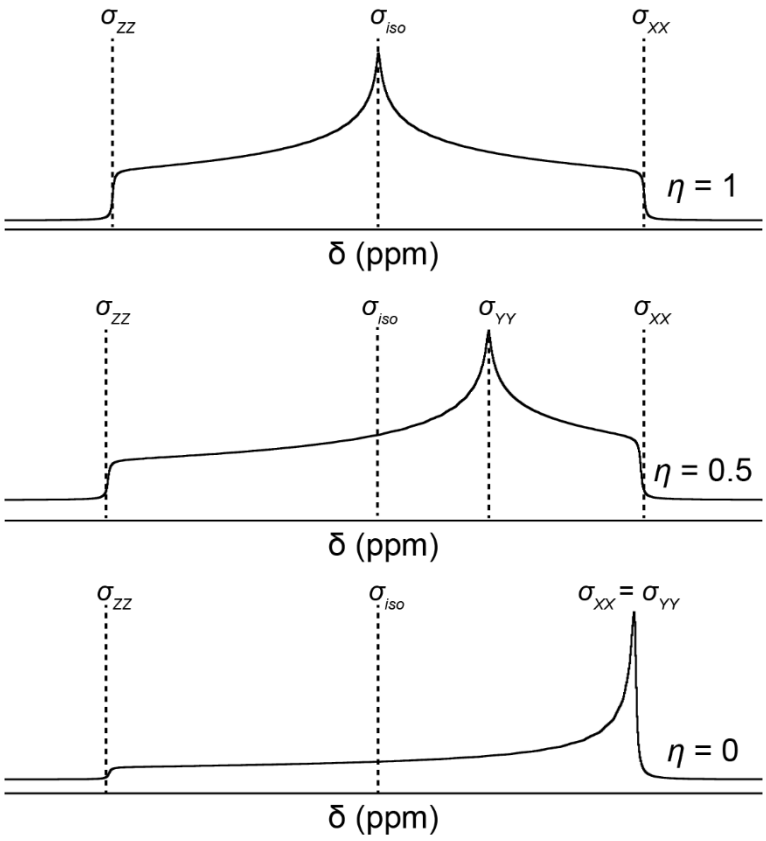

Figure 3.8: Powder lineshapes resulting from chemical shift anisotropy, with different asymmetries (η).

In an actual NMR experiment, the chemical shielding is not measured. Instead, a chemical shift, δ, is defined relative to a reference and reported in parts per million (ppm). This is calculated using Equation 3.31.[176]

$$\delta = 10^6 \times \frac{(\omega_{obs} - \omega_{ref})}{\omega_{ref}} \tag{3.31}$$

Chemical shift is used as it is independent of field, allowing spectra recorded at different fields to be compared.

The size of the chemical shift interaction that nuclei experience depends on the surrounding electron density. This means it is affected by factors such as the size of the atom and the electronegativity of its neighbours.[176] Circulating electrons in π systems nearby can also influence the chemical shift (termed ring-current shift).[185]

3.1.5.3. J coupling

The J coupling, also referred to as scalar or indirect coupling, is typically described as a through bond interaction, mediated by the electrons present in the bond. It can therefore be used to provide information about bonding arrangements. In addition, J coupling can provide information about less well-defined bonding interactions like hydrogen bonding.[179]

In a solution sample, J coupling manifests as a splitting of the peaks. For example, two magnetically inequivalent spin-1/2 nuclei that are J-coupled together would result in the peak for each environment being split in two. The size of the splitting of this "doublet" peak is the J coupling constant. It is independent of the external field and given in hertz.[177]

As shown in Table 3.2, J coupling is very small compared to the other NMR interactions. As such it is usually dominated in the solid-state by the dipolar interaction.[179] This is not to say that it is not useful, as even when it cannot be observed it can be leveraged to provide information such as in the heteronuclear multiple quantum correlation (HMQC) experiment.[186]

3.1.5.4. Dipolar coupling

In classical physics, two magnetic moments separated from each other in space, can interact through dipolar (or dipole-dipole) interactions. It has no isotropic component and so does not affect the isotropic chemical shift observed. It does however result in an orientation-dependent splitting, which for an isolated spin pair is given by Equation 3.32.[187]

$$\omega_D = -\frac{\mu_0}{4\pi}\frac{\gamma_I\gamma_s}{r_{IS}^3}\frac{1}{2}(3cos^2\theta - 1) \tag{3.32}$$

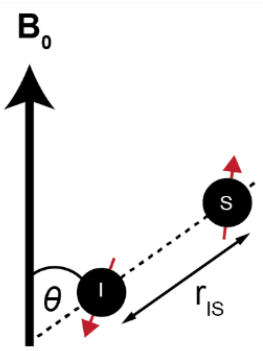

Figure 3.9: Diagram illustration the dipolar interaction between two spins (I and S) as per Equation 3.32.

As mentioned, the size of the splitting depends on the orientation relative to the external field. In a solution, where the molecules can freely tumble, the dipolar coupling is averaged to its isotropic value of zero. On the other hand, in a powdered sample, where all orientations are present, a "Pake doublet" will be obtained. However, this is only true in the case where the spin pairs are isolated. These however are typically not observed, particularly when the nucleus in question has a high gyromagnetic ratio and is abundant within the material being studied. In these cases, there will be many possible dipole-dipole interactions between the various spins in the sample. This results in a Gaussian-like peak, typically many kHz wide.[174,179]

3.1.5.5. Quadrupole interaction

The final main internal interaction is the quadrupole interaction, which unlike the others is due to electric fields rather than magnetic effects. This applies to quadrupolar nuclei ($I > 1/2$), which is the case for more than 70% of the isotopes on the periodic table.[188]

Quadrupolar nuclei possess a nuclear electric quadrupole moment, owing to the distribution of charge inside the nucleus. This can interact with electric field gradients (EFGs) that arise at the nucleus when the local environment is asymmetric (*i.e.*, not cubic).[188] The intrinsic size of the interaction depends on the size of both parameters, and is described by the nuclear quadrupolar coupling constant, C_Q:[187]

$$C_Q = \frac{eQV_{zz}}{h} \tag{3.33}$$

Here eQ is the quadrupole moment of the nucleus (with e being the charge of a proton) and V_{zz} is the largest of the principal values of the EFG tensor. As with the chemical shielding, we can also define an asymmetry based on the principal components of the tensor, as shown in Equation 3.34.[187]

$$\eta_Q = \frac{V_{YY} - V_{XX}}{V_{ZZ}} \tag{3.34}$$

The potential size of the quadrupole interaction means that it can significantly perturb the energy levels of the Zeeman interaction. Figure 3.10 shows the energy levels for a spin-3/2 nucleus in the presence of the quadrupole interaction.

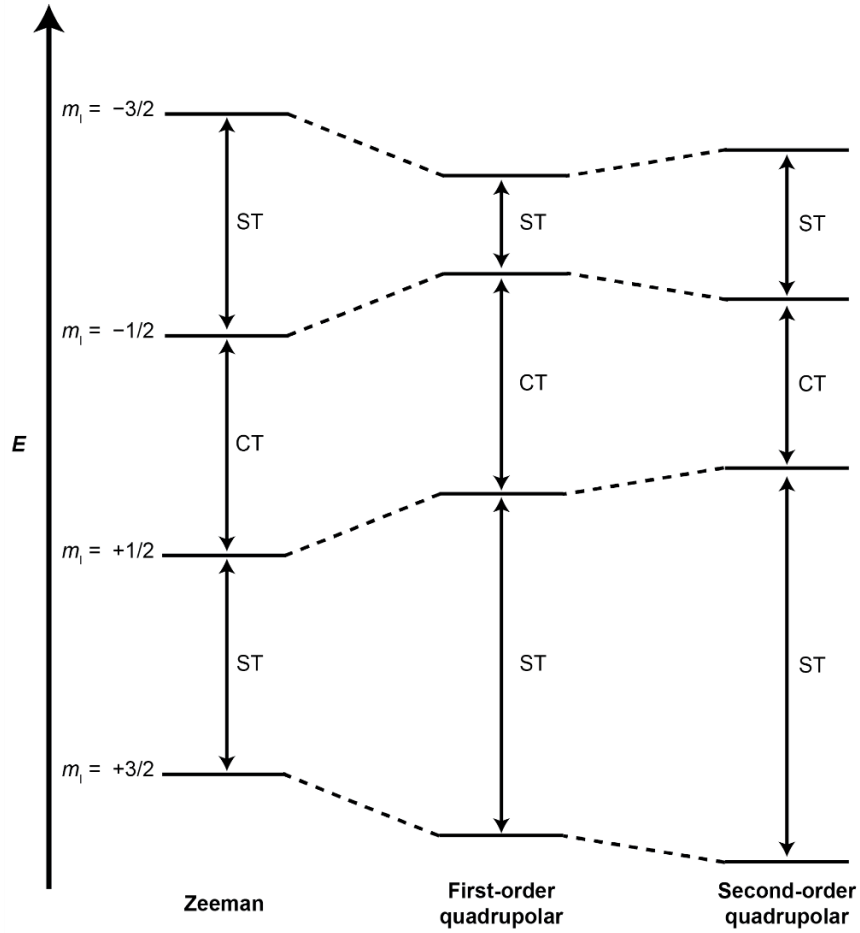

Figure 3.10: The nuclear spin states for a spin-3/2 nucleus in the presence of the Zeeman interaction (*i.e.*, an applied external magnetic field) and the first and second order quadrupole interactions.

The size of the perturbation is given by the quadrupole splitting parameter, Equation 3.35. This is related to C_Q as shown in Equation 3.36.[187]

$$\omega_Q = \left(\frac{\omega_Q^{PAS}}{2}\right)[(3cos^2\theta - 1) + \eta_Q(sin^2\theta cos2\varphi)] \tag{3.35}$$

$$\omega_Q^{PAS} = \frac{3\pi C_Q}{(2I(2I-1))} \tag{3.36}$$

As with dipolar coupling, this angle dependence results in a powder lineshape for solid samples, as shown in Figure 3.11. Solution samples do not show quadrupolar coupling, as the rapid tumbling averages it to zero.[179]

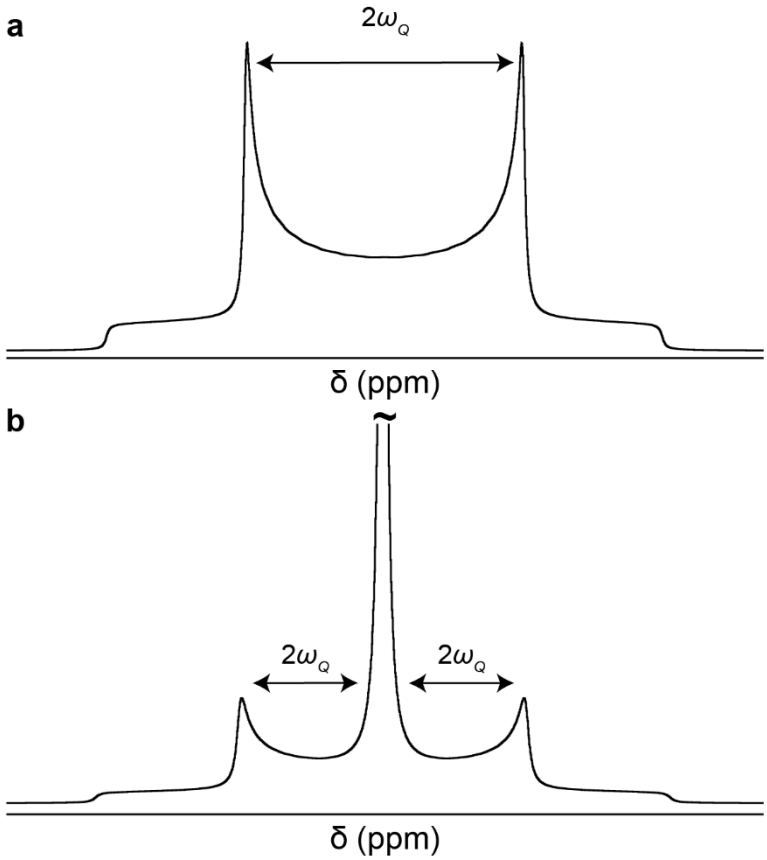

Figure 3.11: Quadrupolar powder patterns for (a) a spin-1 and (b) a spin-3/2 nucleus.

It should be noted for a half integer nucleus, the central transition is unaffected by the quadrupole interaction, so long as the interaction is relatively small. In this case, the quadrupole interaction can be treated as a first-order perturbation of the Zeeman energy, as with the other internal interactions discussed. However, if the nucleus resides in an asymmetrical site, there will be a large EFG. In these cases, second order contributions to the quadrupole interaction become significant. This is shown by Equation 3.37, assuming $\eta_Q = 0$ for simplicity.[187]

$$\omega = \frac{\left(\omega_Q^{PAS}\right)^2}{\omega_0}\left(A^0 + A^2 d_{00}^2(\beta) d_{00}^2(\chi) + A^4 d_{00}^2(\beta) d_{00}^4(\chi)\right) \tag{3.37}$$

$$d_{00}^2(\chi) = \frac{1}{2}(3cos^2\chi - 1) \tag{3.38}$$

$$d_{00}^{4}(\chi) = \frac{1}{8}(35cos^4\chi - 30cos^2\chi + 3) \quad (3.39)$$

Here β is the angle of an individual crystallite relative to the field and χ is the axis of rotation relative to the field (this will be discussed in Section 3.1.7.).

This additional second order perturbation affects the energy of the central transition. As such the central transition experiences further broadening.

3.1.6. Relaxation

RF pulses can manipulate the magnetisation because they have an oscillating field at close to the Larmor frequency. However, local oscillating fields can also occur naturally in the sample, driven by thermal motion of the material. Such fields randomly vary in terms of their direction and magnitude. For spin-1/2 nuclei, changing local fields are caused by dipolar interactions and the chemical shift anisotropy. In the case of quadrupolar nuclei, the quadrupole interaction can also participate. In fact, in solution, the rapid relaxation caused by the quadrupole interaction can make recording spectra difficult for quadrupolar nuclei. All these interactions are anisotropic and so any motion in the sample will cause changes in these interactions leading to changing local fields. If the field fluctuates at the Larmor frequency, it will drive the bulk magnetisation back to its equilibrium position along the z-axis. This is called relaxation.[177]

The random motion in the sample is characterised by the correlation time τ_c. This can then be used to define the reduced spectral density $j(\omega_0)$, which is a measure of how much of the motion occurs at the Larmor frequency. This is calculated using Equation 3.40.[177]

$$j(\omega_0) = \frac{2\tau_c}{1 + \omega_0^2\tau_c^2} \quad (3.40)$$

From this, two limiting cases can be defined. When motion is fast, and so $\omega_0\tau_c << 1$, meaning that $j(\omega_0)$ is given by Equation 3.41. When motion is slow and $\omega_0\tau_c >> 1$, $j(\omega_0)$ is given by Equation 3.42.[177]

$$j(\omega_0) = 2\tau_c \quad (3.41)$$

$$j(\omega_0) = \frac{2}{\omega_0^2\tau_c} \quad (3.42)$$

After a $90_x°$ pulse, the magnetisation precesses in the xy plane. To return to its equilibrium position along the z-axis, it needs to recover its z-component, and the x- and y-components

need to decay to zero. There are therefore two types of relaxation: longitudinal and transverse.[179]

Longitudinal or spin-lattice relaxation is the process by which the z-component of the magnetisation, M_z, is recovered. It is characterised by the time constant T_1, as per Equation 3.43, where M_0 is the initial magnetisation.[176,179]

$$M_z(t) = M_0\left(1 - \exp\left(-\frac{t}{T_1}\right)\right) \tag{3.43}$$

To obtain an NMR spectrum, it is normal to repeat the experiment multiple times, so that the signal from the individual scans can be added together.[175] This can offset the low intrinsic sensitivity of NMR.

The individual scans are separated by a time period called the recycle delay, sometimes referred to colloquially as *D*1. This is to give the magnetisation time to decay back to its equilibrium state. If the recycle delay is too short, each subsequent scan will have reduced intensity. Full recovery of the magnetisation along the z-axis would take an infinitely long time, and so often a recycle delay of $5T_1$ is used as this recovers > 99% of the magnetisation. This is shown in Figure 3.12. However, increasing the number of scans, whilst using a shorter recycle delay can lead to better signal-to-noise per unit time. In this case, the optimum recycle delay is $1.26T_1$.[179]

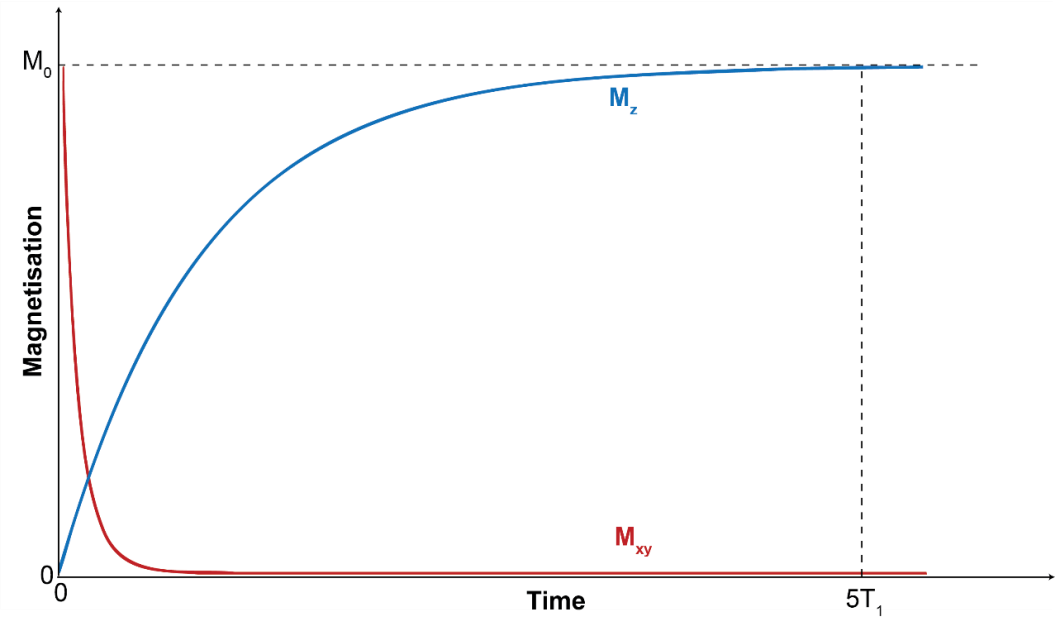

Figure 3.12: Time-dependence of the M_{xy} and M_z components of the magnetisation.

In the rotating frame in the presence of a spin locking pulse (as will be discussed in the cross-polarisation experiment) it is also necessary to define another constant for spin-lattice relaxation within the rotating frame. This is called $T_{1\rho}$, and is usually much shorter than T_1, as it requires fluctuations at the RF frequency, rather than the Larmor frequency.[179]

In addition to recovering the z-component, the xy-component of the magnetisation needs to decay. As this occurs in the transverse plane, it is called transverse relaxation (or spin-spin relaxation). Transverse relaxation is characterised by the time constant T_2, as shown in Equation 3.44, where $M_{x,y}(t)$ is the x- or y-component of the magnetisation as a function of time and $M_{x,y}(0)$ is the initial magnetisation.[177]

$$M_{x,y}(t) = M_{x,y}(0)\exp\left(-\frac{t}{T_2}\right) \tag{3.43}$$

Transverse relaxation results from dephasing caused by the magnetic moments that make up the bulk magnetisation precessing at different rates. This is due to motion in the sample causing random variations in local magnetic fields. Over time this leads to the effective magnetisation in the xy plane decaying to zero, as shown in Figure 3.13.

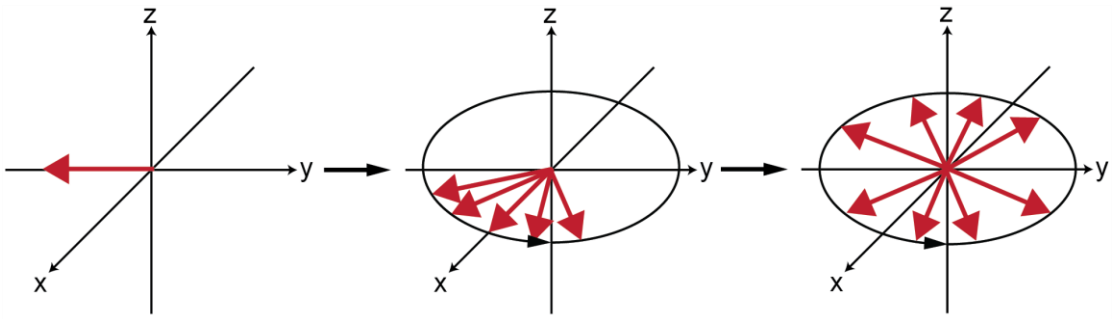

Figure 3.13: Dephasing of the bulk magnetisation.

In addition to the interactions between spins causing relaxation, inhomogeneities in the external magnetic field also cause dephasing. These two contributions can be used to define a new time constant, T_2*, as shown in Equation 3.44.[178]

$$\frac{1}{T_2^*} = \frac{1}{T_2} + \frac{1}{T_2'} \tag{3.44}$$

Here T_2 refers to the relaxation that is related to interactions, whilst T_2', is due to field inhomogeneity. However, T_2 is the most interesting component, as this relates to the sample properties.

3.1.7. Experimental methods in solid-state NMR

3.1.7.1. Magic-angle spinning (MAS)

As has been mentioned, the internal interactions give rise to broad peaks in the solid state, owing the fact that the anisotropy is not averaged by molecular motion. Whilst these can be useful, the loss of resolution and signal-to-noise ratio that they cause complicates interpretation.

The anisotropic component of each of the internal interactions contains the same factor to describe the angle dependence, which is $3\cos^2\theta-1$. If the sample is spun about an axis set at an angle θ_R, relative to the external field, the average value of this angle dependence is given by Equation 3.45, where β is the angle between the z-axis of the tensor and the rotation axis.[174]

$$\langle 3cos^2\theta - 1\rangle = \frac{1}{2}(3cos^2\theta_R - 1)(3cos^2\beta - 1) \qquad (3.45)$$

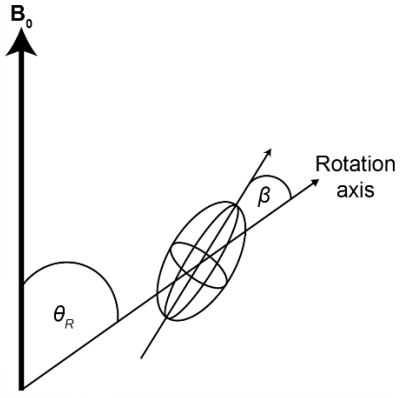

Figure 3.14: An illustration of the angles used in Equation 3.45. θ_R is the angle of rotation relative to the external field whilst β is the angle of the PAS relative to the rotation axis.

If θ_R is set to 54.74°, the average value of $3\cos^2\theta-1$ becomes zero, provided that the spinning frequency is fast enough. This angle is the eponymous "magic angle". Spinning about this angle, *i.e.*, magic-angle spinning (MAS), results in narrowing of the peaks observed in the NMR spectrum, improving the resolution and signal-to-noise. To remove the anisotropy completely, the MAS frequency needs to be at least three times as large.[174] If this is not the case, the powder pattern will break up into an isotropic peak and artifacts called spinning sidebands. These appear at multiples of the rotation frequency and are typically identified in a spectrum by asterisks (*).[179] At the time of writing, MAS frequencies of up to 60 kHz are frequently used in literature, with up to 200 kHz being reported.[189]

MAS requires the ability to spin the sample. This is achieved by using sample tubes called rotors. These are zirconia cylinders, fitted with a plastic cap that has fins built into it, allowing the rotor to spin when air is blown across them.[178] Rotors are often referred to by their outer diameter. Larger diameter rotors hold more sample but cannot spin as fast as smaller rotors. Selecting the correct rotor size for an experiment is therefore a balancing act between sensitivity and achieving sufficient resolution, as well as considering any requirements of the pulse sequence(s) being used.[187]

Figure 3.15: Examples of rotors used for NMR experiments. Outer diameters are 2.5, 3.2, 4 and 7 mm, left to right.

Provided the spinning frequency is fast enough, MAS can effectively remove the first-order contributions from the different internal interactions. However, it cannot remove second order quadrupolar broadening. This is because, as can be seen in Equation 3.37, this term has two angular dependencies, and so no one angle can average both terms to zero. In this case, it is possible to use specially designed rotors that have a smaller rotor inside a larger one. This approach is known as double-angle rotation (DOR) and allows the samples to spin at two angles simultaneously, reducing second-order broadening. However, the MAS frequencies achievable by this method are lower (because of the larger size required) and it is technically challenging to prepare and spin the samples.[174,178]

3.1.7.2. Decoupling

For very strong dipolar interactions, such as those involving ^{1}H, normal MAS frequencies are not enough to completely average the interaction. Whilst very fast MAS is possible, it depends on the availability of equipment to perform it. An alternative method is to remove the interactions by applying RF pulses. This is called decoupling.

In the case of heteronuclear decoupling, such as between ^{1}H and ^{13}C, the simplest method is to apply a high-power RF pulse at the ^{1}H Larmor frequency whilst acquiring the

spectrum for the coupled nucleus. This causes rapid transitions between the spin states of ^{1}H ($m_I = \pm 1/2$), averaging the dipolar interaction to zero.[174] This method however is can lead to large residual dipolar couplings in solid samples.[190]. Therefore, other methods such as two pulse phase modulation (TPPM) have been designed, which involves applying a continuous set of RF pulses, but alternating the phase of the pulse.[174,191]

One of the problems with decoupling is that it requires very high RF powers, at least three times the size of the dipolar interaction being removed. The decoupling pulses are also applied for a relatively long time. This can cause damage to the probe, and so it is important that the acquisition time is as short as possible. Furthermore, adequate time needs to be left between acquisitions, such that the RF pulse is only applied for at most 10 – 20% of the recycle delay.[179]

Homonuclear decoupling is more complex as a spectrum is acquired on the same channel as the decoupling is being applied. In these cases, decoupling is achieved using pulse sequences such as WAugh-HUber-HAeberlen (WAHUHA) or Decoupling Using Mind-Boggling Optimisation (DUMBO).[192,193]

3.1.8. One-dimensional NMR

3.1.8.1. Cross polarisation

The cross polarisation (CP) experiment transfers the magnetisation from an abundant spin-1/2 nucleus to another nucleus. CP is often used to study organic materials, with polarisation transfer between ^{1}H and ^{13}C, but it can be used for other nuclei. Transfer of magnetisation is mediated by dipolar coupling between the two nuclei. Figure 3.16 shows the pulse sequence for the CP experiment.[179]

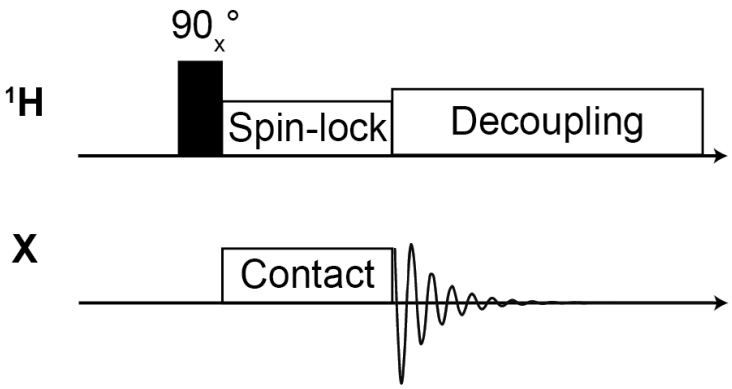

Figure 3.16: Pulse sequence for a CP experiment between a ^{1}H nucleus and another nucleus X.

The first step is a 90° pulse, applied to the ^{1}H channel, rotating the magnetisation to lie along the –y-axis. Next a spin locking pulse is applied along this axis, which acts to maintain the magnetisation along this axis. Simultaneously, another pulse, known as the contact pulse, is applied to the X channel, which transfers magnetisation between the nuclei, provided the following condition is met:[174]

$$\gamma_H B_{1(H)} = \gamma_X B_{1(X)} \tag{3.46}$$

This is known as the Hartmann-Hahn matching condition and means that the nutation frequencies of the two nuclei are equal. As a result, the separation of energy levels for both nuclei are equal. As the spins are dipolar coupled, transitions between the ^{1}H spin states can be balanced by transitions between the spin states of X. This results in a larger population difference building up for the X nucleus, and therefore an increase in the magnetisation. Finally, the X signal is acquired, often with decoupling on the ^{1}H channel.[179]

CP has several uses. Firstly, the increase in magnetisation of X enhances the signal up to a limit of γ_H/γ_X. For ^{1}H/^{13}C this is a factor of four, resulting in the experimental time decreasing by a factor of 16. This makes it useful for studying nuclei with low sensitivity and/or low natural abundance. Furthermore, such nuclei often relax slowly either due to weak dipolar coupling or low abundance isolating the nuclei from each other. However, in a CP experiment, relaxation is determined by the ^{1}H nuclei, which relax much faster due to their stronger dipolar coupling. This therefore means that individual scans take less time. Together the signal enhancement and faster recycle delays mean that CP spectra are much faster to acquire than by direct excitation. Since dipolar coupling is distance dependent, CP can also be used to provide insight into distances between the two nuclei. Increasing the length of the contact pulse (known as the contact time), means that environments further away can be observed. However, this distance dependence does mean than CP spectra are non-quantitative.[174,179]

There are several situations where CP is not suitable. As previously mentioned, it is non-quantitative. In addition, if there are no protons, or other nuclei, then CP cannot be used. CP also does not work if the material is paramagnetic, or highly mobile, due to fast relaxation and averaging of the dipolar interaction respectively. In these cases, spectra should be recorded by direct excitation, as in use a variation of the pulse-acquire sequence.[179] When studying proteins it may be preferable to use ^{13}C labelling to boost signals of specific sites.[194]

CP is not limited to pairs of spin-1/2 nuclei but can also be applied to study quadrupolar nuclei. However, this can be challenging to implement, particularly under MAS. In the case of quadrupolar nuclei, the Hartmann-Hahn matching condition depends on the size of the quadrupolar splitting relative to the nutation frequency. The two limiting cases when $\omega_{1S} >> \omega_Q$ and $\omega_{1S} << \omega_Q$ are shown in Equations 3.47 and 3.48. The intermediate range is poorly defined.[188]

$$\omega_{1I} = \omega_{1S} \tag{3.47}$$

$$\omega_{1I} = \left(S + \frac{1}{2}\right)\omega_{1S} \tag{3.48}$$

Despite this difficulty, quadrupolar CP can still be useful when exploring whether nuclei are close in space.[174]

3.1.8.2. Spin (Hahn) echoes

As described when discussing the vector model previously, a spin echo refocuses the magnetisation by applying a 180° pulse. Whilst such pulses are useful as parts of other pulse sequences, spin echoes have several uses on their own as an alternative to standard pulse-acquire experiments.[174,177]

Signal acquisition cannot begin immediately after the end of an RF pulse, to allow the pulse to dissipate and avoid "ringdown". This necessitates a period after the end of the pulse before the spectrum is recorded, known as deadtime. However, broad peaks have FIDs that die away quickly. This can pose a problem if a significant proportion of the FID occurs during the deadtime, as Fourier transforming this signal will lead to distortion of the spectrum.[178] Spin echoes can be used to avoid this issue. This is because the signal is not refocussed immediately (Figure 3.17). Instead, the maximum echo intensity is delayed by a time equal to the difference between the two pulses. This means that maximum signal intensity is not observed until well after the end of the deadtime.[187]

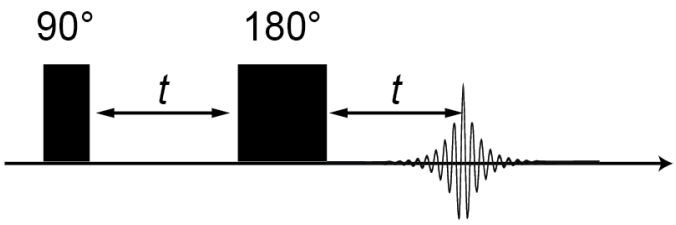

Figure 3.17: Pulse sequence for a spin echo experiment.

This particular property of echoes makes them particularly useful in pulsed EPR owing to the extremely fast relaxation of unpaired electrons (Section 3.2.5.). It is important to note that relaxation due to T_2 relaxation, is not refocussed by a spin echo, meaning that the intensity will be reduced. However, this does make echoes useful for determining T_2, as the experiment can be repeated multiple times, with increasing echo delays. The loss of intensity as the delay period is increased can then be fitted to determine T_2.

Another use of echoes is to suppress background signal, arising due to the components of the probe. Typically, this is done by chaining two echoes together as part of a so-called "depth" experiment. Signals originating from outside the coil experience a weaker field and so are not perfectly refocussed by the 180° pulse. The contributions from these signals to the spectrum can then be removed by phase cycling.[195]

3.1.8.3. Transfer of population in double resonance (TRAPDOR)

The transfer of population in double resonance (TRAPDOR) experiment performed under MAS and utilises dipolar coupling between spin-1/2 and quadrupolar nuclei, to gain information about environments where the nuclei are close together. In a TRAPDOR experiment, the spin-1/2 nucleus is observed, whilst a pulse is applied to the quadrupolar nucleus.[174] Observing the spin-1/2 nucleus makes it a particularly useful tool for studying systems where observation of the quadrupolar nucleus is either challenging or uninformative due peaks being broadened by the quadrupole interaction.[196,197]

A TRAPDOR experiment comprises two steps shown in Figure 3.18. The first is simply a Hahn echo, acquired for the spin-1/2 nucleus. This is then repeated, but during the first delay, a pulse is applied to the quadrupolar nucleus, altering the populations of the spin energy levels. This changes the strength of the dipolar coupling between the different nuclei, preventing its complete averaging by MAS. As a result, the intensity of the second spectrum is lower than the first.[174] Subtracting the second spectrum from the first gives the TRAPDOR difference spectrum.[197,198] As only environments where the two nuclei are dipolar coupled are affected by the pulse, peaks in the difference spectrum must arise from environments where the two spins are close in space.

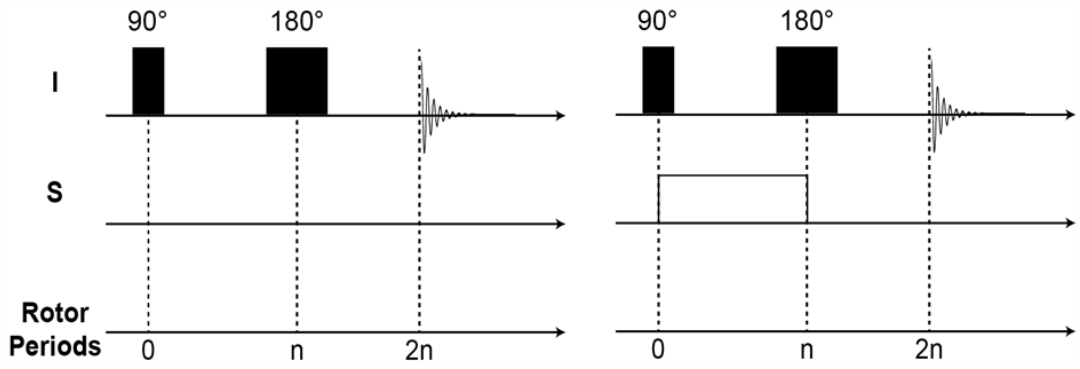

Figure 3.18: TRAPDOR pulse sequence between two spins I and S. Based on Figure 1 in the paper by Lang *et al.*[198]

The intensity of the difference spectrum depends on three main factors. First is whether the transitions between spin states are adiabatic. This is quantified by the adiabaticity parameter, α, expressed in terms of the RF frequency, ν_1, the spinning frequency, ν_r and the size of the quadrupole interaction, ν_Q. Adiabatic transitions occur when $\alpha > 1$.[196]

$$\alpha = \frac{\nu_1^2}{\nu_r \nu_Q} \tag{3.49}$$

The second factor that determines the intensity of the TRAPDOR difference spectrum is the strength of the dipolar coupling. As this experiment prevents complete refocussing of dipolar coupling by MAS, environments with stronger dipolar coupling are more strongly supressed in the second part of the experiment. The final factor is the number of rotor periods in the delay. Longer irradiation leads to greater dephasing of the dipolar coupling. However, it can also lead to reduced signal intensity due to T_2 relaxation, so it is important to balance an increased TRAPDOR effect with increased signal-to-noise.[199]

3.1.9. Two-dimensional NMR

The previously discussed experiments result in 1D NMR spectra, with a single frequency axis. However, it is often helpful to acquire 2D NMR spectra, with two frequency axes to gain further insight into the relationships between environments.[179]

The general pulse sequence for a 2D experiment (Figure 3.19) starts with a pulse (or block of pulses) referred to as preparation pulses. This is followed by a delay, t_1, during which time the state of the sample evolves according to the effects of the preparation pulses. No signal is acquired during this time. t_1 is followed by a second block of pulses, called mixing pulses, which allows the signal to be measured in the period t_2. This process is repeated many times, with t_1 being incrementally increased. The signal acquired is affected by the

state of the sample, meaning that it will change as t_1 is increased. A Fourier transform of both axes yields the 2D spectrum.[177]

Figure 3.19: The basic form of the pulse sequence for a 2D experiment.

A relatively simple example of a 2D experiment is the HETeronuclear CORrelation (HETCOR) experiment. This is essentially a 2D version of the CP experiment previously discussed. In this experiment, the initial $90_x°$ pulse is the preparation pulse, which is followed by a delay, during which time the magnetisation of the ^{1}H nuclei evolves. This evolved state is transferred to the X nucleus by the spin lock and CP pulses, which serve as the mixing pulses. This yields a 2D spectrum, where peaks are observed where the ^{1}H environment is close in space to the X environment.[179]

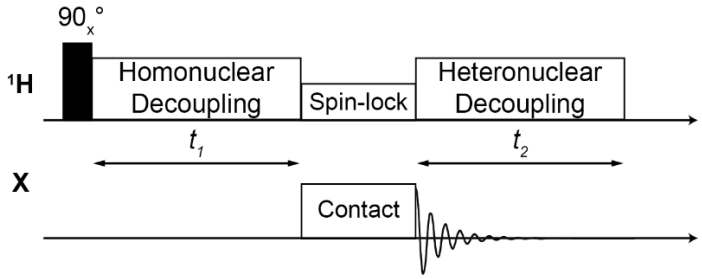

Figure 3.20: Pulse sequence of a HETCOR experiment between ^{1}H and ^{13}C.

3.1.9.1. Radiofrequency-driven recoupling

As discussed with TRAPDOR, dipolar coupling can be employed to provide information about the arrangements of different sites in space. Doing so under MAS requires the application of pulses to selectively reintroduce dipolar coupling, which is known as recoupling. One approach to do this for homonuclear dipolar interactions is to use radiofrequency-driven recoupling (RFDR). This uses 180° pulses, synchronised with the middle of the rotor period to reintroduce the dipolar interactions. The resulting 2D spectrum then shows correlations between sites that are close enough in space to be recoupled. Pulses can be repeated for many rotor periods, extending the range over which recoupling can occur.[200,201] For example, Roos *et al* report ^{19}F cross peaks for sites separated by up to 9.5 Å.[202] Figure 3.21 shows the pulse sequence used for RFDR.

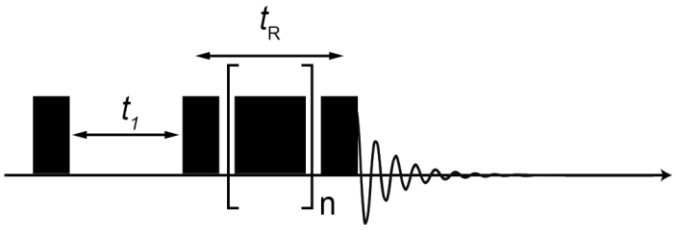

Figure 3.21: The pulse sequence for an RFDR experiment. The pulse in brackets is a 180° pulse, which is repeated n times as set by the user.

3.1.10. Paramagnetic NMR

3.1.10.1 Overview

A paramagnetic species is one that possesses unpaired electrons, such as organic free-radicals or transition metal ions with partially filled *d* orbitals. Electrons are spin-1/2 and therefore possess a magnetic moment that can interact with external magnetic fields through the Zeeman interaction as well as other spins.[203] This is the basis of electron paramagnetic resonance (EPR) spectroscopy, as will be discussed later, but this also has ramifications for the acquisition and interpretation of NMR spectra.

The coupling between electron and nuclear spins is called the hyperfine interaction, which has two components. These are the Fermi contact and dipolar interactions, also referred to as the isotropic and anisotropic hyperfine interactions, respectively.

The Fermi contact interaction depends on the interactions between the electron and nuclear dipole moments because of there being electron density at the nucleus. It is described by the isotropic coupling constant given by Equation 3.50, where $\Psi(0)$ is the value of the electron wavefunction at the nucleus, $\gamma_{e/I}$ is the gyromagnetic ratio of the electron/nucleus and μ_0 is the permittivity of free space.[203,204]

$$A^{FC} = \left(\frac{2\mu_0}{3}\right)\gamma_e\gamma_I\hbar^2|\Psi(0)|^2 \tag{3.50}$$

This part of the hyperfine interaction results in a shift to the isotropic chemical shift of the nucleus, referred to as the Fermi contact shift. The size of this shift is proportional to the electron density transferred into the orbitals of the nucleus of interest. These orbitals must be *s* orbitals or have *s* character, to have electron density at the nucleus. There are two mechanisms for electron density transfer, which are electron delocalisation and spin

polarisation. Electron delocalisation involves overlap with the half-filled orbital, resulting in an increased electron density at the nucleus being observed. As a result, the nucleus is more shielded and therefore has a more negative shift. Spin polarisation involves overlap with an empty orbital on the metal ion, orthogonal to the half-filled orbital. This results in the electron density at the nucleus of interest decreasing, and a more positive chemical shift. As the mechanism is determined by orbital overlap, which in turn depends on the bonding arrangements, Fermi contact shifts can be used to infer structural information.[204]

The mechanism of the dipolar contribution to the hyperfine interaction is similar to the dipolar interaction between nuclei previously discussed. However, electrons have a larger gyromagnetic ratio (roughly 660 times that of a proton), and so the dipolar interaction between electrons and nuclei is much larger as per Equation 3.32. This leads to additional, large shift anisotropies and consequently further line broadening in the spectra recorded.

In addition to affecting the chemical shift and anisotropy of the observed peaks, paramagnetic ions significantly increase the relaxation rate of nuclei. This is called the paramagnetic relaxation enhancement (PRE). For insulating solids, the effect on the nuclear T_1 and T_2 are described using the Solomon-Bloembergen-Morgan equations (Equations 3.51 and 3.52). Here S is the total electron spin, A^{FC} is the size of the Fermi contact interaction (Equation 3.50), T_{1e}/T_{2e} are the electron relaxation times, $\omega_{S/I}$ are the electron and nuclear Larmor frequencies and b_{SI} is the size of the dipolar interaction (Equation 3.53).[204]

$$\frac{1}{T_1} = \frac{2}{3}S(S+1)\left(\frac{A^{FC}}{\hbar}\right)^2 \frac{T_{2e}}{1+(\omega_s-\omega_I)^2T_{2e}^2} + \frac{2}{15}S(S+1)\left(\frac{b_{SI}}{\hbar}\right)^2 \times \left[\frac{3T_{1e}}{1+\omega_I^2T_{1e}^2} + \frac{6T_{2e}}{1+(\omega_s+\omega_I)^2T_{2e}^2} + \frac{T_{2e}}{1+(\omega_s-\omega_I)^2T_{2e}^2}\right] \tag{3.51}$$

$$\frac{1}{T_2} = \frac{1}{3}S(S+1)\left(\frac{A^{FC}}{\hbar}\right)^2 \left[T_{1e} + \frac{T_{2e}}{1+(\omega_s-\omega_I)^2T_{2e}^2}\right]\frac{1}{15}S(S+1)\left(\frac{b_{SI}}{\hbar}\right)^2 \times \left[4T_{1e} + \frac{6T_{2e}}{1+\omega_S^2T_{2e}^2} + \frac{3T_{1e}}{1+\omega_I^2T_{1e}^2} + \frac{6T_{2e}}{1+(\omega_s+\omega_I)^2T_{2e}^2} + \frac{T_{2e}}{1+(\omega_s-\omega_I)^2T_{2e}^2}\right] \tag{3.52}$$

$$b_{SI} = \frac{\mu_0 \gamma_e \gamma_I \hbar^2}{4\pi r^3} \tag{3.53}$$

Whilst these equations are very complex, they highlight two things. First, the PRE is due to both components of the hyperfine interaction, not just the dipolar term. Second, the relaxation time of the nuclei is tied to both electron relaxation times.[204]

Another interaction that should be mentioned is the Knight shift, which operates in metals and metallically conductive materials. The Knight shift arises due to the interaction of the nuclear magnetic moment with conduction electrons, and results in large changes in chemical shift. For example, metallic lithium and sodium have chemical shifts of ~ 250 and ~ 1100 ppm, respectively, compared to chemical shifts of ~ 0 ppm for diamagnetic compounds.[15]

3.1.10.2. Experimental methods in paramagnetic NMR

The previously outlined qualities of paramagnetic NMR mean that it is challenging to record useful spectra. However, many useful materials (particularly for batteries) are paramagnetic and so there is interest in developing experimental methods that address the challenges.

The first consideration is the magnetic field used in the experiment. Paramagnetic interactions scale with field, and so it is common where possible to perform measurements using a spectrometer that is 200 MHz or less.[130,159,204] However, quadrupolar broadening is increased at low field, which may lead to poor resolution when recording ^{23}Na spectra for example. Using low fields can also result in problems with low sensitivity, although the short relaxation times of paramagnetic samples can mitigate this issue, owing to the shorter recycle delays required. However, as discussed previously, fast relaxation can lead to a significant amount of the FID occurring during the deadtime. Rotor-synchronised spin echoes can mitigate this although fast spinning is advisable to minimise the echo delays and any resulting loss of signal due to T_2 relaxation.[204]

Fast spinning is also important to remove dipolar coupling. The decoupling pulses typically employed to remove dipolar interactions are not effective over wide frequency ranges. The wide chemical shift ranges and large anisotropies can also pose an issue if using spin echoes to acquire the spectrum, as 180° pulses cannot excite as wide a range of frequencies as

shorter pulses. However, repeating the experiment at different offset frequencies (known as frequency stepping) allows the complete lineshape to be mapped out. This can be inefficient and so people have developed different ways of exciting wide spectral widths in a single experiment.[204]

One such approach is the 2D projection Magic-Angle Turning Phase-Adjusted Spinning Sidebands (pj-MATPASS) experiment.[205] As suggested by the name, this is a combination of the MAT and PASS experiments.[174,201]

A MAT experiment is a 2D experiment that separates the isotropic and anisotropic components of the chemical shift. It is conducted under very slow spinning (~50 Hz), which means that during acquisition, the rotor is quasi-static, resulting in a powder lineshape. However, it is still possible to average out the anisotropy by recording at least three such spectra at equally spaced orientation. Figure 3.22 shows the pulse sequence for the MAT experiment.[174,201]

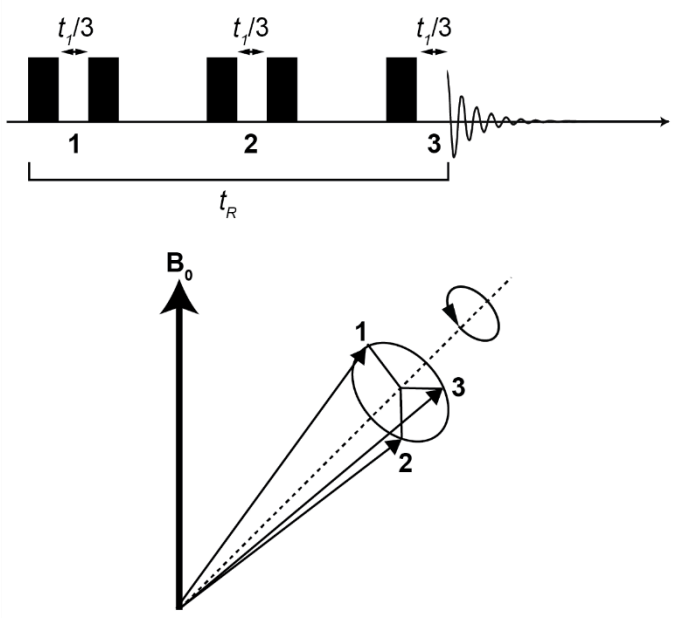

Figure 3.22: Pulse sequence for a MAT experiment (top) and a diagram showing the three rotor positions used during acquisition (bottom). All pulses are 90° pulses.

The initial 90° pulse is followed by a delay equal to $t_1/3$, during which time the magnetisation evolves, but the rotor appears static. After this, another 90° pulse moves the magnetisation back along the z-axis, whilst the rotor moves to its second quasi-static position. This process is repeated a third time, followed by acquisition. The 2D data set is then generated by incrementing t_1. A Fourier transform of this gives a 2D spectrum with a static lineshape in the direct dimension, and the isotopic chemical shifts in the indirect

dimension. This is because the anisotropy is averaged by the three equally spaced evolution periods, and so evolution in t_1 depends only on the isotropic chemical shift.[174,201]

A PASS experiment is a method of separating out spinning sidebands. The pulse sequence consists of a 90° pulse, followed by five 180° pulses, which is repeated with different timings of the 180° pulses. This means that each sideband has a different phase according to its order, *i.e.*, what multiple of the spinning rate it is away from the isotropic peak. Each row then contains one sideband, with the number of rows being determined by the number of sidebands.[174,201]

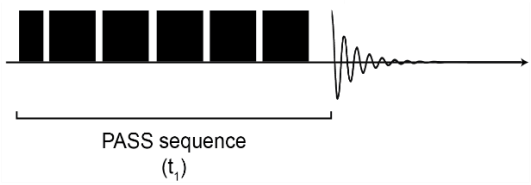

Figure 3.23: Pulse sequence for a PASS experiment, consisting of a 90° pulse followed by five 180° pulses.

A pj-MATPASS experiment combines features of both experiments (Figure 3.24). It is based on the MAT experiment, using 90° pulses and containing three delays equal to $t_1/3$, although the third is part of a longer delay. The phases of the pulses are determined by a 20-step cogwheel phase cycle, but this will not be discussed here. t_1 evolution gives phase information based on the order of the sidebands, turning it into a PASS experiment.[205]

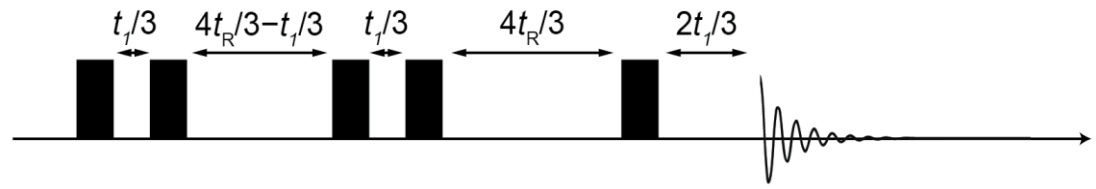

Figure 3.24: The pulse sequence for a pj-MATPASS experiment. All pulses are 90° pulses, with phases determined by a 20-step cogwheel phase cycle. t_R refers to a rotor period.

The pj-MATPASS experiment has several advantages when considering its application to paramagnetic systems. Firstly, it is quantitative and can be used at high fields. pj-MATPASS also avoids the use of 180° pulses, unlike a PASS experiment, which improves the bandwidth that can be excited. The first t_1 increment is also not required to be zero, meaning that no spin echoes are required to avoid deadtime effects.[205]However, the sensitivity of the experiment is reduced compared to a PASS because of the coherence

transfer pathway used. In addition, the evolution periods do not have fixed durations, which means that the effects of T_2 dephasing can be inconsistent, leading to imperfect separation of sidebands.[204]

3.1.11. *In situ* NMR

When studying battery materials, it is simplest to perform *ex situ* analysis, where the cell is disassembled at a particular state of charge and studied with NMR. However, this may miss metastable or short-lived species that form during cycling. Therefore, an alternative approach is to perform NMR experiments *in situ*. This involves making a cell out of a bag or a plastic shell which is inserted into the coil. The cell is connected to an external potentiostat allowing NMR data to be collected during cycling, typically following the behaviour of lithium or sodium ions.[206,207]

Whilst it can provide useful insight, *in situ* NMR is not trivial, and has several practical challenges. Firstly, experiments are normally performed without MAS, meaning resolution can be poor, particularly in the presence of quadrupolar and paramagnetic broadening. This can be mitigated somewhat by the chemical shift of metallic lithium or sodium being Knight shifted, and therefore easier to resolve.[208] However, the broad chemical shift ranges can make it difficult to excite the entire spectrum simultaneously, meaning that retuning may be required. Furthermore, changes in the characteristics of the cell on cycling mean that recalibration may be required.[15]

It is worth mentioning that progress has been made on performing *in situ* experiments under MAS conditions. For example, Mohammed *et al*, assembled a cell that can be taken in and out of a 4 mm rotor, allowing it to be cycled outside the rotor.[209] However, it is not clear as to whether the required manipulation of the cell would affect its electrochemical behaviour.

3.1.12. Predicting NMR parameters using density functional theory

Whilst NMR spectra can be assigned based on experimental information, it can be helpful, indeed sometime necessary, to predict the NMR parameters of a given structure. This is often done using density functional theory (DFT) calculations.

The time-independent nonrelativistic Schrödinger equation is given by Equation 3.54, where $\hat{H}$ is the Hamiltonian, Ψ is the wavefunction and E is the energy associated with that wavefunction.

$$\hat{H}\Psi = \mathrm{E}\Psi \tag{3.54}$$

The Hamiltonian contains contributions from all kinetic and potential energies in the system and can be expressed as shown in Equation 3.55. Here $\hat{T}_e$ is the electron kinetic energy, $\hat{T}_n$ is the nuclear kinetic energy, $\hat{V}_{en}$ is the electron-nuclear potential energy, $\hat{V}_{ee}$ is the electron-electron potential energy and $\hat{V}_{nn}$ is the nuclear-nuclear potential energy.[210]

$$\hat{H} = \hat{T}_e + \hat{T}_n + \hat{V}_{en} + \hat{V}_{ee} + \hat{V}_{nn} \tag{3.55}$$

This is a many-body problem that cannot be solved. However, it is possible to simplify the problem by invoking the Born-Oppenheimer approximation. This means that the nuclei are considered as stationary from the perspective of electrons (due to their much larger masses). Based on this, Equation 3.55 can be simplified to give Equation 3.56, the electron Hamiltonian.[210]

$$\hat{H}_e = \hat{T}_e + \hat{V}_{en} + \hat{V}_{ee} \tag{3.56}$$

Using the electron Hamiltonian in the Schrödinger equation gives the electronic wavefunction. Wavefunctions cannot be measured directly, but the related electron density can. DFT is based on the idea that the ground state energy of a system is a functional of the electron density. The form of this functional is not known and is instead approximated by using a combination of known functions, called basis functions. These can be localised, atomic-centred orbitals or planewave functions. Whilst atomic orbitals may be more accurate, they are more demanding computationally, and so, for large periodic systems, planewaves are more practical.

There are several considerations when performing DFT calculations. First is the number of k-points or the k-point spacing. A greater number of k-points means that more basis functions are used, resulting in a more accurate result. However, more k-points requires more computational power, with often only small improvements in accuracy. The number of k-points is therefore optimised on a known system, prior to starting calculations on the systems of interest.[210]

Another consideration is the use of pseudopotentials. These replace the electron density associated with core electrons with a fixed, approximate value. This reduces the computational expense of the calculations. NMR parameters are intrinsically linked to the electron density at the nucleus and so NMR calculations require suitable pseudopotentials, with gauge including projected augmented wave (GIPAW) being a popular approach.[211]

In addition, when considering heavier elements, relativistic effects start to manifest as the electrons close to the nucleus start to travel close to the speed of light. In these cases, relativistic corrections, such as zero-order regular approximation (ZORA) should be included in the calculation.[212]

Finally, whilst DFT calculations can be performed on any structure, be it experimentally determined or created for a specific purpose, it is necessary to make sure that the structure is an energy minimum. This is because, even for experimentally determined structures, light atoms, such as hydrogen may be difficult to locate using X-ray diffraction (from which many structures are derived). Furthermore, DFT calculations are performed at 0 K rather than at room temperature. Therefore, prior to an NMR calculation being performed, the structure is subjected to a geometry optimisation calculation. This makes small changes to atomic positions and unit cell parameters to minimise the forces exerted on individual atoms. It should be said that these parameters may be fixed at the user's discretion. This process is repeated until the changes between each iteration fall below a user-defined limits. When this happens, the optimisation is concluded.[210]

3.2. Electron Paramagnetic Resonance spectroscopy

Electron paramagnetic resonance (EPR) spectroscopy is sensitive to the local environment of unpaired electrons, such as those found in free-radicals or transition metal ions. Given the challenges of observing paramagnetic species with NMR, EPR is a useful complementary tool. The information in this section is taken from the primer by Chechik *et al*, unless otherwise stated.[203]

3.2.1. The electron Zeeman interaction

As has already been mentioned, electrons possess spin (spin-1/2) and so can interact with external magnetic fields through the Zeeman interaction. Figure 3.25 shows the effect of an external magnetic field on the electron spin states. Note that the signs of the quantum number m_s are reversed compared to those shown in Figure 3.1, with the β state being lower energy.

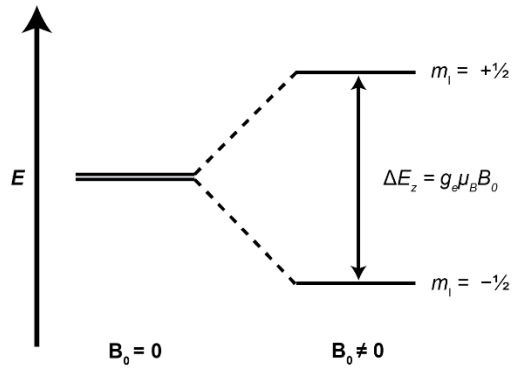

Figure 3.25: The relative energies of the two spin states for an unpaired electron in the absence of and in the presence of an external magnetic field.

The energy of the Zeeman interaction for an unpaired electron is given by Equation 3.57.

$$\Delta E_Z = g_e \mu_B B_0 \tag{3.57}$$

Here g_e is the free-electron g-value (known also as the g-factor) and μ_B is the Bohr magneton, 9.274×10^{-24} J T^{-1}. The g-value is a dimensionless constant used in EPR spectroscopy in place of the gyromagnetic ratio (Equation 3.58).

$$\gamma_e = \frac{g_e \mu_B}{\hbar} \tag{3.58}$$

A free electron has a g-value of 2.0023, however g-values recorded experimentally for samples are often shifted from this. This is because of mixing between energy levels because of spin orbit coupling. The g value of a system is given by Equation 3.59, where *a*

is the covalency parameter, λ is the spin-orbit coupling constant and ΔE is the difference in energy between the mixed states. This change in g-value is also expressed in terms of g-shift, as per Equation 3.60.

$$g = g_e - \frac{a^2 n\lambda}{\Delta E} \tag{3.59}$$

$$\Delta g = g - g_e \tag{3.60}$$

Spin-orbit coupling is a relativistic effect and so λ is larger for heavier elements, resulting in larger g-shift. Organic radicals have small shifts of $\Delta g < 10^{-2}$, whereas for first row transition metal $\Delta g \sim 10^{-1}$.

It is also important to realise that the Zeeman interaction is anisotropic and so the g-value is better described as a g-tensor. In solid samples, this results in powder lineshapes, similar to what is observed in powdered NMR samples (Figure 3.26).

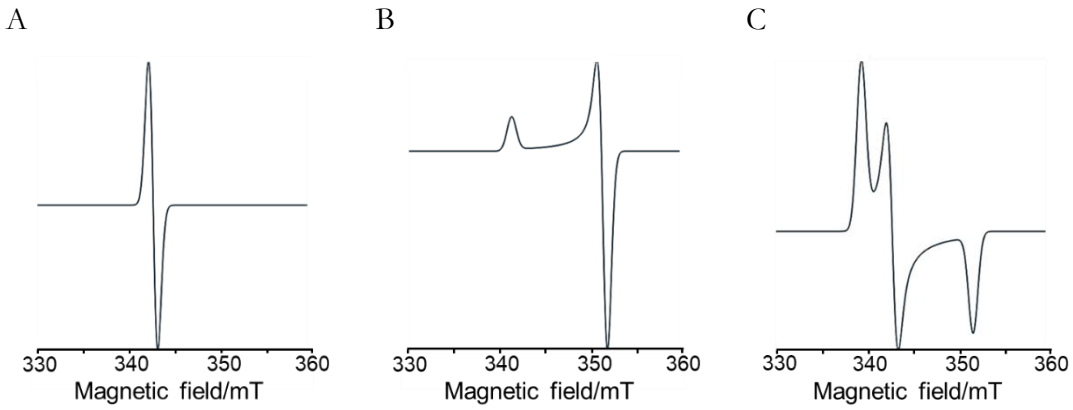

Figure 3.26: Effect of g-anisotropy on the EPR spectrum recorded. (a) isotropic case, (b) axial case and (c) rhombic case.

3.2.2. Other interactions of unpaired electrons

As with NMR, there are several other interactions electrons can experience, some of which have already been discussed in the context of paramagnetic NMR.

The first of these interactions is the hyperfine interaction between electrons and nuclei. In an EPR spectrum, this results in a splitting of the peaks, into $2I+1$ lines (where I is the spin of the nucleus) in a manner like J coupling. Hyperfine splitting is most often associated with EPR spectra recorded of solutions and can provide structural information. It can be observed in the solid-state but is often hard to resolve because of the broadening from g-anisotropy.

There are also interactions between electrons that result in additional broadening. First is dipolar coupling, like what is observed between nuclei, but much stronger. Electrons can also interact through an exchange interaction. This requires orbital overlap, making it a short-range interaction. Exchange interactions can broaden spectra due to increased relaxation but can also cause narrowing at high concentrations due to the loss of hyperfine splitting. Transition metal ions with more than one unpaired electron can also experience something called zero-field splitting. Like the other interactions, this causes broadening, but it also causes the appearance of an additional peak at a field half that of the resonance condition. It should be noted that for ions with integer electron spin, it is very difficult to observe spectra due to the broadening present in these "non-Kramer's" ions.

3.2.3. Continuous wave EPR

The gyromagnetic ratio for an unpaired electron is around 660 times larger than that of a ^{1}H nucleus, resulting in a much larger Zeeman splitting between the spin states. This has ramifications for the acquisition of EPR spectra.

Firstly, the greater energy gap requires MW rather than RF sources to excite transitions. This greater energy gap also means that the population difference between the spin states is larger, resulting in a larger magnetisation. Consequently, EPR is much more sensitive than NMR, and is practical at much lower fields ($B_0 < 1$ T).

A higher gyromagnetic ratio also means that the dipolar coupling is stronger leading to much faster relaxation, resulting in much faster experiments. However, stronger interactions means that EPR spectra are much broader than NMR spectra, making it challenging to excite the entire spectral width with a single pulse. Fast relaxation means that a significant amount of the signal is lost in the deadtime. Even with an echo, it can be impossible to acquire a signal if T_2 is too quick. For these reasons, it is far simpler to record EPR spectra using a continuous wave (CW) approach rather than by applying pulses (although this will be discussed in Section 3.2.5.). In CW EPR, a fixed MW frequency is applied, and the external field is swept. When the field is such that the resonance condition is met (Equation 3.54) a spectrum is recorded. Sometimes the x-axis is expressed in terms of g-value rather than magnetic field, as g-value is independent of frequency.

To improve the signal-to-noise of the spectra recorded, the EPR signal is not recorded directly. Instead, it is modulated by the application of a small oscillating magnetic field (typically 100 kHz). Only signal with the same modulation as the reference is detected.

Therefore, random noise is not detected. Using this approach also results in the derivative lineshape associated with EPR. Figure 3.27 illustrates the effect of signal modulation.

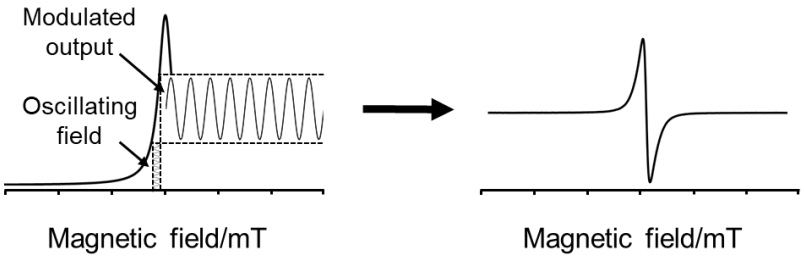

Figure 3.27: The effect of field modulation on the EPR signal recorded.

As mentioned, in an EPR experiment, the MW frequency is kept constant. EPR spectrometers are therefore classified into bands, according to their MW frequency. The most common spectrometer is an X-band spectrometer (~9.5 GHz), which is suitable for organic systems. However, if greater resolution of the different components of the g-tensor is required, higher frequencies may be required, such as Q-band (34 GHz) or even W-band (95 GHz). It should be noted that increasing the frequency means that smaller sample tubes need to be used.

3.2.4. Sample considerations

It is worth briefly discussing the properties of the samples that can be studied with EPR. Whilst spectra can be recorded for both solid and liquid samples (sometimes even gases), it is important to consider the dielectric constant of the sample. This is because the sample sits inside an area called the cavity which has a standing MW inside it. As an electromagnetic wave, the MW consists of a magnetic and electric field, and the cavity is designed so that the sample sits at the maximum magnetic field and minimum electric field. This is to minimise energy losses due to interactions with electric dipoles in the sample. However, if the dielectric constant is high, a large amount of energy is dissipated this way.[213] This makes tuning the spectrometer difficult and affects the acquired signal. In the case of such samples, it is important to use small sample vessels that sit in the electric field minimum as best as possible.

3.2.5. Pulsed EPR

CW EPR is the simplest and most widely used form of EPR, for the reasons previously outlined. However, sometimes it is beneficial to use pulsed EPR, to gain access to greater structural information, such as interelectron distances or relaxation times. Such

measurements are often acquired at low temperatures, to slow electron relaxation to acceptable levels, using echoes to avoid the issues of deadtime.

3.3. Dynamic Nuclear Polarisation

3.3.1. Introduction

NMR and EPR are based on the same fundamental spin physics. It is therefore natural that there is overlap manifesting as paramagnetic effects in NMR spectra or hyperfine splitting in EPR spectra. However, it is also possible to combine the two techniques, an approach that is called dynamic nuclear polarisation (DNP).

As mentioned previously, NMR is sometimes referred to as being intrinsically insensitive, due to the size of the Zeeman interaction. This can be further compounded by nuclei of interest having low natural abundance (^{29}Si = 4.7%, ^{13}C = 1.1%), or the element simply not being present in high proportions in the sample.[179] On the other hand, EPR is highly sensitive owing to the higher gyromagnetic ratio of the electron when compared to nuclei.[203] The premise of DNP is to use unpaired electrons to increase the polarisation of nuclear spins, enhancing the NMR signal.

Using DNP, enhancements of 20 – 200 times are routinely achievable.[214] Whilst an enhancement of 20 may seem small when compared to the theoretical maximum, this enhancement would allow an equivalent experiment to be performed 400 times faster than without DNP. This means that an experiment that would otherwise take a year, could be completed in around one day. Not only does this have the potential to speed up acquisition of normal experiments, but it can also make experiments that would otherwise be unfeasible, achievable. For example, Hope *et al* were able to record ^{17}O spectra for the surfaces of CeO_2 nanoparticles, at natural abundance.[215]

3.3.2. Mechanisms of polarisation transfer

The enhancement obtained from a DNP experiment depends on how efficiently polarisation is transferred from the unpaired electron to the nuclei of interest. Polarisation transfer is governed by one of four mechanisms: the Overhauser effect (OE), the solid effect (SE), the cross effect (CE) and thermal mixing. Which mechanism operates depends on the system DNP is being applied to. Thermal mixing is not often encountered and so will not be discussed here.[214]

The OE transfers polarisation between an electron and a nuclear spin, interacting via the Fermi contact component of the hyperfine interaction.[216] For the OE to operate, the hyperfine interaction must vary with time, to drive the relaxation of electrons. This is simplest to achieve in liquids, due to the motion of the molecules, making the OE the dominant mechanism for solution-state DNP. The OE can also operate in solids, such as metallic conductors using the mobile conduction electrons as a polarisation source. There are some reports of the OE operating in insulating solids, like the *a,γ*-bisdiphenylene-*β*-phenylallyl (BDPA) radical, where the conjugated structure causes fluctuations in spin density at the protons in the structure.[217]

The SE operates in insulating solids and requires a nucleus coupled with an electron through the dipolar interaction. Unlike for the OE, these should be in a rigid arrangement. This interaction causes partial mixing of the different spin states, allowing for zero- and double-quantum transitions to be excited. These are formally forbidden as $\Delta m_I \neq 1$. (Section 3.1.2.). The two transitions are then excited by applying MW radiation at $\omega_{0,e} \pm \omega_{0,n}$, resulting in positive and negative enhancements depending on the transition irradiated. It is important to note that the SE scales poorly with field as the transition probability decreases at higher field, owing to decreased mixing of the spin states.[218,219]

The final mechanism that will be considered here is the CE. This is a 3-spin process, involving two electrons dipolar coupled to a nucleus. Unlike the formally forbidden zero- and double-quantum transitions used in the OE and SE, the flip-flop-flip transitions involved in the CE are allowed as $\Delta m_I = 1$. As a result, the CE is the most efficient method of polarisation transfer, and therefore the most desirable.[218]

The CE requires two unpaired electrons whose Larmor frequencies are separated by the nuclear Larmor frequency. This can either be achieved by using radicals with broad EPR lines, or two radicals with narrow EPR lines tethered together. When this condition is met, irradiating the sample with MWs at the frequency of the one of the electrons results in a positive enhancement. Irradiating at the frequency of the other electron results in a negative enhancement.[220]

3.3.3. Polarisation transfer

To enhance an NMR spectrum, each unpaired electron needs to polarise many nuclei. This can happen either by direct transfer or by spin diffusion. Direct transfer is where polarisation is transferred to many nuclei via one of the mechanisms described previously,

resulting in homogenous polarisation. Direct transfer dominates when paramagnetic relaxation enhancement is the dominant relaxation mechanism.[221] Most DNP experiments rely on spin diffusion for transferring polarisation. In this case, polarisation is transferred to nuclei close to the polarising agent (core nuclei). Strong homonuclear dipolar coupling then allows for polarisation transfer by flip-flop transitions. The distance spin diffusion is effective over can be estimated using Equation 3.61, where D is the spin diffusion constant that depends on the dipolar coupling and T_1 is the longitudinal relaxation time.[221]

$$L = \sqrt{DT_1} \tag{3.61}$$

Equation 3.61 highlights the fact that for spin diffusion to be effective, the relaxation time must be sufficiently long and the dipolar coupling sufficiently strong. This latter point can cause problems when the nucleus of interest is insensitive, like ^{17}O, making spin diffusion slow.[215]

3.3.4. Polarising agents

The unpaired electrons source used for DNP is called a polarising agent. Polarising agents can be split into two types: endogenous and exogenous. Endogenous polarising agents are those found inside the material, such as dopants, or defects, whilst exogenous polarising agents are those added to the sample.[214]

3.3.4.1. Transition metal dopants

Many materials contain paramagnetic transition metal ions. Whilst in principle, any paramagnetic ion could be used as an endogenous polarising agent, in practice the number of suitable ions is limited.

When using transition metal ions for DNP, it is unlikely the enhancement will come through the CE, as the concentration of ions required to achieve a broad enough line would result in very short relaxation times. Therefore, enhancement normally arises from the SE.[221]

Electron relaxation time can also be affected by ZFS and spin-orbit coupling. These also cause broadening of the EPR line, which, as previously mentioned, may lead to excitation of both the zero- and double-quantum transitions simultaneously and consequently a significant reduction in enhancement. ZFS can be reduced by ensuring dopant ions are in highly symmetrical sites. On the other hand, SOC can be quenched by using ions with half-filled shells. This limits the number of ions that can be used dramatically, and so in DNP

literature Cr^{3+}, Gd^{3+}, Mn^{2+} and Fe^{3+} are the ions most encountered.[221] Hyperfine splitting can also play a role with Fe^{3+} being preferable to Mn^{2+}, but this choice may depend on the system.[222]

3.3.4.2. Nitroxide biradicals

Most materials are either diamagnetic or contain paramagnetic ions unsuited to DNP. As a result, it is often easier to add radicals to the sample, via a solution which is then frozen, forming a glassy matrix.[223] The most common radicals used for this purpose are nitroxide biradicals. These are based on the 2,2,6,6-tetramethylpiperidine-1-oxyl (TEMPO) radical, The structure of which is shown in Figure 3.28.[224]

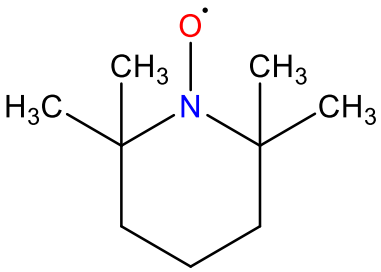

Figure 3.28: The structure of TEMPO.

Nitroxides are popular as they have large g-anisotropies, leading to broad lines that can satisfy the requirements of the CE previously discussed, resulting in in large enhancements. Originally, the CE was performed using TEMPO and its derivatives. However, this requires high concentrations to result in dipolar couplings large enough for the CE, which leads to short relaxation times and inefficient transfer. As a result, it was proposed that TEMPO moieties could be tethered together to create biradicals, the first being the BTnE series (Figure 3.29). Using these radicals reduces the concentration required (as the radicals are guaranteed to be close together) and allowed for enhancements of up to 175 for BT2E (as against 45 for 4-hydroxy-TEMPO).[224]

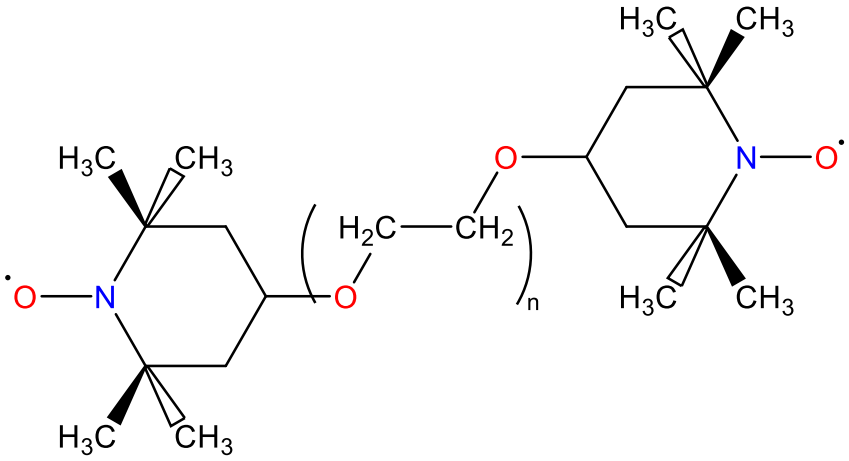

Figure 3.29: Structure of the BTnE series of radicals.[224]

In the years since this development, a substantial amount of research has gone into further optimising these materials. Adding OH groups to the tether as in TOTAPOL, improved the water solubility of the radicals, increasing the number of systems that could be studied.[225] Even shorter, rigid tethers were then used for AMUPOL, increasing the dipolar coupling further, whilst locking the radicals into favourable orientations relative to each other. In addition, the methyl groups that surround the radical centre were replaced by rings, with the reduced motion increasing the electron T_1 time. Together, these improvements lead to an enhancement of up to 400.[226]

Accessibility of the radical centre to the solvent molecules has also been suggested to be important with polarising agents with restricted access to the radical centre showing smaller enhancements. This is thought to be because greater accessibility allows for more efficient transfer to the protons in the solvent molecules, making spin diffusion more efficient.[227]

The poor scalability of the CE with field has been another line of inquiry with radicals being designed that operate well at high field. One example of this are "TinyPol" radicals. These use shorter, mobile tethers and perform roughly twice as well as TEKPol and AMUPol at high field. This suggests that at high field, orientation is less important than strong dipolar coupling.[228]

3.3.4.3. Metallic polarising agents

As mentioned previously, the OE is not often applicable to solid materials, as they lack the motion required to cause fluctuations in the hyperfine interaction. However, metals can be used if present in the sample. For example, Hope *et al*, used lithium metal as a polarisation source to study the SEI formed in batteries and compare the effect of different additives.

What is particularly interesting about this is that whilst the enhancements are relatively small ($\varepsilon < 15$), it can be done at room temperature, rather than cryogenic temperatures. This is because the relaxation time of the electrons does not change dramatically at lower temperatures. As a result, this approach can also be applied to *in situ* measurements, as the electrolyte will not freeze.[216]

3.4. X-ray diffraction and Pair Distribution Function analysis

Unless stated otherwise, the information in this section is taken from *Basic Solid-State Chemistry*.[229]

3.4.1. X-ray sources

In a laboratory instrument, X-rays are generated by an X-ray tube. This contains a tungsten filament that is heated, giving off an electron beam. These electrons are then accelerated by a high voltage at a metal target, which gives off X-rays. This method produces two types of X-rays. These are white radiation, which has a range of wavelengths and monochromatic X-rays. Monochromatic X-rays are produced by ionising the 1s orbital, which is then filled by a higher energy electron releasing an X-ray of fixed energy. The X-ray is designated according to the orbital the electron comes from, with K_α referring to an electron coming from a 2*p* orbital and K_β, the 3*p* orbital. The wavelength of K_α radiation is given by Equation 3.62.

$$\lambda^{-\frac{1}{2}} = C(Z - \sigma) \tag{3.62}$$

Here C and σ are constants, and so the wavelength depends on the mass of the atom. Typical sources for a lab-based instrument are copper and molybdenum which have wavelengths of 1.54 Å and 0.71 Å, respectively. If higher resolution is required, synchrotron sources may be used instead.

3.4.2. Crystal structures

Crystalline materials are made from regular, three-dimensional arrangements of atoms or ions. The repeating nature of these structures means that it is possible to define a single repeat unit, that shows the full symmetry of the material. This is referred to as the unit cell. A unit cell can be defined by the length of its three axes (a, b and c) as well as the three angles between them (α, β and γ). Together, these six values are termed the unit cell parameters. There are seven possible different combinations of these parameters, which are called crystal systems. These are summarised in Table 3.3.

Table 3.3: The seven crystal systems and their unit cell parameters.

Crystal system	Unit cell shape
Cubic	$a = b = c$, $\alpha = \beta = \gamma = 90°$
Tetragonal	$a = b \neq c$, $\alpha = \beta = \gamma = 90°$
Orthorhombic	$a \neq b \neq c$, $\alpha = \beta = \gamma = 90°$
Hexagonal	$a = b \neq c$, $\alpha = \beta = 90°$, $\gamma = 120°$
Trigonal (a)	$a = b \neq c$, $\alpha = \beta = 90°$, $\gamma = 120°$
Trigonal (b)	$a = b = c$, $\alpha = \beta = \gamma \neq 90°$
Monoclinic	$a \neq b \neq c$, $\alpha = \gamma = 90°$, $\beta \neq 90°$
Triclinic	$a \neq b \neq c$, $\alpha \neq \beta \neq \gamma \neq 90°$

In addition to the seven crystal systems, there are four types of lattice centring (Figure 3.30). These refer to how the atoms are arranged. The simplest case is a primitive lattice (denoted P), where there are only lattice points on the corners of the unit cell. Body-centred lattices (I) have an additional lattice point at the centre of the cell, whilst a face-centred lattice (F) has lattice points on the corners and at the centres of each face. There are also side-centred lattices (A, B or C) which have lattice points on two opposite faces, in addition to each corner.

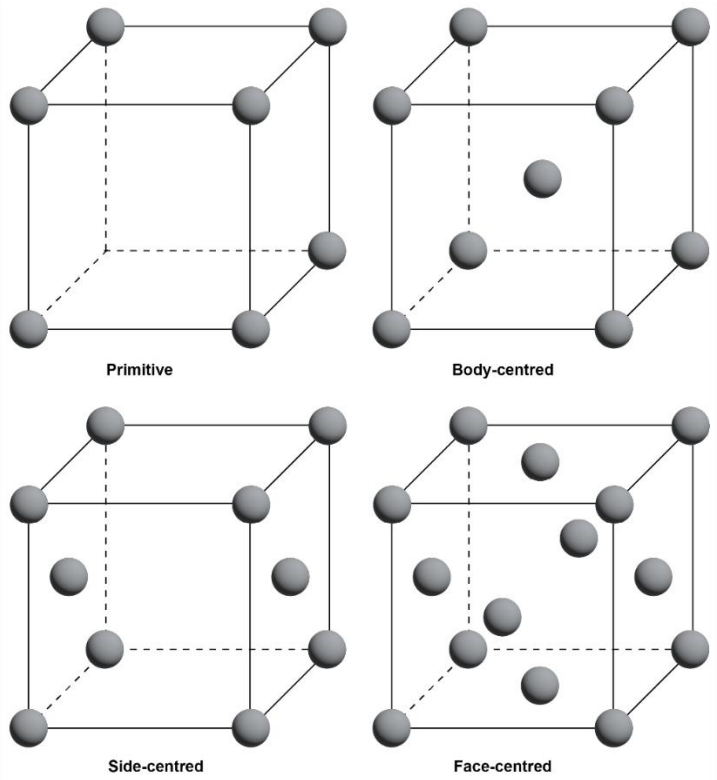

Figure 3.30: The four lattice centring types.

The combination of the seven crystal systems with the four lattice centring types results in 14 unique combinations, called Bravais lattices. Crystal structures can also be described by a collection of symmetry elements (mirror planes, rotational axes, *etc.*). These collections of symmetry elements are called space groups and there are 230 unique groups.

An example crystal structure is the so-called "rocksalt" structure, shown in Figure 3.31. This belongs to the cubic crystal system and has a face-centred lattice, with a 1:1 ratio of cations to anions occupying octahedral sites. The rocksalt structure, along with its variants, are also often referred to by its space group, Fm-3m (number 225). As the later chapters of this thesis are concerned with disordered rocksalt materials, this is a useful example to aid the following discussion of X-ray diffraction (XRD) and pair distribution function (PDF) analysis.

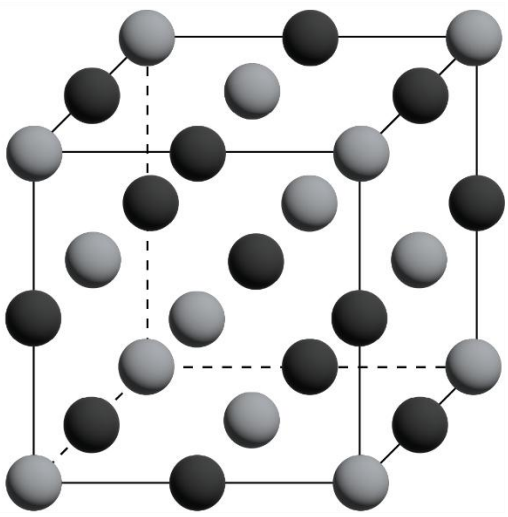

Figure 3.31: The rocksalt structure.

Lattice planes are imaginary, parallel planes through a crystal structure. These serve as a reference grid and can be used when understanding diffraction-based techniques. Lattice planes are described by Miller indices, written in the form (*hkl*). *h, k* and *l* are calculated from the points at which the plane intercepts the *a*, *b* and *c* axes of the unit cell, respectively, and taking the reciprocal of the resulting fractions to obtain three integer values. A rocksalt structure has six visible planes: (111), (200), (220), (311), (222) and (400).

The perpendicular distance, *d*, between the lattice planes for an orthorhombic crystal is related to *h, k* and *l* by Equation 3.63.

$$\frac{1}{d_{hkl}^2} = \frac{h^2}{a^2} + \frac{k^2}{b^2} + \frac{l^2}{c^2} \tag{3.63}$$

For a cubic system, the fact that $a = b = c$, means that this can be rewritten as shown in Equation 3.64.

$$\frac{1}{d_{hkl}^2} = \frac{h^2 + k^2 + l^2}{a^2} \tag{3.64}$$

3.4.3. X-ray diffraction

The regular structure of a crystal means that they can diffract radiation that has similar wavelengths to the spacing between lattice planes, in a manner like how an optical grating diffracts light.

There are two ways this can be described, either using the Laue equations or Bragg's law. Whilst the Laue equations are more mathematically rigorous, Bragg's law offers a simpler

approach that agrees with more robust treatments. Therefore, Bragg's law is the standard way to discuss the diffraction of X-rays.

The derivation of Bragg's law considers two incident X-ray beams, reflected off two adjacent lattice planes, A and B. This is shown in Figure 3.32.

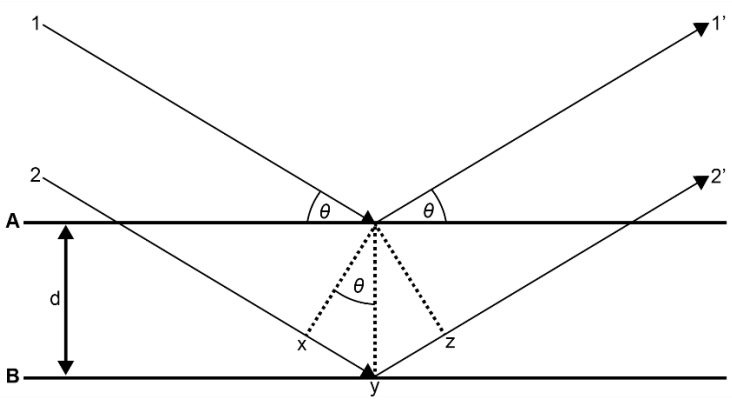

Figure 3.32: Scattering of two parallel X-ray beams (1 and 2) off two adjacent lattice planes (A and B).

The additional distance travelled by beam 2 before it is reflected, is related to the d spacing and the angle of incidence by Equation 3.65.

$$XY = dsin\theta \tag{3.65}$$

The additional distance travelled by beam 2 after being reflected is equal to the additional distance travelled before being reflected. As such, the total additional distance travelled can be calculated using Equation 3.66.

$$XYZ = 2dsin\theta \tag{3.66}$$

To avoid destructive interference between the two X-ray beams the additional distance travelled must equal to some number of wavelengths. Thus, Bragg's law can be expressed according to Equation 3.68.

$$n\lambda = 2dsin\theta \tag{3.68}$$

3.4.4. Powder X-ray diffraction

Single crystals scatter X-rays when the crystal is oriented so that it satisfies Bragg's law. This allows for accurate crystal structures to be obtained. However, it can be difficult to obtain suitable single crystals, particularly of inorganic materials, which typically exist as powders. A powder consists of many individual crystallites, with randomly distributed orientations. This means that Bragg's law will be satisfied by at least some of the crystallites, resulting in a powder diffraction pattern.[230]

Powder X-ray diffraction (PXRD) patterns give information about the crystalline compounds/phases present in a material. Each phase has a characteristic pattern of peak positions and intensities. Each peak corresponds to a separate lattice plane, with the position depending on the *d* spacings. This in turn depends on the size and shape of the unit cell. As such, even materials with the same symmetry, will have peaks in different positions.

The intensities of the peaks in a diffraction pattern first depend on the size of the atoms in the structure, or more specifically, the number of electrons that they have. Heavier elements with more electrons scatter more effectively than lighter elements. Intensities are also affected by systematic absences. These arise if the lattice is non-primitive and mean that certain reflections are not observed as they destructively interfere with each other. Whether or not a reflection is observed depends on the system and the Miller indices. As an example, for a face-centred cubic structure like a rocksalt, *h, k* and *l* must all be odd or all be even. This means that the (110) plane for instance, is systematically absent. Even planes that satisfy this rule, may have reduced intensities. Again, in a rocksalt structure, the (111) reflection may have lower intensity as the anions are midway between the cations and so scatter 180° out of phase. The intensity of this peak therefore depends on the difference in scattering strengths between the cations and anions.

It is also worth noting that the breadth of the peak can be affected by particle size. This is quantified by the Scherrer formula (Equation 3.69).[231] Here L is the particle length (assuming a spherical particle), k is a constant, λ the wavelength, B the peak width and θ the Bragg angle. This is especially important for ball milled samples, where the particle size is small. As such, peaks belonging to phases with different *d* spacings may not be fully resolved.

$$L = \frac{k\lambda}{B\cos\theta} \tag{3.69}$$

A modern powder diffractometer has three key elements: a source, a detector and a sample stage. Measurements are performed by moving the source and detector through a range of angles at a set speed. Data is then displayed on a computer screen in terms of 2θ, which is the angle between the incident and scattered beams.

3.4.5. Pair Distribution Function analysis

Whilst useful in assessing long-range structural features, X-ray diffraction provides little information on local distortions or amorphous materials (where long-range order is absent). This information however can be obtained using total scattering, also known as pair distribution function (PDF) analysis.

In addition to Bragg peaks, X-ray diffraction data contains weak features in the baseline. These arise due to diffuse scattering, which relates to two-body correlations. In a normal PXRD pattern, it is not possible to utilise this information. However, performing a Fourier transform on the collected data gives a pair distribution function (PDF).[232] This is a plot of the probability of finding an atom at a given distance from another atom allowing information about bond distances to be readily obtained by looking at the separation between peaks. More detailed analysis can be performed by fitting the data with theoretical PDF patterns, calculated from the .cif files of known unit cells. This allows unit cell parameters to be calculated, revealing local distortions that may be missed if only a PXRD pattern is recorded.[233]

The resolution of PDF data depends on the magnitude of the scattering, Q. For a given wavelength λ and a particular angle, Q is given by Equation 3.70, with the resolution being dependent on the maximum value of Q (Equation 3.71).[234]

$$Q = \frac{4\pi sin\theta}{\lambda} \tag{3.70}$$

$$\delta r = \frac{\pi}{Q_{max}} \tag{3.71}$$

Q > 30 Å^{-1} is generally desirable for PDF analysis. This means that PDF is typically reserved for synchrotrons. However, lab-based data can be collected using a diffractometer equipped with a molybdenum source, achieving Q values of at least 14 Å^{-1}.[68]

3.5. Resonant inelastic X-ray scattering (RIXS)

3.5.1. Overview of RIXS

Resonant inelastic X-ray scattering (RIXS) is a combination of XAS and X-ray emission spectroscopy (XES). It is largely considered a bulk technique with a sampling depth of 50 – 100 nm.[235] A RIXS measurement consists of two steps. First, the sample is irradiated with X-rays, exciting core electrons to excited states. These then relax releasing X-rays which are detected. The relaxation of excited states can be elastic, or inelastic, where the energy of the emitted photon is lower than that of the incident photon.[149,235,236] Figure 3.33 summarises the processes involved in a RIXS experiment.

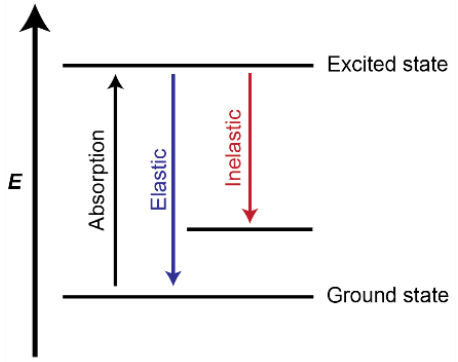

Figure 3.33: The processes involved in a RIXS experiment. Absorption refers to the absorption of the incident X-ray photon, whilst inelastic and elastic refer to the emission of X-ray photons by inelastic or elastic processes.

Measurements are taken at different incident energies and combined to generate a 2D map, with incident energy plotted against emission energy or energy loss. High-resolution line scans may then be performed at specific incident energies, according to the features seen in the RIXS map.[235,236] As discussed in Section 2.4.4.2., the region closest to the elastic peak at 0 ppm is often of interest. Sharp peaks here arise due to molecular vibrations, allowing species present to be identified. Broad features may also be observed in other regions of the spectra, although the origin of these have not been described in detail.

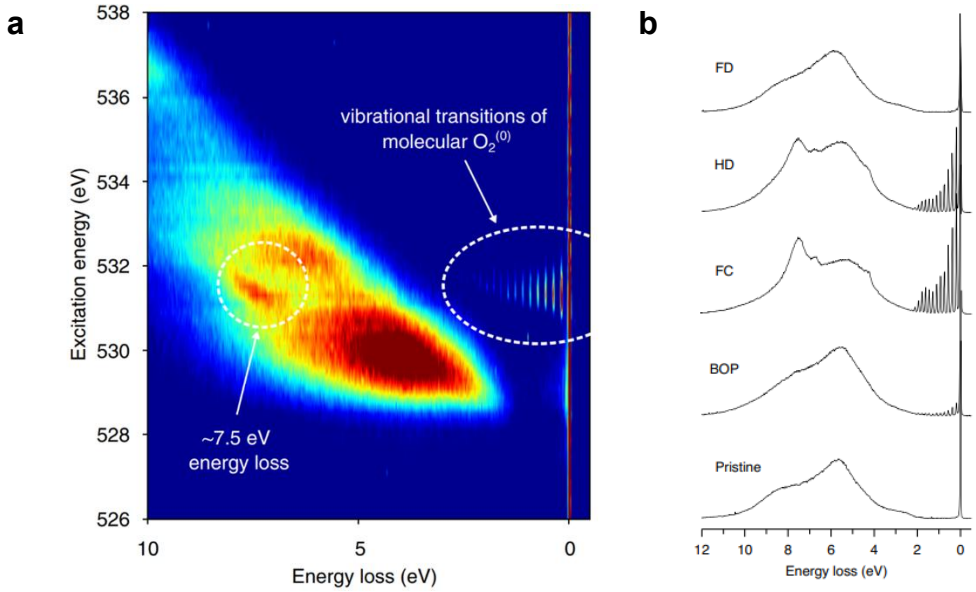

Figure 3.34: (A) a RIXS map. Dotted circles denote features of interest associated with molecular oxygen. (B) Line scans for samples at different states of charge taken at 531 eV. Spectra labelled HD and FC show vibronic features attributed to molecular oxygen in addition to the elastic peak at 0 eV. Reproduced from the Figure 3 (a and b) in the paper by House *et al.*[142]

3.5.2. Application of RIXS to battery materials

Whilst RIXS can be used to give information about transition metal ion oxidation states in battery materials, its most common application to battery materials is to confirm the presence of molecular oxygen thought to be produced as part of O-redox processes.[142,149] This is because of the peak spacings observed at around 531 eV (Figure 3.34), that match those expected for molecular oxygen, although there is still debate as to whether this oxygen arises due to electrochemical activity of the electrode materials.[140,144]

It should be noted that whilst in principle this information is contained within K-edge soft XAS data, the pre-edge region contains contributions from transition metal character. Therefore, any conclusions are unreliable, and so RIXS is required to resolve these features of interest.[149]

3.5.3. Practical considerations

When characterising *ex situ* battery samples, it is important to consider that they are air sensitive and that any states of interest may be unstable. The former is not an issue for RIXS as the equipment is kept under ultra-high vacuum. However, the inelastic processes that are leveraged in a RIXS measurement are low probability, meaning that high flux of

photons is required. This may result in beam damage, particularly for unstable samples. Therefore, high efficiency spectrometers are required to reduce the radiation dose.[149] Part of this involves maximising the resolution, either through improved optics or building spectrometers with longer detector arms.[237]

Figure 3.35: The RIXS spectrometer hall for the I21 beamline at Diamond Light Source. The blue detector arm is set to 90°.

3.6. X-ray photoelectron spectroscopy (XPS)

Unless stated otherwise, the information in this section is taken from Introduction to X-ray Photoelectron Spectroscopy.[238]

3.6.1. Introduction

X-ray photoelectron spectroscopy (XPS) is a powerful surface analysis technique, use to study a wide range of materials. XPS can observe all elements, except hydrogen and helium, and provide quantitative information about the local chemical environments present.

3.6.2. Generation of photoelectrons

XPS is based on the photoelectric effect. When a sample is irradiated with soft X-rays (with energy < 6 keV), electrons are emitted from core orbitals. This is shown in Figure 3.36.

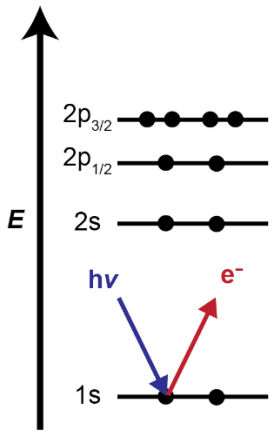

Figure 3.36: Generation of photoelectrons due to the absorption of an X-ray photon.

Electrons emitted have kinetic energy, and this is what is measured in an XPS experiment. The kinetic energy the electron has, depends on the energy of the incident X-rays, the work function (φ) of the sample and electron analyser and the binding energy of the electron. As the other parameters are known or measured, the relationship between these is expressed as shown in Equation 3.72, where E_B and E_K are the binding and kinetic energies respectively and $h\nu$ is the energy of the X-rays.

$$E_B = h\upsilon - E_K - \phi \tag{3.72}$$

The binding energy is a measure of how tightly bound the electron is and depends on the local chemical environment. Increasing electronegativity of the nearest neighbours increases binding energy. For example, the binding energy for a C-C environment is 285

eV which increases to 288 eV in a C=O environment. Binding energy also increases with oxidation state as the greater positive charge makes it harder for electrons to be removed.

3.6.3. Auger electrons

A fact ignored until now is that the emission of photoelectrons generates a hole in the core orbitals, which is unstable. This state can relax by an electron from a higher energy orbital dropping down. The excess energy of this electron can either be released as a photon (X-ray fluorescence, XRF) or transferred to another electron in a high energy orbital, which is then emitted. Figure 3.37 shows these two processes.

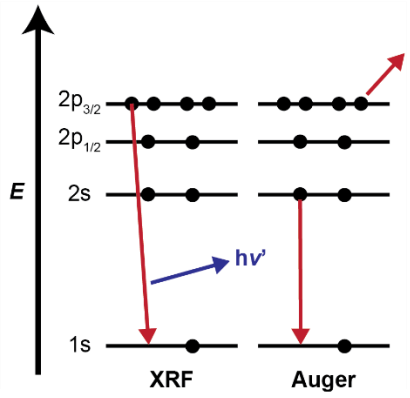

Figure 3.37: The processes leading to XRF and the production of Auger electrons.

The electrons emitted in this way are called Auger electrons, and result in additional peaks in an XPS spectrum. Auger peaks can be useful in qualitative analysis and are identified by moving between X-ray sources. However, they are not important when analysing the XPS spectra presented in subsequent chapters and so will not be discussed further.

3.6.4. Surface sensitivity

X-rays penetrate a sample up to a depth on the order of a few μm. There are then three possible scenarios that the emitted photoelectrons can encounter. First, they can be emitted without experiencing any inelastic collisions and arrive at the detector with maximum kinetic energy. These electrons are what contribute to the main peaks observed in an XPS spectrum. Second, electrons can experience several inelastic collisions but still have enough energy to leave the material. These electrons have lower kinetic energy and so contribute to the background of the XPS spectrum. The third situation is that the electrons experience many inelastic collisions and do not have enough energy to escape the material and are therefore not detected.

The probability of experiencing collisions increases the deeper electrons are generated. The intensity of emitted electrons, I, from a given depth, d, is given by Equation 3.73, where I_0 is the total intensity and λ is the attenuation length.

$$I = I_0 exp\left(\frac{-d}{\lambda}\right) \tag{3.73}$$

For an electron with a kinetic energy of 1000 eV, 95% of electrons escape from the sample from a depth of 10 nm. This is referred to as the sampling depth and is the limit to which XPS measures. Therefore, XPS is considered a surface sensitive technique.

3.6.5. Interpretation

There are two main types of XPS spectra: wide scan (also known as survey spectra) which cover a large range of binding energies and high-resolution spectra which focus on single peaks. Wide scan spectra are used to provide general chemical information, whilst high resolution spectra allow the assignment of different chemical environments. Spectra are plotted in terms of binding energy against intensity (in counts per second), with binding energy going from high to low, moving left to right.

The peaks in XPS spectra are labelled by the element and orbital the electrons come from. For example, an electron from the carbon 1*s* orbital contributes to the C1s peak. The energies for each element are well-defined allowing the peaks to be identified.

Peaks arising from s orbitals are singlets, but those from other orbitals are doublets, due to spin-orbit coupling. Equation 3.74 shows the relationship between the total angular momentum quantum number, j, and the orbital and spin angular momentum, s and l.[239]

$$j = l \pm s \tag{3.74}$$

From this it can be seen that there are two possible states when $l > 0$, resulting in a doublet. If $l = 0$, there can only be one state (as j must be positive), which leads to peaks from s orbitals being singlets. The intensities of the peaks in the doublet can then be determined from the degeneracy of the spin states, $(2j + 1)$.

Systems with many electrons, such as aromatic materials can result in additional features, such as so-called shake up peaks.

It should be noted that it is necessary to calibrate the spectra, before making detailed assignments. This is typically done using the C1s peak which is set to 284.5 eV. Carbon

contamination is ubiquitous in surface samples, meaning this approach can be applied even when analysing materials that should in theory not contain carbon.

3.7. Summary

The techniques outlined in this chapter each allow for specific aspects of a material's structure to be studied. PXRD provides information about long-range structural features, whilst NMR and PDF are sensitive to local structure. These are all generally bulk techniques and so exploring the surface is best done using XPS. Probing specific species such as radicals or molecular oxygen require more specialised techniques, namely EPR and RIXS, respectively. Understanding complex materials, like those described in Chapter 2, therefore requires strategic deployment of multiple techniques, as will be discussed in the following results chapters.

4. Plasma polymer coatings for extending electrode lifetimes

4.1. Introduction

As discussed in the introduction, the planned widespread adoption of electric vehicles has spurred interest in new cathode materials with high energy densities.[4] High energy densities can be achieved by using cathode materials with high operating voltages or high capacities. This chapter will focus on the high-voltage materials.

Whilst high-voltage materials, such as the spinel lithium nickel manganese oxide (LNMO), result in high energy densities, they are prone to parasitic side reactions. This is because the voltages achieved exceed the stability of the electrolyte solvent. For example, LNMO has a voltage of 4.7 V (vs Li/Li^+), which is higher than the upper limit of stability for ethylene carbonate (> 4.5 V).[38,39,240] Furthermore, high voltage materials often also form reactive oxygen species on cycling that can attack the solvent molecules.[52] In addition to these processes at the cathode, degradation reactions at the anode (electrolyte reduction) result in decomposition products that can migrate to the cathode (referred to as crosstalk).[55] Together, these processes lead to the formation of a layer called the cathode-electrolyte interphase (CEI). This is a thin layer, comprised of both inorganic species, such as Li_2CO_3, and organic deposits.[55,241] Formation of the CEI leads to an irreversible loss of capacity but can be important to ensure the long-term performance of the cell.[241] It is therefore important to develop strategies to control the formation of the CEI.

One approach is to coat the cathode with a coating that has a specifically chosen chemistry. There are many such materials that have been investigated as discussed in Chapter 2.[56,65,76] However, no perfect preparation method has been devised. For example, atomic layer deposition is slow but provides uniform coatings.[71] Meanwhile, sol-gel methods, whilst simple to implement, require extensive drying steps to remove any residual solvent but are practically simple to implement.[33,56]

The work in this chapter will investigate the use of plasma polymerisation to prepare protective coatings. Plasma polymerisation is a solvent-free method of creating thin and uniform coatings and could be applied to powders or completed electrodes. In addition, it

is fast with deposition times of minutes rather than hours.[90] Furthermore, plasma polymerisation can be used to create coatings from a diverse range of precursors, allowing for a wide range of coating types to be created and tested.[87]

Chapter 2 discussed several different possible coating types that could serve as protective cathode coatings. However, it is important that the cathode coating serves not only as a barrier layer but is also ionically conductive.[56] Poly(ethylene oxide) (PEO) is one possible material that could be used as an inspiration. It is organic and its C-O bonds allow for lithium ions to move through the structure.[102] Therefore, polymers containing C-O bonds were chosen for this initial investigation, specifically ethanol-based coatings.[104,106] Ethanol is a small molecule, meaning that the coatings prepared will have limited complexity. Furthermore, it is simple to handle, making it a useful model precursor. This will allow unforeseen challenges with the technique to be more easily identified.

Another possible coating type, that leverages the diversity of coatings possible using plasma polymerisation are coatings based on the 2,2,6,6-tetramethylpiperine-1-oxyl (TEMPO) radical. This is a stable oxygen-centred radical, the structure of which is shown in Figure 4.1. TEMPO-based plasma polymers have been previously reported, with the first work being by Michl *et al* in 2018.[242] In the battery field, TEMPO has seen use as an electrolyte additive, with it being suggested that it can mitigate side reactions by reacting with radical species formed during cycling. However, TEMPO is electrochemically stable up to 3.5 V, making it more suited to being used as an anode coating, rather than a cathode coating.[243] However, as mentioned already, CEI formation is not exclusively due to reactions at the cathode and has been shown to be influenced by "crosstalk" with the solid-electrolyte interphase (SEI) that forms on the anode.[55] An alternative or complementary strategy to controlling CEI formation could therefore be to modulate SEI formation, *i.e.*, by applying a coating to the anode as well.

Therefore, the second part of the work in this chapter will focus on investigating whether these coatings provide a viable way of attaching radicals to the electrode surface. Radical-containing surface coatings could also serve as a means of polarising the nuclei on the surface, allowing DNP-enhanced NMR to be performed.[214] DNP-enhanced NMR has been used on several occasions to study interphases.[50,64,244] Therefore, this could be a useful approach to provide greater insight into the layer that forms, whilst avoiding the standard DNP sample preparation steps.

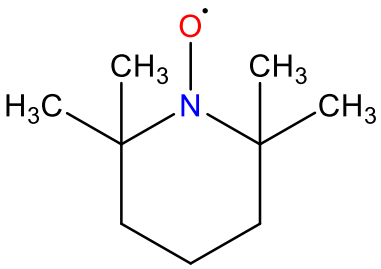

Figure 4.1: The structure of the TEMPO free-radical.

4.2. Experimental

4.2.1. Plasma polymer coatings

Plasma polymer coatings were prepared using a custom-made reactor with a driving frequency of 13.56 MHz. An image of the reactor used may be found in Chapter 2 (Figure 2.1), with the specifics of the design being described elsewhere.[245] Prior to each experimental day, the reactor was cleaned with water and isopropanol, followed by an air plasma (10 Pa, 60 W) for 10 minutes.

Coatings were prepared using three different precursors: ethanol (Fisher Scientific, ≥ 99.8%, HPLC grade), TEMPO (Alfa Aesar, 98%+) and 2,2,6,6-tetramethylpiperidine (TMP) (Alfa Aesar, 98%). The reactor barrel, precursor flask and needle values were switched between using ethanol and the nitrogen-containing precursors, to avoid contamination of the coatings. When using ethanol and TMP, ~ 5 ml of precursor was added to the sample flask and degassed by freeze-thawing. When using TEMPO, ~ 1 g of precursor was used, which was degassed by opening the needle valve to vacuum three times. In addition, when using TEMPO, the precursor flask was submerged in a water bath set at 25°C throughout deposition, to ensure a stable pressure.

Ethanol-based coatings were prepared on silicon wafers (Inseto), Al_2O_3 powder (Acros Organics, chromatography grade, 50 – 200 μm) and $LiNi_{0.5}Mn_{0.3}Co_{0.2}O_2$ (NMC532) electrodes (MTI, 0.6 μm, batch number: 0011511). Specific plasma deposition conditions for the ethanol-based coatings are given in the text.

TEMPO-based coatings were prepared on SiO_2 powder (Alfa Aesar, 99.5%), NaCl (Sigma Aldrich, > 99.5%), Al_2O_3 powder and polytetrafluoroethylene (PTFE) (Goodfellow). Coatings were deposited using a pressure of 10 Pa, a power of 5 W and a deposition period of 3 x 10 minutes. Powdered materials were mixed between each deposition period to maximise coverage. Samples were also prepared by exposing the substrates to TEMPO

vapour (pressure of 10 Pa with the power set to 0 W) and air plasma (10 Pa, 60 W) for the same length of time.

TMP-based coatings were prepared on Al_2O_3 powder, using a pressure of 20 Pa and a power of 20 W, for 3 x 10 minutes, with the powder being mixed between each deposition period.

4.2.2. Electrochemical tests

12 mm NMC532 electrodes (uncoated and ethanol-coated) were assembled into half cells under argon atmosphere (< 0.1 ppm O_2/H_2O). The cells were constructed using parts made from 304 steel (TOB machine), 1 M $LiPF_6$ in EC:DMC (1:1) (Sigma Aldrich) as the electrolyte, Whatman glass fibre separators (18 mm) and lithium wafers (15 mm x 1 mm) (TOB machine). Cells were cycled at a rate of 1 C between 2.5 and 4.2 V using Neware electrochemical cyclers.

4.2.3. X-ray photoelectron spectroscopy

X-ray photoelectron spectroscopy (XPS) spectra were recorded by Drs Alex Robson and Alessio Quadrelli, using a Kratos AXIS Supra spectrometer using monochromatic Al Kα 1486.7 eV operating at 15 kV and 15 mA. Spectra were fitted with CasaXPS and the spectra were referenced to the C1s peak at 284.5 eV.

4.2.4. Solid-state NMR spectroscopy

Solid-state NMR experiments were performed using a Bruker Avance III HD spectrometer operating at a magnetic field strength of 16.4 T, equipped with either a 3.2 mm or 4 mm probe. ^{1}H and ^{13}C NMR spectra were referenced to tetramethylsilane using *L*-alanine as a secondary reference. ^{1}H spectra were referenced to the $-NH_3^+$ peak (8.5 ppm) whilst the ^{13}C spectra were referenced to the $-CH_3$ peak (20.5 ppm). Depth experiments were used to acquire the ^{1}H spectra and ^{13}C spectra were acquired using cross polarisation (CP). The ^{1}H pulse length was optimised to 2.5 μs, whilst the contact pulse power (85 W) was linearly ramped from 70 – 100 %, and ^{1}H decoupling was applied using a two-phase pulse modulation scheme. The contact time was 1 ms. Further experimental details can be found in the figure captions of the spectra.

4.2.5. Electron paramagnetic resonance spectroscopy

EPR spectra were recorded on a Bruker EMXplus spectrometer (9.8 GHz) and 4 mm quartz EPR tubes. The microwave power in all cases was 2.135 mW and modulation frequency was 100 kHz. Unless stated otherwise the number of scans, time constant and conversion time were 16, 5.12 ms and 20 ms, respectively. Other experimental details are detailed in the figure captions of the spectra. To account for the discrepancy between the measured field and the field at the centre of the cavity, spectra were recorded for strong pitch and TEMPO. Based on these known g-values (2.0028 and 2.006, respectively) a correction of –0.01684 was applied to all g-values calculated by WinEPR processing.[246]

4.3. Results

4.3.1. Ethanol-based cathode coatings

There are several precursors that could be used to achieve coatings containing C-O groups, such as crown ethers.[79,104,106] However, plasma polymers have only rarely been applied to battery materials. Therefore, to begin this investigation, a precursor that is simpler to use is a more suitable choice, allowing potential issues with the process to be identified. Ethanol has a low boiling point, making it practically much simpler than using crown ethers, which would require heating elements to ensure a uniform and adequate vapour pressure in the reactor barrel. Crown ethers, such as 12-crown-4, are also more hazardous than ethanol.[105] For these reasons, ethanol was chosen as the precursor for this initial investigation.

4.3.1.1. Effect of plasma conditions on coating properties

The functional groups present in a plasma polymer coating are largely determined by the precursor used, as this provides the basis for the coating. However, the coating is also influenced by the deposition conditions, namely the precursor pressure, radiofrequency (RF) power and deposition time. It is therefore useful to explore the effect of these conditions prior to optimising the coating chemistry or coating electrodes for testing in coin cells.

First, the effect of precursor pressure was investigated by preparing coatings on silicon wafers at a fixed RF power (5 W) using pressures from 2 - 10 Pa. The deposition time in all cases was 10 minutes. For each of these samples, wide scan XPS spectra were recorded to determine the elemental composition. These are shown in Figure 4.2.

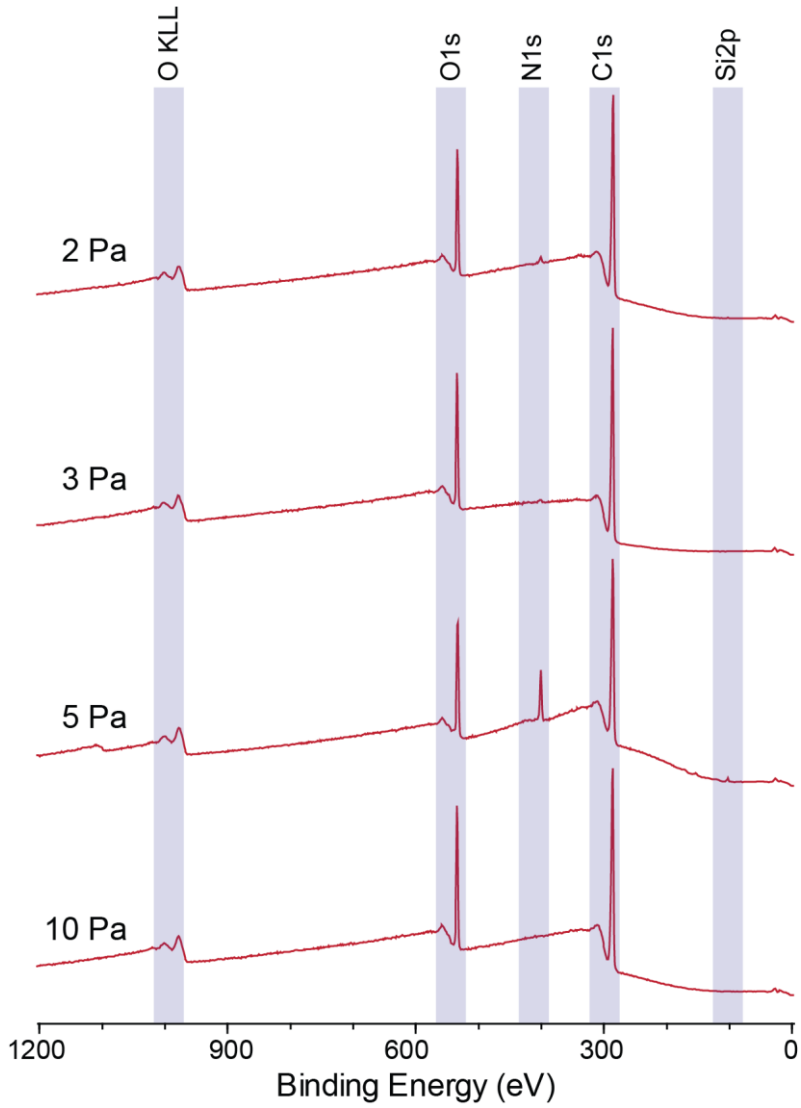

Figure 4.2: Wide scan XPS spectra recorded for ethanol-based coatings deposited onto silicon wafers for 10 minutes with a power of 5 W and a pressure of 2 Pa, 3 Pa, 5 Pa and 10 Pa.

All the XPS spectra recorded for the coated silicon wafers show C1s and O1s peaks (at 285 and 531 eV, respectively). This means that an organic layer has successfully been deposited onto the silicon wafer. It can also be seen that the baseline of each spectrum rises between 0 – 300 eV. This rise can be attributed to the silicon substrate, and the fact that it is visible means that all these coatings are less than 10 nm thick (as this is the sampling depth of XPS). There is some variation in the extent of this rise, with it being most pronounced in the spectrum recorded for the 5 Pa sample, and least pronounced in the spectrum for the 3 Pa sample. This is indicative of different thicknesses between the samples, possibly arising from differences in plasma density. It is not possible to quantify the differences from this data.

From Figure 4.2 it can also be seen that all spectra, aside from the one recorded for the 10 Pa sample, contain an N1s peak (400.5 eV), meaning that nitrogen has been incorporated into the polymer. There are two likely explanations for this. Either this could come from contamination of the reactor barrel with an amine precursor or from leaks allowing air into the barrel during deposition. The intensity of the peak does not follow a trend, in terms of precursor pressure. This would suggest that it does not originate from contamination, as the coatings were prepared in order of increasing pressure. If contamination was the cause, the N1s peak would be expected to be most pronounced for the 2 Pa sample, as this was produced first, with the intensity decreasing with each increase in pressure as the contaminant is burnt off. Therefore, this N1s peak is more likely to stem from leaks, caused by slight shifts in the reactor set up as the system is cycled between base pressure and atmospheric pressure.

It should also be noted that the spectrum recorded for the 2 Pa coating shows a peak at 1071 eV, indicative of sodium. This could originate from sample preparation and handling, with the source being sweat. However, if this is the case, it would also be expected that a Cl2p would also be present (~199 eV). Therefore, this is likely an artifact/noise that CasaXPS has incorrectly identified as a peak.

Following this, the effect of RF power was investigated. Coatings were prepared with a precursor pressure of 5 Pa, and the power was varied, with coatings prepared using 5, 10 and 20 W RF power. Again, the deposition time was 10 minutes. Figure 4.3 shows the wide scan XPS spectra recorded for these samples.

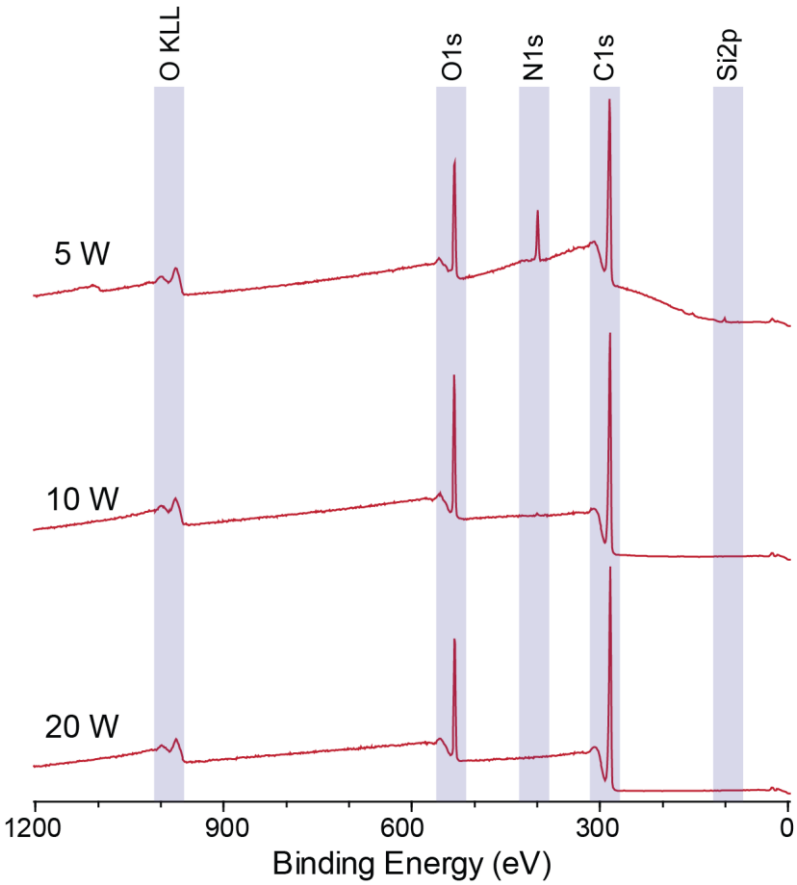

Figure 4.3: Wide scan XPS spectra recorded for ethanol-based coatings deposited onto silicon wafers for 10 minutes with a pressure of 5 Pa and a power of 5 W, 10 W and 20 W.

As with the previous spectra, all the spectra show peaks C1s and O1s peaks, indicating the successful deposition of an organic coating. The spectra for the coatings produced using 5 and 10 W also show N1s peaks, which as discussed before may just be the result of random leaks. For the spectrum recorded for the sample prepared using an RF power of 5 W, the Si2p peak is visible at 99.4 eV, and the baseline rises between 0 – 300 eV. The baselines for the two spectra recorded at higher powers are flat in this region. This would suggest that the coating produced at lower power is less than 10 nm thick, whilst the other two coatings are thicker than 10 nm. One explanation for this is that the increased power results in more reactive species in the plasma phase and therefore a thicker coating.

The final factor to address during this initial exploration of parameters the effect of deposition time. Therefore, a coating was deposited using 5 W RF power and a pressure of 5 Pa, with a deposition time of 5 minutes as opposed to 10 minutes. The wide scan spectrum for this sample is shown in Figure 4.4.

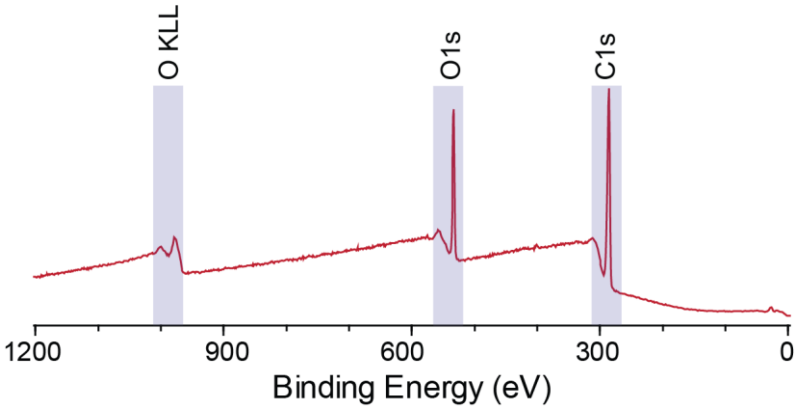

Figure 4.4: Wide scan XPS spectra recorded for an ethanol-based coating deposited onto a silicon wafer using a pressure of 5 Pa and a power of 5 W for 5 minutes.

The spectrum in Figure 4.4 shows a C1s, O1s and N1s peak, with a rise in the baseline between 0 – 300 eV. This agrees with the spectrum for the sample with the same conditions and a 10-minute deposition, as would be expected. To gain more insight into any differences, high resolution C1s spectra were recorded for both samples. Figure 4.5 shows these spectra overlaid.

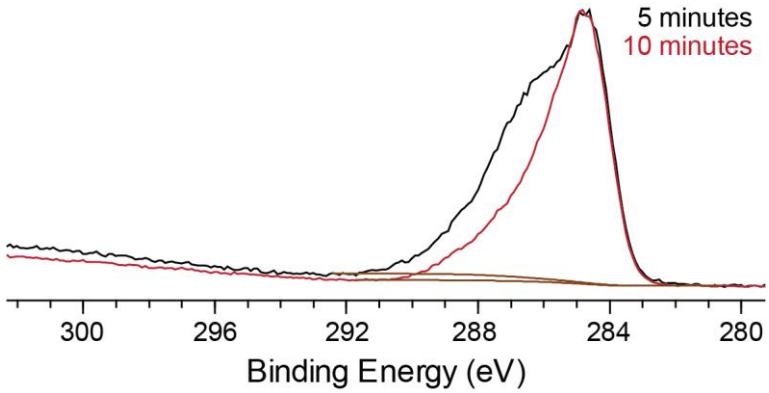

Figure 4.5: High-resolution C1s spectra recorded for ethanol-based coatings prepared using a pressure of 5 Pa and a power of 5 W, deposited for 5 (green) and 10 minutes (red).

The C1s spectrum recorded for the coating deposited for 5 minutes is broader than the spectrum recorded for the 10-minute coating. As this broadening is on the higher binding energy side of the peak, this likely comes from increased C-N and C=O environments. One explanation for this is that the coating prepared with a shorter deposition time is less stable and so reacts with air forming more C=O bonds. The coating prepared with a longer deposition time spends more time in contact with neutral precursor molecules, and so reactive species in the coating could be quenched by reactions with the precursor instead.

The results in this section demonstrate that it is possible to successfully deposit ethanol-based coatings onto silicon wafers. These coatings can be made to be less than 10 nm thick,

with high RF powers resulting in thicker coatings. The coatings can be prone to nitrogen contamination, likely from leaks in the reactor barrel. There is also an indication that deposition time influences the functional groups present in the final coating, with coatings deposited for shorter periods having a greater proportion of C=O environments.

4.3.1.2. Effects of deposition conditions on C-O incorporation

The previous work served as a preliminary investigation of the main parameters that can be changed when depositing plasma coatings. However, before coating actual electrodes it would be useful to optimise the parameters to control the proportion of C-O bonds. As a starting point, it may be advantageous to prepare coatings with the most C-O bonds, as these could help facilitate ion diffusion through the coating.

Coatings were prepared on silicon wafers using different conditions within the range explored in the previous section. C1s spectra were then recorded and deconvoluted to determine the proportions of the peak that could be attributed to C-C and C-O bonds. The results of this are shown in Figure 4.6, with the y-axis given as the ratio of the two environments. It is not possible to include error bars due to CasaXPS no longer being accessible at the time of writing.

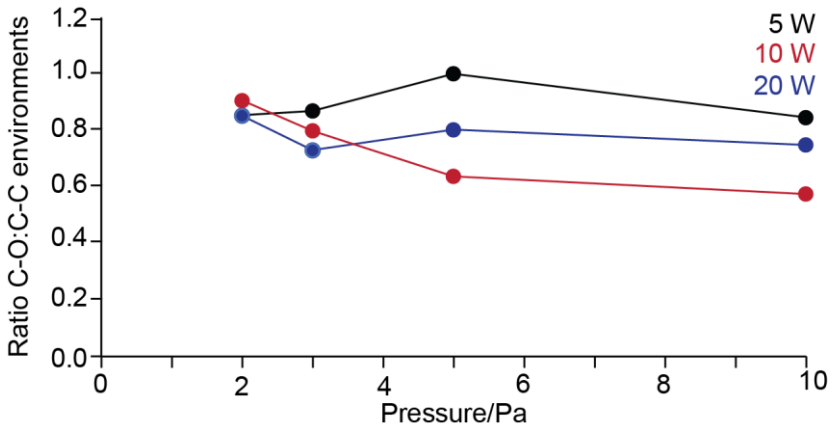

Figure 4.6: The ratio of C-O:C-C environments in ethanol-based coatings deposited using different combinations of pressure and power for 10 minutes.

From Figure 4.6 for the coatings produced using 5 and 10 W RF power, the ratio of the two environments increases to a maximum at 5 Pa before decreasing at 10 Pa. The coatings produced using an RF power of 20 W follow a different trend, with the proportion of the two environments decreasing with increasing pressure. This means lower pressure is likely better for producing coatings containing the most C-O bonds. Furthermore, aside from the coatings prepared using a pressure of 2 Pa, the coatings prepared using an RF power

of 5 W show the highest amount of C-O bonds. This is likely due to the lower power fragmenting the precursor to a lesser extent. However, it should be noted that in all cases the C-O environments may include C-OH environments as well as the desired C-O-C environments. This is because they cannot be distinguished using XPS. Whilst -OH groups may facilitate ion transport, they are undesirable as they may reduce the electrochemical stability of the coating.[247]

Based on these results a second set of coatings were prepared using an RF power of 5 W and pressures of 4, 5, 6 and 7 Pa, to further narrow down the optimum conditions. The previous fitting procedure was repeated, and the results are shown in Figure 4.7, along with the results from the first attempt for comparison.

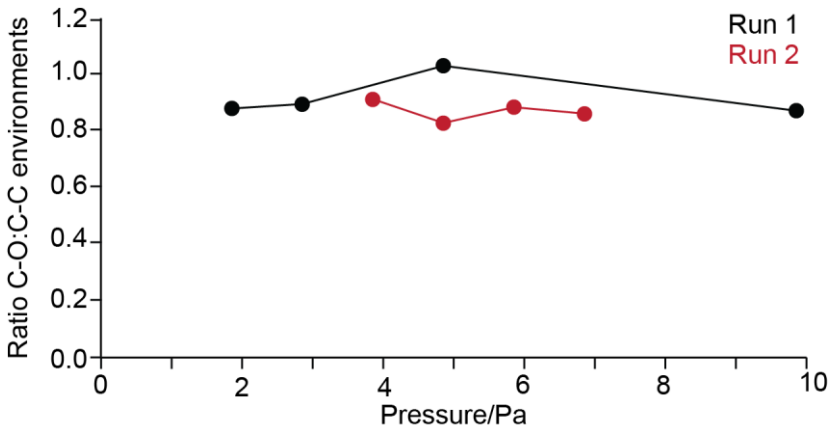

Figure 4.7: The ratio of C-O:C-C environments in ethanol-based coatings deposited using different pressures at a power of 5 W for 10 minutes.

Figure 4.7 shows that the ratio of the two environments is quite consistent across the second series of samples, with the ratio staying between 0.8 and 0.85. This would suggest that the pressure does not exert significant influence over the coating chemistry, although there is a slight downward trend. A notable point is that the coating prepared using a pressure of 5 Pa shows the lowest proportion of C-O environments, whereas for the first series of coatings, this coating shows the highest proportion. This raises a question of the reproducibility of plasma polymer coatings. However, this could also be due to error in the fitting and so this discrepancy is something that requires further investigation in the future.

4.3.1.3. Uniformity of plasma polymer coatings

It is important that the plasma polymer coatings be uniform across the electrode surface, to ensure consistent protection. A first attempt at exploring this was made using scanning

electron microscopy, however the sub-10 nm coating thicknesses meant that it was not possible to observe the coating.

Another approach to gain some insight into coating uniformity is to use XPS to record C1s spectra at different sites. Figure 4.8 shows the C1s spectra recorded for coatings prepared using an RF power of 5 W.

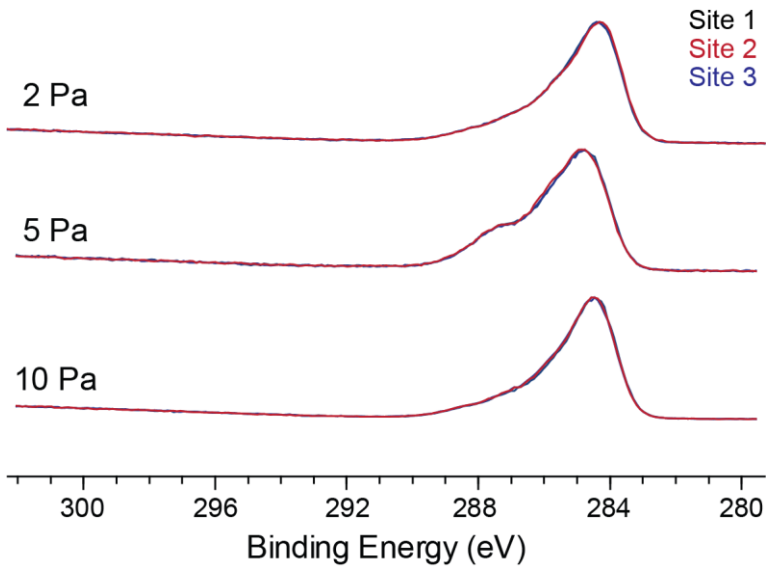

Figure 4.8: Overlaid C1s spectra for coatings deposited for 10 minutes using a power of 5 W and a precursor pressure of 2 Pa, 5 Pa and 10 Pa.

For all three coatings there is good agreement between the three C1s spectra recorded. This indicates that the coatings produced could be considered uniform across the silicon wafer, an area which is comparable to the size of electrodes used in coin cells.

4.3.1.4. Ethanol-coated electrodes

Up to this point, all the coatings prepared were prepared on silicon wafers. Whilst this is a convenient model substrate, testing the electrochemical properties of the coatings requires coating actual electrodes. Commercially manufactured NMC532 electrodes were chosen for this purpose, to reduce any variation between the electrodes caused by making them by hand. Figure 4.9 shows the wide scan XPS spectra recorded for a pristine NMC532 electrode and for a plasma-coated electrode.

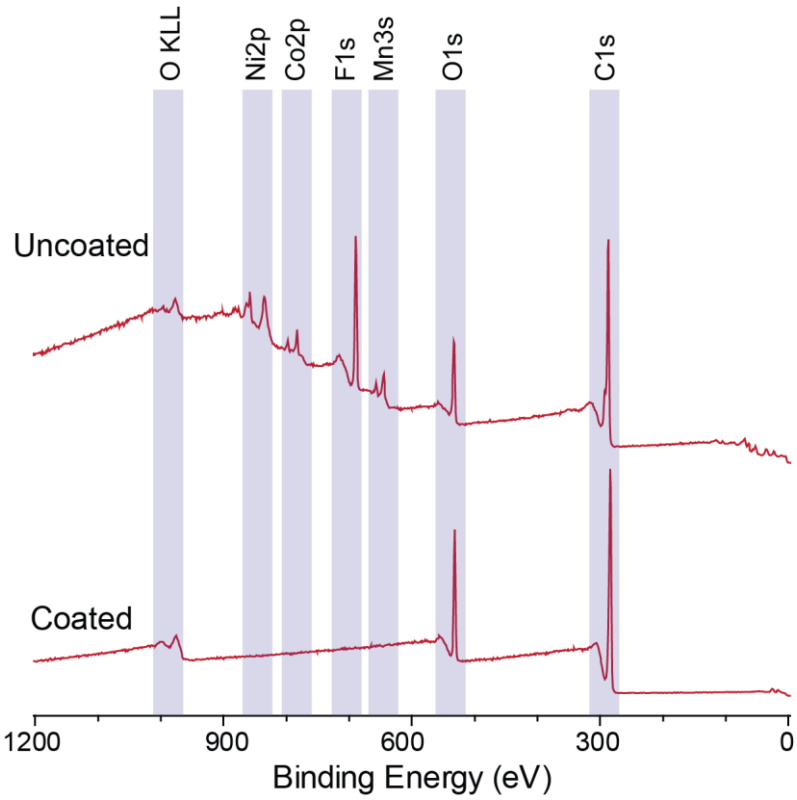

Figure 4.9: Wide scan XPS spectra recorded for a pristine NMC532 electrode and ethanol-coated NMC532 electrode.

The spectrum in Figure 4.9 for the uncoated electrode shows several peaks, which can be attributed to the different elements present in the electrode. Specifically, nickel (853 eV), manganese (641 eV), cobalt (779 eV) and oxygen (531 eV). Peaks are also observed at 685 eV and 285 eV which correspond to fluorine and carbon, respectively. The fluorine signal likely originates from the binder used, whilst carbon is present both as an additive as well as in the binder.

Figure 4.9 also shows the wide scan spectrum for the ethanol-coated NMC532 electrode. This spectrum contains only two prominent peaks, which come from carbon (285 eV) and oxygen (531 eV). None of the other peaks previously observed are seen here. This means that the peaks present can be attributed to an ethanol-based coating and that it is greater than 10 nm thick. It should be noted that this means that the coating is thicker than the coating deposited onto the silicon wafer (Figure 4.2). This would imply that the different substrates result in different deposition rates.

The XPS results suggest that coatings can successfully be deposited onto electrodes. Therefore, four coated electrodes were used to assemble cells. As a comparison, three cells

were also assembled using uncoated NMC532 electrodes. Figure 4.10 shows the specific capacities obtained during the charging step for each of these cells for the first 100 cycles.

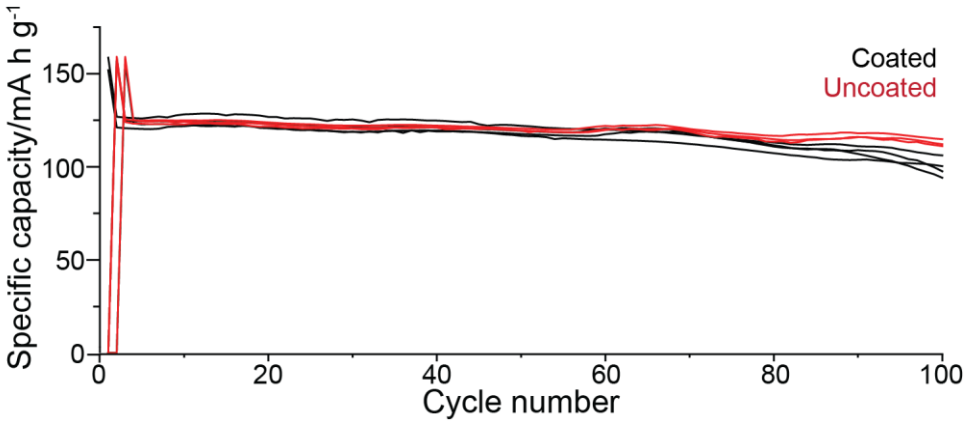

Figure 4.10: Specific capacities for the charging step for the first 100 cycles. Red lines show the data for the three cells prepared using uncoated electrodes, black lines the data for the cells prepared from ethanol-coated electrodes.

The first thing to note about the data shown in Figure 4.10 is that five of the cells show negligible capacity for the first cycle. Two of these cells also show negligible capacity for the second cycle. This is likely due to a technical fault, as only two data points were recorded for each of the defective cycles.

Aside from the delay in starting point, the behaviour of all cells during the initial cycles is similar. A capacity on the first (or first correctly operating cycle) of over 150 mA h g^{-1} is achieved followed by a drop to around 125 mA h g^{-1} on the next cycle. The initial capacity, whilst lower than the theoretical capacity, is in line with the practical capacities commonly reported for this material.[248] Whilst higher capacities can be achieved, the high C-rate used here means that a lower capacity would be expected. The drop between the first and second cycles suggests irreversible reactions occur during the first cycling step, possibly because of the high C-rate.

The capacities for all cells are consistent, up until around cycle 60. After this point the capacities of the cells assembled using coated electrodes start to be lower than those assembled using uncoated electrodes. This is particularly noticeable beyond cycle 80 and would suggest that these coatings negatively impact performance.

Figure 4.11 shows the charge-discharge curves recorded for all cells for the first and second (complete) cycles.

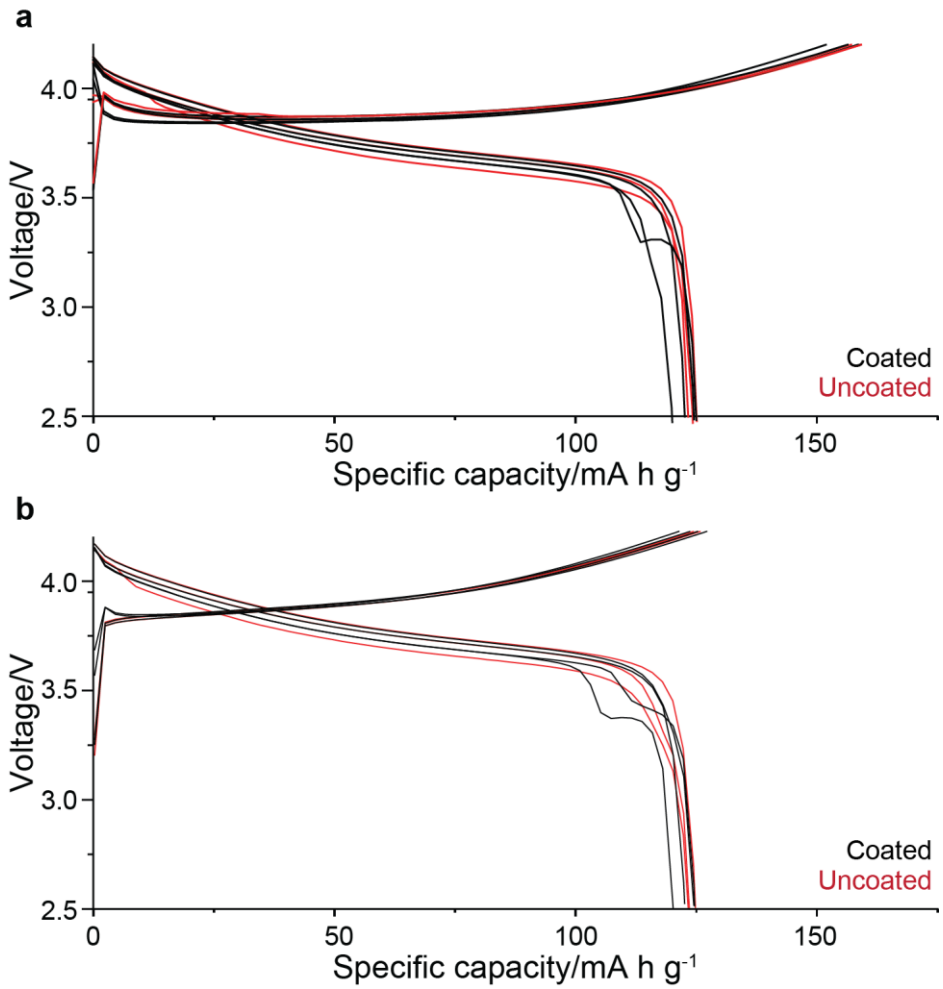

Figure 4.11: Galvanostatic charge-discharge plots for the (a) first and (b) second complete cycles. Red lines refer to cells assembled using pristine electrodes, black line cells assembled with ethanol-coated electrodes.

During the first and second discharges, two of the cells constructed using coated electrodes show an additional plateau at around 3.4 V. This is not seen for the other cells and could suggest that the coating or coating process affects the performance. However, there were issues with assembling the cells and so it is not possible to confidently say that the additional features are not an experimental error. Whilst this would ideally be investigated further, this was not possible due to equipment availability. It is therefore difficult to say whether the coatings impact performance or whether they are destroyed under electrochemical conditions.

4.3.1.5. Solid-state NMR studies of ethanol-based coatings

The electrochemical stability of a polymer-like coating is dictated by the functional groups present. For PEO, Yang *et al* note that C-O-CH_3 groups lead to higher electrochemical stability than C-OH.[247] These two environments cannot be distinguished by XPS. NMR

however can distinguish these environments, although silicon is not a suitable substrate for NMR. Furthermore, the low surface area of a wafer means that the amount of coating would be undetectable. Therefore, ethanol-based coatings were prepared on Al_2O_3 powder, to increase the surface area that could be coated. In addition, NMR is a bulk technique and so to see a surface coating, the substrate should ideally not contain any nuclei that are of interest for the coating.

Figures 4.12 and 4.13 shows the ^{1}H and ^{13}C spectra recorded for the ethanol-coated Al_2O_3.

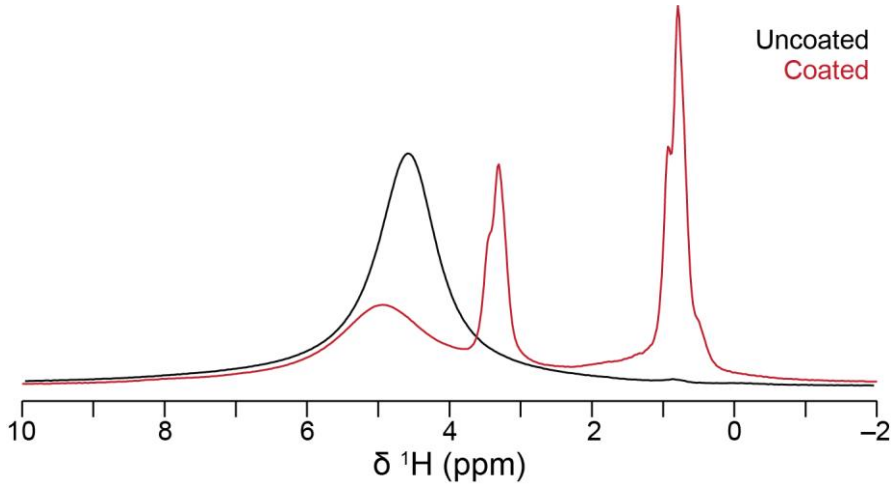

Figure 4.12: (a) ^{1}H depth NMR spectra acquired for ethanol-coated Al_2O_3 (red) and pristine Al_2O_3 (black). ^{1}H spectra are the sum of 16 transients. Spectra were acquired using a 4 mm probe, spinning at 12.5 kHz.

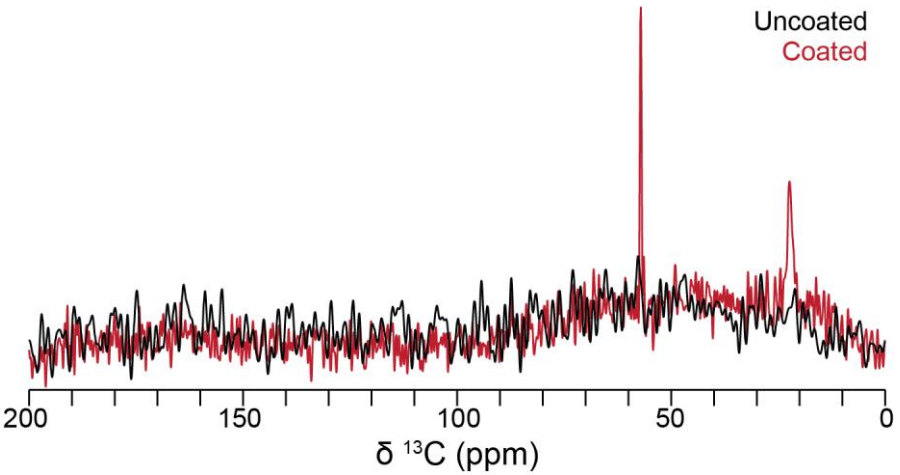

Figure 4.13: ^{13}C CP MAS NMR spectra acquired for ethanol-coated Al_2O_3 (red) and pristine Al_2O_3 (black). The ^{13}C spectrum for the ethanol-coated sample is made of 6144 transients, whilst the spectrum for the pristine material is 1024 transients, multiplied by six. Spectra were acquired using a 4 mm probe, spinning at 12.5 kHz.

The ^{1}H spectrum recorded for pristine Al_2O_3 shows an intense peak at 4.6 ppm, which can be attributed to water adsorbed to the surface the surface.[249] The ^{1}H spectrum recorded

for the ethanol-coated Al_2O_3 also shows a peak at 4.9 ppm, which could also be attributed to the Al_2O_3 surface. However, overlaying the two spectra shows that the intensity of this peak appears to be reduced compared to the pristine material and the position is shifted. This suggests that the surface species from the pristine material have been removed by the plasma treatment. In addition to this peak, the ^1H spectrum also shows two additional peaks at 0.8 ppm and 3.4 ppm. The alkyl protons in ethanol itself have ^1H chemical shifts or ~1.1 ppm (CH_3) and 3.4 – 3.7 ppm (CH_2), depending on the solvent.[250] As such the peaks in the ^1H spectrum for the coated sample could be assigned to CH_3 (0.8 ppm) and CH_2 (3.4 ppm) protons. It is hard to predict where the OH peak for ethanol would appear as it varies substantially, depending on the solvent. However, as previously mentioned, OH groups on the surface of Al_2O_3 are expected at 4.6 ppm, and so the peak at 4.9 ppm is likely some kind of OH group. It should be noted that the spectra are not mass normalised. However, since the size of the rotors used for both spectra were identical, the sample masses should be roughly equivalent.

The ^{13}C CP MAS spectrum recorded for the coated Al_2O_3 shows two sharp peaks at 22.4 and 57.2 ppm, as well as a broad feature between 0 and 100 ppm. This broad feature matches well the ^{13}C spectrum recorded for the pristine material and therefore cannot be attributed to the plasma coating process. The ^{13}C chemical shifts expected for ethanol in solution are around 18 ppm for the CH_3 carbon and 56 – 58 ppm for the CH_2 carbon.[250] The two peaks observed in the experimental spectrum likely belong to CH_3 (22.4 ppm) and CH_2 (57.2 ppm) carbons, which is consistent with the results of the ^1H NMR experiments.

Plasma polymers are described as random, cross-linked structures. This would be expected to yield broad peaks in the NMR spectra. However, the peaks observed are quite sharp and are consistent with the chemical shifts observed for ethanol. Therefore, the peaks observed could come from ethanol molecules, adsorbed to the surface. These would be relatively mobile as they do not form part of the polymer network, resulting in broad peaks. It could be possible that the ^{13}C peaks arising from the plasma polymer are too broad to be detected. However, ^1H NMR is relatively sensitive, yet shows no further environments beyond those attributed to adsorbed ethanol. On this basis, it could be concluded that no true plasma polymer is deposited onto the surface. Adsorbed ethanol molecules if present on the surface of the electrodes could dissolve into the electrolyte, leading to the reduced performance of the coated electrodes. Another explanation for the absence of peaks from a plasma polymer deposit, is that the process of deposition incorporates radicals into the

polymer structure. The resulting paramagnetic relaxation enhancement could then make it difficult to observe any peaks. Whilst, in principle, EPR measurements could have provided clarity on this, it is likely the results would have been ambiguous. As will be discussed in the following sections, fluorinated polymers (used as binders in the electrode) can form radicals when exposed to plasma. It would therefore be challenging to know whether the signal observed comes from the deposit or reactions with the binder.

4.3.2. Radical-containing electrode coatings

The ethanol-based cathode coatings previously described have a negative impact on cell performance. This effect is slight, and it is unclear whether the coatings survive in the cell environment. Whilst it may be possible to optimise these coatings to improve performance, it was decided to try an alternative strategy.

The objective of a cathode coating is to form a CEI that has a favourable chemistry and therefore improves long-term cycling performance. However, the CEI is heavily influenced by the structure of the SEI that forms on the anode. Therefore, an alternative strategy to influencing the CEI is to instead control the SEI formation with an anode coating.

For this work, it was decided to explore coatings derived from the TEMPO radical, as reported by Michl *et al* in 2018.[242] TEMPO has been successfully employed as an electrolyte additive previously by Lin *et al*.[243] Here the authors propose that TEMPO molecules trap hydrogen radicals formed during SEI formation on a mesocarbon microbead anode. Using TEMPO-based coatings is perhaps preferable to the ethanol-based coatings previously described as the stability of TEMPO is known (up to 3.5 V), which is above the voltage experienced by typical anode materials. Furthermore, dissolution of the coating into the electrolyte is not necessarily an issue as in this case the TEMPO is essentially an electrolyte additive, which as previously mentioned can benefit performance.

TEMPO is also the basis for many of the most popular polarising agents used for enhancing NMR spectra using DNP.[224,228] Therefore, even if unsuccessful at improving performance, the coating could be used to enhance the signals observed, allowing the interphase that forms to be studied in greater detail.

4.3.2.1. Reproducing literature work

The key to using TEMPO-based coatings as anode coatings, for electrochemical performance or signal enhancement, is whether the coating deposited contains nitroxide radicals. Some studies employ EPR spectroscopy to confirm the presence of radicals, whilst others rely solely on XPS.[96,251–254] XPS is unable to explicitly "see" radicals, and so its use in the absence of EPR data is questionable. In the cases where EPR has been used, it is unclear whether the signals observed come from the successful deposition of TEMPO radicals, or radicals created by the action of plasma at the substrate surface. As outlined in Chapter 2, the plasma phase is a violent environment, and so it is unintuitive that any radicals would survive. Therefore, for this work, EPR spectra were also recorded for the substrates exposed to an air plasma and for a TEMPO vapour. This allows for a more systematic approach to studying the origin of the EPR signals.

Michl *et al* report EPR spectra in several different works for quartz and NaCl subjected to TEMPO plasma. These indicate successful deposition of radicals.[242,251] Therefore, coatings were prepared on SiO_2 and NaCl powders, to verify that this result could be reproduced. Powdered SiO_2 was chosen instead of quartz wafers as the higher surface area of the powder means that there is a better chance of successfully observing an EPR signal. In addition, powders pack better into the EPR tube, improving the filling factor.[251]

Figure 4.14 shows the EPR spectra collected for the SiO_2 samples exposed to air plasma, TEMPO plasma and TEMPO vapour, whilst Figure 4.15 shows the spectra for the NaCl samples.

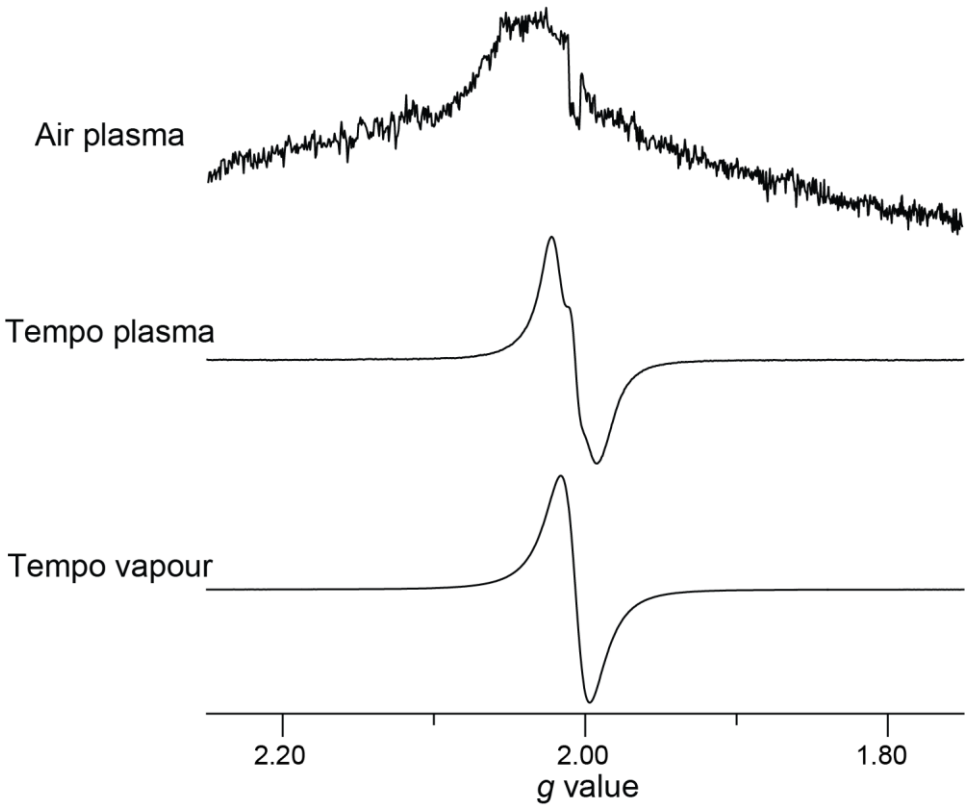

Figure 4.14: CW EPR spectra recorded for SiO_2 exposed to TEMPO vapour (modulation amplitude = 0.5 G, 1 scan), air plasma (modulation amplitude = 3 G, 1 scan), and TEMPO plasma (modulation amplitude = 1 G, 2 scans).

The EPR spectrum for SiO_2 exposed to air plasma shows only a broad feature centred at $g \approx 2.03$, which can be attributed to background as it is repeatedly observed across multiple samples (as will be seen throughout the rest of this chapter). This means that no radicals are created by the action of plasma. The EPR spectrum recorded for SiO_2 exposed to TEMPO plasma shows a signal at $g = 2.0077$. The presence of a signal for this sample but not for the sample exposed to air plasma implies that the signal at $g = 2.0077$ originates from TEMPO. This is supported by the fact that the g-value is close to that reported for pristine TEMPO ($g = 2.006$), with the slight difference possibly being due to interactions with the surface.[246] However, the EPR spectrum for SiO_2 exposed to TEMPO vapour also shows the same signal, centred at $g = 2.0077$. In this case, the only source of an EPR signal is TEMPO molecules, possibly adhering to the surface. Given the g-values are the same for the TEMPO plasma and TEMPO vapour samples, the species they originate from is likely the same, *i.e.*, TEMPO adhered to the surface. This is reasonable as the dominant species in the plasma phase are neutral precursor molecules, and so there are molecules available to adhere to the surface. There may also be contributions from a plasma polymer coating, however, it is difficult to disentangle to the different contributions.

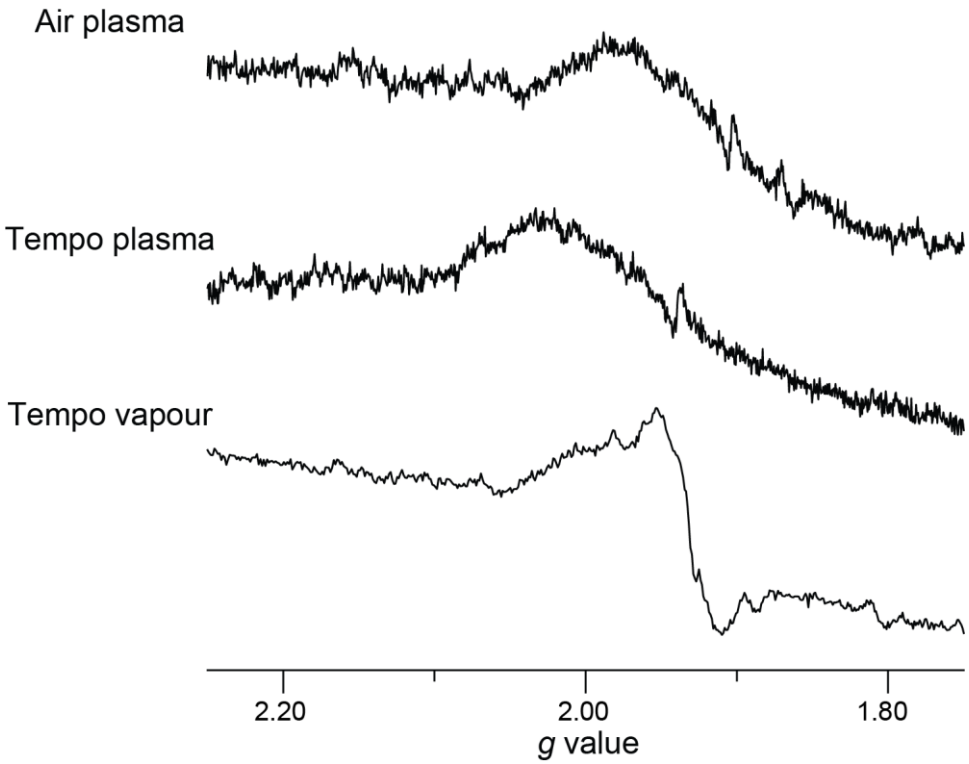

Figure 4.15: CW EPR spectra recorded for NaCl exposed to TEMPO vapour, air plasma and TEMPO plasma. The modulation amplitude used for all spectra was 3 G. The spectrum for the TEMPO vapour sample was acquired using a conversion time of 60 ms and a time constant 10.24 ms.

Figure 4.15 shows that the spectra recorded for all the NaCl samples show the broad background feature at $g \approx 2.03$. In addition, the sample exposed to TEMPO vapour shows a signal at $g \approx 2.009$, although it is difficult to accurately determine the g-value due to the sloping baseline and poor signal-to-noise. This may be the result of the increased conversion time used to acquire the spectrum but could also indicate weak TEMPO adhesion. Therefore, a wide scan XPS spectrum (Figure 4.15) was recorded for the coated NaCl.

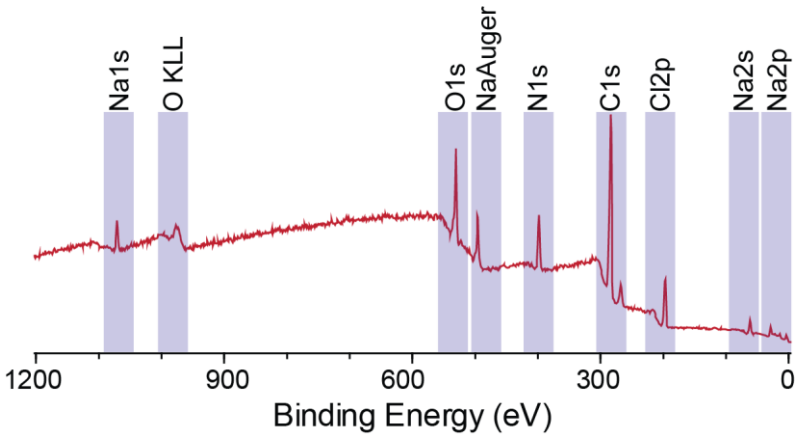

Figure 4.16: Wide scan XPS spectrum recorded for NaCl exposed to a TEMPO plasma.

The XPS spectrum in Figure 4.15 shows peaks that can be attributed to carbon, oxygen, nitrogen, sodium and chlorine. This suggests that a coating derived from TEMPO has successfully been deposited. However, it is very thin (< 10 nm) as the elements in the substrate are still visible. This means that a coating is deposited, but that the radical concentration is very low, either because they do not survive deposition or because the coating is too thin.

The results presented in this section suggest that it is possible to deposit radicals onto substrates when using TEMPO-based plasmas, in agreement with previous reports. However, the signals observed are likely attributable to adhesion of TEMPO molecules onto the substrate surface rather than from a TEMPO-based plasma polymer deposit. This would fit with an observation made by Michl *et al.* In their 2020 work, they washed silicon wafers subjected to a TEMPO plasma with water and recorded an EPR spectrum of the resulting solution.[252] The signal they record is split into three lines, as would be expected for a nitroxide radical in solution. This means that it is possible to dissolve some/all the coating in water, which suggests the radical species are adhered to the surface rather than polymerised.

It should be noted that it is difficult to know whether the radical species observed here are identical to those observed in other works. This is because none of the papers report accurate microwave frequencies, and so it is not possible to calculate accurate g-values from the spectra plotted in terms of field.[251,252] The original paper does plot EPR spectra in terms of g-value, but the g-value for the sample is not explicitly stated.[242] However, from the spectra reported the g-value is approximately 2.006, which agrees with the work presented here.

4.3.2.2. TEMPO-based coatings on Al_2O_3

The work looking at ethanol-based coatings used silicon and Al_2O_3 as a model substrates and so TEMPO-based coatings were prepared on Al_2O_3 to provide a point of comparison between the two coating types. Silicon is not a suitable substrate for EPR owing to its high dielectric constant, which complicates tuning of the spectrometer.

EPR spectra were recorded for Al_2O_3 exposed to the same conditions as the previous substrates (TEMPO vapour, air plasma and TEMPO plasma). Figure 4.17 shows the spectra recorded for these samples.

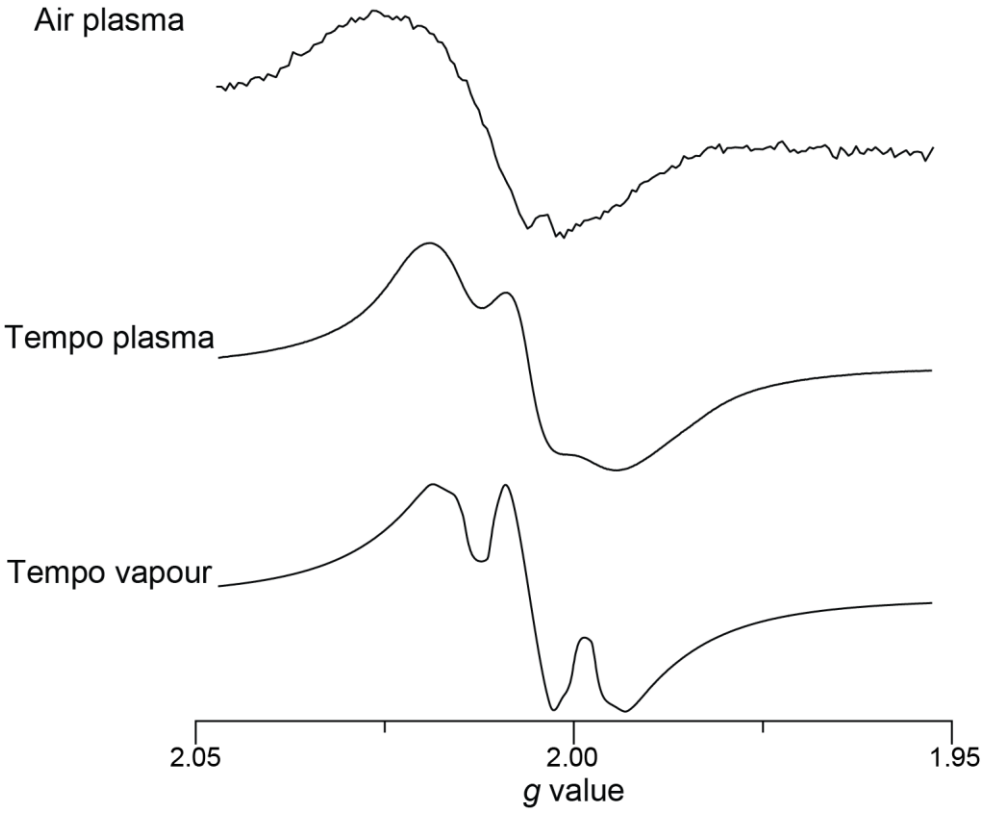

Figure 4.17: CW EPR spectra recorded for Al_2O_3 exposed to TEMPO vapour, air plasma and TEMPO plasma. The modulation amplitude used for all spectra was 3 G.

As can be seen in Figure 4.17, all three spectra show signals. The samples exposed to TEMPO vapour and TEMPO plasma show a signal at g = 2.006, whilst the signal for the sample exposed to air plasma is centred at g = 2.01. This difference in g-values suggests that there are two different species present. As discussed previously, a signal at g = 2.006 indicates deposition of a TEMPO radical, likely through adhesion rather than polymerisation, since the signal is present for the sample exposed only to TEMPO vapour. Meanwhile the signal at g = 2.01 suggests that the action of plasma alone generates radicals

in Al_2O_3. This is in agreement with previous literature, which reports the formation of aluminium peroxyl groups in porous alumina when it is exposed to plasma.[255]

Whilst the two spectra recorded for samples exposed to TEMPO are centred at the same g-value, the spectrum for sample exposed to TEMPO plasma features a shoulder similar to what was observed for the comparable SiO_2 sample. This suggests that the two deposits are not the same, with TEMPO vapour resulting in greater dipolar and/or exchange interactions resulting in broadening. To explore this further, another sample was prepared by exposing Al_2O_3 to TEMPO vapour and an EPR spectrum recorded (Figure 4.18). This sample was then exposed to an air plasma (Figure 4.18) to try and split apart the contributions from the TEMPO vapour and the action of plasma.

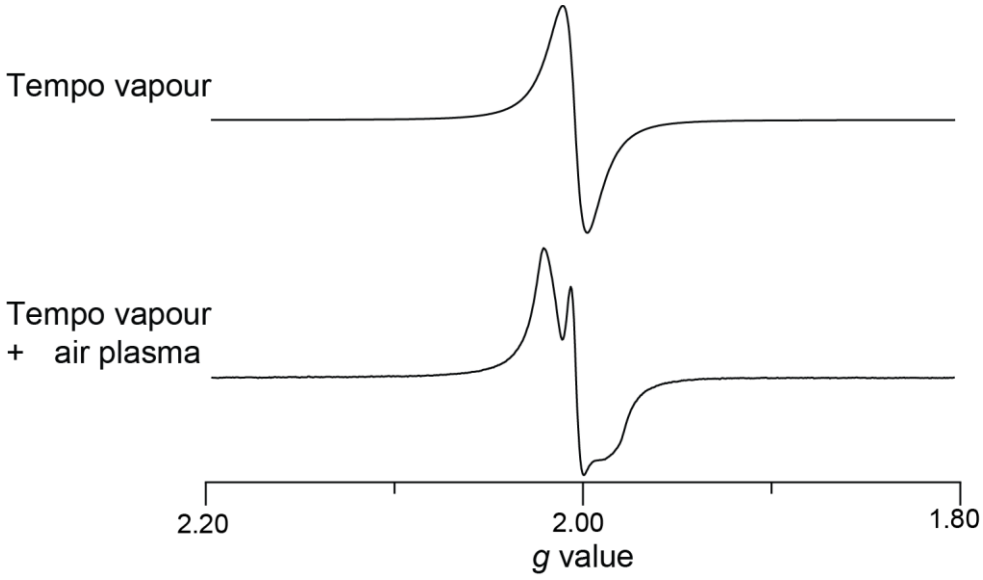

Figure 4.18: CW EPR spectra recorded for Al_2O_3 exposed to TEMPO vapour and TEMPO vapour followed by air plasma. The modulation amplitude used for both spectra was 3 G.

As expected, based on the previous results, both spectra show clear EPR signals centred at the same g-value (g = 2.008), indicating radicals have successfully been deposited. This g-value differs slightly from the previous value obtained (g = 2.006), although this can be attributed to differences in tuning, owing to the age of the instrument. The spectrum recorded for the sample treated by air plasma (Figure 4.18) is also more resolved than the TEMPO vapour sample, which is consistent with the previous set of data. This would suggest that the plasma influences the nature of the radicals deposited, even if it not the primary cause of deposition.

Characterising these TEMPO-based coatings with NMR is not possible. This is because of the unpaired electrons, which will complicate acquisition of a system that is already challenging to study. However, the EPR data collected provides little structural information about any coatings deposited, whilst XPS is insensitive to hydrogen. Therefore, coatings were prepared using TMP (Figure 4.19). This is analogous to TEMPO, but the oxygen is replaced by a hydrogen, removing the radical.

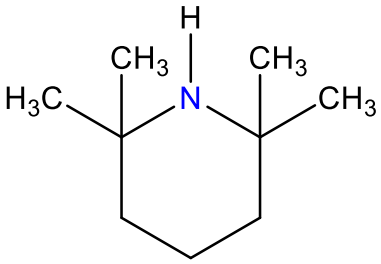

Figure 4.19: Structure of TMP.

Figure 4.20 shows the ^{1}H NMR spectrum acquired for Al_2O_3 exposed to a TMP-based plasma as well as the pristine γ-Al_2O_3.

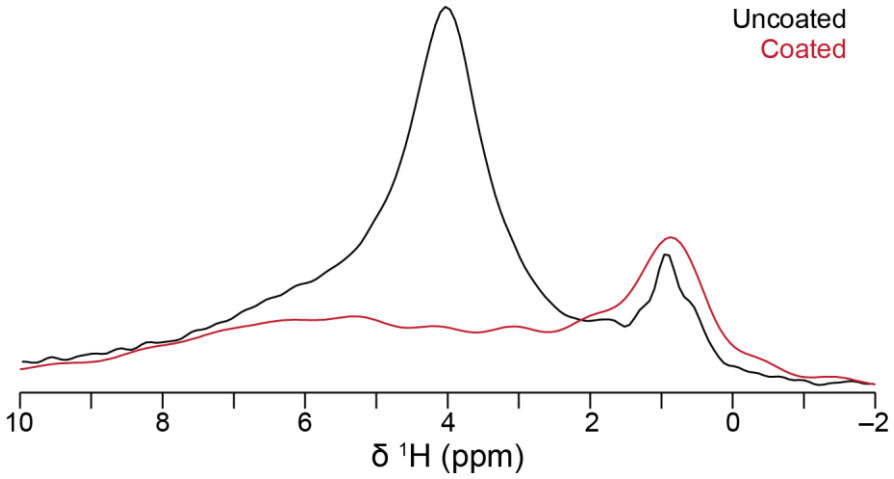

Figure 4.20: ^{1}H depth spectra recorded for Al_2O_3 (black) and TMP-coated Al_2O_3 (red). Spectra were acquired using a 3.2 mm probe and an MAS frequency of 15 kHz. The number of scans for both spectra was 1600. 100 Hz line broadening was applied to the uncoated spectrum to mitigate the effects of truncation.

The spectrum recorded for the Al_2O_3 exposed to a TMP plasma shows a peak at 0.8 ppm. This peak is also present in the spectrum recorded for the pristine material, suggesting that it comes from the Al_2O_3 or is a background feature. The peak at 4.6 ppm is absent in the spectrum recorded for the coated sample. This suggests that proton environments on the surface have been removed, which is consistent with the previous results for the ethanol-based coatings. However, no signal was observed in the ^{13}C CP MAS NMR spectra

recorded for this sample (not shown). This suggests that unlike when using ethanol, TMP does not strongly adhere to the Al_2O_3 surface.

4.3.2.3. TEMPO-based coatings on polytetrafluoroethylene

The objective of this work is to determine whether TEMPO-based coatings would be useful for coating anode materials. Whilst the materials studied this far have been useful in building understanding of the nature of the coatings, they are not representative of the materials found in a functional anode. As discussed in Chapter 1, the active material in an anode is usually graphite, mixed with carbon black and a fluoropolymer binder. Carbonaceous materials are challenging to study with EPR as their high dielectric constants lead to energy losses in the cavity. This makes tuning the spectrometer difficult and so polytetrafluoroethylene (PTFE) was chosen as the first substrate. PTFE is also a carbon-based material, unlike the other materials studied, enabling greater understanding of the deposition mechanism by expanding the types of substrates studied.

Figure 4.21 shows the EPR spectra recorded for PTFE wafers (approximately 1 cm^2) exposed to TEMPO vapour, air plasma and a TEMPO plasma, in addition to the spectrum recorded for a pristine wafer.

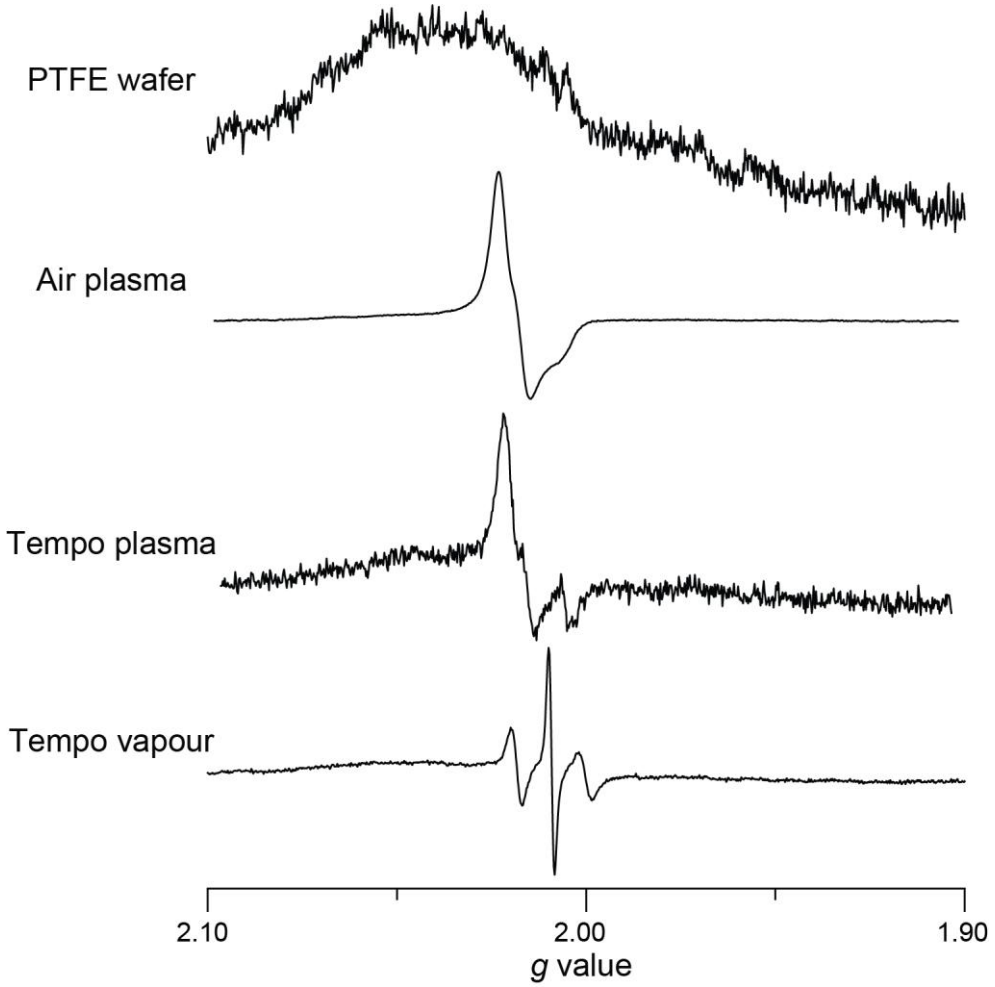

Figure 4.21: CW EPR spectra recorded for a PTFE wafer, a PTFE wafer exposed to TEMPO vapour, a PTFE wafer exposed to an air plasma and a PTFE wafer exposed to a TEMPO plasma. The modulation amplitude used for all spectra was 3 G.

The EPR spectrum for the pristine wafer shows no clear signals, with there only being a broad feature centred at g = 2.03. This can be attributed to the background and so the PTFE wafers are EPR-silent, as would be expected. In contrast, the three other spectra do show clear signals. The signal recorded for the wafer exposed to TEMPO plasma is centred at g = 2.009, which from the previous investigations can be attributed to a nitroxide radical, *i.e.*, TEMPO, adsorbed to the surface. Unlike the previously recorded spectrum, this spectrum is split into three lines, which indicates two things. First, the splitting pattern indicates that the radical is close to a spin-1 nucleus, such as ^{14}N, which supports the assignment of this as coming from a nitroxide radical. Second, the fact that this hyperfine splitting is visible means that electron-electron exchange and dipolar interactions are weaker, improving the resolution. This means that the radicals are distributed at low concentrations such that the average distance between them is large, which is supported by the fact that the background peak is visible to the left of the main signal.

The EPR spectra recorded for the two wafers exposed to air and TEMPO-derived plasmas (Figure 4.21) show signals centred at g = 2.02, meaning that the radical present in both samples is the same or similar. A g-value of 2.02 is significantly shifted from what would be expected for a nitroxide radical, suggesting that this is a different type of radical to what has been observed up this point. This is further supported by the shape of the peak, with more of the peak lying above the baseline than below it, indicating that the g-tensor is axially symmetric, rather than approximately isotropic. The region on the right below the baseline is also split into two peaks, although this is more apparent for the TEMPO plasma sample. Splitting into two lines implies coupling to a spin-1/2 nucleus, which combined with the fact that this signal is observed when an air plasma is used suggests that the radical is present within the PTFE substrate. The radical couples to ^{19}F nuclei, resulting in the splitting pattern observed. The greater resolution of the TEMPO plasma sample implies fewer radicals are present, resulting in less broadening. This would be expected as the air plasma employs higher RF power (60 W), resulting in greater damage to the substrate.

The observation of PTFE-based radicals is not without literature precedent. Oshima *et al*, report EPR spectra of PTFE after exposure to ionising radiation.[256] Whilst no g-values are given, the lineshape resembles that seen here.

It is worth noting that the spectrum for the PTFE sample exposed to TEMPO plasma does not show any evidence of the nitroxide radical observed for the sample prepared by exposure to TEMPO vapour. This means that radicals caused by plasma damage are far more numerous, either because plasma damage generates more radicals or because the TEMPO radicals are destroyed.

Overall, the work in this section shows that radicals can be deposited onto substrates from a TEMPO plasma, in agreement with literature. However, the radicals likely do not reside in a polymeric deposit. Instead, they can either come from adhesion of TEMPO molecules to the surface or damage caused by plasma exposure, with the dominant process depending on the substrate material. Battery anodes are generally made of multiple components, and so any coatings applied to entire electrodes would likely be non-uniform. Furthermore, the radicals that may be generated by plasma damage may promote additional parasitic side reactions, negatively impacting performance. Further electrochemical tests were not possible, due to the necessary equipment being moved to other institutions.

4.4. Discussion

The work in this chapter focussed on two types of plasma polymer coatings derived from ethanol and TEMPO plasmas, with the objective of exploring their use in protecting cathode and anode materials, respectively. However, the results presented show that the process of plasma polymerisation is more complex than what is presented in literature. Ethanol-based coatings were successfully deposited onto model substrates as well as NMC532 electrodes but yielded no positive impact on cycling performance. The coatings are likely mostly unreacted precursors can adhere to the surface, rather than a polymeric deposit as might be imagined based on previous literature work. Meanwhile, the TEMPO-based coatings do contain nitroxide radicals, but they likely do not belong to any polymeric deposit. This work also shows that deposition may result in additional radicals being generated in the substrate which may promote unwanted reactions.

When taken together as a whole, the work in this chapter does provide some insight into the deposition of plasma polymers. The surface sensitivity of XPS makes it particularly useful in characterising plasma coatings. However, it cannot detect hydrogen atoms directly or radical species, but these can be studied with ^{1}H NMR and EPR, respectively. The NMR results highlight the potential for plasma to remove surface species, with the ^{1}H spectra recorded for plasma-coated Al_2O_3 showing a significantly reduced number of surface hydrogen environments. This could be supported by EPR, which shows a weak signal when Al_2O_3 is exposed to air plasma, potentially coming from radical sites generated by the removal of surface species.

The systematic use of EPR also suggests that intact precursor molecules can adhere to substrate surfaces, contributing to the final deposit. This is also a possible explanation for the sharp peaks in the ^{13}C CP MAS spectrum recorded for ethanol-coated Al_2O_3. The EPR results also highlight the risk of damaging substrates because of the action of plasma. These two findings could offer explanations for the slightly negative performance of the ethanol-based coatings, as adhered molecules could dissolve into the solvent, whilst surface radicals may promote unwanted side reactions. However, this requires further investigation.

Finally, regarding the use of TEMPO coatings to study interphase formation with DNP, the results presented in this chapter suggest that it could be possible to deposit radicals. However, it is not clear if they are suitable as polarising agents, in terms of their properties like relaxation time and dipolar coupling. Furthermore, the potential to generate multiple

radicals within the structure may make irradiating the correct EPR transition challenging. Should it prove possible to produce an enhancement, additional radicals may cause additional side reactions, that may influence interphase formation. Therefore, it would not be possible to know if the coating observed is representative of the interphase that forms in the absence of a coating.

4.5. Conclusions

In summary, the work in this chapter serves as an initial investigation into the possible use of plasma polymers as protective coatings in batteries. The initial results utilising ethanol-based coatings, optimised for C-O retention, show a slight negative effect on performance. Meanwhile the TEMPO-based coatings highlight the risk of plasma-induced damage in substrates, the electrochemical impact of which, needs to be investigated further.

However, this work demonstrates a more holistic approach to characterising the local structure of plasma polymers, by employing ^{1}H NMR and EPR as well as the commonly used XPS. Doing so highlights additional processes that need to be considered when discussing the deposition of plasma polymers, specifically precursor adhesion, removal of surface groups and the generation of radicals in the substrate. These findings offer an alternative explanation to the results previously reported in literature, which may have ramifications for applications of TEMPO-based coatings beyond the field of batteries.

4.6. Future work

Whilst it would be possible to investigate coatings made using the other precursors suggested in Chapter 2, it would be first important to determine whether the damage to the substrate caused by plasma has a noticeable impact on electrochemical performance. Whilst some investigation into the effect of plasma was done using the ethanol-based coatings, it is not possible to correlate specific aspects of the plasma with electrochemical performance. This would involve subjecting electrodes to high energy air plasmas, to maximise the damage incurred without introducing any coatings. Presence of radicals would then be confirmed or excluded by EPR. The coated electrodes would then be tested in coin cells for multiple cycles and at different cycling rates to see if any changes in performance are observed.

If no significant impact on electrochemical performance were to be observed, the next step would be to investigate the stability of the coatings, as this is not clear from the work

in this chapter. This would involve preparing coatings using different precursors and plasma conditions and recording XPS spectra before and after immersion in electrolyte solvents. Initially this would just be a mixture of EC and DMC. However, if certain coating chemistries show promise, then this test could be expanded to other combinations of solvents, to explore if there are any limitations.

It would be useful to also investigate the electrochemical stability of the coatings, such as by a similar approach to the one described for solvent stability, but using electrodes extracted from cells. However, this may not be straight forward as CEI formation would contribute to the XPS signal observed or may bury the coating below the sampling depth of XPS. ^{1}H SSNMR could overcome this since NMR is not surface specific, although the contributions from multiple species within the electrode bulk would make the spectra challenging to interpret.

Studies are also required to investigate the reproducibility of the precise coatings of plasma polymers, as variation in coatings will lead to variable performance in the assembled cells. This would therefore be important to establish prior to any further electrochemical tests.

5. Probing local structure in oxyfluoride disordered rocksalt materials

5.1. Introduction

As outlined in Chapter 2, disordered rocksalt (DRX) materials are promising as Li-ion battery cathodes, due to their high capacities and compositional flexibility.[116,117] However, they are prone to rapid losses in capacity, arising due to oxygen redox (O-redox), and therefore are not yet practically viable.

The reliance on O-redox can be reduced by using fluorinated DRXs. Substitution of fluorine into the structure reduces the charge of the transition metal ion(s) required for maintaining charge neutrality. This allows access to double redox processes (*e.g.*, $V^{3+} \rightarrow V^{5+}$), reducing the reliance on O-redox to extract all lithium ions from the structure.[158,159] However, the structures of these materials are not fully understood, which in turn limits understanding of their electrochemical behaviour.[158,163]

When imagining the local structure of an oxyfluoride DRX, it would be easy to assume that the anions are arranged similarly to the cations. This is to say, that they are randomly mixed across generic octahedral anion sites. In such a structure, it would be expected that there are many possible anion environments present, ranging from fully coordinated to lithium to fully coordinated to the transition metal ion. A similar degree of randomness would then be present in the second coordination shell, and so on. However, this is thought not to be the case, with it being suggested that fluoride ions prefer lithium-rich/transition metal-poor regions of the material.[160,164] This is because the bonding present in LiF is stronger than the bonds that might form between transition metal and fluoride ions, limiting the solubility of LiF into the DRX.

Considering this, the work in this chapter has two main objectives. The first is to establish a model of the local structures of oxyfluoride DRX materials, whilst the second is to investigate how this structure evolves during electrochemical cycling. Structural studies of battery materials often use diffraction-based techniques to characterise changes in long-

range structure. However, oxygen and fluorine have similar X-ray scattering strengths and so are difficult to distinguish.[117] Therefore, this work will use solid-state NMR (SSNMR) to probe the local structures of DRX materials. SSNMR has been used in other works for this purpose, however the paramagnetic nature of many of the materials studied makes assignment of the spectra complex.[13,158,257] Therefore, the initial work presented in this chapter will focus on building a structural model using diamagnetic analogue materials. The transition metal ions in these materials are chosen to have no *d* electrons, eliminating paramagnetic effects. This understanding will then be applied to redox-active materials, both pristine and cycled, to understand the structural changes that occur.

5.2. Experimental

5.2.1. Ball mill synthesis

Materials were synthesised using a method that is an amalgamation of those previously published.[141,167,258] Samples of $Li_{1+x}MO_2F_x$ DRX materials were prepared using stoichiometric amounts of M_2O_3 (M=Al, Sc, Ti, V or Y), LiF and Li_2O. Li_2NiO_2F was prepared using $LiNiO_2$ and LiF as precursors. The precursors were added to a zirconia ball mill jar (20 ml) along with ten zirconia balls (10 mm diameter). The total sample mass in all cases was 1 g, and a 10% excess of Li_2O was used to offset any lithium loss. Samples were ball milled for 48 hours total (192 cycles of 5 minutes plus 10 minutes rest). Ball mill jars were sealed and opened inside the glovebox. The manufacturers and purities of the different precursors are shown in Table 5.1.

Table 5.1: Details of the different precursors used to prepare the DRX materials.

Precursor	Manufacturer	Purity
Li_2O	Alfa Aesar	99.5%
LiF	Alfa Aesar	99.5% +
Al_2O_3	Acros Organics	99.7% +
Ti_2O_3	Alfa Aesar	99.8%
Sc_2O_3	Thermo Scientific	99.9%
V_2O_3	Tokyo Chemical Industries	> 95%
$LiNiO_2$	Sigma Aldrich	≥ 98%
Y_2O_3	Thermofisher	99.9%

NbO_2F was prepared by Ellie Dempsey in the group of Dr James Cumby at the University of Edinburgh, as per a method described elsewhere.[259]

5.2.2. Electrochemical tests

Self-standing electrodes were prepared by mixing the active material with carbon black for 15 minutes followed by PTFE pellets. The resulting film was then rolled to a final thickness of 150 μm. 5 mm electrode discs were then assembled into half cells under argon atmosphere (< 0.1 ppm O_2/H_2O). The cells were constructed using parts made from 304 steel (TOB machine), 1 M $LiPF_6$ in EC:DMC (1:1) (Sigma Aldrich) as the electrolyte, Whatman glass fibre separators (17 mm) and lithium wafers (15 mm × 0.38 mm) (Cambridge Energy Solutions). Cells were cycled at a rate of C/20, unless stated otherwise, using Neware electrochemical cyclers. Further details for the cycling protocols for each of the cells are given in the text and summarised in Table 5.2.

Table 5.2: Cycling protocols for each of the cells referred to in this chapter.

Active material	Charge/discharge first	Number of cycles	Lower cutoff voltage/V	Upper cutoff voltage/V
LTOF	Charge	2	1.0	4.6
	Discharge	0.5 (1st discharge)	0.5	N/A
	Discharge	1	0.5	3.0
	Discharge	5	0.5	3.0
Carbon black	Discharge	1	0.5	3.0
LVOF	Charge	0.5 (1st charge)	N/A	4.1
	Charge	1	2.0	4.1
	Charge	5	1.3	4.1
	Charge	50	1.3	4.1
NbO_2F	Discharge	0.5 (1st discharge)	1.1	N/A
	Discharge	0.5 (1st discharge)	1.0	N/A
	Discharge	0.5 (1st discharge)	1.0	N/A
	Discharge	1	1.0	4.0
	Discharge	50	1.0	4.0

Samples for *ex situ* analysis were washed in DMC (TOB machine) and dried at ambient temperature, under vacuum. NMR samples were packed into the zirconia rotors with KBr (Merck, IR spectroscopy grade) to fill the remaining volume. Powder X-ray diffraction (PXRD) samples were prepared by sealing the electrode in Kapton tape.

5.2.3. Powder X-ray diffraction

PXRD measurements were performed using either a Rigaku Smartlab diffractometer equipped with a Cu K_α source or an Agilent Technologies Supernova single crystal diffractometer equipped with a Mo K_α source. These are referred to as the Smartlab and Supernova diffractometers in the text. All patterns were converted to Cu K_α for the sake of comparison. Data collected using the Agilent Technologies Supernova single crystal diffractometer was collected and extracted by Matthew Leesmith and Mingqing Sun.

5.2.4. Solid-state NMR

SSNMR experiments were performed using Bruker Avance III HD spectrometers operating at magnetic field strengths of 9.4 or 16.4 T, equipped with a 2.5 mm probe. Additional experiments were performed using a Bruker Avance Neo spectrometer operating at a magnetic field strength of 20.0 T at the University of Warwick, equipped with a 1.3 mm probe.

$^{6/7}$Li spectra were acquired using a single pulse-acquire sequence and an MAS frequency of 25 kHz unless otherwise specified. ^{19}F spectra were acquired using a depth sequence and an MAS rate of 30 kHz, unless specified otherwise. ^{51}V spectra were acquired using a Hahn echo sequence and an MAS frequency of 25 kHz, whilst ^{93}Nb spectra were acquired using a single pulse-acquire sequence and an MAS frequency of 30 kHz.

$^{6/7}$Li spectra were referenced to $^{6}Li_2CO_3$ (0.11 ppm), ^{19}F spectra to PTFE tape (–122 ppm), ^{51}V spectra to V_2O_5 (–610 ppm) and ^{93}Nb spectra were referenced to $LiNbO_3$ (–1004 ppm).[178,260] Pulse lengths were measured on the reference samples (^{6}Li = 2 μs, ^{7}Li = 1.5 μs, ^{19}F = 2 μs, ^{51}V = 2 μs and ^{93}Nb = 1 μs). Further experimental details are given in the figure captions.

Where given, intensities were measured using TopSpin 4.5.0.

5.2.5. DFT calculations

CASTEP calculations were performed using CASTEP 22.11 on Lancaster University's High End Computing Cluster. To determine NMR parameters, two sets of unit cells were constructed, comprising 48 and 96 atoms. This was done by populating 6×4×2 and 6×4×4 unit cells with the correct number of cations and anions (2:1 Li/O:Sc/F). Geometry optimisations and NMR calculations were performed using the PBE functional and the ZORA relativistic treatment. The cutoff energy was 800 eV, and the k-point spacing 0.04 Å^{-1}. For the geometry optimisations, convergence was reached when the changes in energy, force displacement and stress were below 0.0001 eV, 0.05eV Å^{-1}, 0.001 Å^{-1} and 174 GPa. NMR shieldings were converted to chemical shift based on an identical calculation run for LiF.

5.3. Results

5.3.1. Diamagnetic DRX materials

5.3.1.1. PXRD and SSNMR characterisation

Understanding the incorporation of fluorine into the rocksalt structure requires exploring the local environments of fluorine.[117] For this reason, SSNMR is often utilised when studying oxyfluoride DRXs, as it is sensitive to local structure. Furthermore, ^{19}F is a highly sensitive nucleus, making it a powerful structural probe for these materials. However, typical DRXs contain paramagnetic ions, meaning that the ^{19}F spectra recorded are broad and poorly resolved, even when acquired using fast MAS at low magnetic fields. This makes it difficult to determine how many environments are present, as well as their chemical shifts. As a result, interpretation of the spectra is complex.[155]

Broadening due to paramagnetic effects can be eliminated by studying DRX materials where the non-lithium metal ion(s) have no *d* electrons. Whilst these materials are not electrochemically active, they can provide a model as to the bonding environments present in paramagnetic materials. This insight can then be used to understand the behaviour of redox-active materials.

Three diamagnetic analogues were attempted of the type Li_2MO_2F, where M = Al, Sc and Y (referred to hereafter as LAOF, LSOF and LYOF). These are all 3+ ions without *d* electrons, and all possess an NMR-active isotope, allowing an additional opportunity for structural insight. The synthesis conditions were based on those reported in literature to synthesise electrochemically active materials as will be discussed later.[167,258] Figure 5.1 shows the PXRD patterns for these materials.

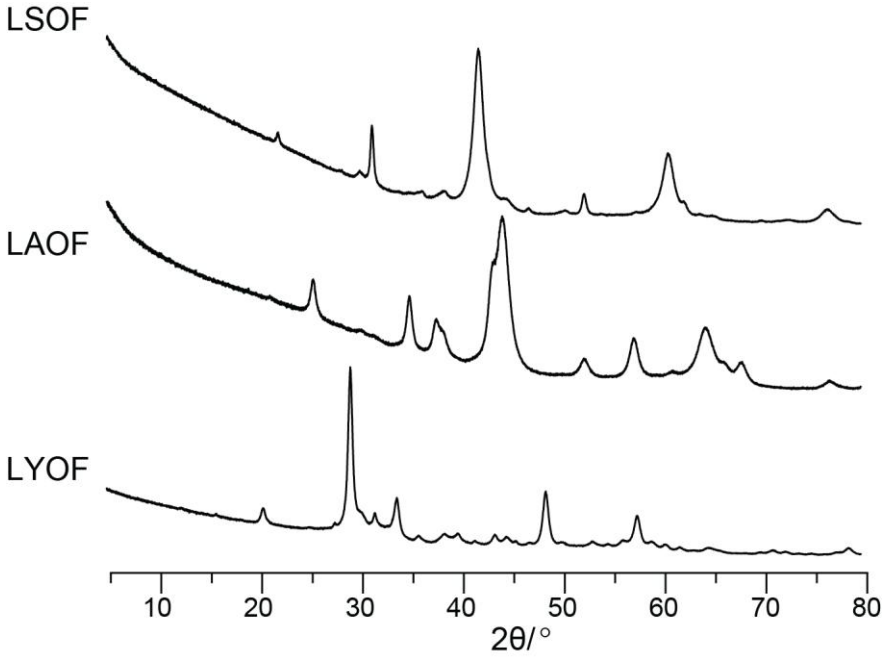

Figure 5.1: PXRD patterns recorded using the Smartlab diffractometer for LSOF, LAOF and LYOF.

As detailed in Chapter 3 (Section 3.4.2.), a rocksalt structure has six possible lattice planes: (111), (200), (220), (311), (222) and (400). Assuming a perfect DRX structure (*i.e.*, perfectly cubic), the expected positions of the resulting peaks can be estimated using Equations 3.61 and 3.65. Table 5.3 contains the predicted peak positions for LSOF, LAOF and LYOF, assuming that the unit cell length is twice the Li/M-O/F distance (M denoting a 3+ ion). This distance was estimated based on the ionic radii, with the average distance also considering the ratio of the different ions (2:1 Li/O:M/F). Table 5.3 also includes the expected positions for LiF as a reference.

Table 5.3: Predicted positions of the PXRD peaks of the different DRXs attempted. Based on the Shannon ionic radii.[261] LiF positions are from the PXRD pattern simulated for the crystal structure from the Materials Project (mp-1138).[262]

Lattice plane	Predicted peak position/°			
	LSOF	**LAOF**	**LYOF**	**LiF**
(111)	36	38	36	38
(200)	42	44	41	44
(220)	61	64	60	64
(311)	74	76	72	77
(222)	77	81	75	82
(400)	92	97	90	98

The PXRD pattern for LSOF shows peaks at 38, 41, 61 and 77°. These positions are a reasonable match for the predicted positions of the (111), (200), (220) and (222) planes for LSOF, suggesting the formation of the DRX phase. The (311) may not be intense enough to be observed, whilst the (400) plane is beyond the range of angles measured. Further evidence for the formation of the DRX phase is that the position of the peaks is shifted slightly from what would be expected for LiF. This indicates that the LiF has reacted and the rocksalt peaks observed are not only due to residual LiF. However, it is not possible to exclude the presence of residual LiF entirely as the peaks are broad due to the small particle sizes created by ball milling (see Equation 3.66). Presence of residual LiF may cause the apparent peak positions to shift slightly. This may be the cause of the slight discrepancy between the predicted and experimentally observed positions of the (111) and (200) peaks arising due to the (111) and (200) planes. The pattern for LSOF also has peaks at 22, 31 and 52°, which can be attributed to unreacted Sc_2O_3.[263]

The PXRD pattern for LAOF shows peaks at 38, 44, 64 and 77°. These match the positions of the peaks from the DRX phase, but also unreacted LiF. The remaining peaks can be attributed to Al_2O_3 (25, 35, 37, 43, 52, 57, 66 and 68°).[264] The presence of peaks that can be attributed to Al_2O_3 mean that it is likely at least some of the rocksalt peaks come from unreacted LiF, but it is not possible to conclusively rule out the presence of a DRX phase.

A similar situation is encountered with the PXRD pattern recorded for LYOF, with there being peaks attributable to LiF, rather than LYOF, with the remainder matching those expected for Y_2O_3.[265] This means that there is likely no yttrium-containing DRX phase present.

To further characterise the structures of the reaction products, ^{19}F SSNMR spectra were recorded. These are shown in Figure 5.2, overlaid with a spectrum for LiF, as the only fluorine-containing precursor.

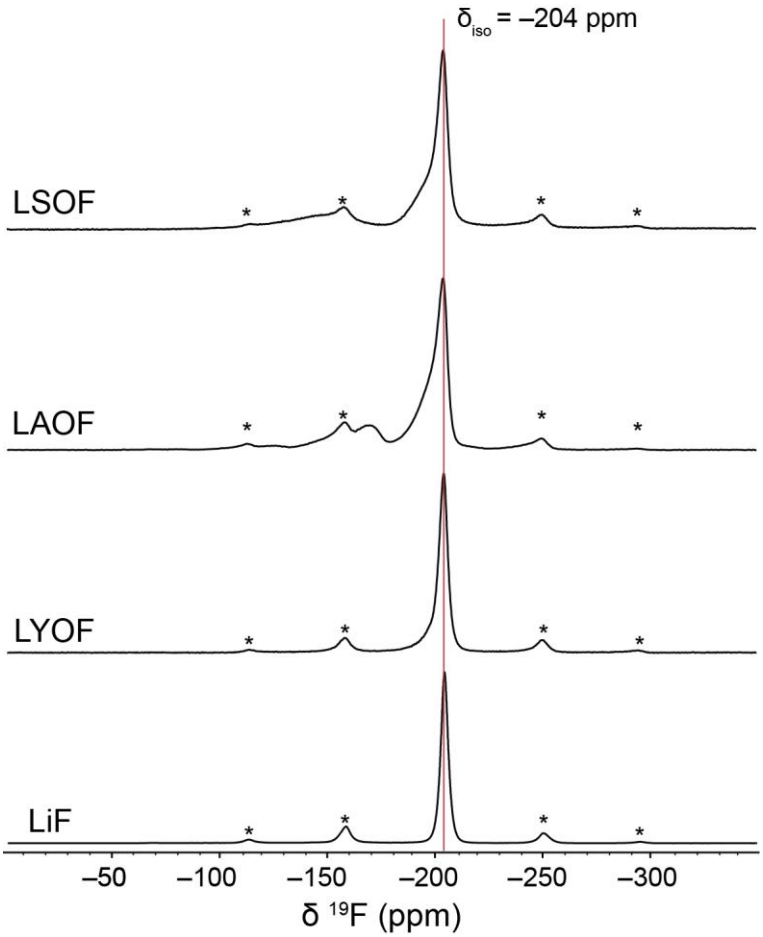

Figure 5.2: ^{19}F MAS NMR spectra recorded for LSOF, LAOF, LYOF and LiF at 16.4 T and an MAS frequency of 30 kHz. Asterisks denote spinning sidebands. Spectra for LSOF, LAOF and LYOF were acquired using a depth sequence, and are the sum of 16 scans with a recycle delay of 3 s. The spectrum for LiF was acquired using a Hahn echo sequence and is the sum of 16 scans with a recycle delay of 20 seconds.

The ^{19}F spectrum for LSOF shows a peak that overlaps with the peak for LiF at –204 ppm. In addition, this peak has a shoulder at ~–194 ppm. There is also a broad peak around – 155 ppm, although this is partially due to a spinning sideband. Therefore, it can be suggested that there are three types of fluorine environment present in this material, meaning that at least some of the LiF precursor has reacted.

The ^{19}F spectrum recorded for LAOF shows a similar pattern of peaks to LSOF, with a peak at –204 ppm, a shoulder around –195 ppm and a peak at –170 ppm. AlF_3 also has a chemical shift of –170 – –180 ppm, which suggests this final environment could be a fluoride anion bridging two aluminium ions.[178,266] This means that despite PXRD showing that some precursors remain, some of them have reacted. However, the product phase(s) are likely not a rocksalt, as bridging fluoride ions are not consistent with this structure.

Therefore, this material may not be useful to study further in the context of developing a model of the DRX structure.

The spectrum for LYOF shows a single peak at –204 ppm. This is consistent with the PXRD data which suggests that the precursors did not react. There is a slight shoulder to the left of the peak, which could suggest that some of the LiF has reacted, but not to the extent of the other samples. This may be due to the ionic radius of the Y^{3+} ion (0.9 Å). This is significantly larger than the 3+ ions used to synthesise other DRX materials (*e.g.*, Ti^{3+} = 0.67 Å, V^{3+} = 0.64 Å), and this mismatch of ion sizes may preclude the formation of the DRX phase.[261] Therefore, like LAOF, LYOF is not a suitable model compound for this work.

From the ^{19}F spectrum recorded, LSOF appears to have three types of fluorine environment present, with shifts of –150, –195 and –204 ppm. This third peak matches the chemical shift of LiF and so this environment could be attributed to fluoride ions octahedrally coordinated to six lithium ions. These could be within the DRX structure or unreacted LiF, but it is not possible to distinguish these from the data collected.

The other environments in the ^{19}F spectrum cannot be so easily assigned. ScF_3 has a chemical shift of –36 ppm, ruling out bridging fluoride environments as were observed for LAOF.[267] Therefore, to further investigate the environments present in the material, ^{6}Li and ^{45}Sc spectra were recorded. These are shown in Figure 5.3. ^{6}Li NMR was chosen over ^{7}Li due to the superior resolution of ^{6}Li spectra.

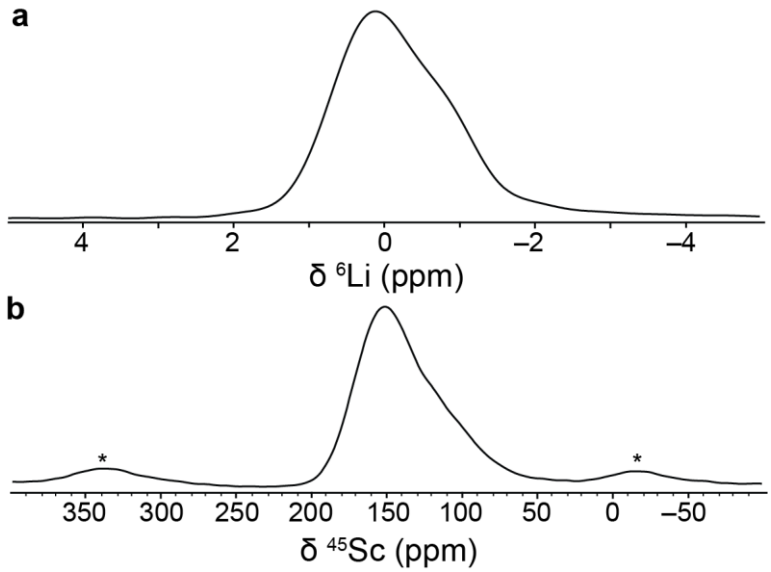

Figure 5.3: (a) ^{6}Li MAS NMR spectrum for LSOF at 9.4 T. The spectrum is the sum of 3072 scans acquired with a recycle delay of 60 s and an MAS frequency of 25 kHz. (b) ^{45}Sc NMR spectrum of LSOF acquired at 16.4 T. The spectrum is the sum of 256 scans collected using a recycle delay of 0.25 s and an MAS frequency of 30 kHz. Asterisks denote spinning sidebands.

The ^{6}Li spectrum shown in Figure 5.3 shows a peak at 0.1 ppm, with a shoulder around –1 ppm. These chemical shifts match Li_2CO_3 and LiF, respectively and so these peaks can be assigned to lithium ions coordinated to oxygen and fluorine, specifically octahedral LiF_6.[45] Therefore, this spectrum is consistent with what would be expected from a lithium-containing rocksalt material. Furthermore, the position of the peak is not at 2.6 ppm, meaning that the Li_2O has reacted.[268]

The ^{45}Sc spectrum has a peak at 150 ppm with a shoulder to the right side. 150 ppm is the chemical shift reported for $LiScO_2$.[269] This material contains alternating lithium and scandium ions octahedrally coordinated to six oxide anions. Therefore, the peak in the experimental spectrum can be assigned to octahedral ScO_6 environments. The shoulder can be assigned to unreacted Sc_2O_3, based on its chemical shift and the PXRD pattern previously discussed.[270]

In a fully random DRX structure, it would be expected that there are scandium sites where scandium is bonded to fluorine. From literature, there are two compounds that contain Sc-F bonding and have ^{45}Sc shifts reported. First is ScF_3, which contains octahedral ScF_6 sites and has a ^{45}Sc chemical shift of ~–50 ppm.[271,272] Second is ScOF, which contains scandium ions coordinated to three oxide ions and three fluoride ions and has a ^{45}Sc chemical shift

of 64 ppm.[270] From these two compounds it would be expected that sites with bonding between scandium and fluorine would have chemical shifts to the right of those observed for ScO_6 sites. There are no peaks between 75 and –50 ppm, meaning that there likely are no sites where there are three or more fluoride ions coordinated to the scandium ion (based on the structures of ScOF and ScF_3). There may however be sites where one or two fluoride ions are coordinated to the scandium ion as these would be expected to have higher chemical shifts. However, because of the breadth of the peaks, these would likely overlap with peaks from ScO_6 sites, making it difficult to confirm or exclude their presence. A ^{45}Sc MQMAS experiment was performed but this did not yield any greater insight.

5.3.1.2. ^{19}F{X} TRAPDOR

Whilst the ^{6}Li and ^{45}Sc NMR spectra show features that would be expected to be found in a rocksalt structure, they do not help in assigning the environments observed in the ^{19}F spectrum. One way to gain information about the fluorine bonding environments present is to use TRAPDOR. This uses dipolar interactions between the metal ions and the fluoride ions to determine whether they are close in space. It is ^{19}F-detected and so capitalises on the better resolution of the ^{19}F spectrum to provide information about the metal ion. The fact that it is ^{19}F-detected also means that TRAPDOR can more readily provide information that can be used to assign the unknown peaks in the ^{19}F spectra, as against quadrupolar CP (notwithstanding the challenges of implementing quadrupolar CP).

As outlined in Chapter 3, TRAPDOR involves acquiring two Hahn echo spectra, with the second employing a low power pulse on the X channel, preventing complete averaging of dipolar interactions. Subtracting the second spectrum from the first gives the TRAPDOR difference spectrum. Peaks that appear in this spectrum correspond to fluorine environments that are near the X nucleus.[197] Larger TRAPDOR effects are achieved by using slower MAS frequencies and longer echo delays. However, slower MAS frequencies lower the resolution of the spectra recorded, whilst longer echo delays result in greater T_2 relation. Therefore, TRAPDOR experiments were performed at 25 kHz MAS and echo delays equivalent to 1 and 5 rotor periods, to balance resolution with achieving TRAPDOR effects.

Figure 5.4 shows the results of the ^{19}F{^{45}Sc} TRAPDOR experiments whilst Figure 5.5 shows the results of the ^{19}F{^{7}Li} TRAPDOR experiments. In both cases, a 40 kHz pulse was applied to the X channel. Whilst this may not be the optimum for both nuclei, this was determined to be a safe power level to use, based on previous literature.[197]

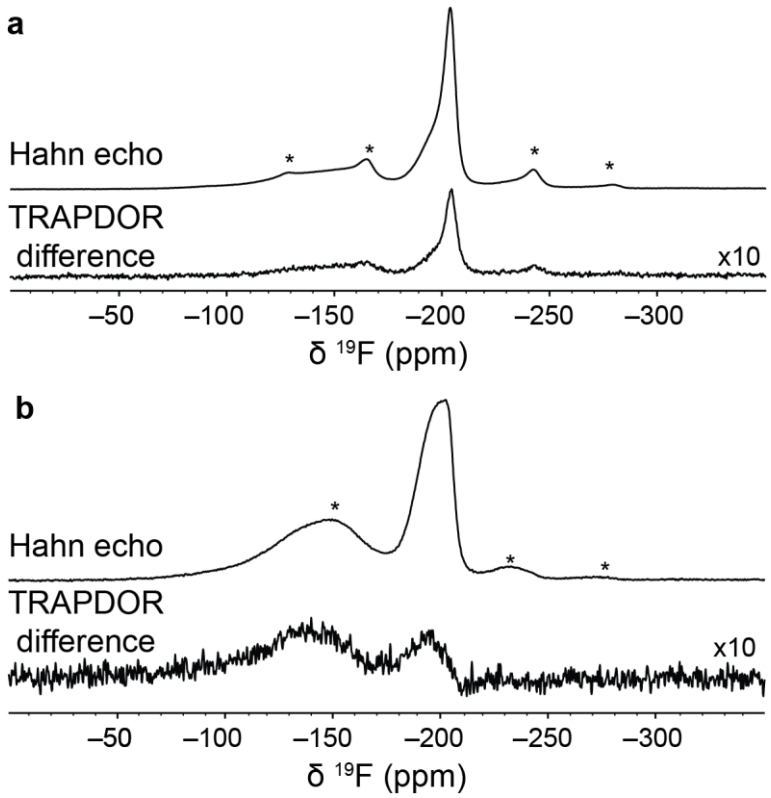

Figure 5.4: Hahn echo and $^{19}F\{^{45}Sc\}$ TRAPDOR difference spectra acquired for LSOF using echo delays of (a) 1 and (b) 5 rotor periods (MAS frequency = 25 kHz). Spectra are the sum of 128 scans, separated by a recycle delay of 3 s. Dipolar couplings were reintroduced by applying a 40 kHz pulse to the ^{45}Sc channel. Asterisks denote spinning sidebands.

The $^{19}F\{^{45}Sc\}$ TRAPDOR difference spectrum recorded at 25 kHz using an echo delay of 1 rotor period (Figure 5.4a) shows the three environments seen in the Hahn echo spectrum (–140, ~–195 and –204 ppm). This confirms that all three environments are real (rather than background) and close in space to scandium ions, including the peak at –204 ppm meaning that it not only from residual LiF, but also LiF-like environments in the bulk structure. The difference spectrum recorded using an echo delay of 5 rotor periods shows peaks at –140 and ~–195 ppm, whilst the peak at –204 ppm is absent. No other sidebands are observed, which means that the peak at –140 ppm, is not simply due to sidebands of the other two peaks and is a distinct environment. The peak at –204 ppm is absent in the difference spectrum recorded using an echo delay of 5 rotor periods. As this peak is present in the difference spectrum recorded with a delay of 1 rotor period, it suggests that this site has a shorter T_2 time. The signal intensity is therefore lost during the longer delay. However, there is still a peak at –204 ppm in the Hahn echo spectrum. This can be explained by there being two types of FLi_6 site. The first site is within the DRX and has scandium ions close by, resulting in a TRAPDOR effect. However, being part of the

disordered structure means that this site has a relatively fast T_2, meaning that no TRAPDOR effect is observed after 5 rotor periods. The second site is unreacted LiF. This likely has a longer T_2 as it does not contain other ions and so is still observed in the Hahn echo spectrum. However, as it is not part of the DRX structure, and therefore separated from the scandium ions, it is not reflected in the TRAPDOR difference spectrum.

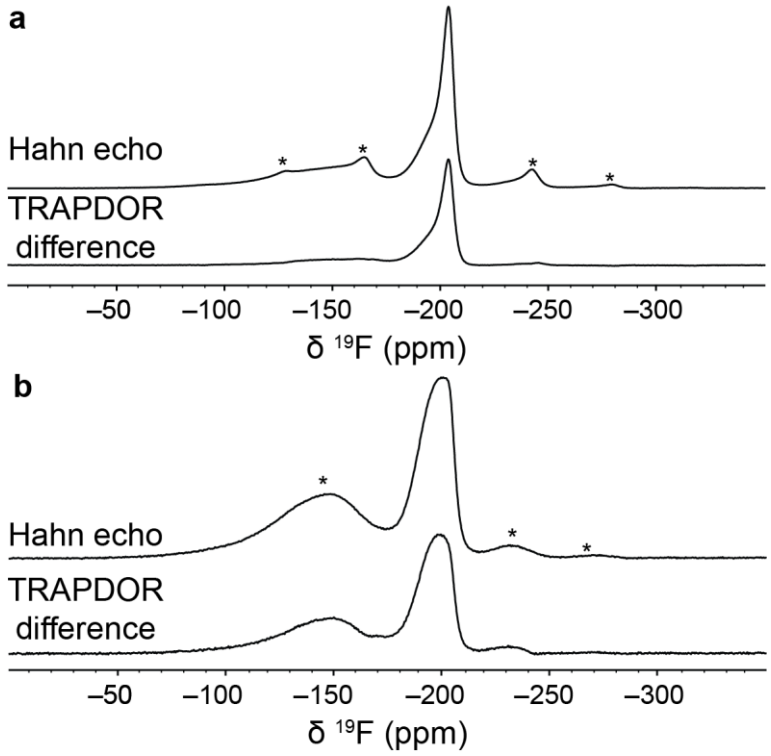

Figure 5.5: Hahn echo and $^{19}F\{^{7}Li\}$ TRAPDOR difference spectra acquired for LSOF using echo delays of (a) 1 and (b) 5 rotor periods (MAS frequency = 25 kHz). Spectra are the sum of 128 scans, separated by a recycle delay of 3 s. Dipolar couplings were reintroduced by applying a 40 kHz pulse to the ^{7}Li channel. Asterisks denote spinning sidebands.

The $^{19}F\{^{7}Li\}$ TRAPDOR difference spectra shown in Figure 5.5 have features at –140, –195 and –204 ppm. This means that all three environments observed in the 1D ^{19}F NMR spectrum for LSOF contain fluoride ions close to lithium ions. Furthermore, the peak at –204 ppm is reflected in the difference spectrum recorded with an echo delay of 5 rotor periods, unlike in Figure 5.4. This means that the site observed here likely has a longer T_2, which supports the suggestion that there are two FLi_6 sites.

5.3.1.3. DFT calculations

From the NMR results presented so far, it can be suggested that LSOF contains a number of different types of lithium, scandium and fluorine sites. However, full assignment of the ^{19}F spectrum is not possible based on this data. TRAPDOR suggests that the unassigned

sites are close in space to both lithium and scandium ions, but it is difficult to say how many of each metal ion are present and how close they are to the fluoride ions. Overlap of sidebands with potential peaks in the ^{19}F spectra also means that it is difficult to be quantitative when interpreting the spectra. Therefore, to aid the assignment, DFT calculations were performed to explore what bonding environments could give rise to the ^{19}F chemical shifts observed. Whilst the output files from the calculations do contain details about the ^{45}Sc parameters, these are not discussed here as the objective of the calculations was to assign the ^{19}F spectra.

To explore this, a set of five, 48-atom model unit cells were created, using the crystal structure of LiF as a starting point. The 24 cations/anions were randomly assigned to their positions according to the stoichiometry of the material (2:1 Li/O:Sc/F). First, geometry optimisations were performed using the PBE functional, to allow the unit cell to expand. Four out of the five structures converged (Structure 2 did not), however the eight fluorine environments in Structures 4 and 5 are identical. As such Structure 4 was not included in subsequent analysis. These optimised structures were then used to calculate ^{19}F chemical shieldings. These were then referenced using LiF, optimised using the same parameters, using the .cif file from the Materials Project as a starting structure.[262]

The relationship between ^{19}F chemical shifts and the number of metal ions coordinated is shown in Figure 5.6.

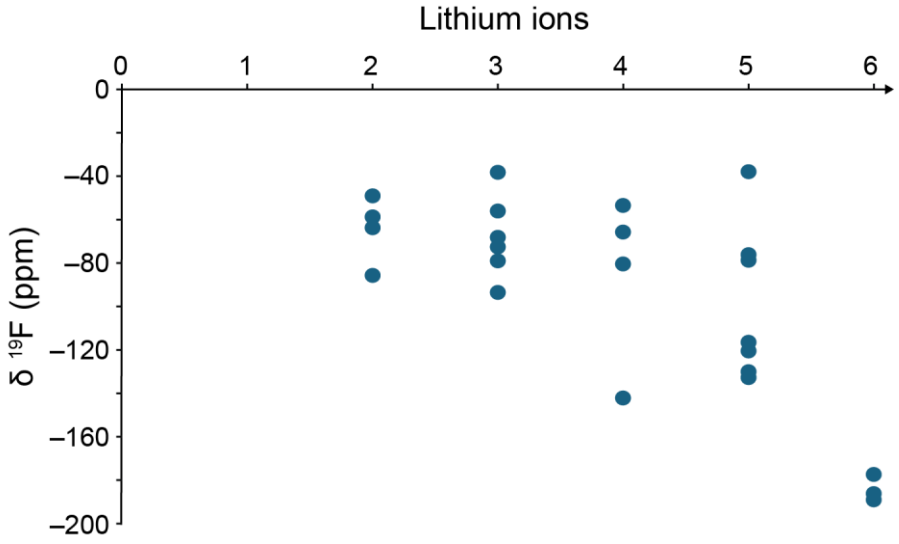

Figure 5.6: A plot showing the calculated ^{19}F chemical shifts of the different environments in the 48-atom unit cells, based on the number of lithium ions immediately coordinated to the F^- ion (0 – 6).

Figure 5.6 shows that, in general, as the number of lithium ions in the coordination shell increases, the chemical shift becomes more negative. The chemical shifts of sites with six lithium ions coordinated to the fluoride ion are also noticeably separated from the other environments by at least 30 ppm. This would suggest that the addition of scandium to the coordination sphere noticeably affects the chemical shift. The chemical shifts for the six-coordinate environments also cover a much smaller range than the other types of environments, which span 40 ppm up to over 100 ppm. This however may be because there are fewer six-coordinate environments, and so the full spread of chemical shifts is not seen.

Figure 5.7 shows the calculated chemical shifts overlaid with the experimental spectrum.

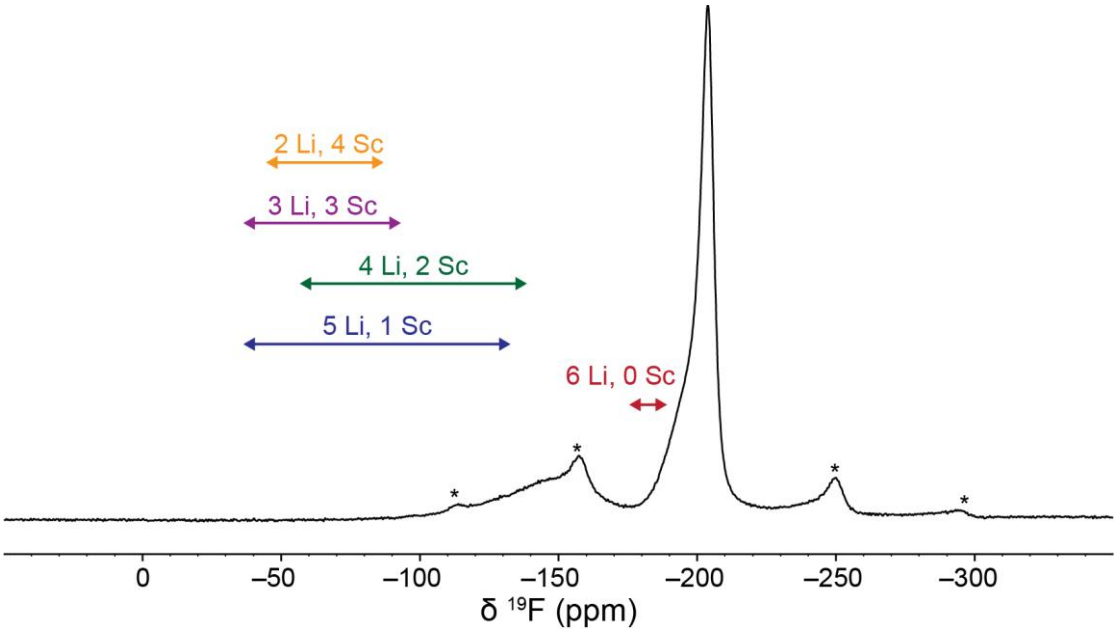

Figure 5.7: The ranges of the calculated ^{19}F chemical shifts for the 48-atom unit cells, overlaid on the experimental spectrum for LSOF (Figure 5.2). Chemical shifts are divided according to the number of lithium and scandium ions directly coordinated to the F^- ion ("X Li, Y Sc", where X + Y = 6).

The calculated chemical shifts do not match the experimental spectrum perfectly, with the bulk of the chemical shifts being more positive than any of the experimentally observed peaks. However, as noted already, there is a separation between the environments that include scandium in their coordination shell with those that are fully coordinated to lithium. This does qualitatively agree with the experimental spectrum, as there is a gap in the peaks, rather than a continuous distribution of environments.

It would be expected that the distances between the fluoride ions and the metal ions are shortest as these are directly bonded. However, inspection of the optimised structures

reveals that O-F and F-F distances are shorter than the longest F-M distances. This means that the bonding environments cannot be described as perfectly octahedral, as some of the six cations that make up the octahedral site are further away than the nearest anions.

The size of the unit cell may be a contributing factor to the unexpected bonding environments, and so two random 96-atom unit cells were constructed, under the assumption that increased size will allow distortions to be better accommodated. In addition to these random structures, it was also decided to investigate a structure where the fluoride ions entirely reside in a segregated LiF-like region. This was to create structures that represent the short-range ordering preferences described in literature for these materials.[155] However, the fully segregated structure did not converge and so four further structures were generated from one of the random structures. Each successive structure had one additional fluoride ion moved into the LiF-like region until the geometry optimisations failed to converge. As with the previous unit cells, the chemical shifts for each fluorine site for each of the six structures were recorded along with the surrounding metal ions. This information is presented in Figure 5.8.

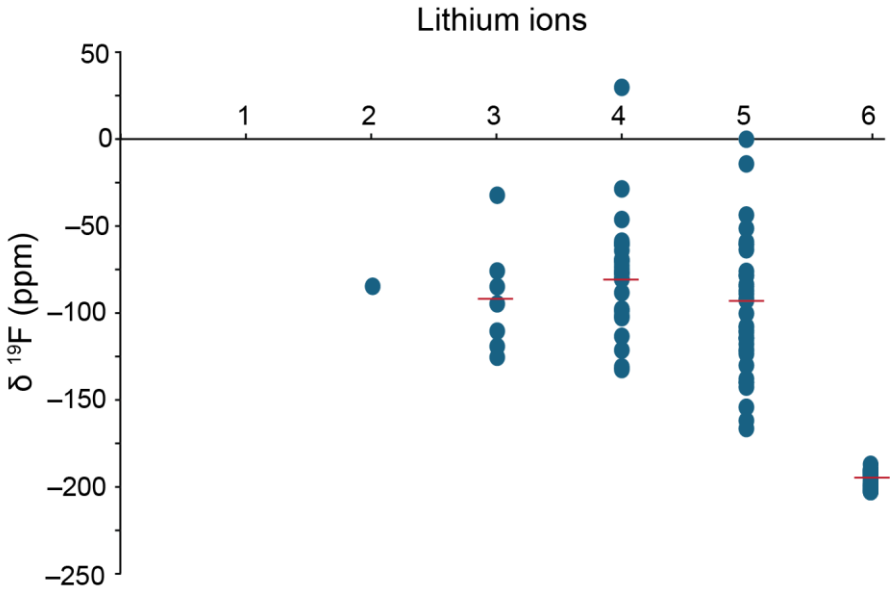

Figure 5.8: A plot showing the calculated ^{19}F chemical shifts of the different environments in the 96-atom unit cells, based on the number of lithium ions immediately coordinated to the F^- ion (0 – 6). Red lines denote the average chemical shift for that type of environment.

Figure 5.8 shows that the chemical shifts calculated for the fully lithiated environments are noticeably separated from those that have scandium ions within the first coordination shell. It can also be seen that the chemical shift ranges for the environments that have scandium ions within the first coordination shell overlap significantly. These observations agree with

the previous set of results obtained using 48-atom unit cells. Furthermore, the chemical shifts recorded for the FLi_6 sites are closer to what would be expected experimentally (–204 ppm), suggesting that the larger unit cell is a better model, at least for this type of environment. This is supported by the fact that the average energy per atom is lower for the 96-atom unit cells than the 48-atom unit cells (Table 5.4), meaning that the 96-atom structures are more stable.

Table 5.4: Energy per atom for each of the different 48- and 96-atom unit cells after geometry optimisation.

Structure	48-atom unit cells Energy per atom/eV	96-atom unit cells Energy per atom/eV
1	–538.406	–538.4
2	–538.385	–538.441
3	–538.385	–538.458
4	-	–538.474
5	-	–538.471
6	-	–538.466
Average	–538.392	–538.452

Figure 5.9 shows the calculated chemical shift ranges overlaid with the experimental spectra.

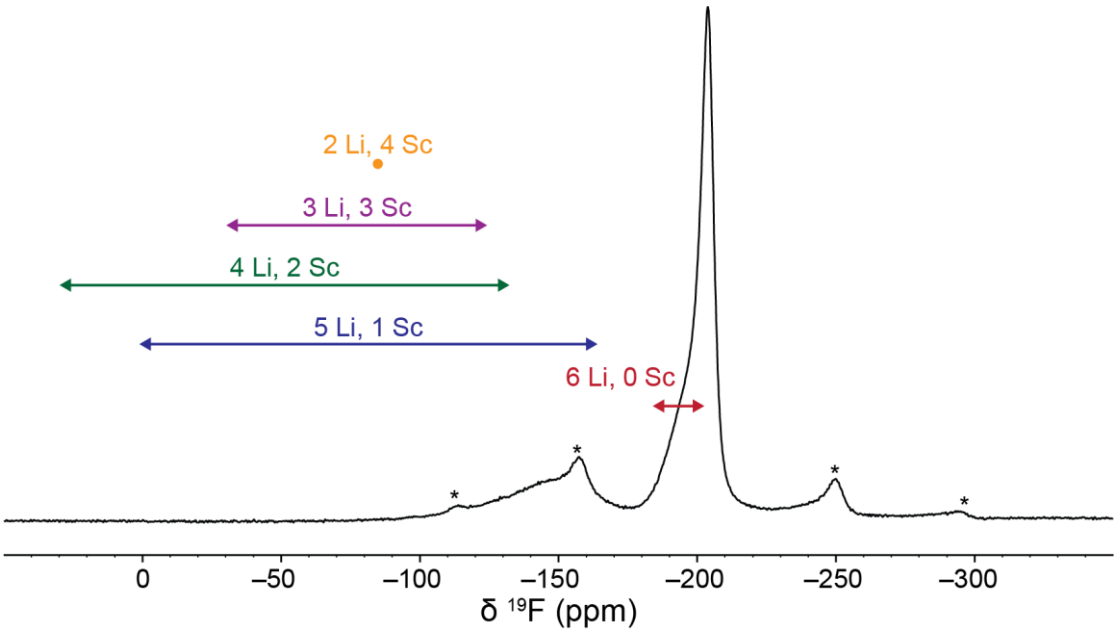

Figure 5.9: The ranges of the calculated ^{19}F chemical shifts for the 96-atom unit cells, overlaid on the experimental spectrum for LSOF (Figure 5.2). Chemical shifts are divided according to the number of lithium and scandium ions directly coordinated to the F^- ion ("X Li, Y Sc", where X + Y = 6).

The chemical shifts of the environments with six lithium ions in the first coordination shell overlap well with the shoulder at –195 ppm observed in the experimental spectrum. These environments differ from pristine LiF as the bond lengths vary from 2.04 Å. This distortion may be the cause of the deviation in chemical shift. The chemical shift ranges calculated for the other environments all overlap with the broad feature at –150 ppm in the experimental spectrum (except for the single 2 Li, 4 Sc site). As such, the larger unit cell seems to give better agreement with the experimental data than the 48-atom unit cells. However, the chemical shifts calculated still cover a much larger range than the peaks in the experimental spectrum. To explore the cause for this, the average Li-F and average Sc-F interatomic distances were plotted against the calculated chemical shifts. Figure 5.10 shows the information for the Li-F distances.

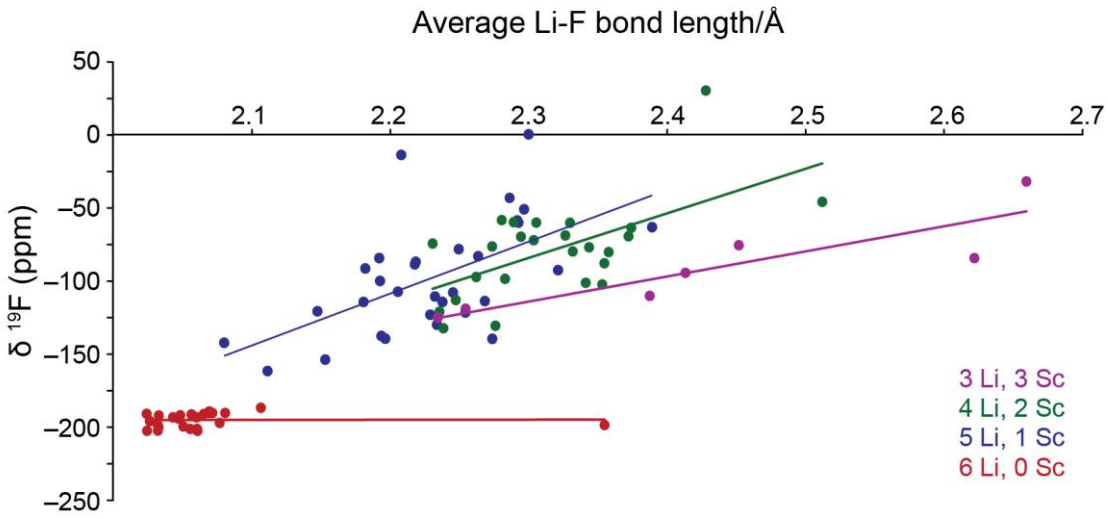

Figure 5.10: A plot of the average Li-F bond lengths against calculated ^{19}F chemical shift for the 96-atom unit cells, separated according to the metal ions directly coordinated to the F^- ion. Lines are included as a guide rather than as lines of best fit.

Figure 5.10 shows that for sites coordinated to six lithium ions, the average Li-F distance is roughly –200 ppm, regardless of average bond length. This includes a structure with an average bond length of ~2.35 Å, which is noticeably larger than the other structures (< 2.1 Å). Therefore, for sites coordinated to six lithium ions, bond length does not affect chemical shift. This means that the improvement in calculated chemical shifts moving from the 48-atom to 96-atom unit cells is likely driven by a more accurate coordination number (six rather than five). The Li-F distances are also generally shorter than those that are coordinated to scandium, which may be partially the reason why there is a separation in chemical shifts for these environments. The other environments show a slight positive correlation between chemical shift and average interatomic distance, although there is a lot of variation between the data points, meaning that average Li-F distances are not a good indicator of chemical shift.

Figure 5.11 shows the calculated chemical shifts plotted against average Sc-F distances.

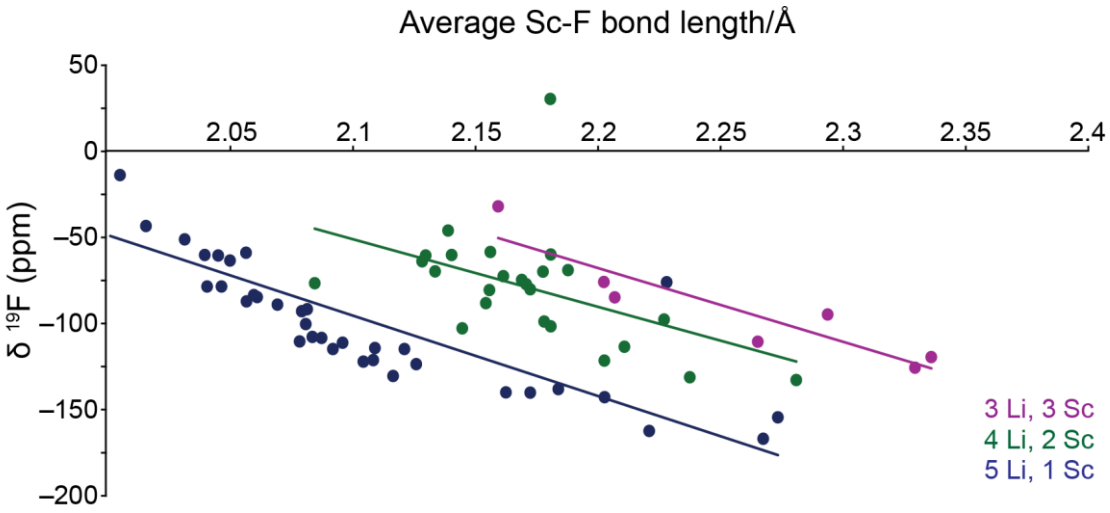

Figure 5.11: A plot of the average Li-F bond lengths against calculated ^{19}F chemical shift for the 96-atom unit cells, separated according to the metal ions directly coordinated to the F^- ion. Lines are included as a guide rather than as lines of best fit.

There is in general a negative correlation between average Sc-F distance and chemical shift, with larger distances giving more negative chemical shifts. This is consistent with the data collected for Li-F distances where the environments close to lithium ions have much larger Sc-F distances, and hence more negative chemical shifts.

The data points for the [5 Li, 1 Sc] sites have a much narrower spread than the other two series. Despite this, there does appear to be a break in the data points at around 2.15 Å, after which the gradient of the data is lower. This may simply be a coincidence. However, after this point, the data seems to follow a shallower trend, suggesting that there are two regimes. Below 2.15 Å, the proximity of the scandium ion has a significant impact on chemical shift, which is lessened beyond 2.15 Å.

5.3.1.4. Local structure of Li_2ScO_2F

The goal of the work so far in this chapter was to prepare a model oxyfluoride material, whose local structure can be comprehensively characterised to provide a basis for understanding the behaviour of other similar materials. Of the materials attempted LSOF was the most suitable choice.

^{6}Li NMR confirms the presence of LiF_6 and LiO_6 structural units, whilst ^{45}Sc NMR suggests the presence of ScO_6 units as well as an Sc_2O_3 impurity. All these observations are consistent with the impure DRX observed by PXRD. No evidence of an ScF_6 site is observed. The ^{19}F NMR spectrum recorded for this material shows three sites, one of which can be readily assigned to FLi_6 sites because of its chemical shift (–204 ppm).

However, some of these environments are close in space to scandium ions as a TRAPDOR effect is observed for this peak. This means that this peak is not entirely from unreacted LiF but also from LiF-like domains in the DRX phase, which are close to scandium ions.

DFT calculations suggest that another one of the ^{19}F environments (at –150 ppm) can be attributed to FLi_xSc_{6-x} sites. This is supported by this peak being affected by both forms of TRAPDOR experiment, implying that these fluorine ions are close to both Li^+ and Sc^{3+}. The DFT calculations performed show that, in general, decreasing the number of lithium ions in the first coordination shell increases the chemical shift. Therefore, the value of X in the FLi_xSc_{6-x} sites is more likely to be higher *i.e.*, X = 4 or 5, in agreement with literature.[155] The presence of mixed coordination sites also implies the existence of $ScO_{6-x}F_x$ and $LiO_{6-x}F_x$ sites. However, these cannot be directly confirmed by ^6Li and ^{45}Sc NMR. This is because of the poor resolution of the spectra owing to the narrow chemical shift range of ^6Li and the large quadrupole moment of ^{45}Sc.

DFT calculations suggest that the final environment observed in the ^{19}F spectrum (–195 ppm) can be assigned to distorted FLi_6 units. This makes sense as its chemical shift suggests that it is chemically similar to LiF. TRAPDOR experiments also suggest that it is part of the DRX phase as TRAPDOR effects are observed in the $^{19}F\{^{45}Sc\}$ difference spectra. This does suggest that there are two types of FLi_6 structural unit within the DRX (in addition to residual LiF), one that is ordered and one that is distorted. Both are close to scandium ions, and so the cause of the distortion is unclear.

5.3.1.5. Incorporation of fluorine into the DRX structure

There are three different fluorine environments in LSOF, which have been assigned in the previous discussion. However, it is not clear how these environments form in the DRX. Therefore, two other samples of the type $Li_{1+x}ScO_2F_x$, where x = 0.2 and 0.6 were prepared. These will be referred to as LSOF0.2 and LSOF0.6 respectively. Figure 5.12 shows the PXRD patterns recorded for these materials.

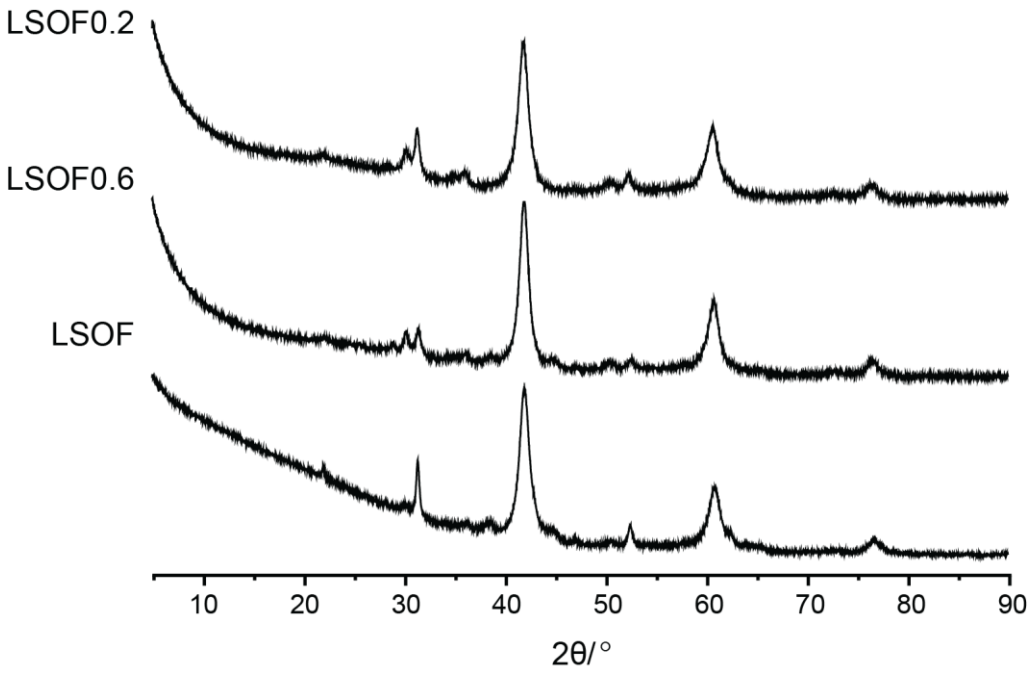

Figure 5.12: PXRD patterns for the LSOF series $Li_{1+X}ScO_2F$ where X = 0.2, 0.4 and 1.0. Patterns were acquired using the Smartlab diffractometer.

As with the PXRD pattern for LSOF, the PXRD patterns recorded for LSOF0.2 and LSOF0.6 show peaks at 38, 41, 61 and 77°. As already discussed, these indicate the presence of a rocksalt phase and confirm successful synthesis. There are also peaks at 22, 31 and 52°, which can be attributed to unreacted Sc_2O_3, like the pattern for LSOF.

Figure 5.13 shows the mass-normalised ^{19}F NMR spectra recorded for LSOF0.2, LSOF0.6 and LSOF.

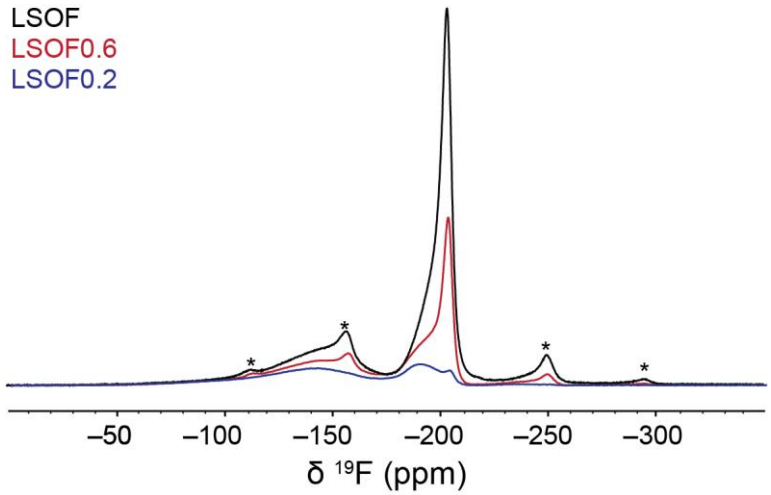

Figure 5.13: Mass normalised ^{19}F NMR spectra acquired at a field of 16.4 T and an MAS frequency of 30 kHz. Asterisks denote spinning sidebands. Spectra were acquired using a depth sequence, and are the sum of 16 scans with a recycle delay of 120 s.

All three spectra shown in Figure 5.13 show the three peaks previously discussed in this chapter. The intensity of all three peaks also grows as the amount of fluorine is increased, however the relative intensities vary. For LSOF0.2, all three peaks have similar heights. On increasing the fluorine concentration to LSOF0.6, the broad peak at –150 ppm does not appear to grow significantly, but the other two peaks do. Increasing again to LSOF sees the peak at –204 ppm grows, whilst the others remain roughly the same. These observations can be rationalised based on the peak assignments. At low fluorine levels (LSOF0.2), the LiF can react with the other precursors, resulting in the formation of the FLi_xSc_{6-x} sites (–150 ppm). However, as the scandium ions never reach full fluorination (ScF_6), the amount of fluorine that can be incorporated into scandium-containing regions is limited. On increasing the fluorination level to LSOF0.6, a smaller proportion of the fluoride ions can be incorporated into scandium-containing sites resulting in an increase in the two FLi_6 sites. This agrees with literature precedent which suggests that oxyfluoride DRXs form transition metal-poor, fluorine-rich regions.[168] Finally, as not all the Sc_2O_3 reacts (based on PXRD), when the fluorine level is increased to LSOF, the remaining LiF is unable to react and incorporate into the DRX structure, increasing the intensity of the peak at –204 ppm.

5.3.2. Redox-active oxyfluoride materials

5.3.2.1. Initial PXRD and ^{19}F SSNMR characterisation

The previous work studying LSOF provides insight into the types of environments that may be present in oxyfluoride DRX materials. However, to understand the structural changes that occur during cycling it is necessary to investigate materials that are redox-active and can therefore function in a battery. A range of different redox-active oxyfluoride DRX materials have been reported in literature.[136,137,150,162] As a starting point, three materials previously reported were prepared by ball mill synthesis. These were Li_2NiO_2F (LNOF), Li_2TiO_2F (LTOF) and Li_2VO_2F (LVOF).[150,258] Figure 5.14 shows the PXRD patterns recorded for these materials, whilst Table 5.5 shows the predicted positions of the peaks for each of the lattice planes present in a DRX.

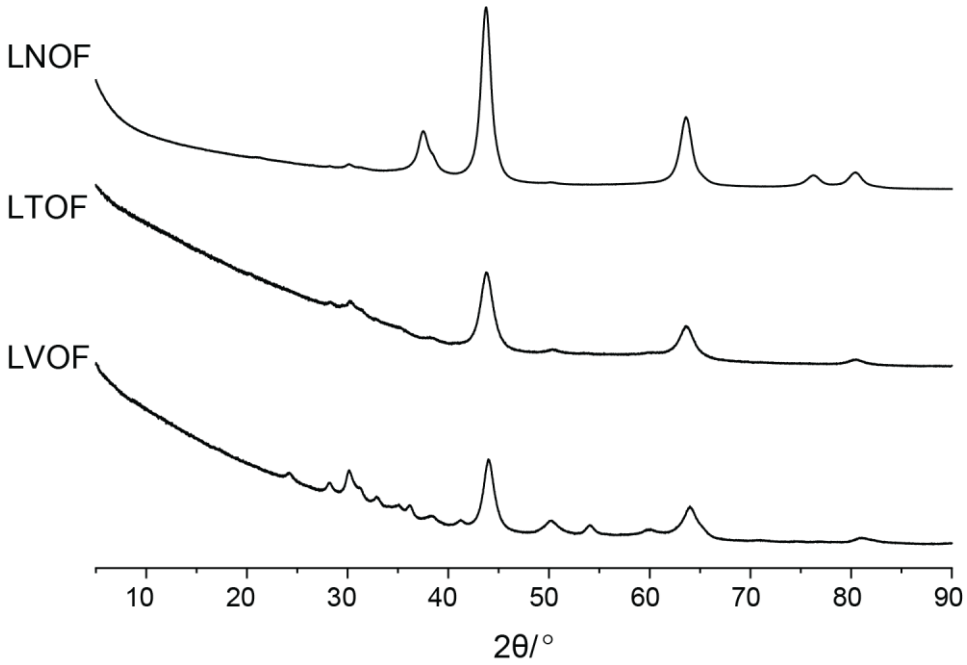

Figure 5.14: PXRD data acquired for LNOF, LVOF and LTOF. Data was acquired using the Smartlab diffractometer.

Table 5.5: Predicted positions of the PXRD peaks of LNOF, LVOF and LTOF attempted. Based on the Shannon ionic radii.[261] LiF positions are from the PXRD pattern simulated for the crystal structure from the Materials Project (mp-1138).[262]

Lattice plane	Predicted peak position/°			
	LNOF	LVOF	LTOF	LiF
(111)	38	37	37	38
(200)	44	43	43	44
(220)	63	63	62	64
(311)	76	75	75	77
(222)	80	79	79	82
(400)	96	94	94	98

The PXRD pattern for LNOF shows peaks at 37, 44, 64, 76 and 81°. This pattern of peaks is in good agreement with what was predicted for LNOF. There are some small peaks at around 20, 30 and 50°, meaning that it is not completely pure. The peaks at 30 and 50° could be attributed to ZrO_2 introduced from the ball milling media. It is not possible to assign the peak at 20° as it is too low intensity and there appear to be no other peaks associated with it, and neither of the precursor materials have a peak in this region.

The LTOF PXRD pattern contains peaks at 38, 44, 64 and 81°, which could be assigned to the LTOF DRX. As with LNOF, there appear to be peaks from ZrO_2, at around 30 and 50°.

The pattern for LVOF also shows peaks at 44, 64 and 81°, meaning that a rocksalt phase is likely present. However, there are many other peaks, meaning that the material is not pure. The peaks at 24, 33, 36, 41, 49 and 54° could originate from unreacted V_2O_3. This means that the rocksalt peaks could be from, at least in part, unreacted LiF. The peaks at 31, 35, 50 and 60° would suggest the presence of ZrO_2, as with the other two samples.

From the PXRD data shown, all samples likely contain a rocksalt phase, although in the case of LVOF, this may be at least partially unreacted LiF. Whilst further optimisation of the synthesis may have yielded purer samples, it was decided that this was unnecessary, as the isotope specific nature of NMR means that ZrO_2 will not be observed. V_2O_3 is paramagnetic and will be invisible to ^{51}V NMR, and the ^{19}F chemical shift of LiF is well known (–204 ppm).[178]

^{19}F NMR spectra were also recorded for each of the materials. These are shown in Figure 5.15.

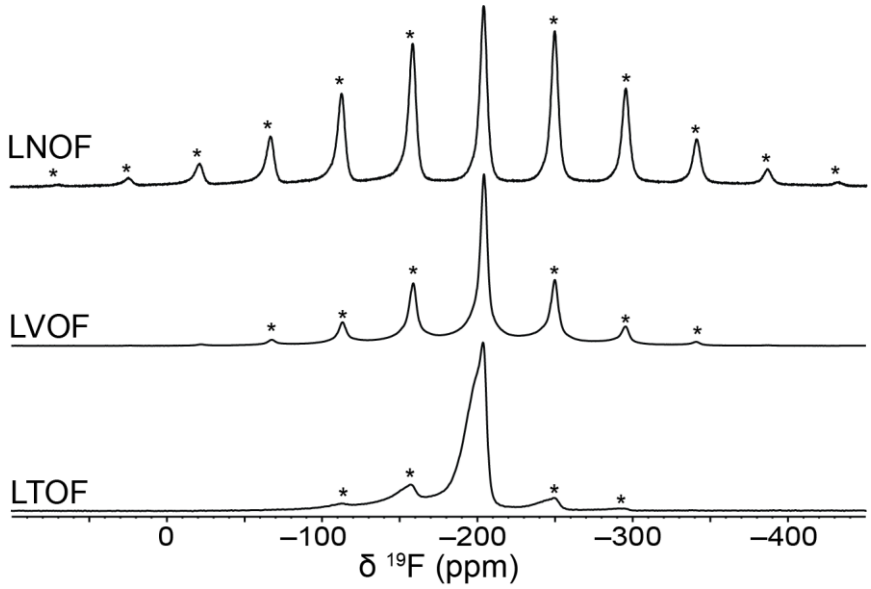

Figure 5.15: ^{19}F NMR spectra of LNOF, LVOF and LTOF acquired at a field of 16.4 T and an MAS frequency of 30 kHz. Asterisks denote spinning sidebands. Spectra were acquired using a Hahn echo sequence, and are the sum of 64 (LNOF), 640 (LVOF) and 16 scans (LTOF), separated by a recycle delay of 1 s (LNOF + LVOF) and 120 s (LTOF).

The ^{19}F NMR spectrum acquired for LNOF contains a single isotropic resonance at –204 ppm, with several spinning sidebands. This agrees with previous reports and can be assigned to LiF_6 sites based on its chemical shift, which matches that of LiF.[150] The large number of spinning sidebands would suggest that at least some of this signal comes from LiF-like regions close to paramagnetic nickel centres (*i.e.*, in the DRX phase), rather than simply unreacted LiF. The peak at –204 ppm is also slightly asymmetric, potentially indicating an additional environment slightly to the left. This is as observed for LSOF and could suggest the presence of distorted FLi_6 sites.

As with LNOF, the spectrum for LVOF shows a single isotropic peak at –204 ppm with associated spinning sidebands, in agreement with previous reports.[167] It can also be seen that the baseline is not flat, with a broad feature being present underneath the isotropic peak and its sidebands. This broad feature was also observed by Chang *et al*, and would suggest that there are other fluorine environments close to vanadium ions.[13] The proximity to these paramagnetic ions would cause any peaks observed to be broad and low intensity.

The spectrum for LTOF shows potentially three environments like the spectrum observed for LSOF. First is a sharp peak at –204 ppm, which as previously mentioned, likely comes

from an LiF-like environment. Next is a shoulder at roughly –195 ppm with a third environment at approximately –150 ppm, causing the left-hand spinning sidebands to rise compared to those on the right of the spectrum. Based on the previous work these would be assigned to distorted FLi_6 and FLi_xTi_{6-x} sites, respectively. It is worth noting that the peak corresponding to a distorted FLi_6 site is more pronounced (relative to the peak at –204 ppm) than was observed for LSOF. This could be due to the smaller size of Ti^{3+} ions resulting in more distorted FLi_6 sites.

To attempt to improve the resolution of the ^{19}F spectrum of LTOF and reduce the overlap of spinning sidebands, a second spectrum was recorded at the National High-Field Solid-State NMR Facility using the 850 MHz spectrometer at 60 kHz MAS. This is shown in Figure 5.16.

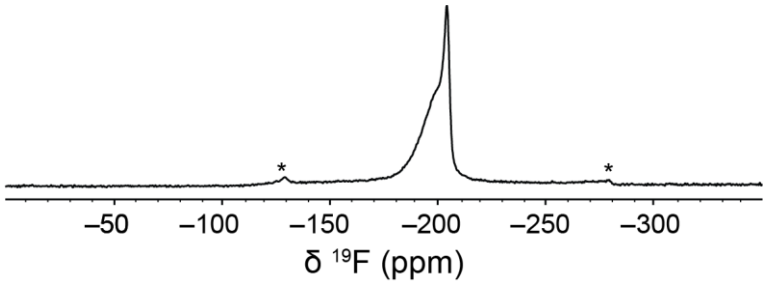

Figure 5.16: ^{19}F NMR spectrum of LTOF acquired at a field of 20 T and an MAS frequency of 60 kHz. Asterisks denote spinning sidebands. The spectrum was acquired using a depth sequence, and is the sum of 64 scans with a recycle delay of 2 s.

Figure 5.16 shows slightly improved resolution of the two peaks around –200 ppm. However, what is more noticeable is the absence of a peak at –150 ppm. This would support the assignment of this peak originating from FLi_xTi_{6-x} sites. Ti^{3+} ions are paramagnetic, and so the paramagnetic broadening would be exacerbated by the higher magnetic field. It could be argued that this peak was originally from background, not observed using this probe. However, subsequent experiments performed at 16.4 T using a depth sequence, also show this feature. Therefore, it is unlikely that this originates from background (see Chapter 3). Furthermore, a similar feature is observed for LSOF, and this feature was observed to show a TRAPDOR effect. For this to occur due to a background signal, the potential background feature would need to also contain bonds between scandium/lithium and fluorine, which seems unlikely.

5.3.2.2. Further characterisation of Li_2VO_2F

Both the ^{19}F NMR spectra recorded for LNOF and LVOF are similar, showing only a single, clear isotropic resonance. It was therefore decided to only continue studying one of these materials. LVOF has an additional viable NMR-active nucleus compared to LNOF (^{51}V) and so further characterisation efforts were focussed on this material.

First, to explore the incorporation of fluorine into the structure of LVOF, a series of samples were prepared with different levels of fluorine, $Li_{1+x}VO_2F_x$ (x = 0.2, 0.4, 0.6 and 0.8). Figure 5.17 shows the PXRD patterns for these materials. These confirm the formation of a DRX phase, although V_2O_3 impurities can still be seen as already noted in the PXRD pattern for LVOF (Figure 5.14).

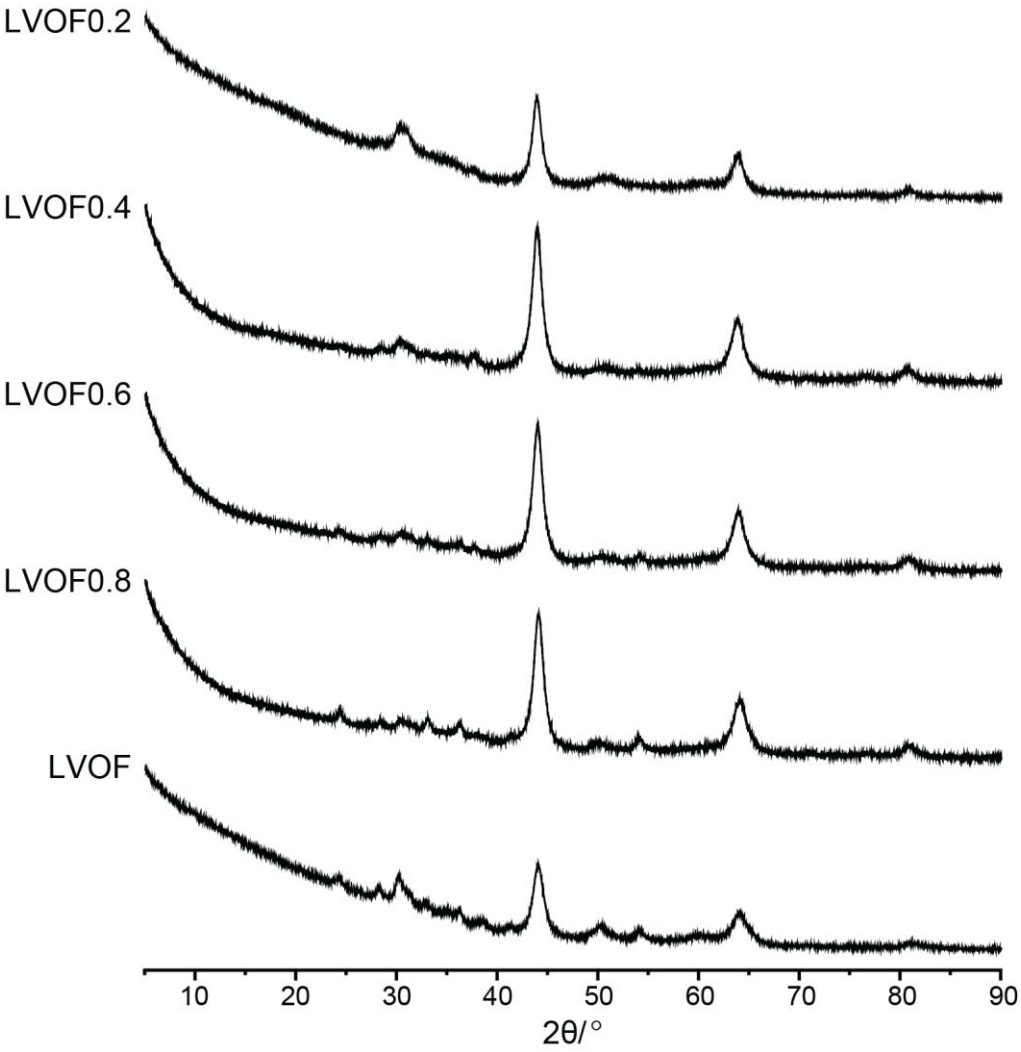

Figure 5.17: PXRD patterns collected for the LVOF series, using the Smartlab diffractometer.

Figure 5.18 shows the ^{19}F spectra recorded using an 850 MHz spectrometer at 60 kHz, whilst Figure 5.19 shows the integrated intensities.

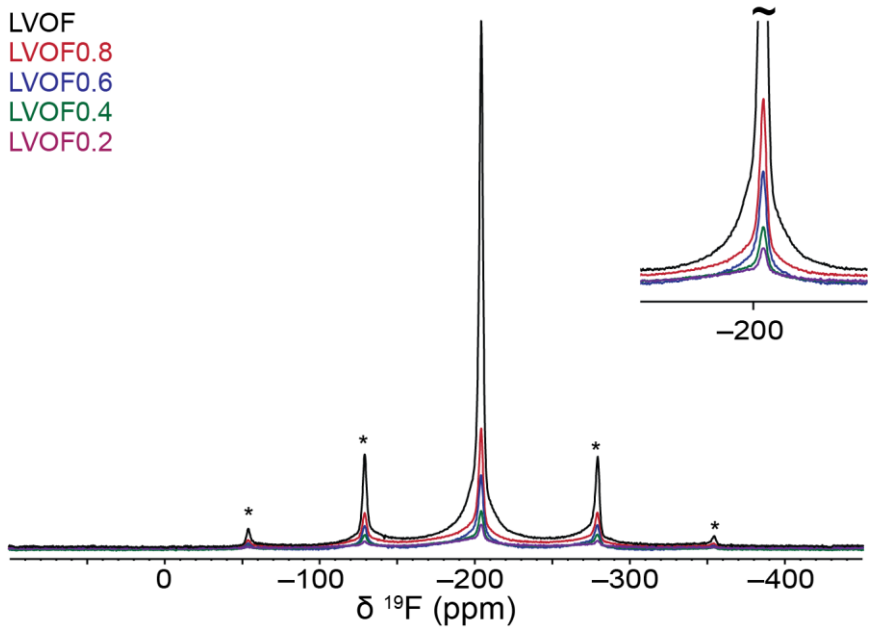

Figure 5.18: ^{19}F NMR spectra of the LVOF series acquired at a field of 20 T and an MAS frequency of 60 kHz. Asterisks denote spinning sidebands. Spectra were acquired using a depth sequence, and are the sum of 256 scans with a recycle delay of 0.5 s.

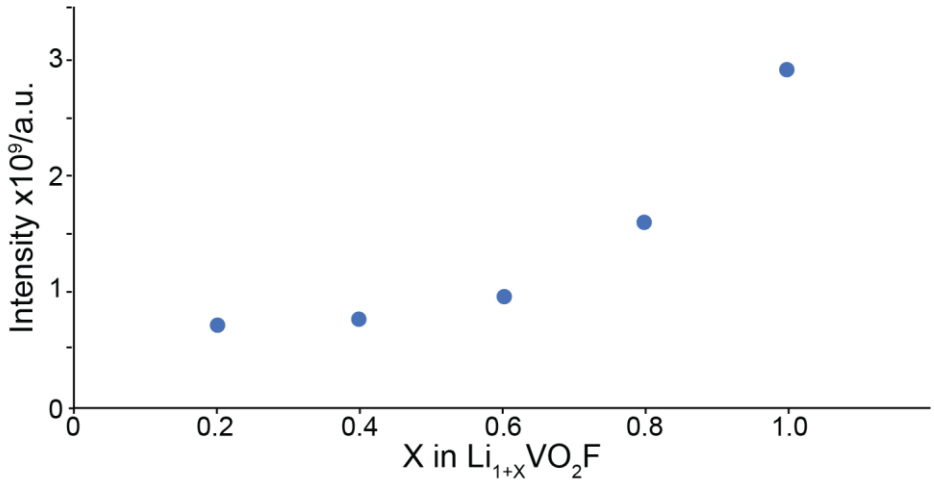

Figure 5.19: Relative total integrated intensities of the ^{19}F spectra for the LVOF series (Figure 5.19). Intensities are normalised to LVOF0.2.

As the amount of LiF in the reaction mixture increases, the normalised intensity of the ^{19}F signal increases. This would be expected to grow linearly, with the intensity of LVOF being roughly five times LVOF0.2. However, this is not the case, with the intensity being around 7×10^{8} for LVOF0.2, 0.4 and 0.6. After this the intensity roughly doubles to 1.5×10^{9} for LVOF0.8 before doubling again to around 3×10^{9}. This would suggest that signal is being

lost at low fluorine concentrations due to proximity to paramagnetic centres. After this the LiF is not being incorporated into the DRX material and so the intensity grows roughly linearly. This agrees with the data discussed for the LSOF series.

Another possible way to probe the structure of LVOF is to use ^{51}V NMR. This is likely complex due to the presence of paramagnetic V^{3+} ions.[273] Nevertheless, ^{51}V spectra have been reported for this material on two occasions, with the isotropic chemical shifts given as –546 and –566 ppm.[13,167] Therefore, ^{51}V spectra were collected for the LVOF series, and are shown in Figure 5.20. These were acquired using a Hahn echo sequence and are the sum of five individual spectra recorded at different offset frequencies. Whilst these could have been acquired using the pj-MATPASS sequence discussed in Chapter 3, the relatively poor signal meant that it was more time-efficient to acquire five 1D spectra with a greater number of scans, than a 2D spectrum.

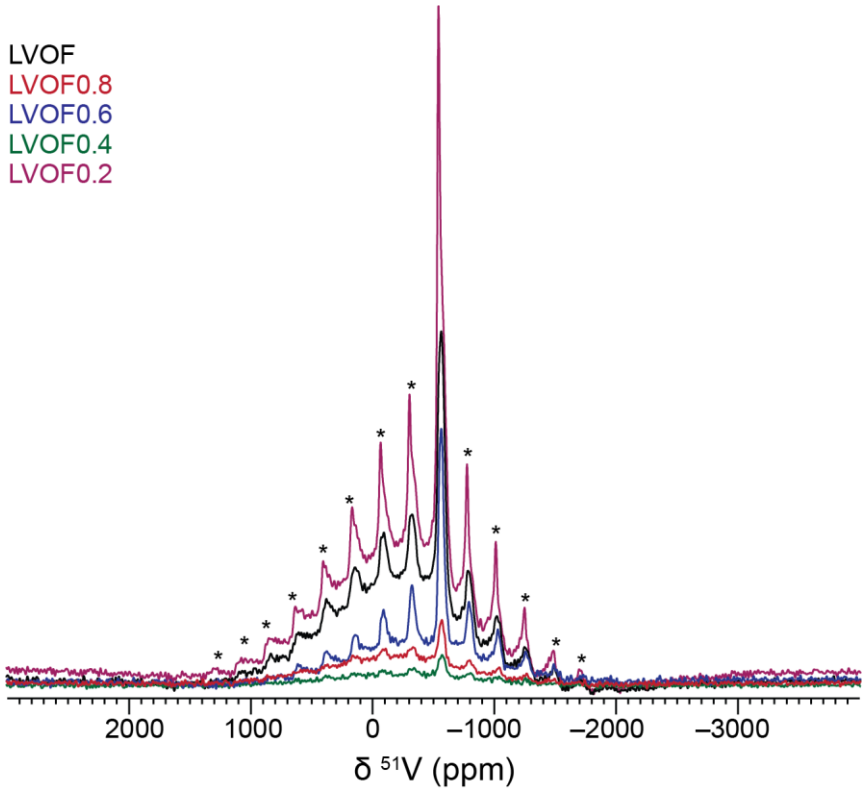

Figure 5.20: ^{51}V NMR frequency-stepped spectra recorded for the LVOF series. Spectra were acquired at 9.4 T, using a rotor-synchronised Hahn echo sequence (MAS frequency = 25 kHz). Spectra are the sum of five individual spectra, each the sum of 6400 scans separated by a recycle delay of 0.25 s.

The spectra in Figure 5.20 contain a peak at ~–550 ppm, with associated spinning sidebands, sat on top of a broad feature approximately 2000 ppm wide. The intensities of the peaks do not appear to follow a clear trend, with LVOF0.2 being most intense followed

by LVOF, LVOF0.6, LVOF0.8 and LVOF0.4. The ^{51}V spectra for LVOF from other works each show a single peak, with chemical shifts of –546 and –566 ppm being reported. In the context of ^{51}V NMR, this chemical shift difference is significant enough to indicate two different materials are being observed (as will be discussed further below). The sharp peak seen here is at –555 ppm but spans both chemical shifts, meaning that both phases are likely present in this sample. As mentioned already, the observation of a V^{3+} containing phase by NMR is unexpected. Both authors offer different explanations for this. Chen *et al* suggest that this comes from V^{4+} that they observe by EPR.[167] However, this seems unlikely as V^{4+} is also paramagnetic, hence it is EPR-observable. Whilst it can be possible to observe V^{4+} species, in such cases the peaks are often dramatically shifted away from the chemical shifts observed (*a*-VO_2: –4766 ppm, *β*-VO_2: 2113 ppm).[274,275] Chang *et al* offer an alternative explanation that V^{3+} trimers form, rendering the material diamagnetic, as demonstrated by magnetic measurements.[13] Similar behaviour has been reported to occur in $LiVO_2$, with the formation of trimers being demonstrated by PDF.[276] Whilst this could occur, the diamagnetic dimers formed in VO_2 still result in marked shifts in peak position as previously mentioned. Therefore, it seems likely that peaks from any V^{3+} trimers would also be shifted.

Ignoring for a moment the expected oxidation state of the material, the chemical shifts seen in the data presented here, and published in literature are close to the chemical shifts reported for Li_3VO_4 (–544 ppm) and $LiVO_3$ (–573 ppm).[178,277] This would imply the presence of lithiated and delithiated regions (Li_3VO_4 and $LiVO_3$, respectively). However, crucially, vanadium is in the +5 oxidation state in these materials. This agrees with literature precedent that suggests that lower oxidation states of vanadium are only visible under specific circumstances, such as in VO_2.[273] It is likely that such phases are only minor impurities as they do not clearly appear in the PXRD patterns recorded. This would potentially also explain why the intensities of the peaks do not appear to follow a clear trend. Whilst chemical shifts and established precedent suggest that the ^{51}V signal observed for LVOF can be attributed to V^{5+} phases, sample preparation occurs under inert atmosphere without a source of V^{5+}. Therefore, for this explanation to be true, V^{3+} would need to be oxidised. To investigate whether this is possible, V_2O_3 was milled using the same conditions used to prepare the LVOF series of materials. Figure 5.21 shows the PXRD pattern recorded for V_2O_3 milled under argon atmosphere, whilst Figure 5.22 compares the ^{51}V NMR spectra recorded for pristine V_2O_3 and V_2O_3 ball milled under argon atmosphere.

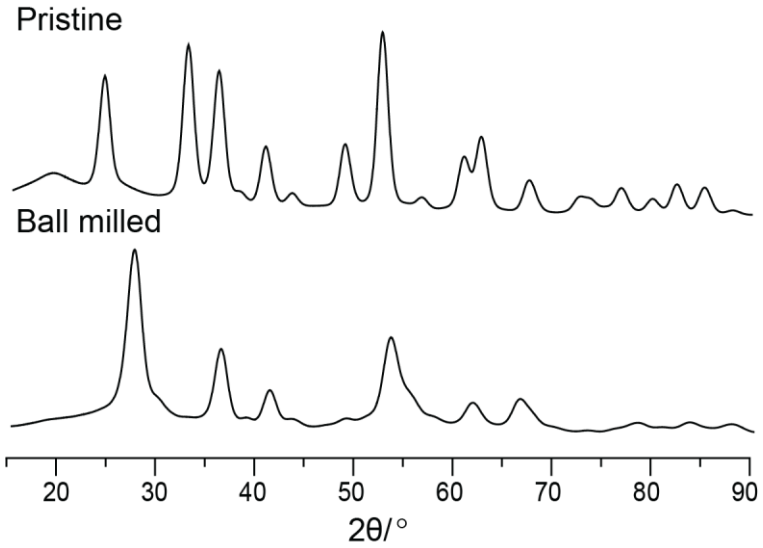

Figure 5.21: PXRD patterns for pristine V_2O_3 and V_2O_3 ball milled for 48 hours under argon. Patterns were acquired using the Supernova diffractometer.

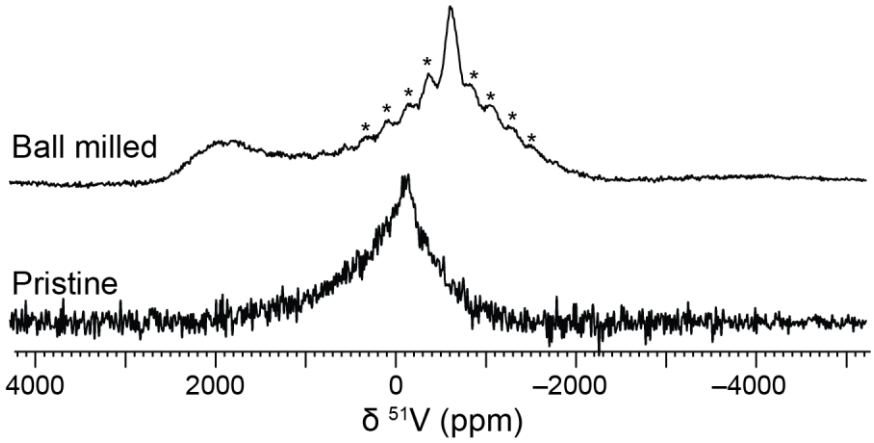

Figure 5.22: Frequency-stepped ^{51}V NMR spectra collected for pristine V_2O_3 and V_2O_3 ball milled under argon. Spectra were acquired at 9.4 T using a rotor-synchronised Hahn echo sequence (MAS frequency = 25 kHz). Spectra are the sum of eight individual spectra each the sum of 6400 scans separated by a recycle delay of 0.25 s.

The PXRD pattern for milled V_2O_3 shows peaks at 30, 38, 42, 54°. These match those expected for VO_2 meaning that in this situation the V^{3+} ions can be oxidised to at least V^{4+}. This is supported by the ^{51}V NMR spectrum recorded for ball milled sample, which has a broad peak at 2110 ppm, which can be attributed to the formation of β-VO_2. The ^{51}V NMR spectrum also shows a peak at –645 ppm. Based on its chemical shift this likely a V^{5+} species. This could either form directly by oxidation of V^{3+} species (like VO_2) or by disproportionation of VO_2.

As mentioned already, the impurity phase(s) observed by ^{51}V NMR for LVOF are likely minor phases as they are not discernible in the PXRD patterns. However, the fact that they cannot be attributable to the DRX itself, means that ^{51}V NMR is likely not a useful tool for characterising the pristine materials. However, it could still be used at high voltages to characterise V^{5+} phases that form on charging.

5.3.2.3. Electrochemical changes in Li_2TiO_2F

LVOF and LTOF possess redox-active transition metal ions and so it is possible to explore the structural changes that occur in the materials on cycling. Therefore, electrodes were prepared for both materials, which were then studied at different states of charge. This discussion will first focus on LTOF, before moving back to LVOF.

Whilst LTOF has been synthesised in previous works, its performance as an electrode material has not been tested. Therefore, it is first necessary to establish an appropriate potential window and cycling protocol for testing the cells.

In LTOF, the titanium ions are Ti^{3+}, if the stoichiometry of the ball milled product is correct. It should therefore be possible to extract lithium ions from this material, by oxidising Ti^{3+} ions to Ti^{4+}. This would be expected to occur around 1.55 V (vs Li/Li^+), based on the behaviour of lithium titanate.[22] On this basis, for the initial exploratory cycling of LTOF, it was decided that (a) the first step should be a charging step and (b) an appropriate lower cutoff voltage would be around 1 V (to allow reduction of Ti^{4+} back to Ti^{3+}). 4.6 V was then chosen as the upper cutoff voltage. Whilst this exceeds the potentials that would be expected for titanium redox, it means that any unexpected processes, such as O-redox can be observed. Figure 5.23 shows the performance of LTOF cycled in this way for two cycles.

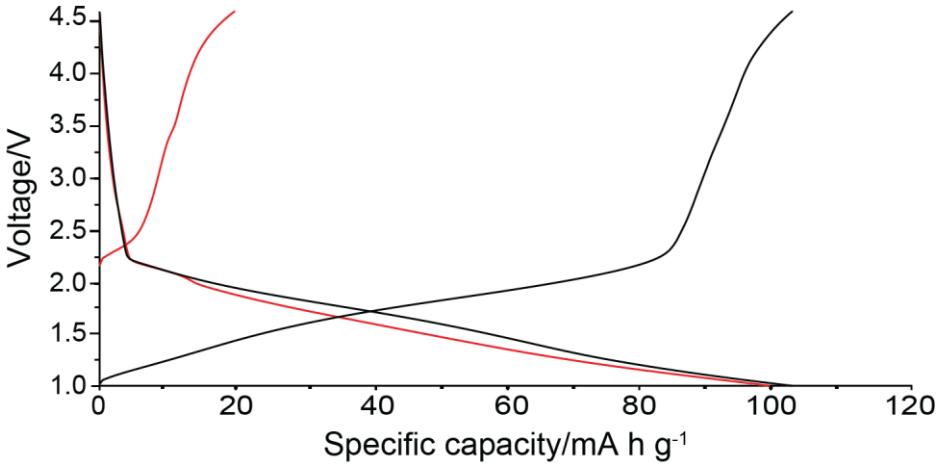

Figure 5.23: The first (red) and second (black) cycles of LTOF. Cycled at C/20 (11.85 mA g^{-1}) between 1 and 4.6 V.

On charging from open circuit voltage to 4.6 V, a capacity of 20 mA h g^{-1}, less than 10% of the theoretical capacity (237 mA h g^{-1}). Discharging from 4.6 V down to 1 V achieves a capacity of around 100 mA h g^{-1}. This is then observed for the second charge and discharge step.

The fact that a larger capacity is observed when discharging the cell (compared to the initial charge), means that more lithium ions are inserted into the electrode than are initially extracted. If it is assumed that the LTOF in the electrode is Li_2TiO_2F, this would mean that some Ti^{3+} ions are being reduced to Ti^{2+}, to accommodate the additional positive charge of the lithium ions. However, the work in the previous sections suggests that transition metal ions are oxidised during the prolonged milling process. Therefore, another explanation for the increased capacity is that during the first discharge, the titanium ions oxidised during synthesis (to Ti^{4+}) can be reduced to Ti^{3+}, allowing greater insertion of lithium ions.

Whilst a reasonable starting point, the capacity achieved when discharging down to 1 V is less than half of the theoretical capacity. Therefore, for the next series of cells, the cycling protocol was revised. First, negligible capacity is observed above 3 V, so this was chosen as the new upper cutoff voltage. Second, the lower cutoff voltage was decreased to 0.5 V, to see if this enables access to greater capacity. Finally, it was decided to discharge the material first, operating under the assumption that the redox activity comes from Ti^{4+} ions introduced during the synthesis (since minimal capacity was observed when charging first).

Figure 5.24 shows the electrochemistry for three cells, disassembled after the first discharge (to 0.5 V), the first charge (to 3 V) and the fifth discharge.

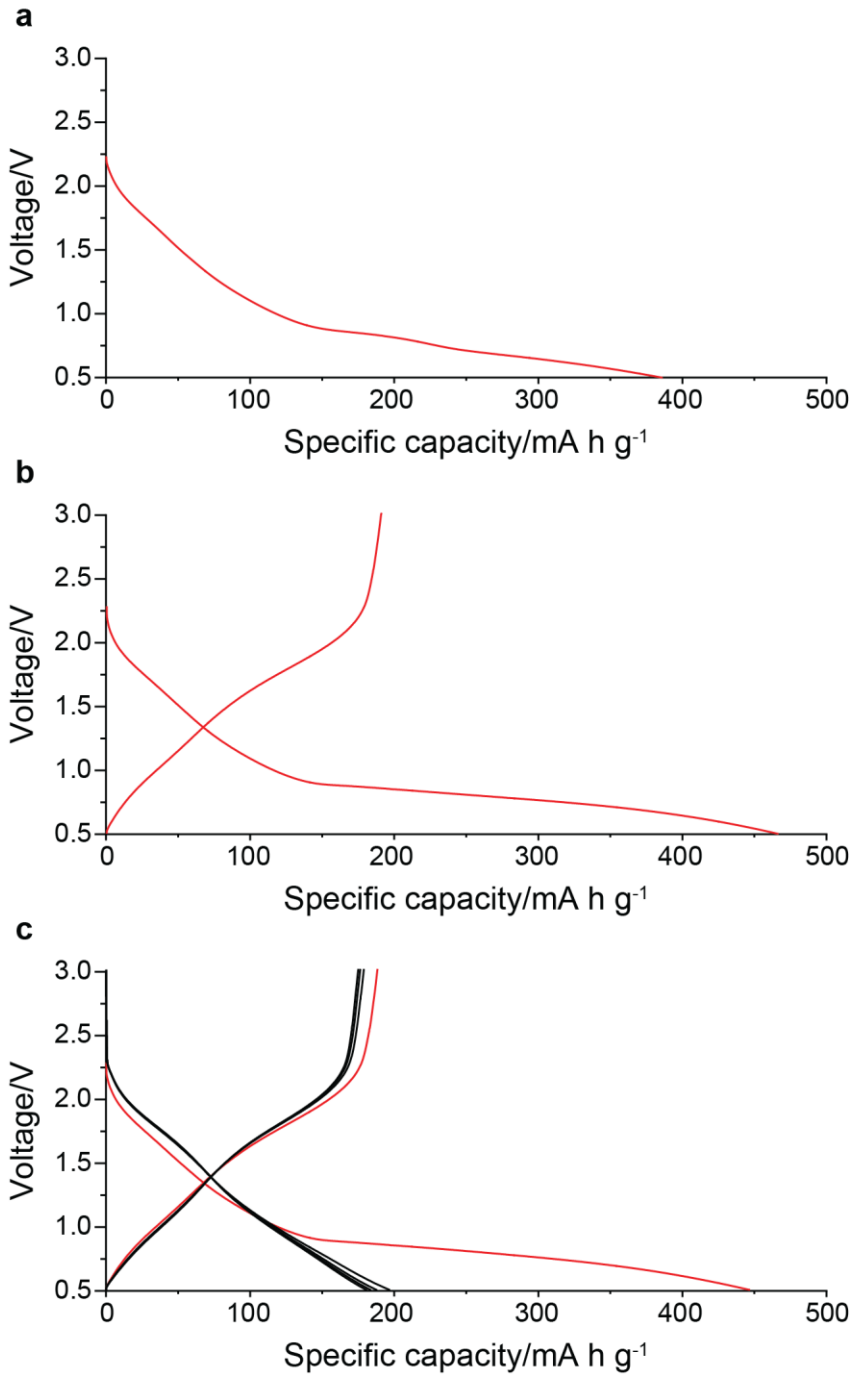

Figure 5.24: Galvanostatic charge-discharge plots for LTOF for (a) the first discharge, (b) the first cycle and (c) the first five cycles. Red lines indicate the first cycle, black line the subsequent cycles. Cells were cycled at C/20 (11.85 mA h g^{-1}) between 0.5 and 3 V.

At the end of the first discharge, the three cells achieve capacities of between 370 and 450 mA h g^{-1}, exceeding the theoretical capacity. The first charge then achieves a capacity

of ~ 200 mA h g^{-1}. Very similar charge capacities are observed for the next four cycles, indicating that this process is highly reversible.

One of the challenges of DRX materials is that they suffer from poor long-term cycling performance (as discussed in Chapter 2). Such highly reversible behaviour without any material optimisation is therefore interesting. However, the presence of significant additional capacity suggests that something else is happening when the electrodes are taken to low voltages. To explore this, a new cell was made using an electrode comprised of only carbon black and PTFE. This was then cycled in the same potential window at a current of 9.41 mA g^{-1} (due to an error 11.9 mA g^{-1} was not used). Figure 5.25 shows the electrochemical performance for the first cycle of this cell.

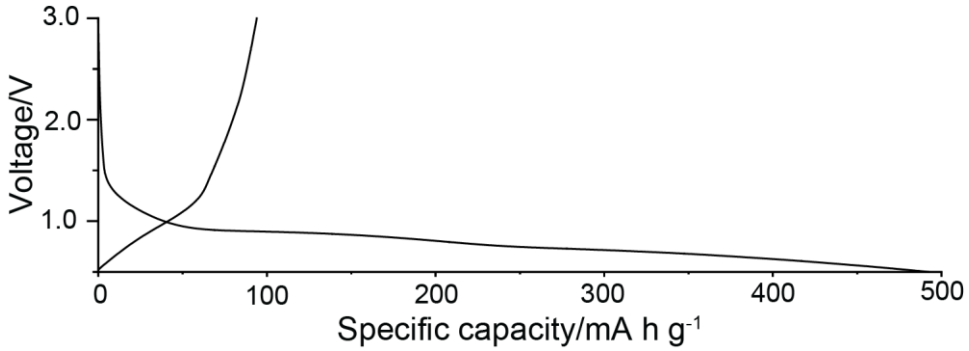

Figure 5.25: electrochemical profile for the first cycle of the carbon black/PTFE electrodes cycled at 9.41 mA g^{-1} between 0.5 and 3 V.

Figure 5.25 shows that when the cell is discharged a capacity of almost 500 mA h g^{-1} is achieved during the first discharge. This is likely due to the carbon black as it is known to exhibit capacity when cycled below 1.5 V.[278] In light of this, it would appear that carbon black can account for most/all of the capacity observed during the first discharge. Then during the first charge, a capacity of 90 mA h g^{-1}. This is lower than what was observed for the LTOF electrodes (~ 200 mA h g^{-1}), meaning that LTOF likely does contribute during this step. With some understanding of the electrochemical behaviour, it is then possible to begin to explore the changes that may occur during cycling. First, PXRD patterns were recorded for the LTOF cells disassembled. These are shown in Figure 5.26.

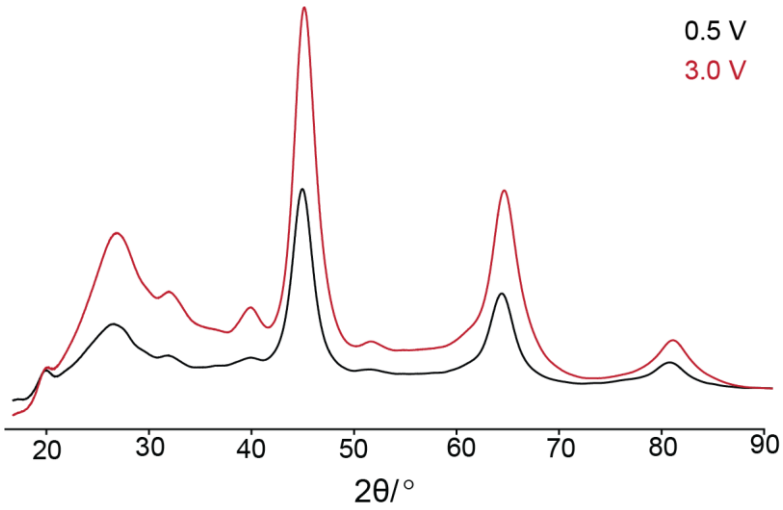

Figure 5.26: PXRD patterns recorded for LTOF after the first discharge to 0.5 V (black) and the first charge to 3 V (red). Patterns were acquired using the Supernova diffractometer.

Both patterns show peaks at 37, 44, 64 and 81° indicating the DRX phase is retained throughout cycling. The peaks at 18 and 25° can be attributed to the PTFE binder and carbon black, respectively.

Figure 5.27 shows the single pulse ^{7}Li NMR spectra recorded for the cycled LTOF electrodes. Table 5.6 contains the absolute integrated intensity of the spectra, and the intensity normalised to the intensity of the pristine spectrum.

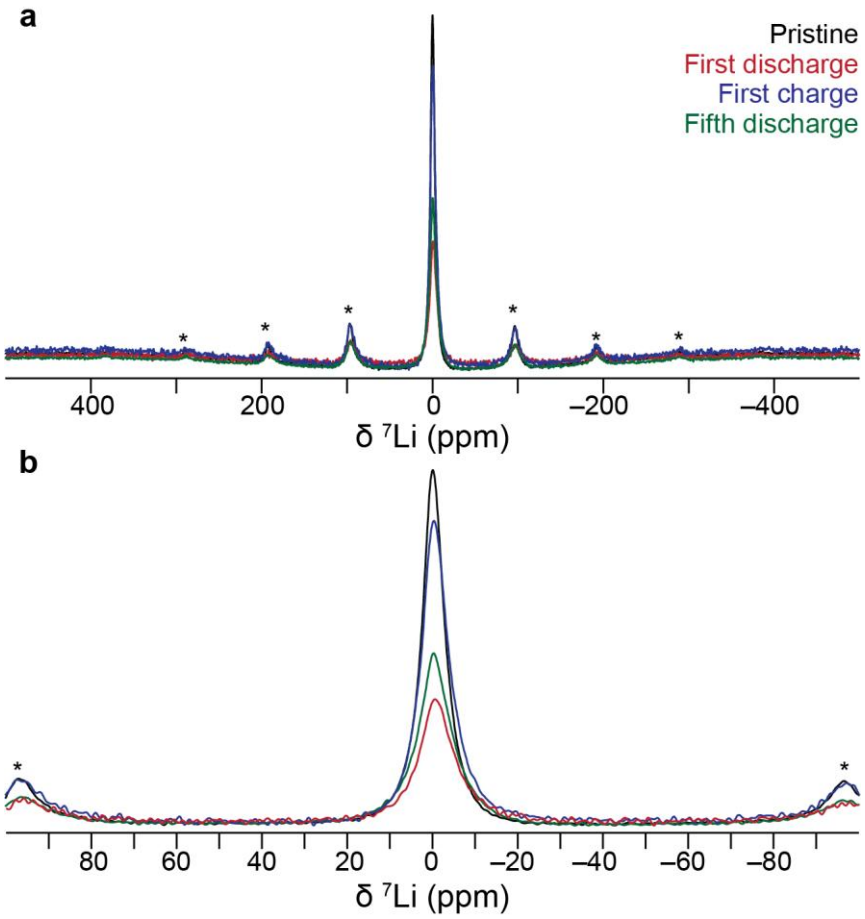

Figure 5.27: ^{7}Li NMR spectra recorded for the LTOF electrodes at different states of charge. (a) shows the full spectral width, whilst (b) shows the region around the isotropic peak. Asterisks denote spinning sidebands. Spectra were acquired using a single pulse experiment at 9.4 T and 15 kHz MAS. Spectra are the sum of 16 scans separated by a recycle delay of 60 s.

Table 5.6: The absolute intensities of the ^{7}Li spectra acquired at different states of charge, as well as the relative intensities, normalised to the pristine electrode. Intensities were measured using TopSpin 4.5.0.

Sample	Absolute intensity (single pulse)	Relative intensity
Pristine	58950000	1
0.5 V (1st discharge)	33580000	0.5696
3 V (1st charge)	66940000	1.136
0.5 V (5th discharge)	45500000	0.7717

When the electrode is discharged to 0.5 V, the intensity of the peak decreases compared to the pristine electrode. On charging to 3 V, the intensity increases again to slightly more than the intensity of the pristine. The intensity then reduces again after the fifth discharge.

During discharging the amount of lithium in the sample should increase, due to lithium intercalation as well as SEI formation on the electrode surface. The fact it decreases suggests that the sample becomes more paramagnetic, resulting in greater paramagnetic relaxation enhancement. This is consistent with the oxidation state of titanium being lowered as more lithium ions enter the structure. As already mentioned, there are likely Ti^{4+} ions present in the sample, introduced during the synthesis. During discharging these could be being reduced to Ti^{3+}, increasing the paramagnetism of the sample. Another source of paramagnetism on discharging could be the PTFE binder. Whilst in a separate phase, PTFE decomposes at low voltages (as will be discussed more in Chapter 6), introducing radicals into the electrode.

The ^{19}F NMR spectra recorded for the LTOF samples are shown in Figure 5.28.

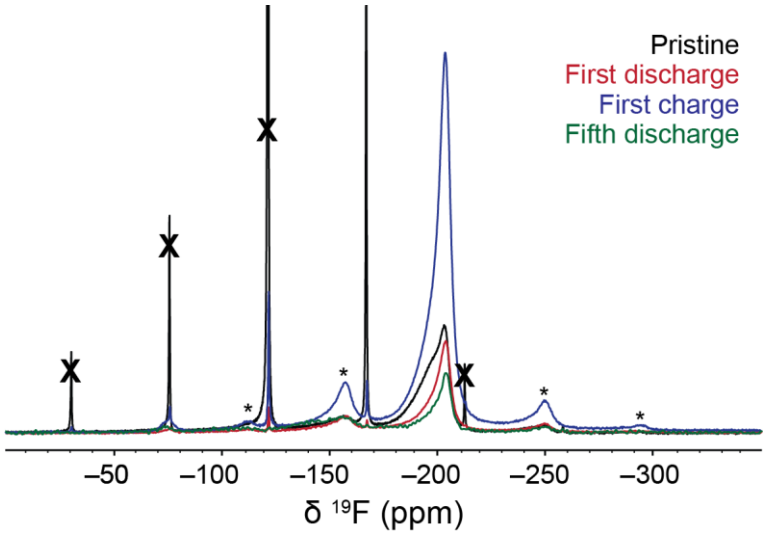

Figure 5.28: ^{19}F NMR spectra recorded for LTOF at different states of charge, acquired at 16.4 T and an MAS frequency of 30 kHz. Asterisks denote spinning sidebands, whilst crosses denote peaks from the PTFE binder. Spectra were acquired using a depth sequence, and are the sum of 1024 scans with a recycle delay of 0.25 s.

When the material is discharged, the intensity of the DRX peaks in the ^{19}F spectrum decreases. This is in line with the ^{7}Li data discussed previously (Figure 5.27) and can be rationalised by the increased paramagnetic relaxation enhancement arising due to the lower oxidation state of titanium. In particular, the peak at –195 ppm is noticeably suppressed, which would suggest that this environment is closer to paramagnetic centres or that there are more such centres nearby. This fits with the assignment of this peak coming from a distorted FLi_6 site, since titanium ions are smaller than lithium ions, and so they likely distort the structure around them.

After charging the electrode, the intensity of the signal increases to more than that seen for the pristine material. This means that the titanium is likely in a higher average oxidation state than in the pristine material. It could also mean that there is some structural rearrangement, moving fluoride ions away from paramagnetic titanium ions. Such changes are likely only minor, as the PXRD data shows that the rocksalt structure is retained. The signal may also partially originate from LiF in the SEI on the electrode surface. However, this would result in increased signal for the discharged sample as well, since surface LiF should be less affected by changes in the transition metal oxidation state. The intensity then decreases again for the fifth discharge, which follows what was observed for the first discharge.

The ^{19}F spectrum for the pristine material also contains a sharp peak at –122 ppm, with associated spinning sidebands. This can be assigned to the PTFE binder. After discharging, the intensity is noticeably reduced, indicating that the PTFE reacts in some way. As already mentioned, this could be due to the formation of radicals, resulting in the signal being suppressed due to an increase nuclear relaxation rate.

5.3.2.4. Electrochemical changes in Li_2VO_2F

The relatively low redox potential of the oxidation of Ti^{3+} to Ti^{4+} means that the carbon black and PTFE contribute to the observed electrochemical behaviour. Vanadium redox however typically occurs at potentials over 3 V (vs Li/Li^+).[273,279] This means that LVOF electrodes are perhaps a simpler system in which to study DRX cycling behaviour.

Unlike LTOF, the electrochemistry of LVOF has been documented previously, meaning that there is already information on what potential windows can be used.[13,167] Therefore, the first cell was cycled five times between 1.3 and 4.1 V. As the pristine material should contain extractable lithium ions, cells were first charged, then discharged. Figure 5.29 shows the galvanostatic cycling data for this cell.

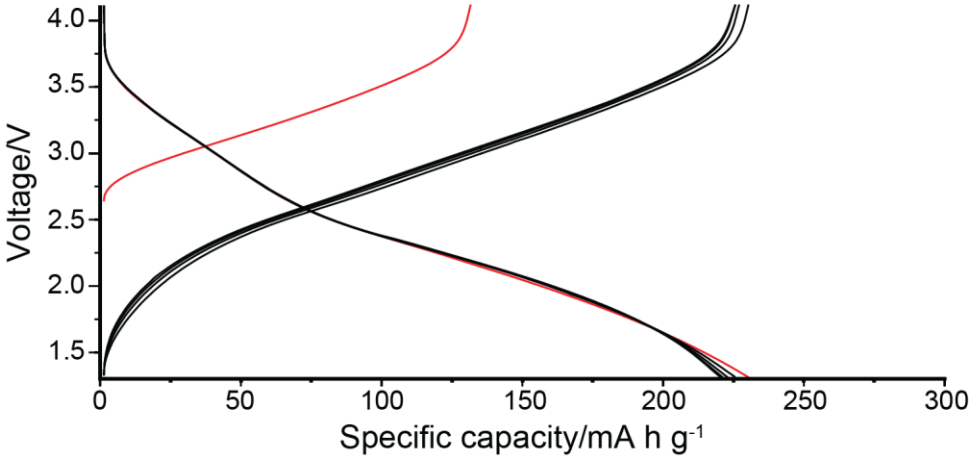

Figure 5.29: Galvanostatic charge-discharge plot for the first five cycles of LVOF, cycled at C/20 (23.1 mA g^{-1}) between 1.3 and 4.1 V. Red lines denote the first cycle.

During the first cycle, a charging capacity of 130 mA h g^{-1} is achieved followed by a discharge capacity of 225 mA h g^{-1}. This capacity is retained on the subsequent cycling steps. The increase in capacity of around 100 mA h g^{-1} agrees with previous work looking at LVOF and is also observed for other oxyfluoride materials. One possibility for why this occurs is the previously discussed oxidation of the precursors during synthesis. Having vanadium in higher oxidation states means that fewer electrons can be transferred and hence less lithium extracted. However, these ions can be reduced, allowing more lithium to be inserted during the discharge step.

It is important to say however that even with this increase in capacity, the capacity falls short of the theoretical capacity of 460 mA h g^{-1}. This is probably because the sample is impure, containing unreacted V_2O_3 and ZrO_2. These do not contribute to the material's capacity and therefore are "dead weight", reducing the capacity. However, previous works also fail to achieve full capacity for this material.[13,167]

To further explore the structural changes during these first five cycles, three additional cells were prepared and disassembled at different states of charge. Specifically, after the first and second charging steps as well as at 2 V during the first discharge. This is because at this point the amount of lithium in the structure should be the same as the pristine material, and so the structures may be expected to be the same. The electrochemical data associated with these cells is shown in Figure 5.30.

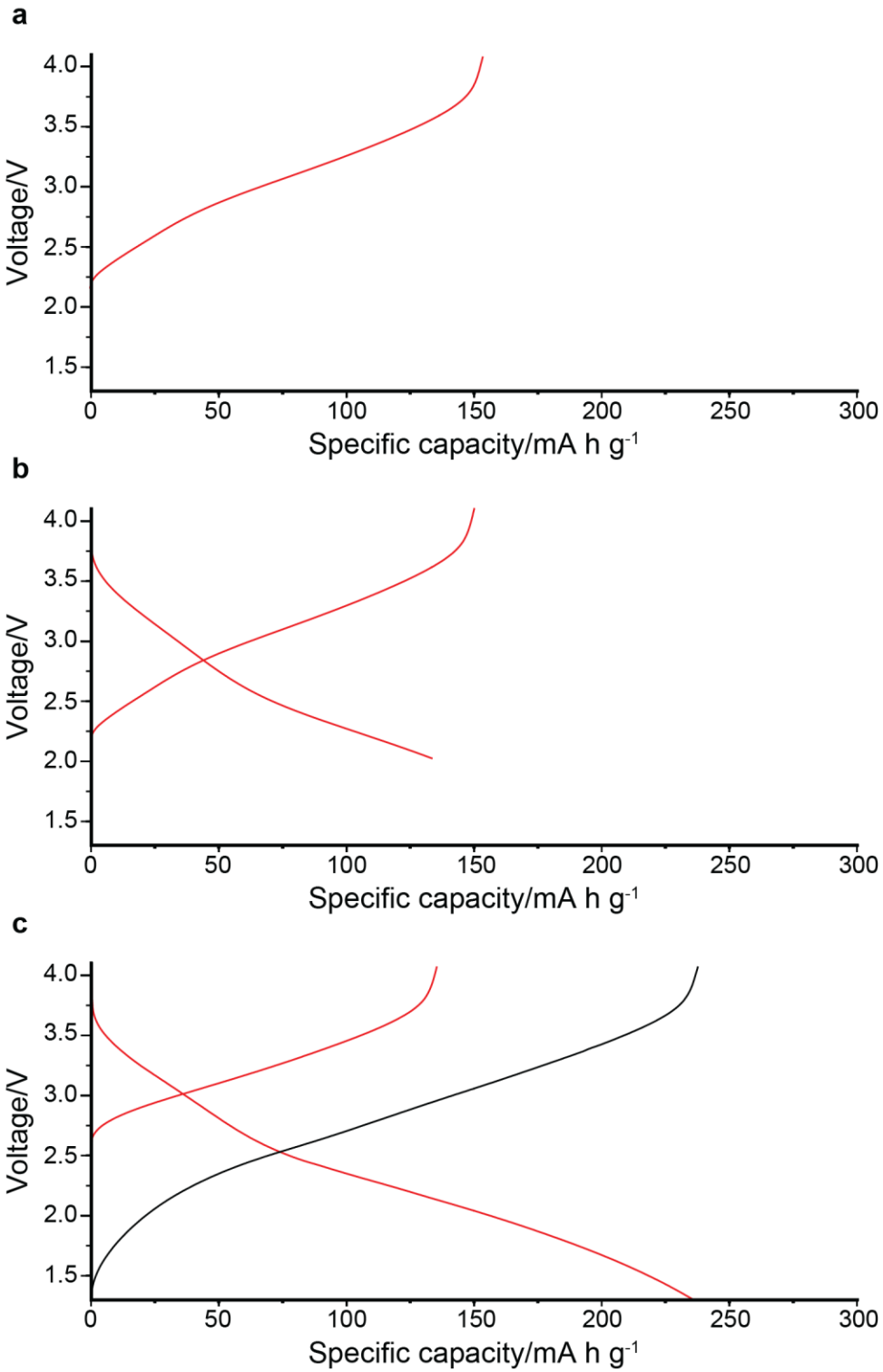

Figure 5.30: Galvanostatic charge-discharge plots for LVOF for (a) the first charge, (b) the discharge to 2 V and (c) the second charge. Red lines indicate the first cycle, black lines the subsequent cycles. Cells were cycled at C/20 (23.1 mA g^{-1}) between 1.3 and 4.1 V unless otherwise stated.

All three cells show a first charge capacity of between 130 – 150 mA h g^{-1}. This is equivalent to the extraction of 0.5 – 0.65 lithium ions, per formula unit (*i.e.*, $Li_{\sim 1.5}VO_2F$).

Discharging to 1.3 V yields a capacity of 210 mA h g^{-1}. This means that there are 0.39 additional lithium ions inserted per formula unit ($Li_{2.4}VO_2F$). Charging to 4.1 V for the second charge results in a capacity of 215 mA h g^{-1}, returning the material to the same lithiation level as the first charge (~ 0.5 lithium ions deintercalated relative to a pristine electrode).

Figure 5.31 shows the PXRD patterns collected for the four samples.

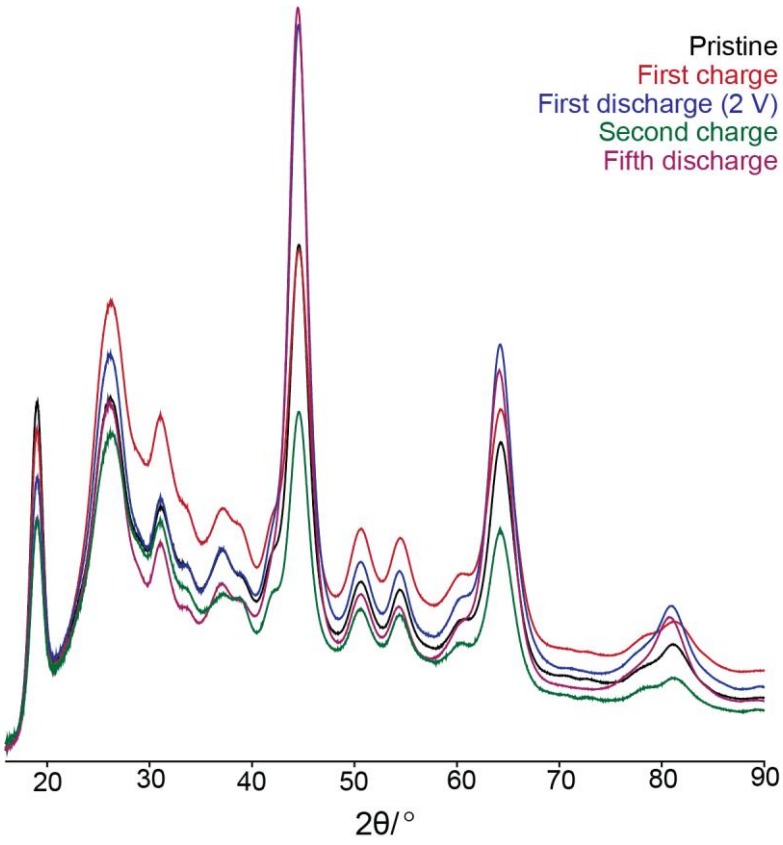

Figure 5.31: PXRD patterns recorded for LVOF at different states of charge. Patterns were acquired using the Supernova diffractometer.

As with LTOF, the intensities of the peaks change throughout cycling. However, the positions remain unchanged, indicating that the rocksalt phase is retained throughout cycling.

Figure 5.32 shows the ^7Li spectra collected for the pristine material and electrodes at the different states of charge previously discussed. Table 5.7 also shows the intensities of the spectra.

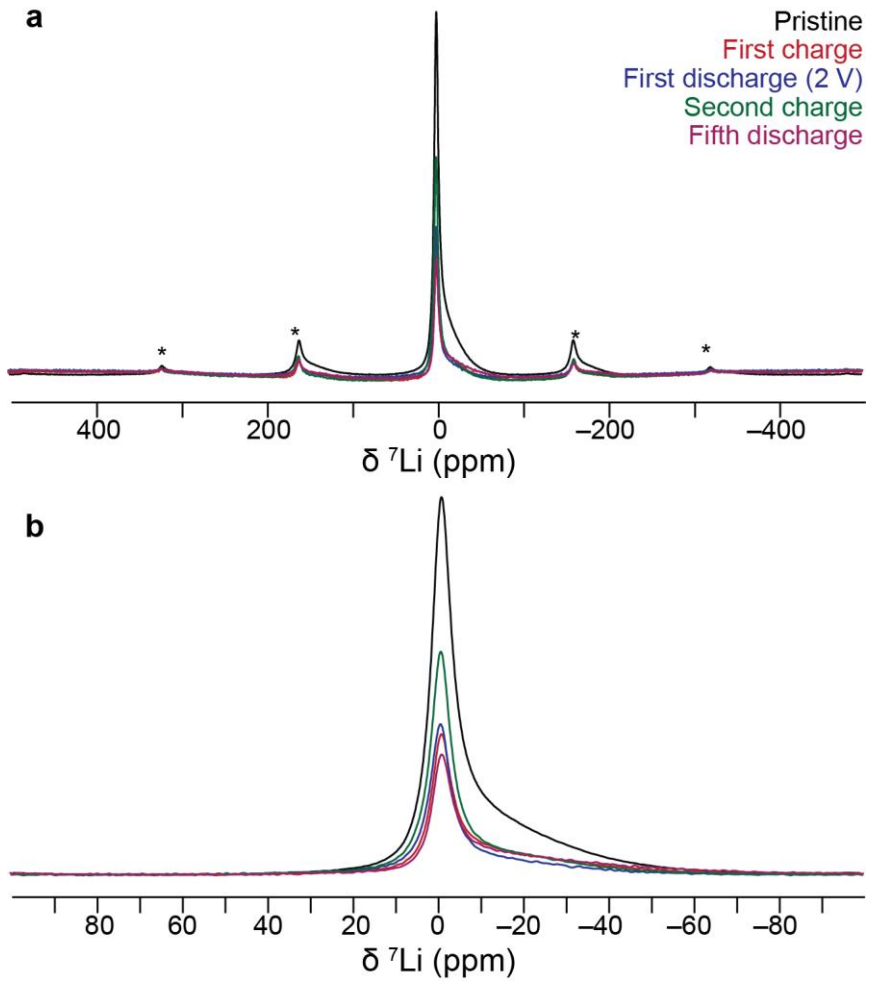

Figure 5.32: ^{7}Li NMR spectra recorded for the LVOF electrodes at different states of charge. (a) shows the full spectral width, whilst (b) shows the region around the isotropic peak. Asterisks denote spinning sidebands. Spectra were acquired using a single pulse experiment at 9.4 T and 25 kHz MAS. Spectra are the sum of 1024 scans separated by a recycle delay of 0.5 s.

Table 5.7: The absolute intensities of the ^{7}Li spectra acquired at different states of charge, as well as the relative intensities, normalised to the pristine electrode. Intensities were measured using TopSpin 4.5.0.

Sample	Relative intensity
Pristine	1
4.1 V	0.3937
2 V	0.1416
2nd charge 1.3 ->4.1V	0.2560
5th discharge 1.3->4.1V	0.2036

The ^{7}Li spectrum for the pristine electrode shows a peak at –1 ppm, which can be attributed to LiF or LiF-like environments. There is also a broad shoulder to the right

which likely comes from lithium ions near to V^{3+} ions. These ions experience a shift away from the normal diamagnetic range of ^{7}Li due to the Fermi contact interaction. A negative shift indicates an increase in electron density at the observed nucleus, and so this can be suggested to be lithium in a Li-O-V environment, where the bond angle is 180°.[280] It should be said however that other environments may be present, but the signal for these sites is lost during the deadtime.

On charging to 4.1 V, the intensity drops to 40% of the intensity of the pristine electrode. This is expected to a degree, as lithium ions are extracted from the structure. However, the specific capacity suggests that around a quarter of the lithium ions are removed from the structure (assuming perfect stoichiometry). The fact that a more significant proportion of the signal is lost means that not all the lithium ions are observed in the pristine material. Instead, the spectrum for the pristine material likely only shows a proportion of lithium ions that are present in regions where there are relatively few vanadium ions. This could explain why the spectrum only contains evidence of a 180° Li-O-V site, despite a rocksalt structure implying that 90° Li-O-V sites should also exist. 90° sites mean that the vanadium and lithium ions are closer together, meaning that the lithium ions likely relax much faster than those in 180° sites.

On discharging to 2 V, the intensity further decreases which can be attributed to increased relaxation because of the decreased vanadium oxidation state. This is even though the lithiation level, and by extension the vanadium oxidation state, should be roughly equivalent to the pristine material. One explanation for this is that the lithium ions do not have the same distribution within the DRX structure when they are reinserted. The reduction in signal intensity would suggest that the lithium ions are closer to the vanadium paramagnetic centres, rather than favouring lithium-rich regions as might be found in the pristine DRX.[1,2,32]

The fifth discharge also shows lower intensity than the pristine material. This would be expected based on the results obtained for the LTOF series, owing to the reduction in transition metal oxidation state.

After the second charge, the intensity increases slightly relative to the discharged states, due to the increased vanadium oxidation state, but remains slightly lower than the first charge.

Figure 5.33 shows the ^{19}F NMR spectra recorded for the cycled electrodes.

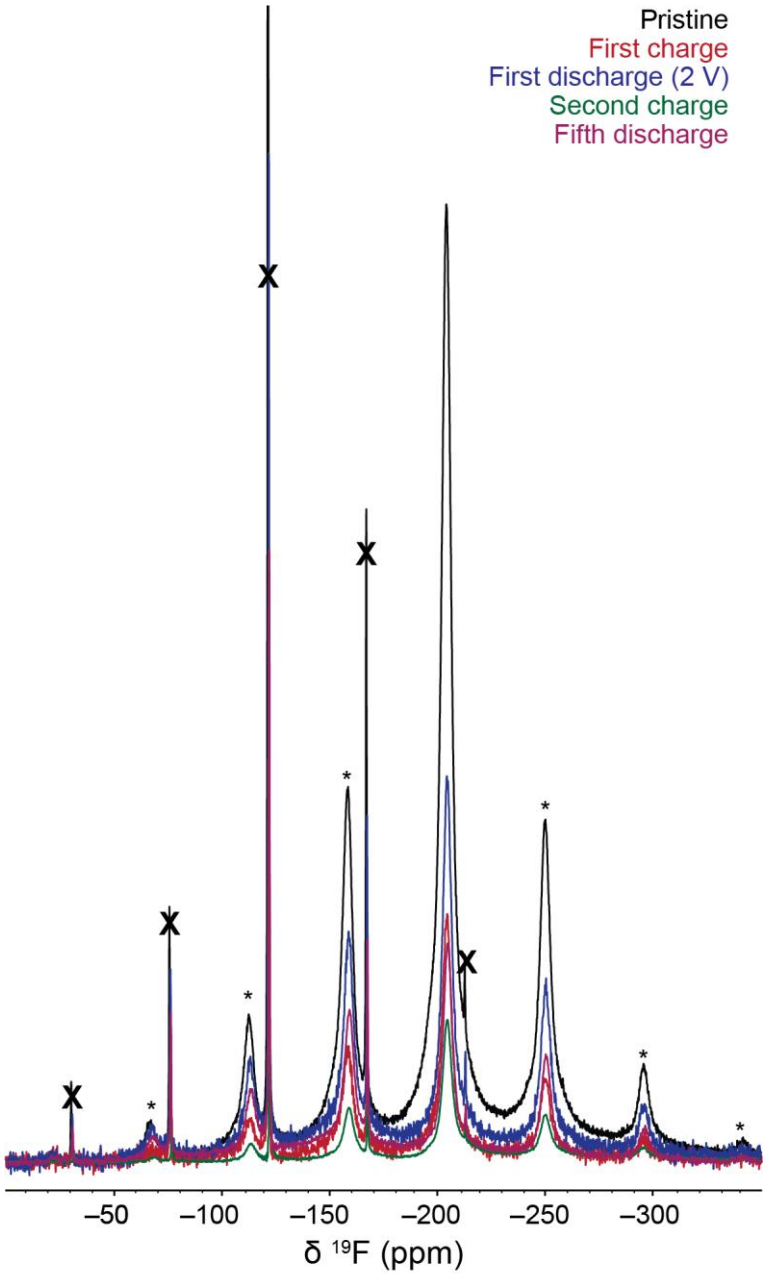

Figure 5.33: ^{19}F NMR spectra recorded for LVOF at different states of charge, acquired at 16.4 T and an MAS frequency of 30 kHz. Asterisks denote spinning sidebands, whilst crosses denote peaks from the PTFE binder. Spectra were acquired using a depth sequence, and are the sum of 1024 scans with a recycle delay of 0.25 s.

All the spectra show a peak at –204 ppm, as well as a peak at –122 ppm (attributed to the PTFE binder). When the material is charged to 4.1 V, the intensity of the peak at –204 ppm decreases (relative to the pristine electrode) but increases again after discharging to 2 V. The second charge to 4.1 V shows reduced intensity compared to the first. Then after the fifth discharge, the intensity returns to a similar level as observed on the first charge. These

changes in intensity are likely the result of the vanadium ions changing oxidation state, and hence their electronic relaxation properties. This would support the idea that the LiF-like environments that give rise to this peak are part of the DRX phase, so that they experience a paramagnetic relaxation enhancement.

Charging the material should oxidise the vanadium ions towards V^{5+}, making ^{51}V NMR viable. Therefore, ^{51}V spectra were recorded for the pristine electrode and the two charged states. These are shown in Figure 5.34.

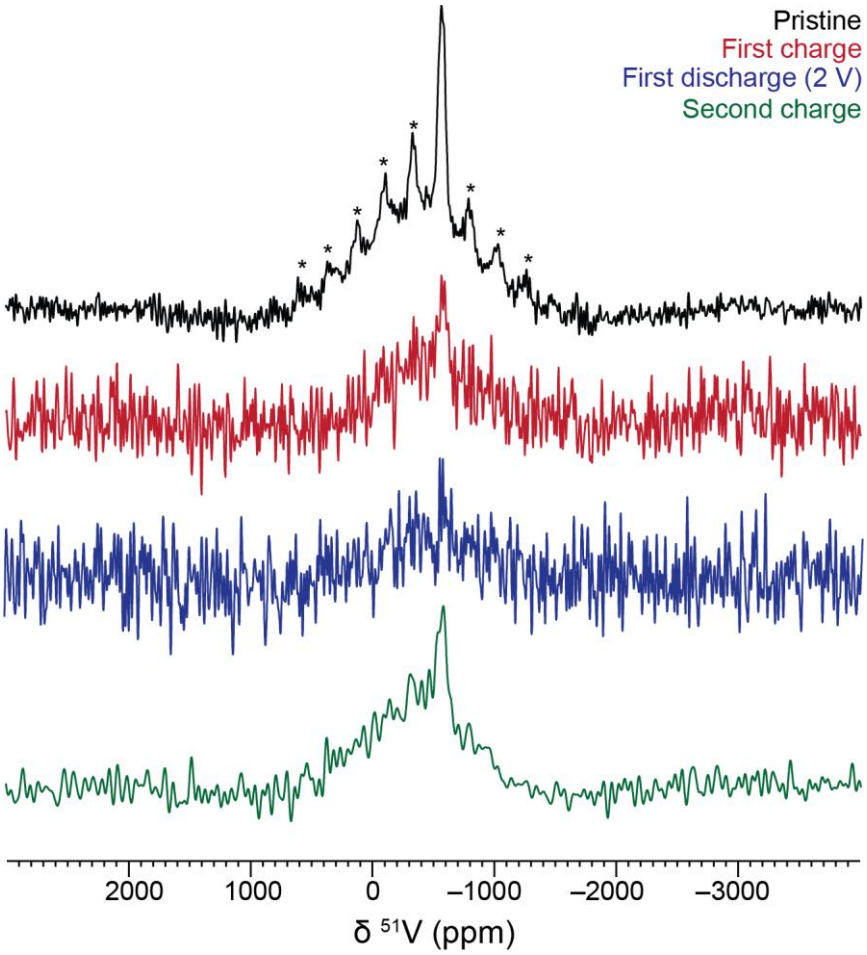

Figure 5.34: ^{51}V NMR spectra recorded for LVOF at different states of charge, acquired at 9.4 T and an MAS frequency of 25 kHz. Asterisks denote spinning sidebands. Spectra were acquired using a rotor-synchronised Hahn echo sequence and are the sum of 10240 (first charge/discharge) or 20480 scans (pristine/second charge) with a recycle delay of 0.25 s. Spectra are mass normalised but have been separated due to the poor signal-to-noise of the spectra.

All four spectra show a peak at –570 ppm. However, the intensity of the peaks for all the cycled samples is lower than for the pristine material, indicating fewer visible V^{5+} ions. Charging should result in more V^{5+} ions and so the reduced intensity observed is likely due

to increased paramagnetic relaxation enhancement, possibly due to a greater presence of V^{4+} ions in the vicinity of the V^{5+} ions that are formed upon charging.

To investigate the long-term structural changes a sample was prepared by cycling a cell 50 times. The galvanostatic charge-discharge plot for this cell is shown in Figure 5.35.

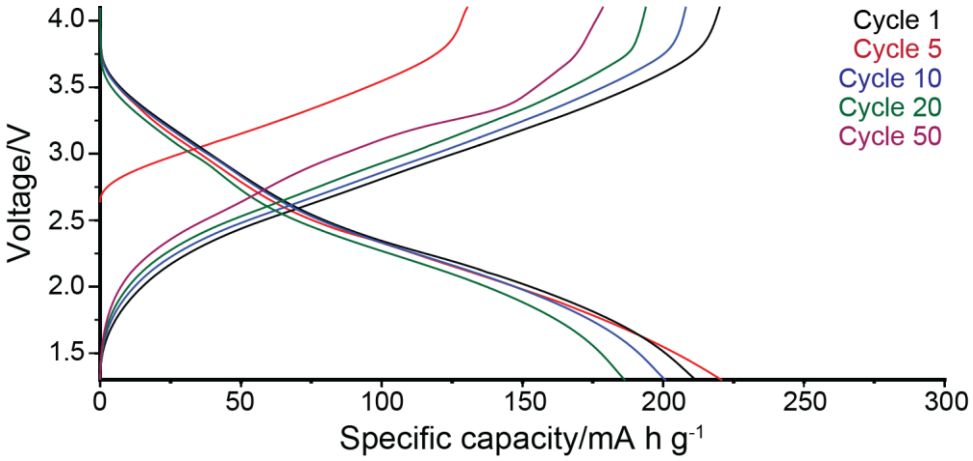

Figure 5.35: Galvanostatic charge-discharge plots for LVOF cyled 50 times. Cells were cycled at C/20 (23.1 mA g^{-1}) between 1.3 and 4.1 V.

From Figure 5.35 after the initial increase in capacity after the first cycle, the capacity decreases with increasing cycle number, with a capacity of around 125 mA h g^{-1} being observed on the 50th charge, compared to around 200 mA h g^{-1} on the fifth charge. This is not surprising and suggests that the insertion and removal of lithium ions is not perfectly reversible. Looking further shows that, aside from for the first cycle, the charging step has a higher capacity than the discharging step. This means that with each cycle, more lithium is extracted from the structure but is not reinserted. After the 50th charge, around 2.5 lithium ions (per formula unit) have been removed from the structure. This means that all the lithium ions, including the extra ions inserted during the first discharge have been removed from the structure. However, this number should not necessarily be treated as an accurate representation of the number of ions removed. This is because the mass used to normalise the capacity will be larger than the mass of the active material, due to the "dead weight" coming from the impurities identified in the pristine material.

Figure 5.36 shows the PXRD pattern for this sample, as well as the previously shown patterns for the pristine material, first charge and second charge.

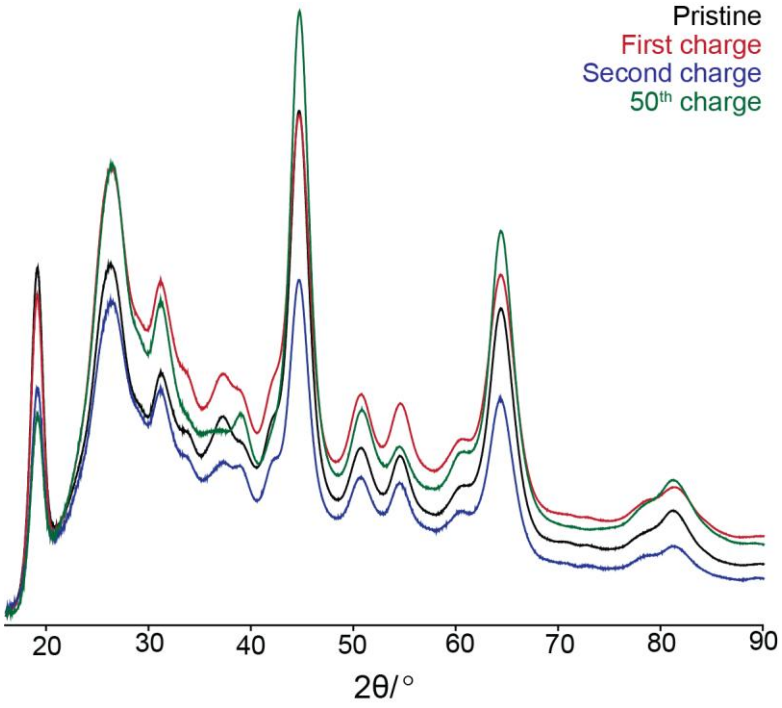

Figure 5.36: PXRD patterns recorded for LVOF at different states of charge, including the 50th charge. Patterns were acquired using the Supernova diffractometer.

The PXRD pattern for the sample prepared after the 50th charge still shows the peaks associated with the rocksalt phase at 44 and 64°. This means that despite the loss of capacity, the rocksalt phase is retained.

Figure 5.37 shows the ^{7}Li spectra recorded for the sample prepared after 50 cycles as well as the pristine material and the first charge sample.

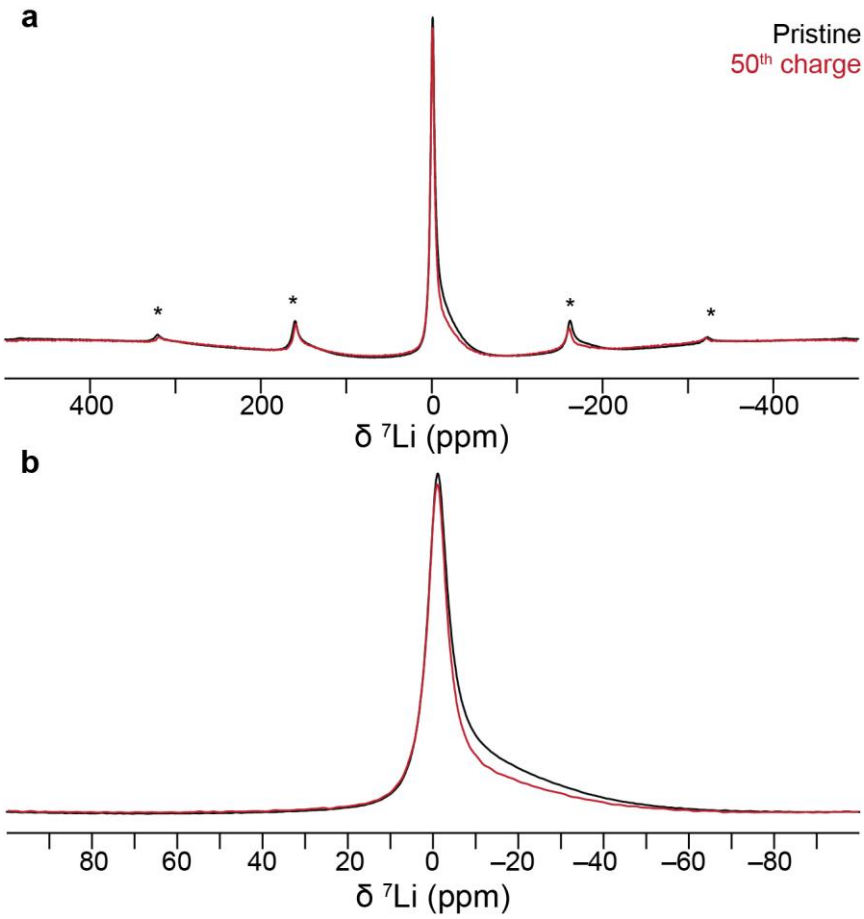

Figure 5.37: ^{7}Li NMR spectra recorded for LVOF after the 50th charge (red) as well as the previously shown spectrum for the pristine material (black). (a) shows the full spectral width, whilst (b) shows the region around the isotropic peak. Asterisks denote spinning sidebands. Spectra were acquired using a single pulse experiment at 9.4 T and 25 kHz MAS. Spectra are the sum of 1024 scans separated by a recycle delay of 0.5 s.

The spectrum recorded for the 50th charge sample contains a peak at –1 ppm and a broad shoulder to the right. The intensity of the peak is the same as for the pristine material, which means that on repeated cycling, the amount of this environment has increased, or the number of paramagnetic vanadium ions nearby has decreased, compared to the first charge. Meanwhile, the intensity of the shoulder is reduced slightly. As the negative shift is caused by the presence of paramagnetic ions nearby, a reduction in this environment would also suggest reduced paramagnetic ions. However, this could alternatively be due to enhanced relaxation, due to a change in the relaxation properties of the ions.

Figure 5.38 shows the ^{19}F spectrum recorded after the 50th charge as well as for the pristine material and first charge.

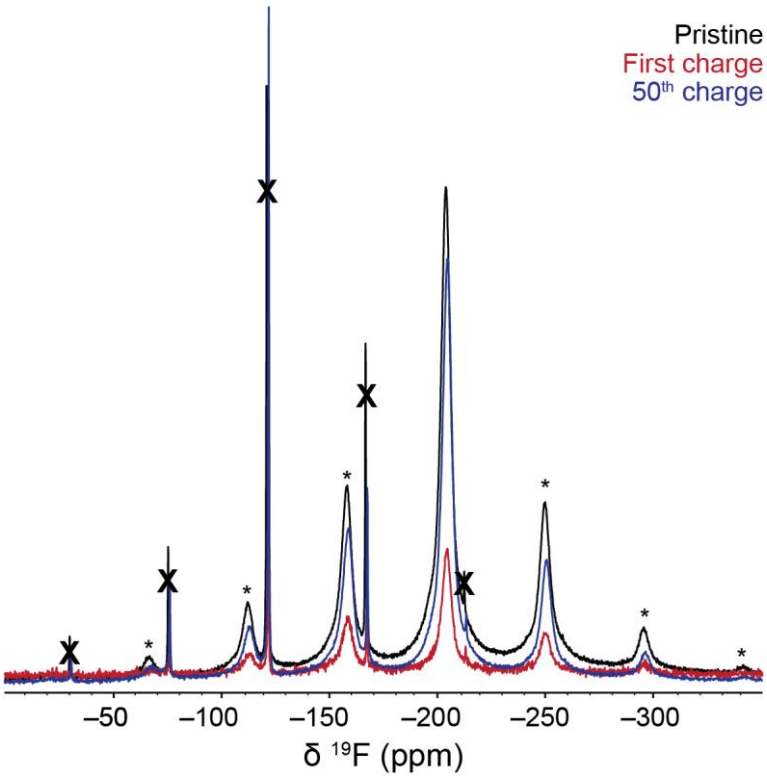

Figure 5.38: ^{19}F NMR spectra recorded for LVOF after the 50th charge as well as the previously shown spectra for the pristine material and first charge. Spectra were acquired at 16.4 T and an MAS frequency of 30 kHz using a depth sequence and are the sum of 1024 scans with a recycle delay of 0.25 s. Asterisks denote spinning sidebands, whilst crosses denote peaks from the PTFE binder.

The spectrum for the cycled electrode shows a single peak at –204 ppm, that is similar in intensity to the pristine material, and much higher intensity than the first charge. This is consistent with the ^{7}Li data and suggests that either more LiF is formed or that more LiF becomes visible due to changes in relaxation rate.

A ^{51}V spectrum was also recorded for the 50th charge sample (Figure 5.39). This shows a single isotropic resonance at –570 ppm as seen for the pristine material, with the intensity being slightly reduced. In the pristine sample, this signal was attributed to a V^{5+} impurity phase. This means that the impurity likely does not participate in the cycling of the material, as it is able to survive up to 50 cycles.

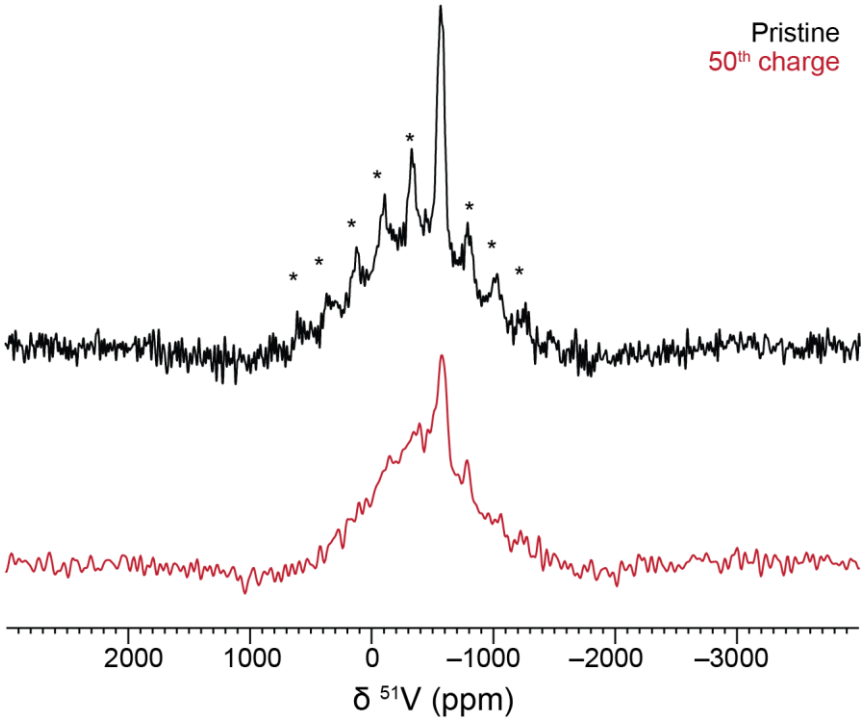

Figure 5.39: ^{51}V NMR spectra recorded for LVOF after the 50th charge (red) as well as the previously shown spectrum for the pristine material (black). Spectra were acquired at 9.4 T and an MAS frequency of 25 kHz using a rotor-synchronised Hahn echo sequence and are the sum of 6400 scans with a recycle delay of 0.25 s. Asterisks denote spinning sidebands.

5.3.3. Electrochemically synthesised oxyfluoride DRXs

The materials studied so far have been prepared by ball mill synthesis, using LiF as the source of fluorine. As discussed, LiF also has a rocksalt structure and so it is difficult to use PXRD to determine whether it has mixed into the DRX structure or whether some exists in a separate phase. The results presented so far indicate that at least some of the LiF is incorporated into the DRX structure. However, it would be useful to compare the results with a similar material were LiF is not used as a fluorine source.

PTFE has also been used as a fluorine source in conventional solid-state synthesis.[158,161] However, this does not result in high levels of fluorine incorporation. Furthermore, the disordering temperatures of the desired compositions may not be practically accessible. An alternative method is to use electrochemical synthesis. This involves lithiating a starting material inside a coin cell resulting in phase transformations.[68] After this initial formation step, the new phase can be cycled like materials synthesised by other methods. Whilst not scalable, this approach allows for the material of interest to be prepared *in situ* and is therefore convenient for mechanistic studies (Chapter 6). However, in the case of oxyfluoride materials, if the initial precursor contains fluorine, LiF is no longer required as part of the synthesis.

An ideal comparison would require synthesis of VO_2F. This can itself be prepared by ball milling V_2O_5 and VOF_3.[281,282] However, as of the time of writing, it has not been possible to acquire VOF_3. Through collaboration with the University of Edinburgh, NbO_2F was identified as an alternative. Figure 5.40 shows the ^{19}F and ^{93}Nb spectra recorded for these materials.

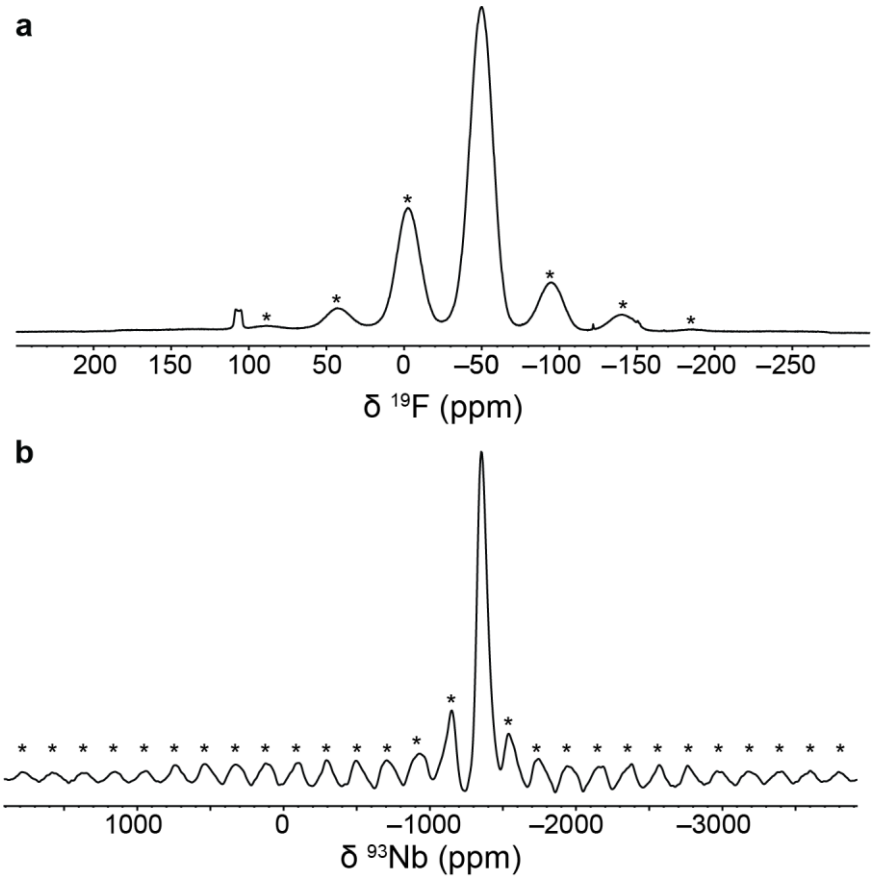

Figure 5.40: (a) ^{19}F NMR spectrum of NbO_2F acquired at 16.4 T and an MAS frequency of 30 kHz. Spectrum is the sum of 5808 scans separated by a recycle delay of 0.25 s. (b) ^{93}Nb NMR spectrum of NbO_2F acquired at the same field and MAS frequency. The spectrum is the sum of 128 scans using a recycle delay of 0.25 s. Asterisks denote spinning sidebands.

The ^{19}F spectrum recorded for NbO_2F shows a peak at –49 ppm. This agrees with literature and can be assigned to Nb-F-Nb sites, broadened due to dipolar coupling between ^{19}F and ^{93}Nb.[36] There is an additional feature at 110 ppm. This is unusually shaped but has been observed for this material before and is attributed to a defect. The ^{93}Nb spectrum shows a single site at –1350 ppm, once again, in agreement with literature.[283] However, six coordinate niobates typically have C_Q values of at least 20 MHz.[284] This means that the observed peak is much narrower than it should be, and so it is likely that only a portion of the lineshape is being observed here. ^{93}Nb NMR is therefore likely not useful for studying this material.

As an initial test to confirm that electrochemical lithiation will form a DRX phase from this material, two cells were prepared using NbO_2F self-standing electrodes and discharged until a capacity of 350 mA h g^{-1} was reached. This occurs around 1 V (vs Li/Li$^+$) and corresponds to two lithium ions being intercalated, resulting in the desired 1:1 ratio of

cations to anions. Figure 5.41 shows the electrochemical data associated with the first discharge of these cells as well as the PXRD data recorded for the two samples after the discharge finished.

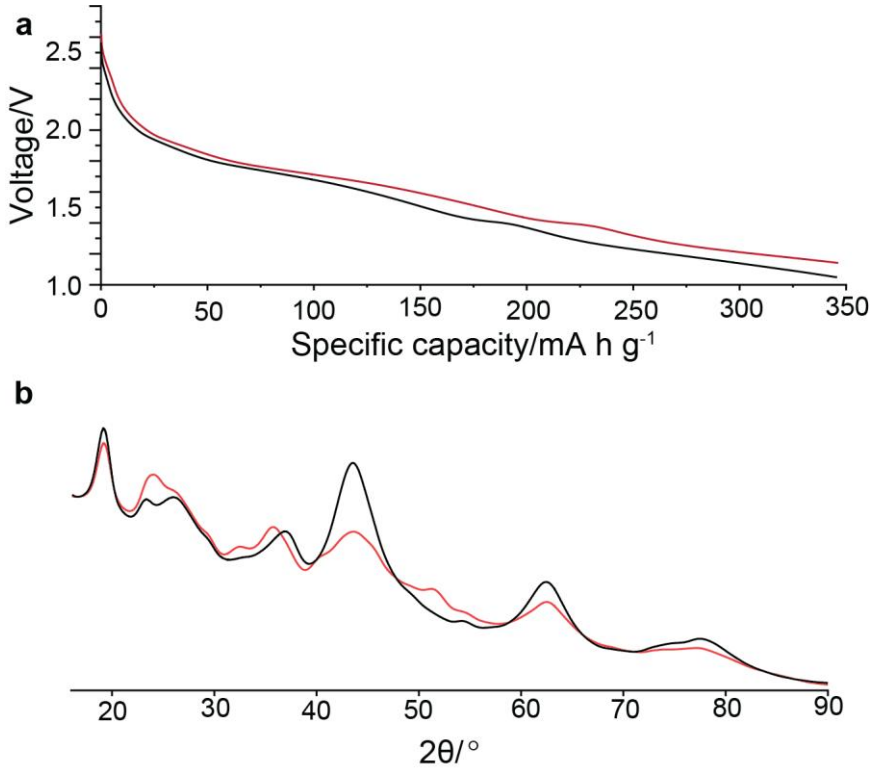

Figure 5.41: (a) Galvanostatic discharge plots for the two cells and (b) PXRD patterns for the electrodes after washing. Red lines denote the sample discharged to 1.1 V whilst black lines denote the sample discharged to 1 V. The cycling rate for both cells was C/20 (17.0 mA g^{-1}). PXRD patterns were collected using the Supernova diffractometer.

Figure 5.41(b) shows that the PXRD patterns for both samples have peaks at ~35, 43 and 62°, suggesting the formation of a DRX phase. Peaks at 18 and 25° can be attributed to PTFE and carbon black respectively, with the remaining extra peaks coming from unreacted precursor material. The DRX peaks are more intense for the sample discharged to 1 V suggesting that this is a better cutoff voltage than 1.1 V.

A new set of cells were prepared with one cell being discharged to 1 V and one subsequently charged to 4 V. The electrochemical profiles for these cells are shown in Figure 5.42.

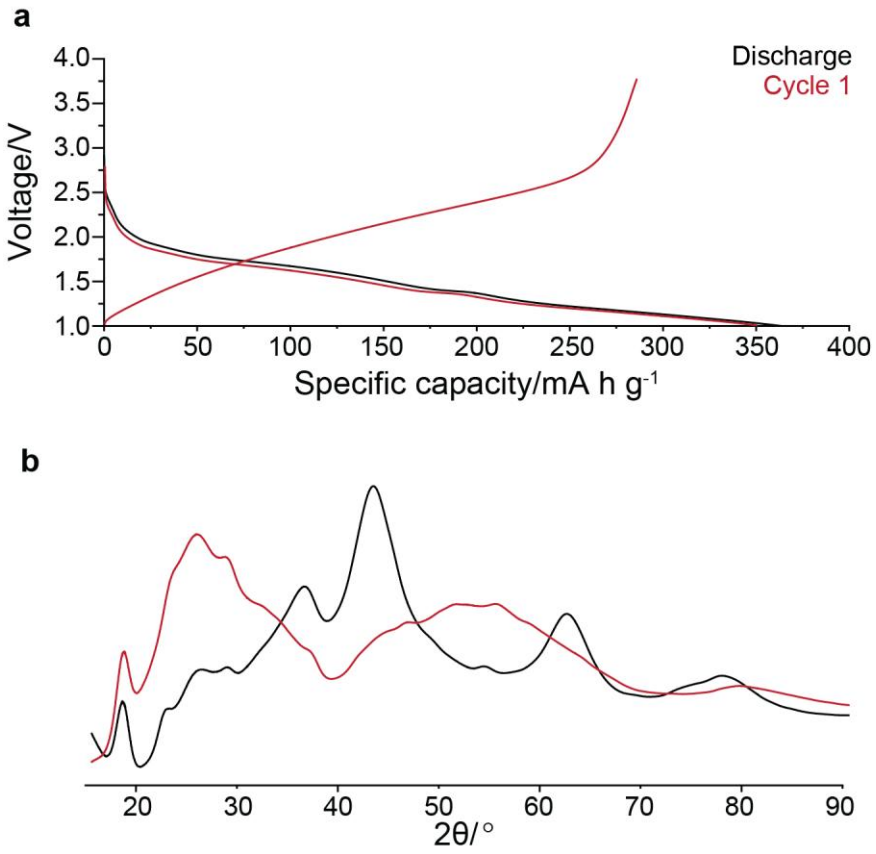

Figure 5.42: (a) Galvanostatic charge-discharge plots and (b) PXRD patterns for the samples prepared after the first discharge and charge (Supernova diffractometer).

Figure 5.42(a) shows that discharging to 1 V results in the theoretical capacity being achieved. For the sample prepared after the first full cycle, this corresponds to approximately 2.1 lithium ions. This is slightly higher than 2 lithium ions, but it should be expected as some capacity will come from electrochemical activity of carbon black.[46] However, charging the material results in a capacity of approximately 300 mA h g^{-1}. This means that there are roughly 0.4 lithium ions remaining in the structure and therefore it is not possible to extract all lithium from the material under these conditions.

Figure 5.42(b) shows that a rocksalt phase is formed on the first discharge, consistent with the previous samples (Figure 5.42(b)). However, the peaks at 36, 43 and 62° are not observed after charging to 4 V. Instead, there are new broad peaks centred at approximately 30 and 55°. This suggests that the rocksalt phase is no longer present on charging. The breadth of the peaks would also suggest that the resulting material is highly disordered.

^{7}Li NMR spectra were recorded for the two samples and are shown in Figure 5.43.

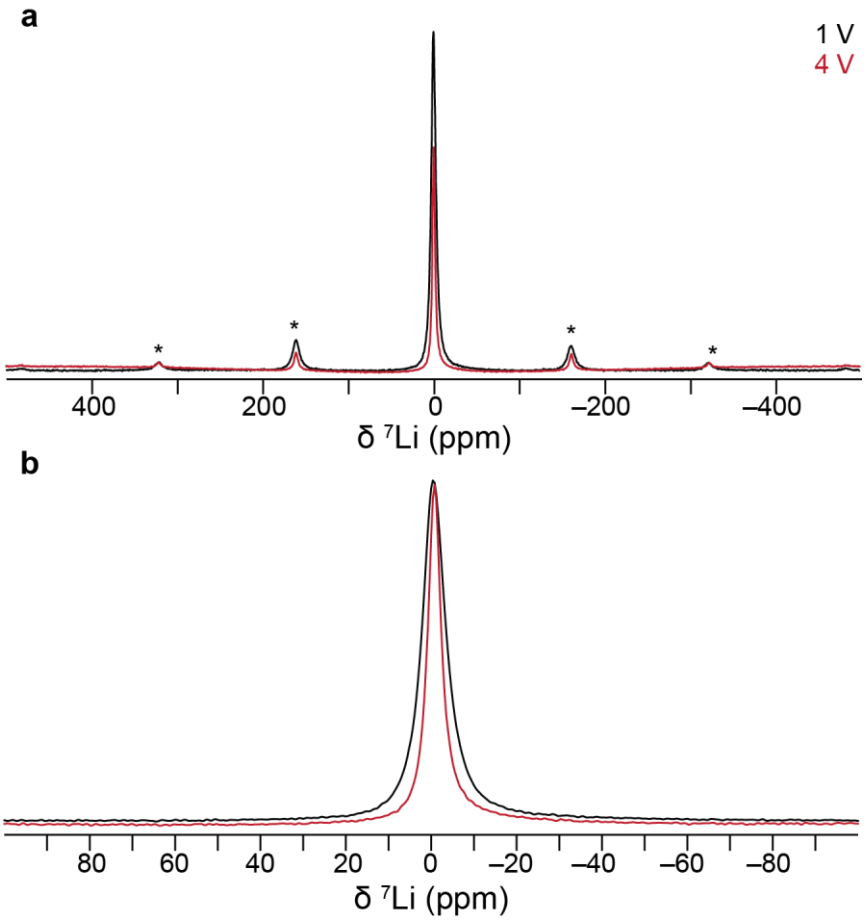

Figure 5.43: ^{7}Li NMR spectra recorded for NbO_2F after the first dischrage (black) and first charge (red). (a) shows the full spectral width, whilst (b) shows the region around the isotropic peak. Asterisks denote spinning sidebands. Spectra were acquired using a single pulse experiment at 9.4 T and 25 kHz MAS. Spectra are the sum of 640 scans separated by a recycle delay of 0.25 s.

The ^{7}Li spectra show single peaks centred at approximately 0 ppm. Whilst in principle, the ^{7}Li NMR spectrum would show nothing for the sample prepared at 4 V, the electrochemistry would suggest that there are still lithium ions present. The spectrum for the sample prepared at 1 V is more intense than the sample prepared at 4 V. This would be expected, as there are more lithium ions in the 1 V sample. However, based on the electrochemistry data, the 1 V spectrum should be around 5 times as intense as the 4 V spectrum. Instead, the difference is a factor of 2.2. This means that not all the lithium ions can be observed, likely due to their proximity to Nb^{3+} ions, resulting in paramagnetic relaxation enhancement.

^{19}F spectra were recorded for the two cycled samples and these are shown in Figure 5.44.

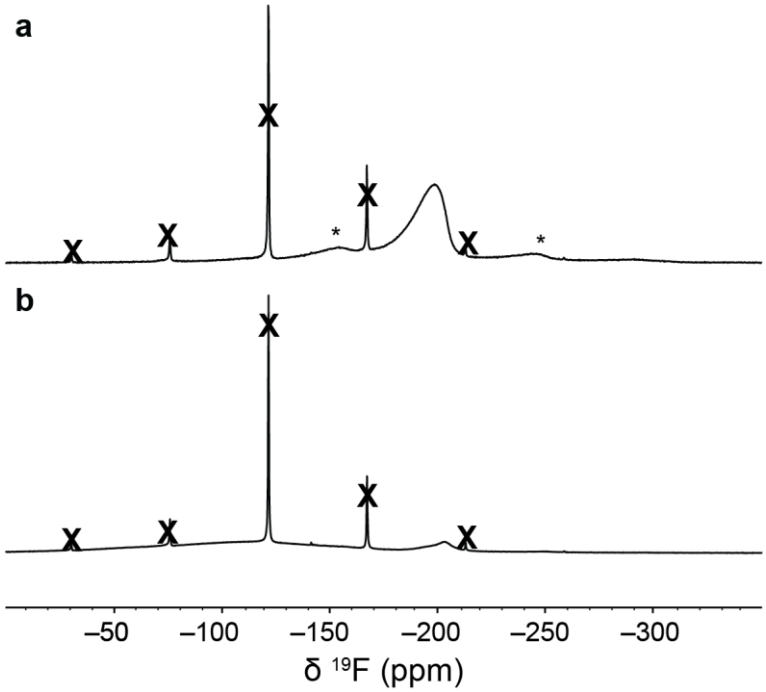

Figure 5.44: ^{19}F NMR spectra recorded for NbO_2F at (a) 1 V and (b) 4 V. Asterisks denote spinning sidebands, whilst crosses denote peaks and spinning sidebands from the PTFE binder and may be ignored. Spectra were acquired at 16.4 T and an MAS frequency of 30 kHz. Spectra are the sum of 5808 scans separated by a recycle delay of 0.25 s.

Figure 5.44(a) shows a broad peak around –190 ppm, with another broad peak at –150 ppm, causing the left spinning sideband to be raised relative to the one on the right. These features are similar to those observed for LSOF and so can be assigned to distorted FLi_6 (–190 ppm) and FLi_xSc_{6-x} (–150 ppm) environments. It should be noted that there is no clear peak at –204 ppm, suggesting that there are fewer LiF-like domains. This absence can be attributed to the fact that no LiF is used in the synthesis. However, not all the LiF previously observed is an impurity. This would suggest that this electrochemically synthesised DRX is not a perfect analogue of those produced by ball milling.

The spectrum recorded for the 4 V sample (Figure 5.44(b)) shows a small peak at –204 ppm and a broad, low intensity feature between –50 and –150 ppm. This is consistent with the PXRD data that shows that the structure formed at low voltage is destroyed at high voltages. Furthermore, a change in chemical shift to more positive values suggests that the fluoride ions are coordinated to niobium cations, as in pristine NbO_2F. The breadth of the peak means that these ions, or ions nearby are not Nb^{5+}, resulting in broadening of the observed peaks. This is supported by the electrochemical data for this material that suggests that not all lithium ions are extracted, meaning that not all the niobium ions can be fully oxidised.

From the PXRD and NMR data collected, the structural transformation between low and high voltages is dramatic. Therefore, to see if it is reversible, samples were prepared after the end of the second, fifth and 50th discharges. The electrochemical data for the sample prepared after the 50th discharge is shown in Figure 5.45.

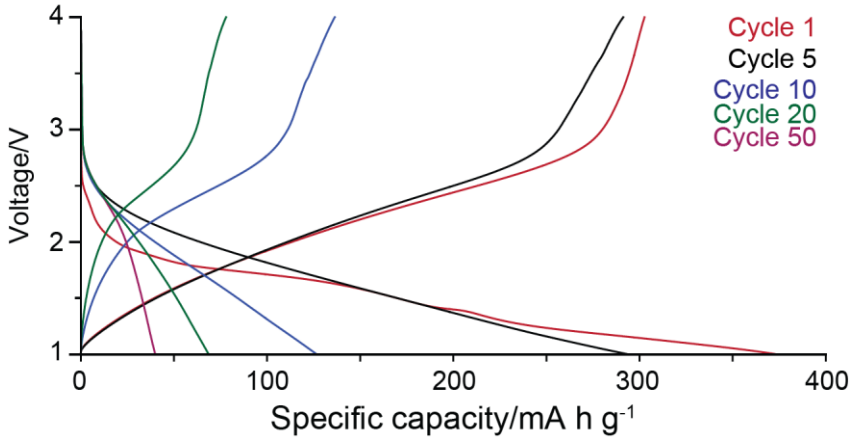

Figure 5.45: Galvanostatic charge-discharge plot for NbO_2F cycled 50 times at C/20 (17.0 mA g^{-1}) between 1 and 4 V.

It can be seen from Figure 5.45 that as the cycle number increases, the specific capacity decreases. For example, a capacity of 365 mA h g^{-1} is achieved on the first discharge, compared to 40 mA h g^{-1} on the 50th discharge, equivalent to 11%.

Figure 5.46 shows the PXRD pattern acquired for NbO_2F after the 50th discharge.

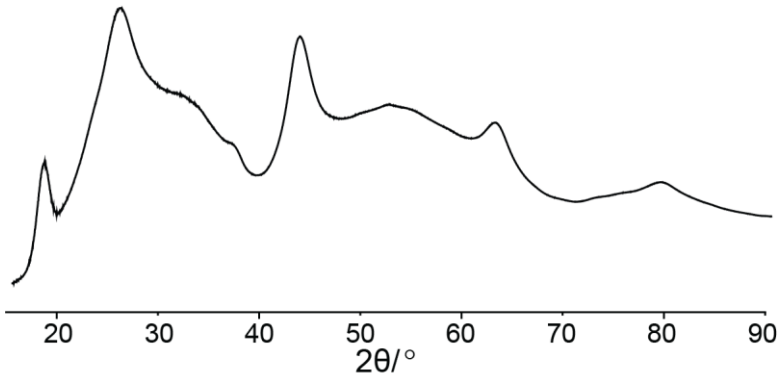

Figure 5.46: PXRD pattern recorded using the Supernova diffractometer for NbO_2F after the 50th discharge.

The PXRD pattern shows peaks at 37, 43 and 63° which were previously observed and suggest the formation of the rocksalt phase. However, there are also broad peaks at 30 and 55° which were previously observed in the charged state. This means that after the 50th

discharge the sample is a mixture of both phases, and this could be the origin of the poor cycling performance.

Figure 5.47 shows the ^{19}F NMR spectra recorded for the pristine electrode, and after the 1st, 2nd and 50th discharge.

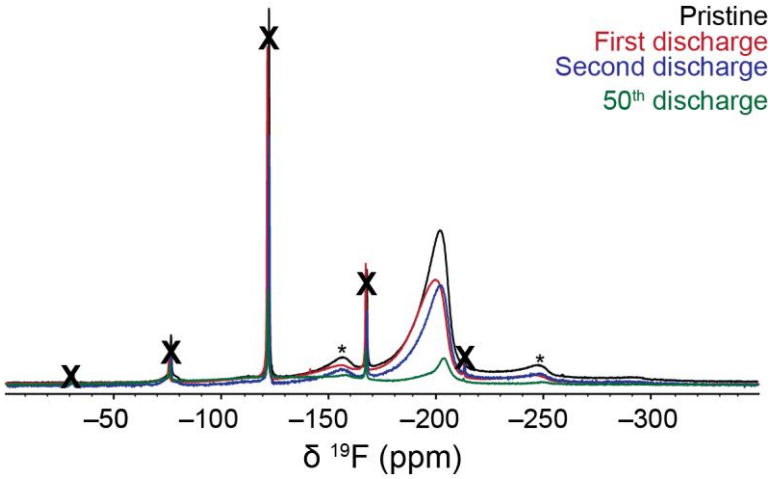

Figure 5.47: ^{19}F spectra recorded for NbO_2F at 1 V after the 1st, 2nd, 5th and 50th discharges. Asterisks denote spinning sidebands, whilst crosses denote peaks and spinning sidebands from the PTFE binder and may be ignored. Spectra were acquired at 16.4 T and an MAS frequency of 30 kHz. Spectra are the sum of 5808 scans separated by a recycle delay of 0.25 s.

The spectra in Figure 5.47 show a broad feature at –190 ppm, with spinning sidebands. This is the same as the first discharge sample and means that the fluorine environment returns to a similar structure on subsequent discharges. However, the intensity of the peak decreases as the number of cycles increases, until there is only a peak at –204 ppm after the 50th discharge. This agrees with the PXRD data that shows that after prolonged cycling, both the DRX and the charged phase are present.

5.4. Discussion

The work undertaken in this chapter had two objectives, the first of which was to investigate the local structures of DRX materials to derive a structural model. The model compound LSOF was studied using ^{6}Li, ^{19}F and ^{45}Sc NMR. Assigning the peaks in these spectra provides evidence for the following octahedral environments being present (with the first atom at the centre of the octahedron): LiO_6, LiF_6, FLi_4Sc_4, FLi_5Sc, $FLi_6^{distorted}$, $FLi_6^{ordered}$ and ScO_6. The presence of FLi_4Sc_4 and FLi_5Sc also implies the presence of ScF_xO_{6-x} sites, although these are not observed in the ^{45}Sc spectrum, likely due to quadrupolar broadening. However, there is also no evidence of an ScF_6 site, so this can likely be excluded. TRAPDOR results also indicate that the FLi_6 sites are at least partially within the DRX framework and not just limited to residual LiF impurities.

This approach does have limitations however, as the absence of *d* electrons may mean that the ions in redox-active DRX materials may have different local ordering preferences. In addition, only using one metal cation means that the model is only based on one cation size (aside from lithium). Using a different cation may yield different results as the different size will mean that the extent of distortions within the structure would be different.

Despite this, the model proposed can explain the spectra observed for the redox-active materials reasonably well. The ^{19}F spectra recorded for LNOF and LVOF both show single peaks at –204 ppm, indicating $FLi_6^{ordered}$ units. These are likely not simply residual LiF due to both peaks possessing several intense spinning sidebands, meaning that the fluoride ions are likely close to the 3+ cations. These peaks both also have a shoulder to the left, suggesting the presence of $FLi_6^{distorted}$ sites. Further peaks are not observed as the model would suggest that these environments have direct bonding to the transition metal cation. These are likely difficult to observe owing to the effects of paramagnetism. In the cases of LTOF and NbO_2F the ^{19}F spectra recorded show the same peaks observed for LSOF, suggesting similar bonding environments. This would suggest that the paramagnetic effects of the metal ions in these materials are not as extreme as for LNOF and LVOF. The peak at –150 ppm does disappear at higher field, alluding to a greater level of paramagnetic character, which would fit with the suggestion that this peak contains direct bonding to the transition metal ion.

The second objective of this work was to understand how the structure changes as the DRX materials are cycled, and whether this can explain their poor capacity retention. This

is not straightforward as the intensities of the ^{7}Li and ^{19}F peaks vary, but do not necessarily follow clear trends. This is because the relaxation properties of the transition metal ions change which may alter the intensities observed. It is also possible that the intensities may also be affected by some local structural rearrangement, bringing the transition metal ions into closer contact with the nuclei of interest. However, there are differences between the ball milled DRXs and the DRX prepared electrochemically. From PXRD, the ball milled samples seem to retain their DRX structure, even after prolonged cycling, although any truly amorphous regions would be invisible to PXRD. On the other hand, the electrochemically synthesised material does not, with the structure forming a mixture between the DRX and another phase. This second phase likely sees the fluoride ions associating with transition metal ions based on the ^{19}F NMR data collected. One possible explanation for this difference is that the ball milled DRX seems to have more of the fluoride ions in LiF-like environments, and hence more lithium ions in these environments. These lithium ions may possibly be more difficult to extract, due to the strong bonding between lithium and fluorine. Removing less lithium means that the delithiated structure is more stable and less likely to collapse, unlike in the electrochemically synthesised system. This agrees with the idea of "lithium-gettering", put forward by Kitchaev *et al*,[168] where undercoordinated fluoride ions, bind more strongly to remaining lithium ions, preventing their extraction. Niobium ions are also larger than vanadium ions and so this may play a role in why this material is less stable than those prepared by ball milling.

Another finding from this work is that the precursors used in the synthesis of DRX materials can be oxidised during the synthesis, despite being prepared under inert atmosphere. This can explain the previously reported ^{51}V signals for LVOF, as lithiated V^{5+} regions, rather than sites with vanadium in lower oxidation states. Furthermore, this could offer an explanation as to why LVOF and many other oxyfluoride materials reported in literature show an increase in capacity between the first and second charge. This is because after the first charge, there are additional ions in higher oxidation states, beyond those formed by delithiation of the active material. These ions can then allow for greater lithium insertion into the material when the voltage is decreased.

A common discussion point in the literature on oxyfluoride DRXs is the suppression of oxygen redox processes. This is thought to be because the lower anion valence, increases the amount of lithium that can be extracted by transition metal redox, reducing the need for oxygen redox. However, it is still observed for some materials. Considering the model here could suggest that there are other factors at play in suppressing O-redox. Specifically,

Seo *et al* propose that O-redox requires the presence of Li-O-Li structural units, which possess labile electrons that can facilitate O-redox.[122] However, this model suggests that all fluoride ions are bonded to multiple lithium ions. This reduces the number of lithium ions that could possibly fulfil the Li-O-Li criteria. Furthermore, transition metal ions overwhelmingly do not bond to fluoride ions and are more likely to associate with oxide anions. This will further reduce the number of Li-O-Li sites available for oxygen redox. The apparent suppression of oxygen redox may therefore be also in part due to a reduced probability of suitable environments. There will still be some Li-O-Li configurations which may be why weak O-redox activity is often observed, and disordering preferences of certain transition metal ions could lead to a greater number of Li-O-Li sites. However, this requires further investigation.

5.5. Conclusions

The work presented in this chapter investigated the local structures of oxyfluoride DRX materials. Through the use of a diamagnetic analogue, LSOF, a model structure was proposed that was then applied to redox-active DRX material. This model structure suggests that DRX structures are not completely random, but that certain environments are more favourable, in agreement with prior literature. This structural model was applied to understanding how the structures of these materials change throughout electrochemical cycling. However, the influence of paramagnetic ions means that it is not fully possible at this stage to understand the behaviour of these materials.

5.6. Further work

The only successful diamagnetic analogue produced was LSOF. However, it would be useful to revisit LAOF and LYOF, perhaps using other mechanochemical synthesis methods. LAOF has been reported previously and so should be possible to synthesise.[285] Including other ions sizes will give better insight into how distortions can influence the structure of the materials and how these differences manifest in the NMR spectra and in the DFT calculations. Furthermore, ^{89}Y is spin-½, and so any ^{89}Y spectra recorded may have better resolution than the ^{45}Sc spectrum presented here, owing to the absence of any quadrupolar broadening. This could allow any mixed coordination transition metal sites to be identified, allowing the structural model to be further refined. It would also be interesting to prepare these materials using ScF_3, AlF_3 and YF_3 as precursors. This is because this approach would avoid any residual LiF, so the signal at –204 ppm would only

arise from LiF-like regions in the DRX. In the case of ScF_3, the ^{19}F chemical shift should be well removed from the chemical shifts of the DRX phase, removing the ambiguity of the assignment.

As already mentioned, a better comparison than NbO_2F would be VO_2F, as this would allow a direct comparison between ball milled LVOF and electrochemically synthesised LVOF. This material has been studied in literature but not in the same way as the ball milled samples discussed in this chapter, limiting the comparisons that can be made.

It would also be useful to address some of the paramagnetic effects encountered in the cycled samples to reduce the ambiguity surrounding this data. First would be to use XAS to establish what oxidation states are present. Then the experiments performed here could be repeated using low field and/or fast MAS to try and improve the spectra recorded.

6. Exploring Oxygen Redox in Vanadium-based Disordered Rocksalt Materials

6.1. Introduction

The oxyfluoride DRX materials discussed in the previous chapter are of interest because fluorination suppresses oxygen redox (O-redox) processes. As discussed in Chapter 2, these processes are often considered as undesirable as they can lead to rapid losses of capacity. However, oxyfluoride DRX materials still exhibit limited long term electrochemical performance. In addition, the fact that many compositions are only accessible via ball milling may make their commercial implementation challenging. Furthermore, if controlled, O-redox could provide an additional source of capacity. Therefore, oxide DRX materials are still of active interest in the community.[117]

Combating degradation due to O-redox requires understanding the structural changes that occur at high voltages when O-redox is active. Solid-state NMR is therefore, once again, a useful tool to investigate these processes. However, the challenge of paramagnetism is ever-present when studying battery materials. Whilst in the previous chapter paramagnetic effects were avoided by exploring diamagnetic analogues, such an approach is not possible in this case. This is because O-redox is intrinsically linked to electrochemical activity and so the materials studied must be redox-active. A possible way to deal with this is to instead use redox-active materials that become diamagnetic at high voltages, *i.e.*, the transition metal ion is fully oxidised. As a result, the work in this chapter will focus on the DRX $Li_3V_2O_5$, which if fully delithiated will contain V^{5+} ions which are d^0.

To be useful for this work, $Li_3V_2O_5$ needs to be able to be fully delithiated. Luger *et al*, report that this is not possible, with 0.4 lithium ions remaining within the structure.[286] This work used an upper cutoff voltage of 3.8 V, and so further extraction may be possible at higher voltages. However, there is limited information on the high voltage behaviour of $Li_3V_2O_5$, as most studies use it as an anode material.[287,288] There are reports of other lithiated V_2O_5 phases being used as cathodes. For example, $Li_xV_2O_5$ ($0.2 < x < 1$) can be fully

delithiated when charged to 4.5 V.[279] Whilst this is a different structure to $Li_3V_2O_5$, it does indicate that full delithiation may be possible.

Alongside $Li_3V_2O_5$, this work will also study the high voltage behaviour of the Li_2VO_2F (LVOF) DRX discussed in the previous chapter. This is because, as already mentioned, the substitution of fluorine into the structure should suppress any O-redox, but the material is still vanadium-based and so should be diamagnetic at high voltages. LVOF is therefore useful as a comparison.

6.2. Methods

6.2.1. Material synthesis

V_2O_5 was used as purchased (Alfa Aesar 99.6% +), without further processing. LVOF was prepared by ball milling using the method described in Chapter 5.

^{17}O enrichment of V_2O_5 was performed by Heitor Secco Seleghini in the group of Prof. Sharon Ashbrook at the University of St Andrews. V_2O_5 was heated in a 70% $^{17}O_2$ (Cortecnet) atmosphere for 72 hours at 600°C.

6.2.2. Electrode fabrication and cell assembly

Powder electrodes were prepared by mixing the active material with carbon black (2:1). Approximately 5 mg was used in constructing coin cells. Self-standing electrodes were prepared by mixing the active material with carbon black for 15 minutes followed by polytetrafluoroethylene (PTFE) pellets (6:3:1, V_2O_5: carbon: PTFE). The resulting film was then rolled to a final thickness of 150 μm and the electrode was cut into 5 mm diameter discs.

Coin cells were assembled under argon atmosphere (< 0.1 ppm O_2/H_2O). The cells were constructed using parts made from 304 steel (TOB machine), 1 M $LiPF_6$ in EC:DMC (1:1) (Sigma Aldrich) as the electrolyte (150 μL), Whatman glass fibre separators (17 mm) and lithium wafers (15 mm x 0.38 mm) (Cambridge Energy Solutions). Cells were cycled at a rate of C/20, using Neware electrochemical cyclers. Voltage windows are given in the figure captions.

In situ cells were assembled using PEEK *in situ* cells (NMR Service GmbH). A V_2O_5 self-standing film was pushed into an aluminium mesh for the cathode, a lithium wafer and copper wire were used as the anode and 1 M $LiPF_6$ in EC:DMC was used as the electrolyte

(80 μL). PTFE wafers were used to maintain pressure inside the cell, whilst PTFE tape was used to seal the openings for the current collectors. Cells were cycled using a Biologic SP 150 potentiostat and a static H/F-X probe (NMR Service GmbH) equipped with 5 MHz pass filters.

Samples for *ex situ* analysis were washed in DMC (TOB machine) and dried at ambient temperature, under vacuum. NMR samples were packed into the zirconia rotors with KBr (Merck, IR spectroscopy grade) to fill the remaining volume. PXRD/PDF samples were prepared by sealing the washed electrodes in Kapton tape. RIXS samples were mounted onto the stubs using carbon tape and the samples were always kept either under argon or vacuum.

6.2.3. Powder X-ray diffraction and PDF

PXRD and PDF measurements were performed using an Agilent Technologies Supernova single crystal diffractometer equipped with a Mo K_α source. All patterns were converted to Cu K_α for the sake of comparison. PDF data was collected and extracted (using PDFgetX2) by Dr Nathan Halcovitch.

6.2.4. Solid-state NMR

^{7}Li and ^{51}V solid-state NMR experiments were performed using a Bruker Avance III HD spectrometer operating at a magnetic field strength of 9.4 T equipped with a 2.5 mm HX probe, using an MAS frequency of 25 kHz. ^{7}Li spectra were acquired using a single pulse-acquire sequence and ^{51}V spectra were acquired using a rotor-synchronised Hahn echo sequence, unless otherwise stated. ^{17}O solid-state NMR experiments were performed Bruker Avance III HD spectrometer operating at a magnetic field strength of 16.4 T equipped with a 2.5 mm probe, using an MAS frequency of 30 kHz. Spectra for pristine ^{17}O-enriched V_2O_5 were acquired using single pulse-acquire experiments with a dead time of 15 μs. Spectra for the cycled electrodes were acquired using a rotor-synchronised Hahn echo sequence.

^{7}Li spectra were referenced to $^{6}Li_2CO_3$ (0.11 ppm), ^{51}V spectra to V_2O_5 (–610 ppm) and ^{17}O spectra were reference to H_2O (0 ppm).[178] Pulse lengths for ^{7}Li and ^{51}V were optimised on the reference samples (^{7}Li = 2.5 μs and ^{51}V = 2.5 μs) whilst ^{17}O pulse lengths were optimised on ^{17}O-enriched V_2O_5 (3.5 μs).

In situ ^{51}V NMR experiments were performed using a Bruker Avance III HD spectrometer operating at a magnetic field strength of 9.4 T equipped with a static H/F-X probe (NMR Service GmbH). Individual rows were the sum of 1024 scans, separated by a recycle delay of 0.5 s. Spectra were referenced to the V_2O_5 signal prior to the start of the experiment (200 ppm).

6.2.5. Resonant inelastic X-ray scattering measurements

O K-edge (532.1 eV) RIXS measurements were performed at the I21 beamline at Diamond Light Source. Measurements were performed with the detector arm set at 90° and at cryogenic temperatures with continuous rastering to avoid beam damage.

6.2.6. Electron paramagnetic resonance spectroscopy

EPR spectra were recorded on a Bruker EMXplus spectrometer (9.8 GHz). The microwave power in all cases was 2.135 mW and modulation frequency used was 100 kHz. Unless stated otherwise the number of scans, time constant and conversion time were 16, 1.28 ms and 4 ms, respectively. To account for the discrepancy between the measured field and the field at the centre of the cavity, spectra were recorded for strong pitch and TEMPO. Based on these known g values (2.0028 and 2.006, respectively) a correction of –0.01684 was applied to all g values calculated by WinEPR processing.

To keep the samples under inert atmosphere, the washed electrodes were packed into 2.5 mm zirconia NMR rotors, with the black mark removed. These were then placed inside 4 mm quartz EPR tubes so that they could be held inside the spectrometer cavity.

6.3. Results

6.3.1. Electrochemical synthesis of $Li_3V_2O_5$

$Li_3V_2O_5$ can be prepared by chemical or electrochemical lithiation of V_2O_5.[68,289] This is a well-known process, with six phases being identified depending on the level of lithiation. These are *a*, *ε*, *δ*, *ζ*, *γ* and *ω* ($Li_3V_2O_5$), with the latter being a DRX phase, formed at 1.9 V and below.[173,290] It should be noted that the *ζ* and *γ* phases are thought to be structurally similar, with most papers referring only to the *γ* phase.[291]

As mentioned, the preparation of $Li_3V_2O_5$ from V_2O_5 is well documented.[292] However, before moving onto studying the structural changes that occur at high voltages, it was first necessary to explore the first discharge and confirm that the desired phase can be reproduced in the system being used (*i.e.*, a coin cell will self-standing electrode). Figure 6.1 shows the electrochemical data associated with the first discharge.

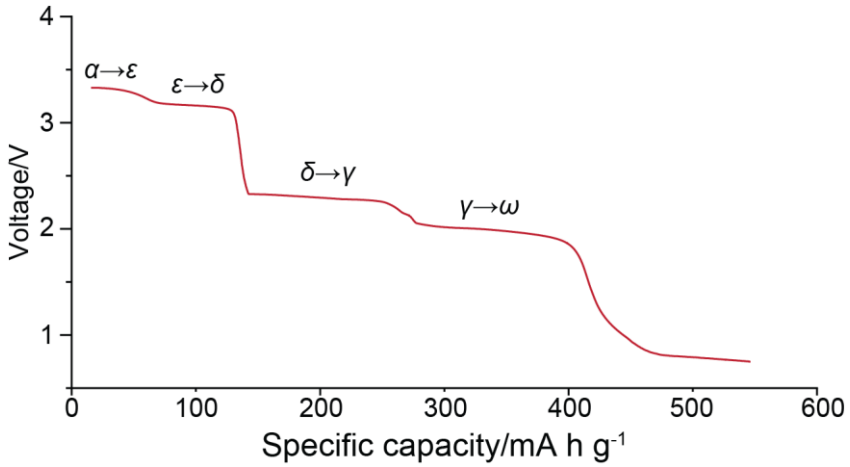

Figure 6.1: Galvanostatic discharge plot for V_2O_5 discharged at C/20 (22 mA g^{-1}) to 0.75 V.

The data in Figure 6.1 shows five plateaus at 3.3, 3.2, 2.3, 2.0 and 0.8 V. This agrees with literature, with each of the plateaus corresponding to transitions between the different phases.[292] In order, these are *a*⟶*ε* (3.3 V), *ε*⟶*δ* (3.2 V), *δ*⟶*γ* (2.3 V) and *γ*⟶*ω* (2.0 V). The final plateau at 0.79 V, is additional capacity, arising from lithiation of the *ω* phase (with lithiation into the tetrahedral sites). Further capacity will also arise from lithiation of the carbon black additive and SEI formation.[293,294]

To study the structural transformations that occur during the conversion of V_2O_5 to $Li_3V_2O_5$, cells were assembled then disassembled at 3.2, 2.7, 2.15 and 0.75 V. The first three voltages correspond to the steps in the voltage profile, whilst 0.75 V is the lower voltage

cutoff used. This point is after the reaction has finished, ensuring that a DRX should be present. The samples were then studied with PXRD as shown in Figure 6.2.

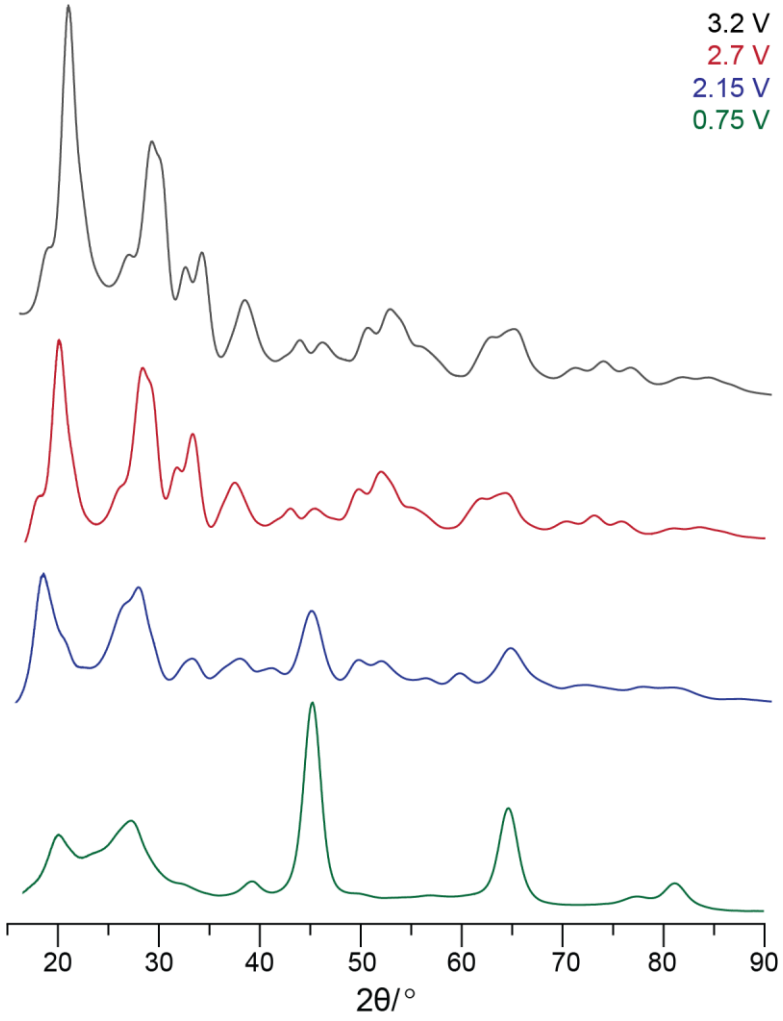

Figure 6.2: PXRD patterns for V_2O_5 at different voltages during the first discharge.

Figure 6.2 shows that as the voltage decreases the PXRD pattern changes. The pristine V_2O_5 pattern shows peaks at 15.3, 18.0, 20.3, 26.1, 31.1 and 34.2°. On discharging to 3.2 V, several of the peaks shift to 15.8, 26.5 and 31.6°. The peak at 18.0° remains but grows in intensity, whilst the peak at 20.3° disappears. Three new peaks also appear at 23.9, 27.3 and 29.9°. This means that the V_2O_5 is lithiated forming one or more new phases. Based on the voltage this is likely the ε phase.[292,295] It is not possible to rule out the presence of other phases based on this data, as the breadth of the peaks may disguise lower intensity reflections. On further discharge to 2.7 V, the pattern does not change aside from the intensity of the drops as they become broader.

At 2.15 V the pattern changes, with the first peak shifting to 17.1°. This shift indicates increased lithiation, with the structure moving towards the δ and γ phases.[295] New peaks

also appear at 25.3, 32.3, 44.2 and 64.5°. The latter two peaks can be assigned to a rocksalt phase, meaning that the *ω* phase is forming. These two peaks increase in intensity further on discharging to 0.75 V, with peaks also becoming visible at 38° and 81.2°, further confirming the presence of the rocksalt phase. Aside from these peaks, only peaks at 18.2° and 25° are observed. These can be assigned to PTFE and lithiated carbon black, respectively.[296,297] The fact that these peaks are visible suggests that most of the V_2O_5 has reached the rocksalt phase, and no longer dominates the PTFE/carbon peaks.

To further explore the phases present at each of the states of charge, ^{7}Li NMR spectra were recorded. These are shown in Figure 6.3, with expanded views shown in Figure 6.4.

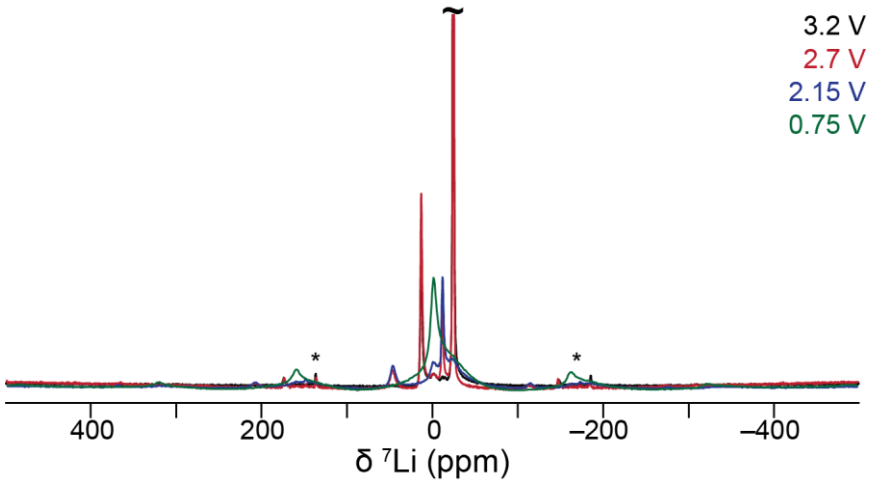

Figure 6.3: ^{7}Li MAS NMR spectra recorded for V_2O_5 at different states of charge during the first discharge. Asterisks denote spinning sidebands. Spectra are the sum of 320 scans separated by a recycle delay of 3 s.

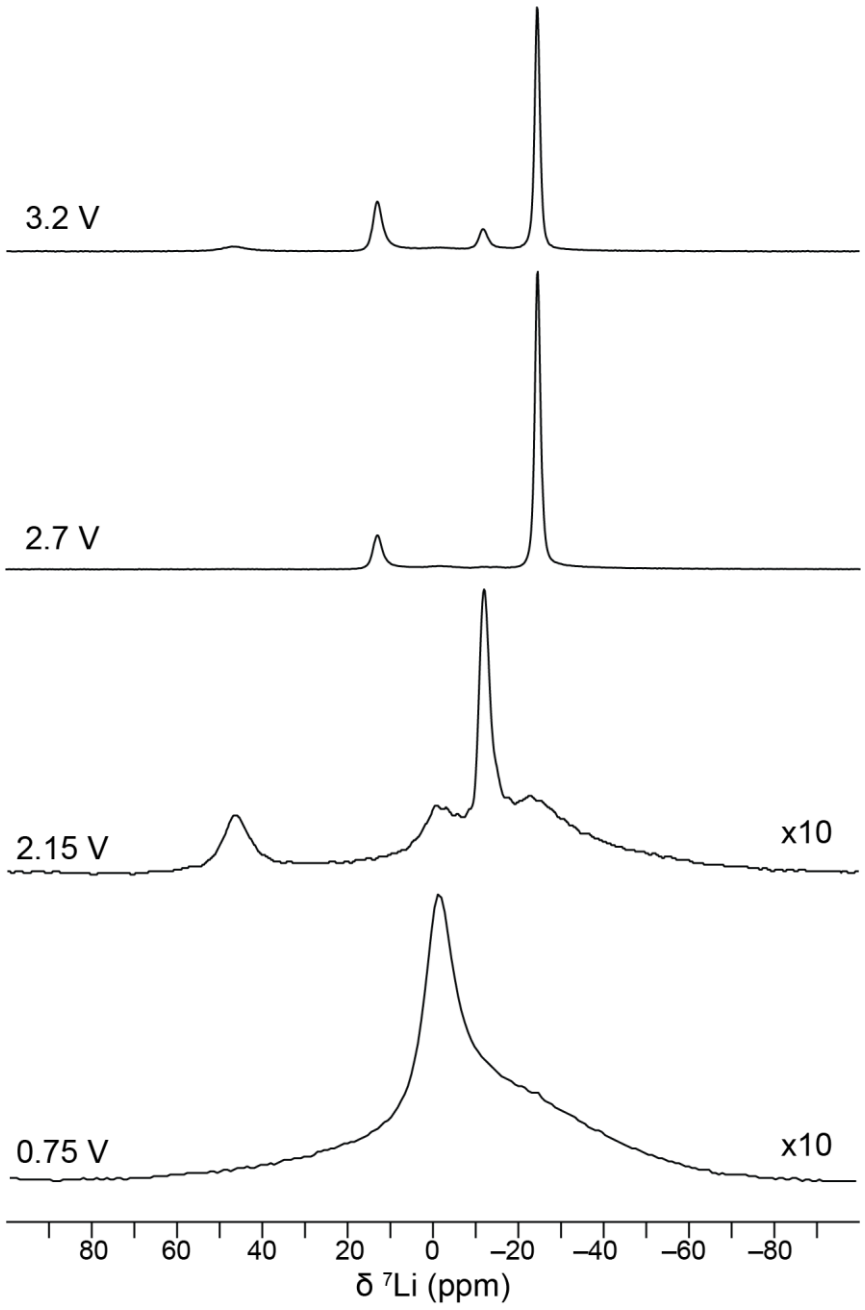

Figure 6.4: The region of the ^{7}Li NMR spectra shown in Figure 6.3 between 100 – –100 ppm.

The NMR spectra shown in Figures 6.3 and 6.4 show several peaks indicating the presence of several phases. The spectrum for sample at 3.2 V shows peaks at 12, and –25 ppm. These peaks are also present when the voltage is decreased to 2.7 V although the intensity of the peak at –25 ppm is reduced, whilst the peak at 12 ppm has grown. In addition, two new peaks can be seen for the 2.7 V sample at 45 and –12 ppm. This means new phases have formed on lowering the voltage despite the PXRD patterns being very similar.

Continuing to decrease the voltage to 2.15 V sees the peak at 12 ppm disappear and the intensity of the one at –25 ppm be significantly reduced. In addition, a new peak starts to appear at 0 ppm. Finally, for the 0.75 V sample, there is a peak at 0 ppm with a broad shoulder at ~–10 ppm.

Assigning which of the six observed peaks originates from which phase is not straightforward as only the δ and γ phases have reported chemical shifts, and these vary by publication (as will be discussed further later).[298,299] Considering the spectrum for the 0.75 V sample, there are two peaks at 0 and ~–10 ppm. The PXRD patterns previously shown suggest that the DRX phase dominates the other vanadium-containing phases at this voltage, as also reported in literature.[173] This means that one or both peaks come from the DRX. However, the vanadium ions are either in the V^{3+} or V^{4+} state. Environments within the DRX would therefore be expected to experience Fermi contact shifts and should not appear around 0 ppm. Another possibility is that this peak comes from SEI species, as SEI formation has been reported to occur below 2.3 V.[300] Another possibility is that the carbon is lithiated and this could contribute to the peak. To test this idea, a new cell was made with an electrode made of carbon and PTFE. The ^{7}Li NMR spectrum for this is shown in Figure 6.5, overlaid with the spectrum recorded for a V_2O_5 cell, both discharged to 0.75 V.

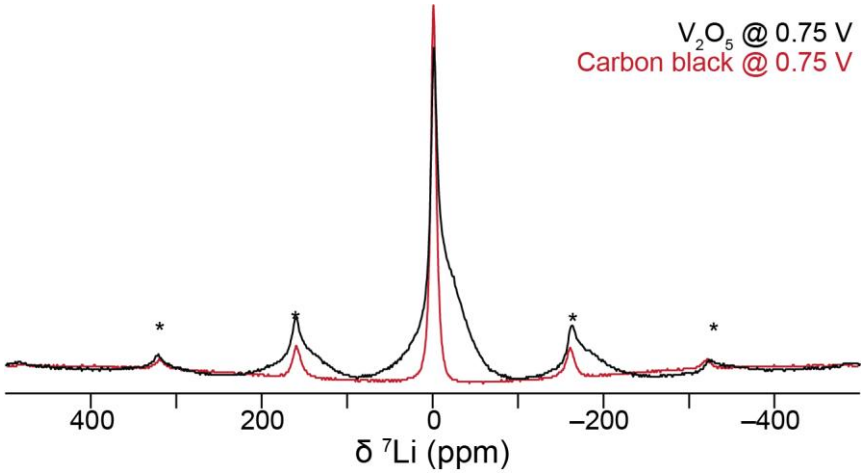

Figure 6.5: ^{7}Li NMR spectra recorded for the carbon black electrode discharged to 0.75 V and for V_2O_5 at 0.75 V. The spectrum for the carbon electrode is the sum of 160 scans whilst the spectrum for V_2O_5 is the sum of 320 scans. The recycle delay in both cases was 3 s. Asterisks denote spinning sidebands.

The spectrum for the carbon electrode shows a sharp peak at 0 ppm. Therefore, the shoulder at ~–10 ppm can be attributed to the DRX. This would agree with the assignments of the LVOF spectra discussed in Chapter 5. The other peak likely comes from SEI species such as Li_2O.[300] Assuming these assignments to be correct, four peaks

remain to be assigned to five phases. However, the *γ* and *ζ* phases are thought to be structurally similar, so their peaks may overlap, leaving four peaks for four phases. It may be possible that the peak at 0 ppm also has some contribution from the DRX, however this is unlikely as it would be expected that such environments would be paramagnetically shifted to lie outside the diamagnetic range of ^{7}Li.

The first two peaks to appear are at 12 and –25 ppm. These are therefore likely from the *α* and *ε* phases as these form at the lowest levels of lithiation. As the *α* phase has the lower amount of lithium in its structure, it would be expected that that this phase disappears at higher voltages than the ε phase. This would disagree with literature as the *δ* phase has been reported to appear at –22 ppm.[299] However, the presence of the *δ* phase at this state of charge would mean that different regions of the sample are lithiated at different rates. If this were the case, it would be expected that three peaks should be visible as to get to the *δ* phase, the sample would have to pass through the preceding two phases. Literature also suggests that there could be some variability in chemical shift for phases formed under different conditions, but this will be discussed more below.

The final two peaks to be assigned are at 45 and –12 ppm and could be assigned to the *δ* and *γ* phases respectively. This is because they form at lower voltages than the preceding phases and persist until 0.75 V, when the sample is, at least in the most part, a DRX. The reason for the specific assignment is that the *γ* phase has been reported to appear at –7.8 ppm, which is relatively close to –12 ppm, especially when it has been suggested that the synthesis route can change the chemical shift.[298] It is important to note however, that the *γ* phase has been reported to have a chemical shift of 0 ppm.[299,301] This could be a misinterpretation of surface species or impurities present in the samples studied, as it seems unusual that a formally paramagnetic material should result in a peak so close to 0 ppm. It should also be said that based on the PXRD, whilst present at 2.7 V, they are likely not the dominant phase.

The ^{7}Li NMR discussed supports the presence of multiple phases throughout cycling ending up with a single phase, that is similar to what has been discussed in the previous chapter for other DRX materials. However, the presence of paramagnetic effects means that these assignments should be considered as tentative, as certain peaks may not be visible.

PDF data was also collected for this series of samples and is shown in Figure 6.6.

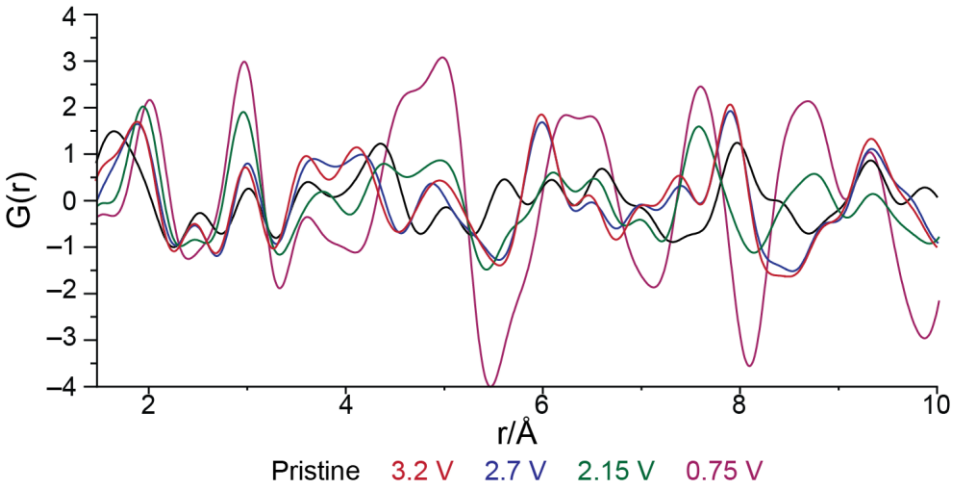

Figure 6.6: PDF data (r = 1.5 – 10 Å) collected for V_2O_5 at different states of charge during the first discharge.

Figure 6.6 shows a broad peak for the V_2O_5 electrode between 1.4 and 2.2 Å. This is due to the range of V-O bond lengths present in V_2O_5 (from 1.6 – 2.0 Å). On discharging to 3.2 V there is a shift to 1.89 Å with a peak still being present at 1.6 Å. This shift continues as the voltage is decreased further to 1.99 Å at 0.75 V. Lengthening of the V-O bond suggests that the vanadium coordination number has increased from five (in V_2O_5). This would agree with the PXRD data previously discussed that shows the formation of a rocksalt-like phase, implying octahedral coordination. 1.99 Å is in the range that would be expected for octahedral vanadium compounds such as V_2O_3 (1.99 – 2.06 Å), VO_2 (1.91 – 1.99 Å) and Li_2VO_3 (1.9 – 2.05 Å). Since the material is reduced to accommodate the lithium ions, it is unlikely that the vanadium remains as V^{5+}. As the V-O bond distance is in between those found in V_2O_3 and VO_2, it could be inferred that the vanadium ions are mixed between V^{3+} and V^{4+}, which is what would be predicted based on the formula $Li_3V_2O_5$.

Based on Pythagoras' theorem, assuming a face centred cubic structure, the second peak, corresponding to the shortest V-V distance, should appear at 2.81 Å. The third peak should then appear at twice the V-O distance *i.e.*, 3.98 Å. However, this is not the case, with the second peak at 2.96 Å and the third at 4.06 Å. This means that whilst by PXRD, the material appears to be a rocksalt, it is slightly distorted. This agrees with previous literature, that suggests that the ω phase exists in the C2/m space group, rather than as a perfect Fm3-m structure.[291]

6.3.2. Structural changes in $Li_3V_2O_5$ on electrochemical cycling

The previous data confirms the presence of a rocksalt-like phase after the end of the first discharge. This means that the $Li_3V_2O_5$ can be formed *in situ* by lithiating V_2O_5, making this a convenient starting point to study further structural transformations on subsequent cycles. Figure 6.7 shows the galvanostatic charge-discharge data for the first cycle of V_2O_5 between 0.75 and 4.6 V.

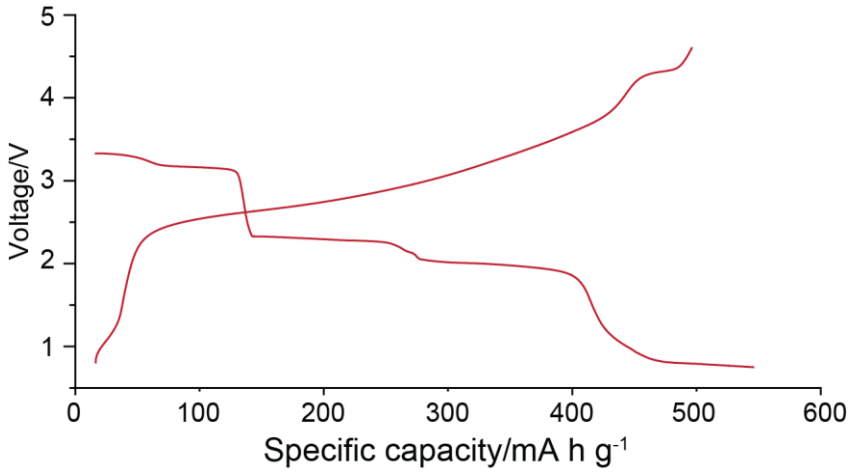

Figure 6.7: The galvanostatic charge-discharge plot for the first cycle of V_2O_5 between 0.75 and 4.6 V at C/20 (22 mA g^{-1}).

The data shown in Figure 6.7 shows that during charging the theoretical capacity of 440 mA h g^{-1} appears to be achieved by 4 V, although some of this capacity will arise from carbon being delithiated. Above 4.3 V, there is an additional plateau, indicating another process occurring. For example, it may be necessary to utilise O-redox to extract the lithium remaining in the structure. Alternatively, this could be due to electrolyte decomposition.

To study the changes that occur throughout the first charge, samples were prepared at 3, 3.5, 4 and 4.6 V. The PXRD patterns for these samples are shown in Figure 6.8.

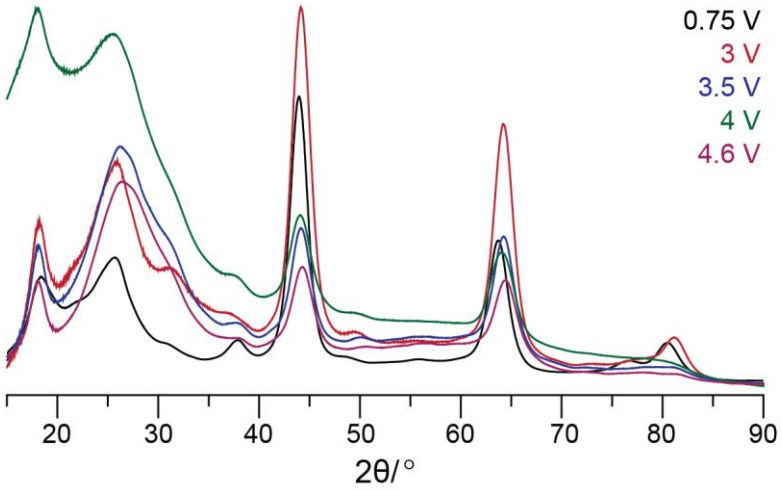

Figure 6.8: PXRD patterns for V_2O_5 at different voltages during the first discharge.

In Figure 6.8 the peaks at 44° and 64° are retained throughout cycling, although the intensity is reduced at high voltages. This suggests that the original DRX structure is retained somewhat when charged to high voltages, although it becomes less ordered leading to broader, lower intensity peaks. This is likely a consequence of lithium extraction, leading to partial structural collapse.

From Figure 6.8, it can also be seen that the peak at 25° shifts right as the voltage is increased. This peak corresponds to carbon black, a shift to higher angles indicates that it is being delithiated. This indicates that some of the observed capacity of the electrode likely comes from the carbon.[302]

Figure 6.9 shows the mass-normalised ^{7}Li NMR collected for the samples prepared during the first discharge

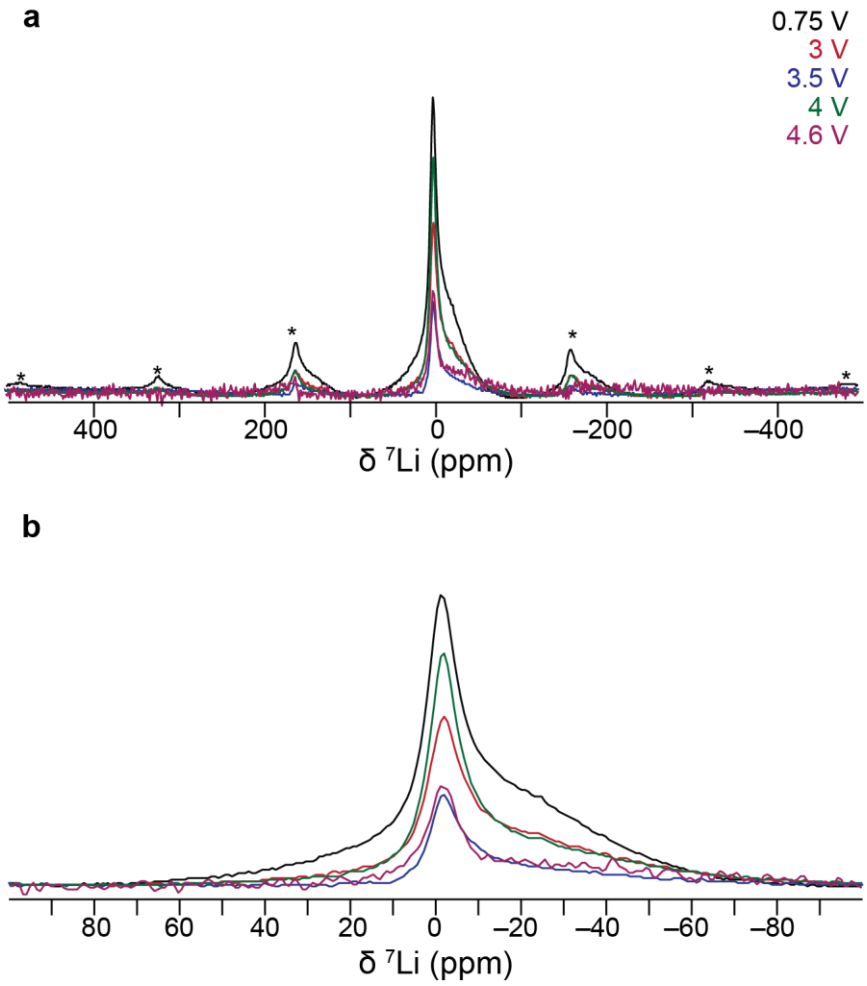

Figure 6.9: ^{7}Li NMR spectra recorded for the V_2O_5 electrodes at different states of charge during the first charge. (a) shows the full spectral width, whilst (b) shows the region around the isotropic peak (100 – –100 ppm). Spectra are the sum of 320 scans separated by a recycle delay of 3 s.

Throughout charging, the spectra retain the same overall shape previously discussed, with a sharp peak at 0 ppm and a broad peak to the right. This is consistent with the PXRD previously shown and further suggests that the structure that is created on discharging to 0.75 V is retained on charging. It can also be seen that as the voltage is increased, the intensity of the peaks decreases, which indicates that lithium is being removed from the sample, as would be expected on charging. The exception to this is the sample recorded at 4 V, which has significantly higher intensity before decreasing again at 4.6 V. This was observed in a second set of samples, and so likely is not experimental error. One explanation for this is that due to paramagnetism of the V^{3+} and V^{4+} ions a significant quantity of the lithium in the sample is invisible to NMR at lower voltages, as it relaxes too quickly to be detected. At 4 V, enough of the vanadium has oxidised to V^{5+} enabling more of the lithium to be seen. Another factor that may play a role is the migration of lithium

ions to tetrahedral sites. This has been investigated experimentally in the material $Li_{2-x}VO_3$ and was found to occur at 3.1 V.[303] Perhaps in this material it occurs at a higher voltage and may lead to the movement of lithium ions towards V^{5+} ions and therefore an increase in signal. A final point to mention is that there is still lithium present in the sample at 4.6 V, which means that it is not possible to remove all lithium from the structure, even at high voltages.

PDF patterns for the samples prepared from the first charge are shown in Figure 6.10.

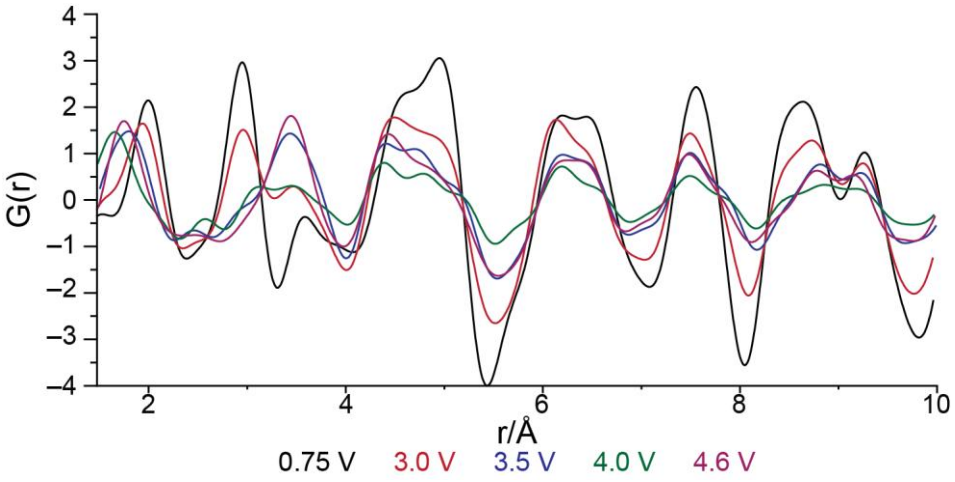

Figure 6.10: PDF data (r = 1.5 – 10 Å) collected for V_2O_5 at different states of charge during the first discharge.

As the voltage is increased, the position of the first peak shifts to smaller values of *r*. This means that the V-O bond is shortening and is consistent with oxidation of the vanadium ions. The exception to this is the 4 V sample which has a shorter V-O bond length than the 4.6 V. This implies that the V-O bond length contracts before expanding again, and this unexpected structural change may lead to the unexpected ^{7}Li results.

The PDF pattern for the sample prepared at 4.6 V has peaks at 1.74, 3.4, 4.4 and 4.87 Å. The shortest distance is likely the V-O bond length, meaning the next shortest distance is the V-O-V bond length, which appears at roughly twice the V-O bond length. Assuming again a cubic structure, the next distance would be the diagonal distance between vanadium ions on the corners of the unit cell at 4.81 Å. However, the presence of a peak at 4.4 Å once again suggests that this is distorted from a perfect cubic structure. Furthermore, there is no peak at 2.43 Å, which would correspond to the diagonal distance between vanadium ions on the corners and on the faces in a Fm3-m structure. This means that the structure is likely a primitive structure without ions on the faces of the unit cell, implying some migration of the vanadium ions.

To confirm that the structural transformations that occur on delithiation are reversible, a PXRD pattern, ^{7}Li NMR spectrum and a PDF pattern were acquired for a sample prepared after the second discharge to 0.75 V. These are shown in Figures 6.11, 6.12 and 6.13, respectively.

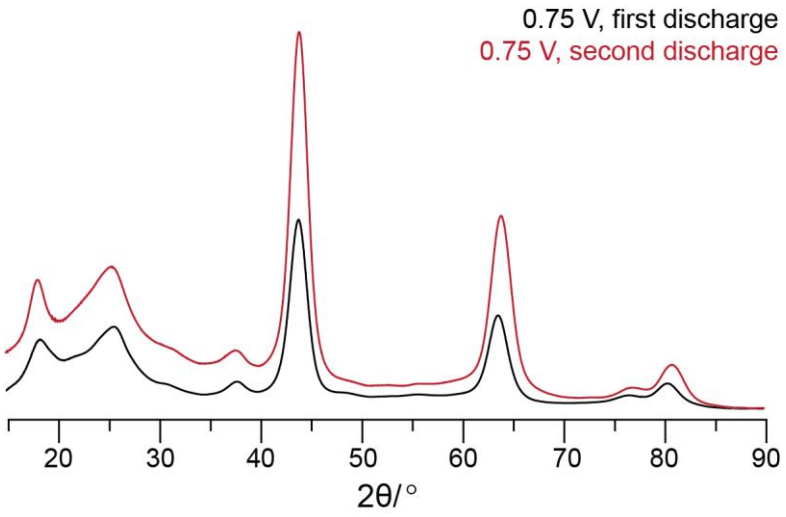

Figure 6.11: PXRD patterns collected for V_2O_5 at 0.75 V at the end of the first and second discharges.

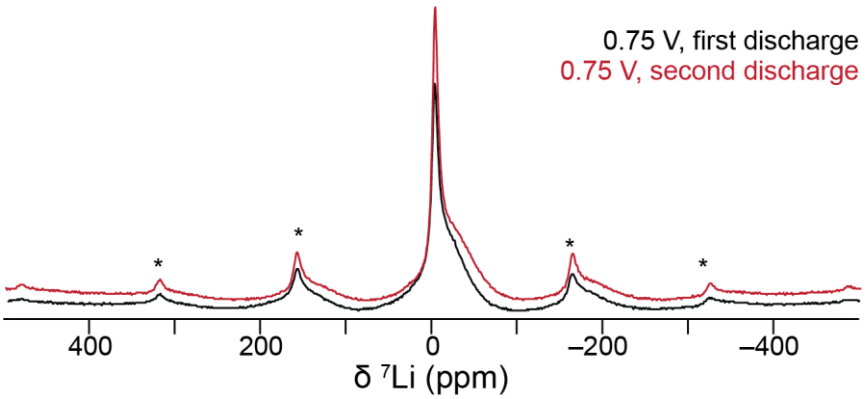

Figure 6.12: ^{7}Li NMR spectra recorded for V_2O_5 at 0.75 V at the end of the first and second discharges. Spectra are the sum of 320 scans separated by a recycle delay of 3 s.

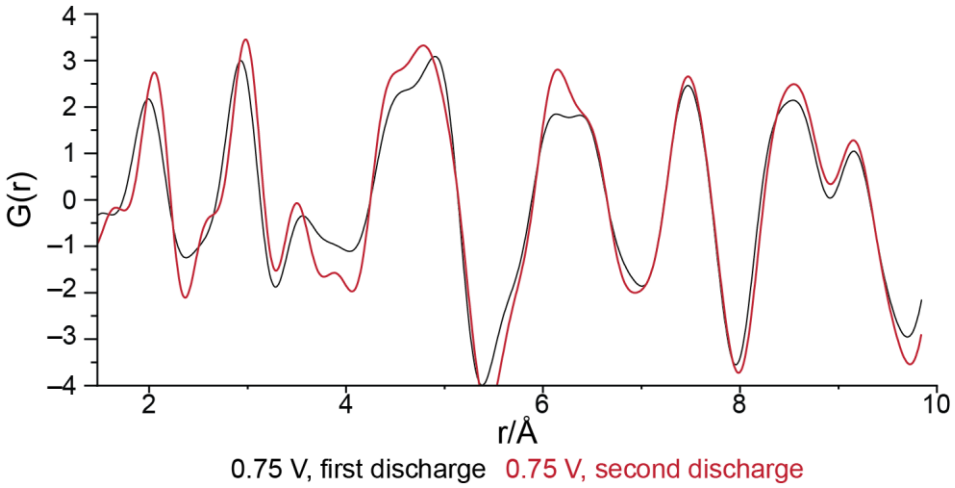

Figure 6.13: PDF data (r = 1.5 – 10 Å) collected for V_2O_5 at 0.75 V at the end of the first and second discharges.

The PXRD patterns shown in Figure 6.11 show that the peaks at 44.2 and 64.5° are present for both samples, indicating that the DRX phase is still present after the second discharge. This is supported by the ^{7}Li NMR spectra (Figure 6.12), which is similar for both samples as are the PDF patterns (Figure 6.13). However, the positions of the peaks in the PDF pattern recorded for the second discharge are shifted slightly, indicating that the process is not fully reversible.

6.3.3. Exploring the high-voltage behaviour of $Li_3V_2O_5$

The previous sections address the broad changes in structure that occur up to the second discharge. However, O-redox, if present, will occur at high voltages. ^{7}Li NMR is not very informative at high voltages because as the voltage is increased the amount of lithium present in the sample decreases, meaning that there are fewer nuclei to study. In addition, any regions with lithium still present likely have not undergone any reactions, meaning that ^{7}Li NMR may not provide insight into processes that are happening.

An alternative way to explore the high voltage region is to use ^{51}V NMR. This is because as the material is charged, the oxidation state of vanadium will increase towards V^{5+}, making ^{51}V more viable. Furthermore, regions that are observed will have had to have reacted to form V^{5+}, making this useful for studying the processes that are occurring above 4 V.

Initially, ^{51}V spectra were recorded at three voltages. These were 0.75 V (*i.e.*, at the end of the first discharge), 3 V and 4.6 V (during the first charge). This was done to see at whether

^{51}V NMR is viable, and if so, what approximate voltages are practical. The spectra recorded for these samples are shown in Figure 6.14.

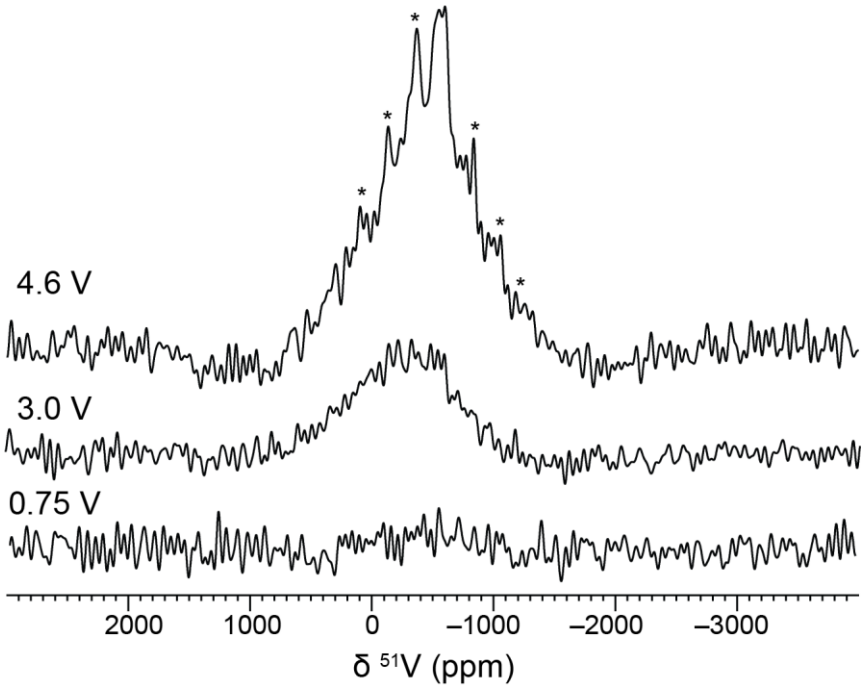

Figure 6.14: The ^{51}V spectra recorded for V_2O_5 at 0.75, 3 and 4.6 V. Spectra are the sum of 6400 scans separated by a recycle delay of 0.25 s. Asterisks denote spinning sidebands.

The ^{51}V spectrum recorded at 0.75 V shows no signal, consistent with the material containing entirely V^{3+} and V^{4+} ions. At 3 V, a broad peak is observed, centred at around –400 ppm. This indicates that there are some V^{5+} ions present, but the presence of many lower oxidation state ions nearby, results in a broadened peak. At 4.6 V there is an isotropic peak observed at –570 ppm. This can be attributed to lithiated V^{5+} phases.[178]

The ^{51}V spectra initially recorded suggest that ^{51}V NMR is particularly viable at high voltages, as would be expected. Therefore, further samples were prepared at voltages above 4 V. Spectra were acquired using frequency stepping to ensure no features of interest were missed. These spectra are shown in Figure 6.15.

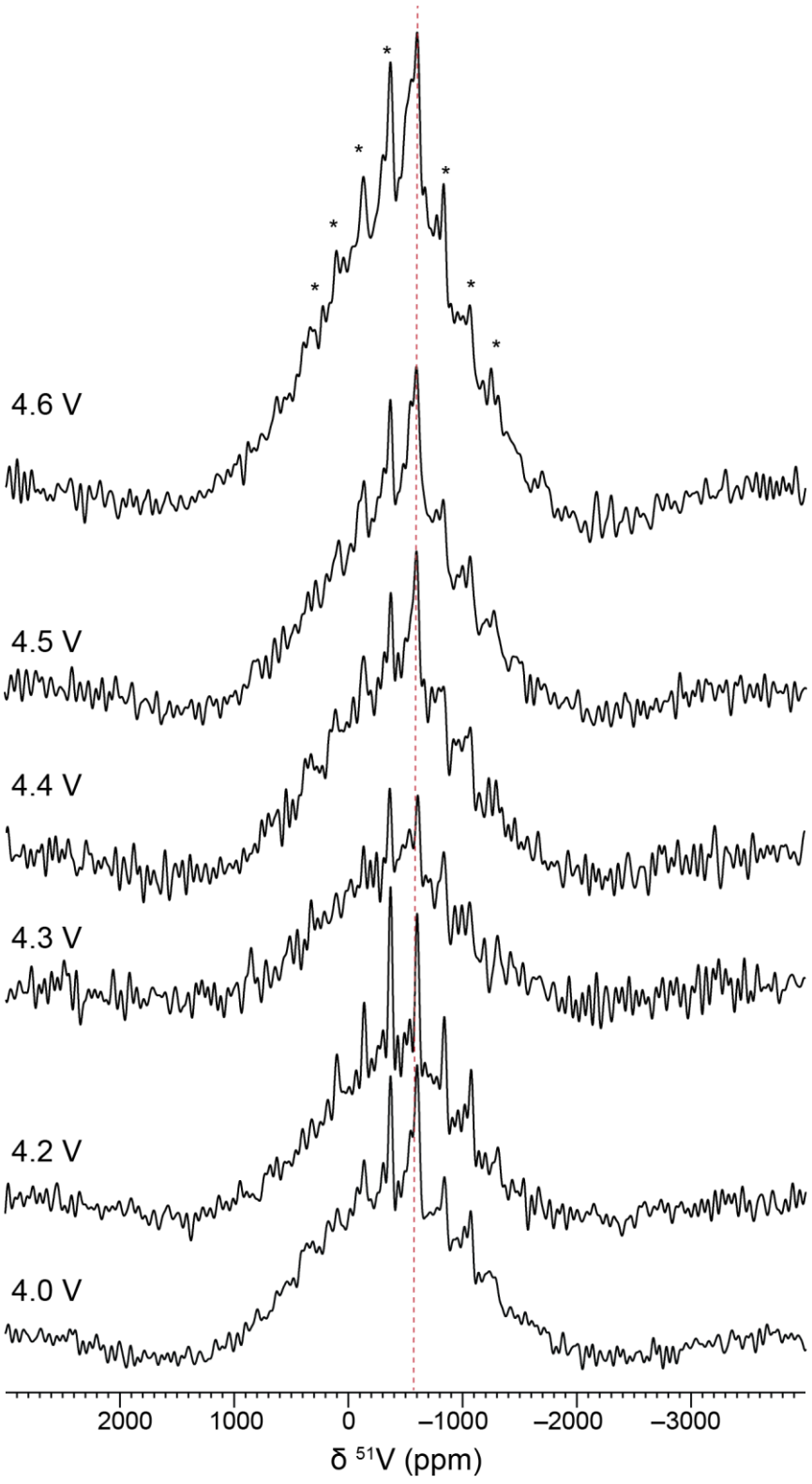

Figure 6.15: The ^{51}V spectra recorded for V_2O_5 above 4 V, obtained by frequency stepping. Frequency stepped spectra are comprised of four individual spectra of 6400 scans separated by a recycle delay of 0.25 s. Asterisks denote spinning sidebands, whilst the red line marks the position of the sharp feature in the spectra recorded for the 4.6 V sample.

All the frequency stepped spectra show a broad peak, several thousand ppm wide, with a sharp feature at ~–600 ppm. The sharp feature can be attributed to diamagnetic V^{5+} phase(s) whilst the broad feature likely comes from V^{5+} close to paramagnetic ions, with the breadth cause by increased relaxation. As the voltage is increased the intensity of the peaks increases (Figure 6.16). This is consistent with further oxidation of the vanadium ions.

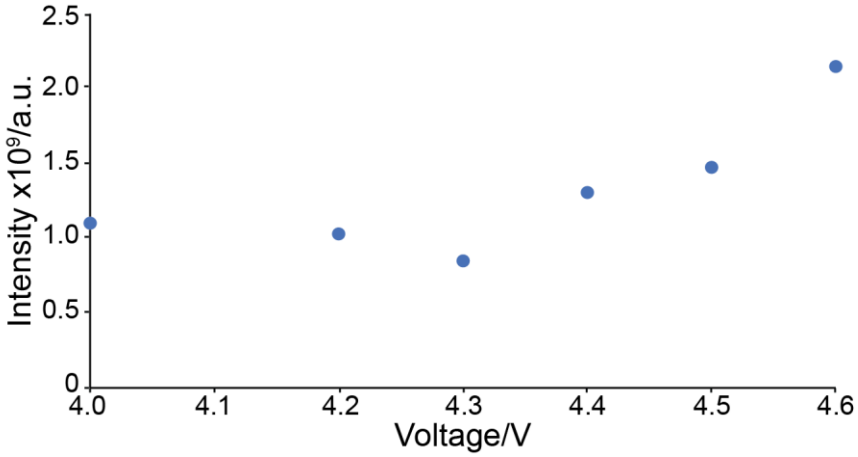

Figure 6.16: Intensities of the ^{51}V spectra shown in Figure 6.15.

The frequency stepped spectra all show a sharp peak at ~–600 ppm. This peak is broad and appears to contain two peaks. To discern more accurate chemical shifts, spectra were recorded overnight for each of the samples, with the offset frequency at the frequency of the peaks of interest. Whilst this means that the whole spectrum will not be excited, it will improve the signal-to-noise ratio of the region of interest. These spectra are shown in Figure 6.17.

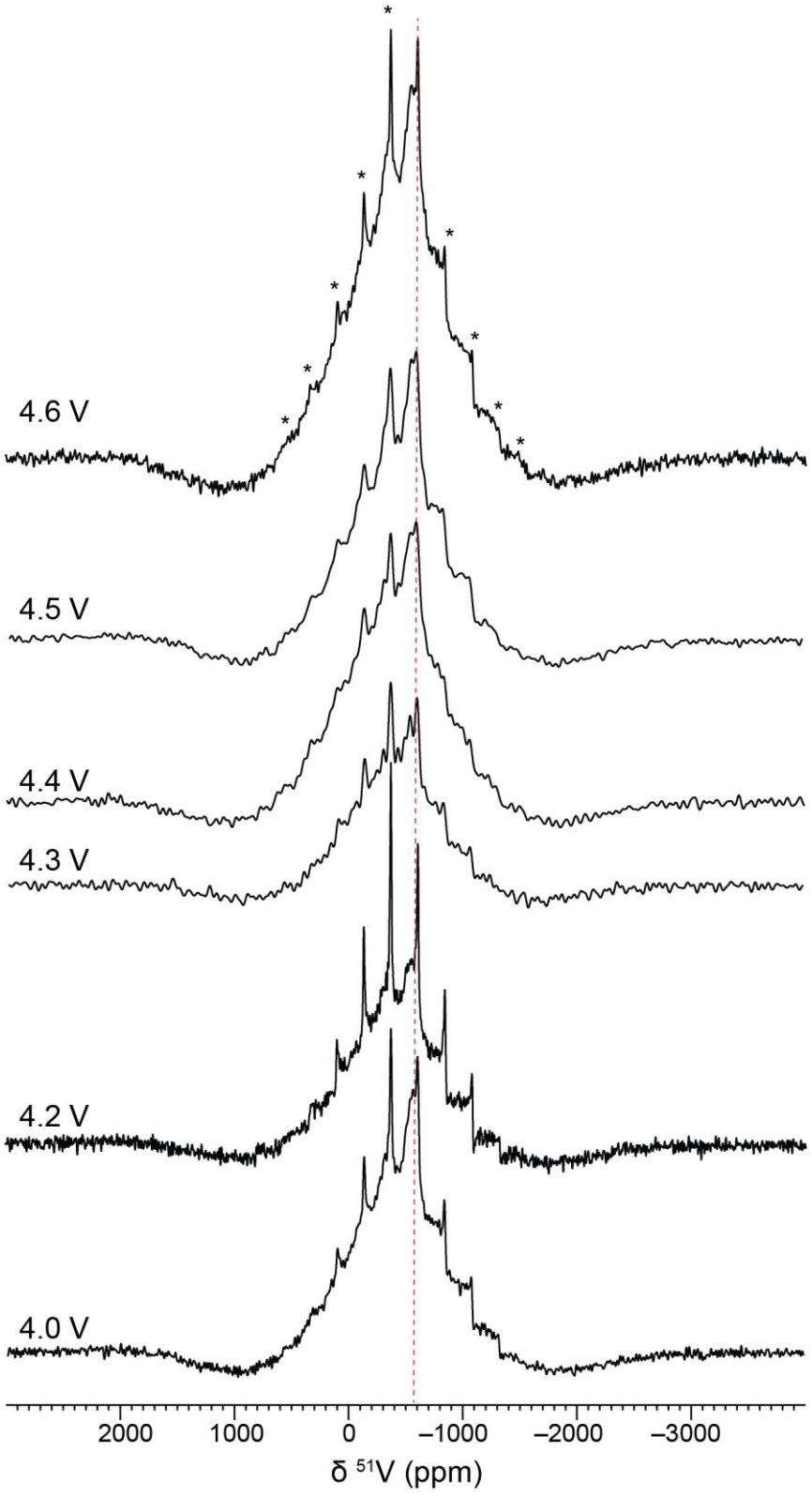

Figure 6.17: The ^{51}V spectra recorded for V_2O_5 at different voltages above 4 V, at an offset frequency of -45000 Hz. Spectra are the sum of 153600 scans separated by a recycle delay of 0.25 s. Asterisks denote spinning sidebands, whilst the red line marks the position of the sharp feature in the spectra recorded for the 4.6 V sample.

Due to the greater number of scans for these spectra, it is also now possible to more clearly see the sharp peaks appearing on the top of the broad peak. It is apparent that there are two peaks at –540 ppm and –600 ppm, and that these peaks grow with increased voltage. The peak at –600 ppm is similar in chemical shift to V_2O_5 (–610 ppm), and so this peak is likely fully delithiated regions of the sample with connected VO_x units and no lithium. The peak at –540 ppm is similar to that reported for Li_3VO_4.[178] This would suggest that there are isolated VO_x units separated from other vanadium units by lithium. This agrees with the ^{7}Li data that suggests that lithium is still present even at high voltages, as well as reports that isolated tetrahedral lithium sites are difficult to delithiate.[303] These assignments are also consistent with ^{51}V NMR literature that suggests increased lithiation of vanadium compounds leads to a more positive chemical shift.[273]

It is important to say that assigning ^{51}V peaks based solely on chemical shift is not ideal; however, in this case it is not possible to accurately measure chemical shift anisotropies, due paramagnetism and disorder giving rise to additional broadening.[178,273]

The characterisation up to this point has been performed *ex situ*, at specific voltages. This means that short-lived intermediate states or unstable species removed by washing, may have been missed. It was therefore decided to attempt *in situ* NMR measurements. *In situ* ^{7}Li NMR is relatively common, but as already mentioned, is likely not particularly informative at high voltages.[15,206,208,216] ^{51}V is more useful at high voltages, but has at the time of writing, not been reported.

In situ NMR experiments are performed under static conditions, due to the need to connect the cell to an external potentiostat. This means that the resolution is reduced, especially when compared to MAS spectra.[15] This can be mitigated to a degree depending on the system. For example, metallic lithium experiences a Knight shift, meaning that it is well resolved from diamagnetic species by several hundred ppm.[15,208] However, ^{51}V has a larger quadrupole moment than ^{7}Li, in addition to broadening from CSA.[178,188] Further broadening would also arise due to the paramagnetism of the vanadium ions. Despite this, it was decided that *in situ* ^{51}V experiments may highlight voltages of interest that could be the targets of further *ex situ* experiments.

Figure 6.18 shows the results of the *in situ* ^{51}V experiment performed. The cell was cycled twice at C/20 (22 mA g^{-1}), to allow enough time to acquire sufficient scans per row. After the end of the second cycle, the cell was left inside the magnet to see if any of the species formed at high voltages persist.

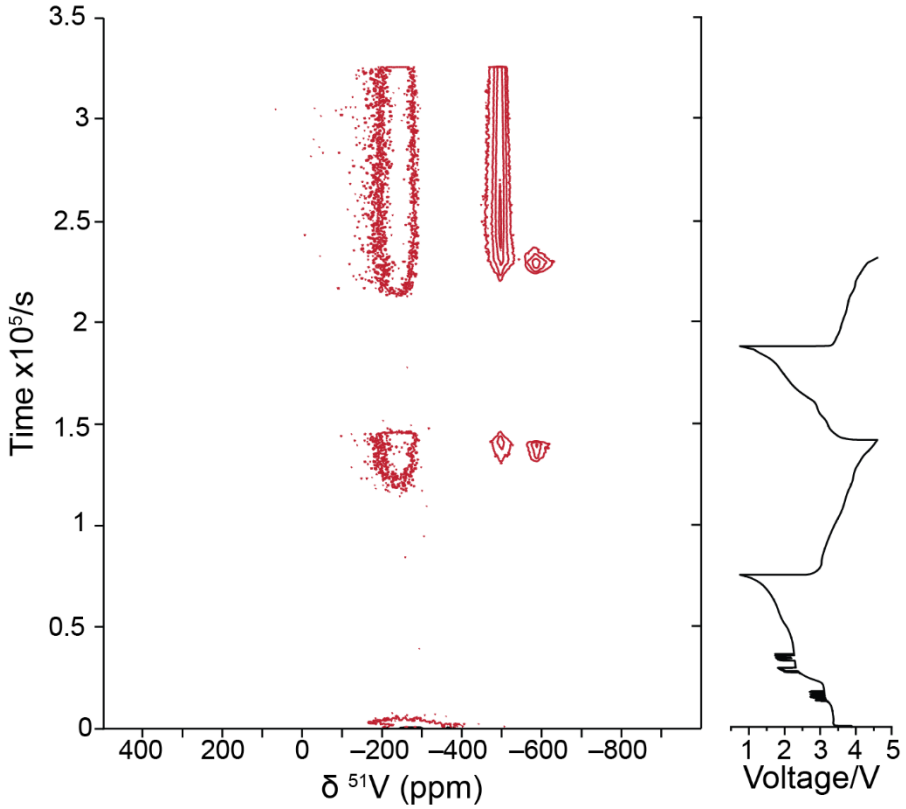

Figure 6.18: *In situ* ^{51}V NMR spectrum acquired for V_2O_5, cycled twice between 0.75 – 4.6 V. The spectrum is made up of 506 rows, with each row being the sum of 1024 scans, separated by a recycle delay of 0.5 s, for a total time of ~8.5 minutes per row.

At the start of the first discharge, a broad feature can be seen between –200 and –400 ppm, which can be attributed to V_2O_5. This quickly disappears, likely due to paramagnetic broadening once the vanadium ions start to be reduced. No signal is observed until around 3.8 V on the first charge, when the signal reappears before disappearing again at the start of the second discharge. This repeats on the second charge but the signal persists as the material is allowed to relax inside the magnet.

In addition, the broad peak, there are two sharp peaks that appear at above 4 V. The first is a peak at –500 ppm and the second appears at –590 ppm. These are observed for both cycles (Figure 6.19), with the first peak persisting as the cell is allowed to relax.

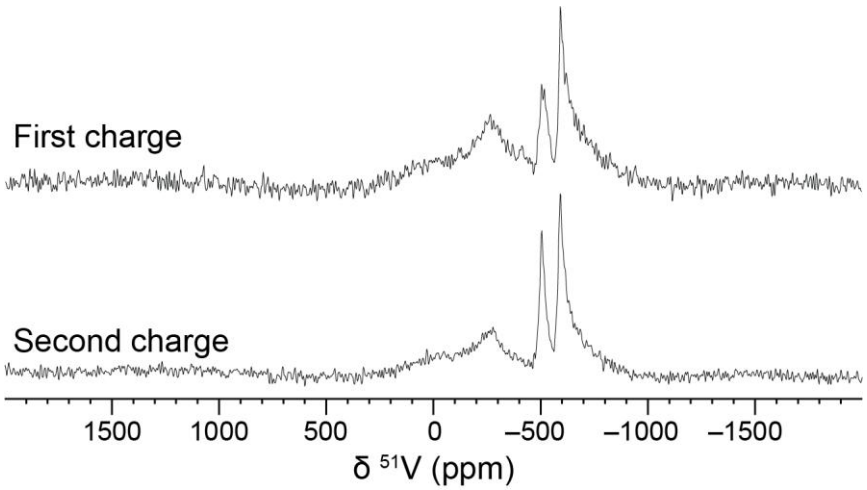

Figure 6.19: Rows 253 and 420 from the *in situ* ^{51}V experiment shown in Figure 6.18. These correspond to 4.6 V for the first and second charges respectively.

To understand what these peaks correspond to, the cell was disassembled, and the separator and electrode were repacked into separate rotors. It is worth noting that a green colour was observed on the separator, although this may just not have been noticeable on the black electrode. Static spectra were then recorded for both samples and are shown in Figure 6.20.

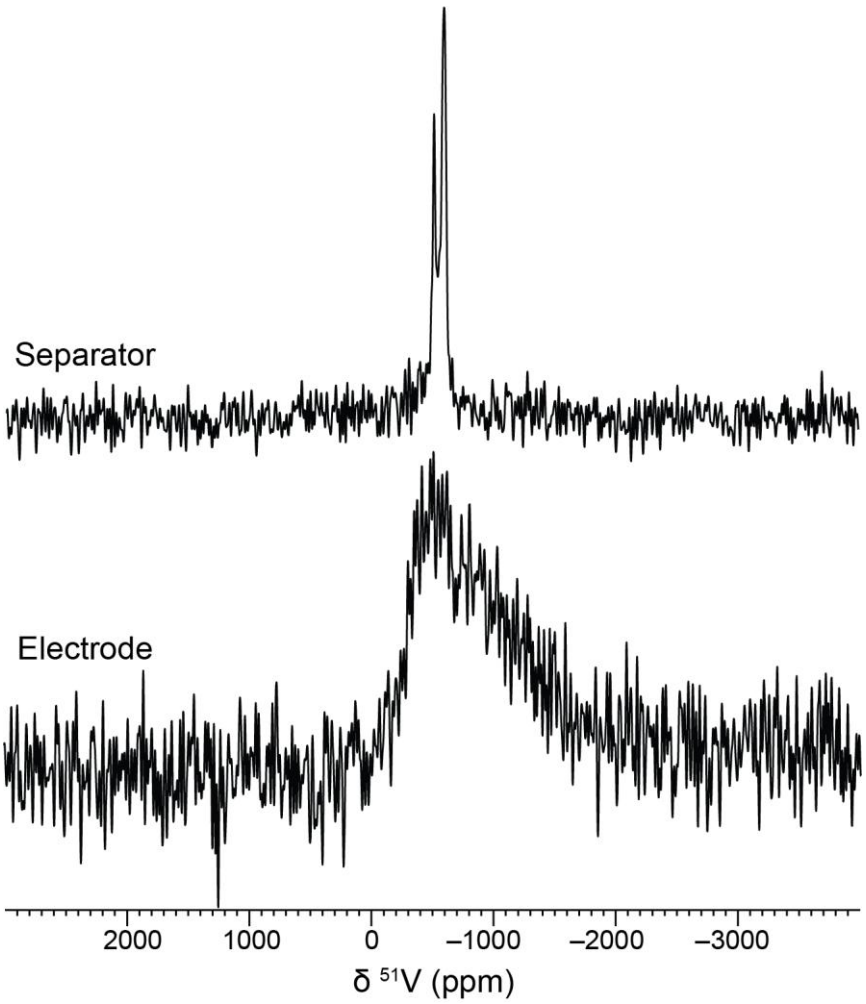

Figure 6.20: Static ^{51}V spectra acquired for the separator and V_2O_5 electrode taken from the *in situ* cell after cycling. Spectra were acquired using a Hahn echo and are the sum of 800 scans separated by a recycle delay of 0.5 s.

The spectrum recorded for the separator shows the two sharp peaks, whilst the spectrum shows a broad peak, which can be assigned to V^{5+} ions in the bulk electrode material, such as unreacted V_2O_5. This means that the species that give rise to the two sharp peaks likely reside in the electrolyte, in order to be observed in the separator. They are therefore likely V^{5+} species formed in solution due to the dissolution of vanadium out of the structure. This is known to occur below 1.5 V, although it is more pronounced at faster cycling rates.[286,304] However, the fact that there are two peaks, that appear and disappear at slightly different voltages, means that there are likely two species present. Considering the species present, the vanadium ions could coordinate to some combination of oxygen, phosphorus and fluorine atoms. Based on the chemical shifts reported, these are more likely to be coordinated to oxygen, as compounds with bonding to phosphorus and fluorine typically have more negative chemical shifts.[281,305] Vanadium dissolution also means that the structure of the DRX will become vanadium deficient. This means that there are fewer

vanadium ions available for charge compensation when extracting lithium ions, which may lead to O-redox at high voltages.

6.3.4. Behaviour of Li_2VO_2F at high voltages

O-redox may or may not be active in $Li_3V_2O_5$, and so it is useful to have a comparison material where O-redox is assumed to be inactive (or at least reduced). As already discussed, oxyfluorides typically have suppressed O-redox making LVOF a useful comparison. Therefore, cells were made using LVOF and cycled to the same voltages as used for the high voltage studies on $Li_3V_2O_5$. The galvanostatic charge plots for these cells are shown in Figure 6.21.

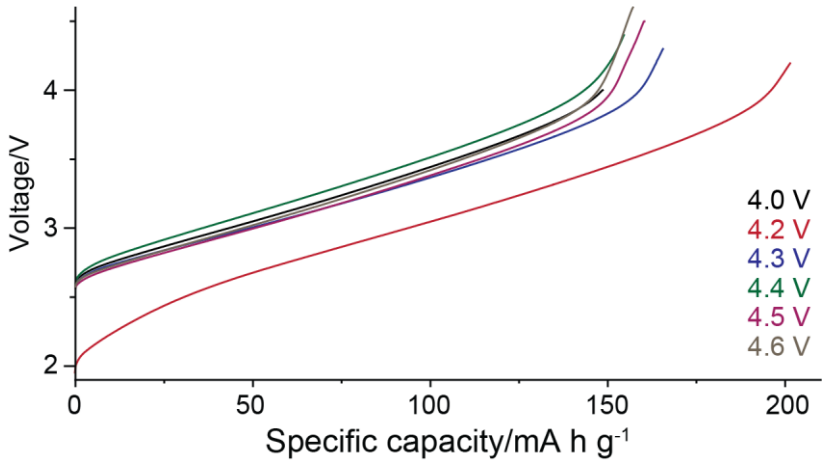

Figure 6.21: Galvanostatic charge plots for separate LVOF cells charged to above 4 V at a rate of C/20.

All the cells assembled have a capacity of around 150 mA h g^{-1}, except for the 4.2 V cell which achieves a capacity of around 200 mA h g^{-1}. This is likely due to the lower open circuit voltage of this cell (~2 V), which is likely caused by a small short circuit in the cell. Regardless, all of these capacities are much lower than the theoretical capacity. However, as discussed in the previous chapter, a lower capacity is consistent with previous literature and may be due to unintended oxidation of the precursors.[167,306] Furthermore, there is no additional plateau above 4 V as seen for $Li_3V_2O_5$. This suggests that whatever process gives rise to the plateau in $Li_3V_2O_5$ is not present here. Therefore, the process is perhaps not electrolyte decomposition, as this would likely also occur for LVOF as well. This could mean that the plateau is attributable to O-redox, but it may also be due to a structural rearrangement that occurs at high voltages.

Figure 6.22 shows the ^{51}V spectra recorded for LVOF over the same voltage range as $Li_3V_2O_5$.

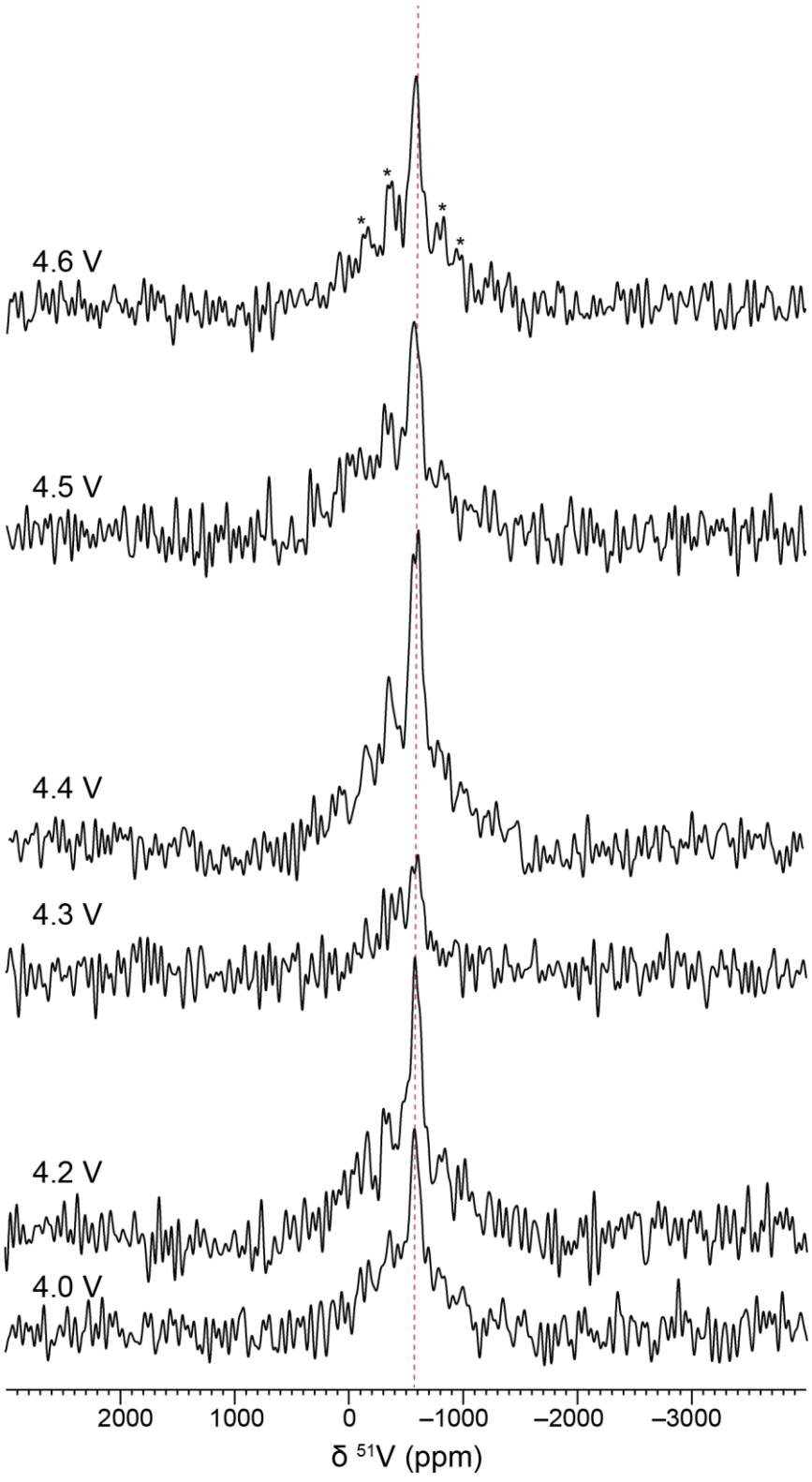

Figure 6.22: The ^{51}V spectra recorded for LVOF above 4 V, obtained by frequency stepping. Frequency stepped spectra are comprised of three individual spectra of 6400 scans separated by a recycle delay of 0.5 s. Asterisks denote spinning sidebands, whilst the red line marks the position of the sharp feature in the spectra recorded for the 4.6 V sample.

The ^{51}V spectra in Figure 6.22, show a single peak at ~–580 ppm along with spinning sidebands. As discussed in the previous chapter, this can be assigned largely to V^{5+} impurity phases. The intensity of the signal observed also does not increase steadily with increasing voltage. This is consistent with the electrochemistry shown in Figure 6.21, as negligible capacity is observed above 4 V. Negligible capacity means that the oxidation of vanadium (from V^{3+} to V^{5+}) has largely finished, and so the intensity of the ^{51}V signal should not increase.

6.3.5. Evolution of the local structure of oxide anions

The work discussed so far has involved probing the structure of the DRX materials using diffraction-based techniques and solid-state NMR. However, none of these techniques probe the local structure of the oxide anions directly, which is important when probing O-redox. Several techniques have been used in literature to try and address this. The following sections attempted to use three techniques previously described: RIXS, ^{17}O NMR and EPR spectroscopy.

6.3.5.1. Resonant inelastic X-ray scattering

RIXS is perhaps one of the most popular, yet controversial ways of studying O-redox. Inelastically-scattered X-rays lead to additional peaks in the RIXS spectra, the spacings of which can be used to determine if there are any species with O-O bonds and identify the specific species.[142,144]

Figure 6.23 shows the RIXS data collected for the pristine V_2O_5 electrode as well as V_2O_5 charged to 4.4 and 4.6 V.

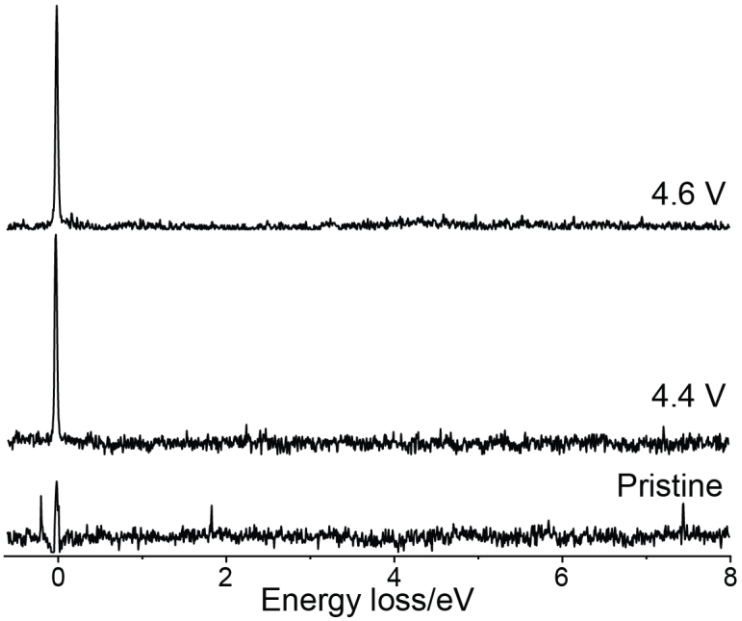

Figure 6.23: O K-edge (531 eV) RIXS spectra for pristine V_2O_5 and $Li_3V_2O_5$ charged to 4.4 and 4.6 V.

All three RIXS spectra show a peak at 0 eV, which arises due to elastic processes.[142,235] No additional features are observed as the signal-to-noise ratio for all three spectra is poor. There may be some very weak features around the elastic peak for the 4.6 V sample, but it is not possible to confirm this.

RIXS data was also collected for LVOF charged to 3, 4 and 4.4 V as shown in Figure 6.24. Equivalent samples were also attempted for V_2O_5, however problems with the beam meant that these could not be measured.

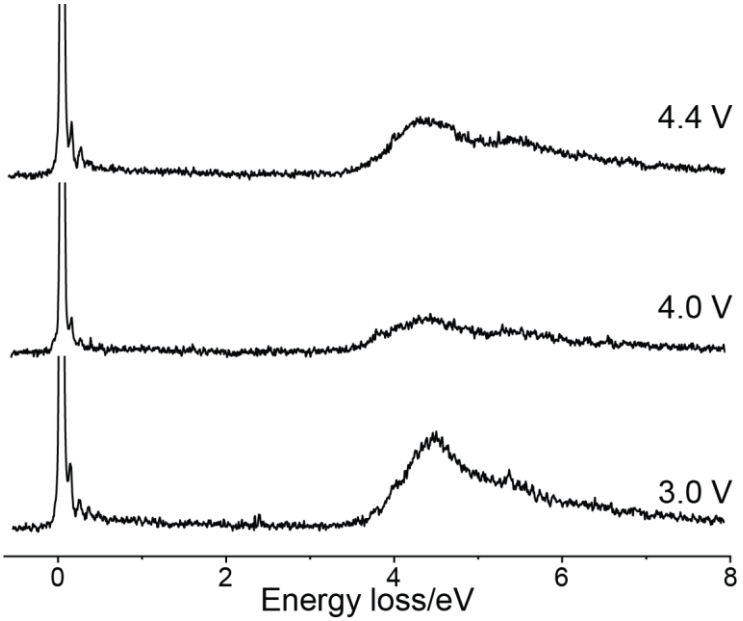

Figure 6.24: O K-edge (531 eV) RIXS spectra for LVOF charged to 3, 4.4 and 4.6 V.

In addition to the elastic peak, the spectra in Figure 6.25 show a broad feature between 4 and 6 eV. Similar features have been attributed in other works to "oxidised oxygen" species. However, in this case this seems unlikely. This is because this feature is observed for the sample prepared at 3 V, which is likely too low for O-redox to occur. The intensity of this feature does vary between samples, but this is likely due to the overall intensity of the spectrum being lower, due to differences in sample quality. Such variations were also observed for the successful V_2O_5 samples, with the intensity of the elastic peak varying between samples.

The region around the elastic peak (0 – 0.5 eV) also contains additional peaks, that could indicate the presence of reactive oxygen species. Figure 6.25 shows an expanded view of this region whilst Table 6.1 displays the positions of the peaks.

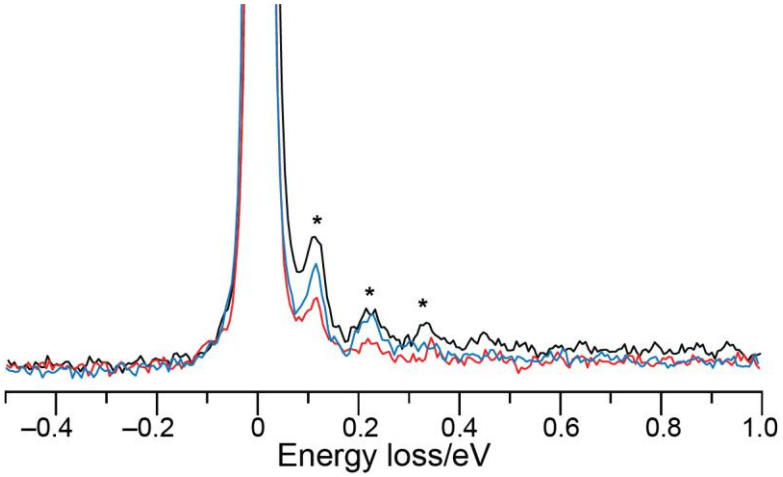

Figure 6.25: The region of the O K-edge (531 eV) RIXS spectra recorded for LVOF around the elastic peak around the elastic peak (–0.5 – 1 eV).

Table 6.1: Positions of the peaks observed in the RIXS spectra for the charged samples of LVOF.

Sample	Peak position/eV			Average
	1	2	3	separation/eV
3 V	0.113	0.223	0.330	0.109
4 V	0.114	0.223	0.343	0.115
4.4 V	0.118	0.231	-	0.113

Figure 6.25 shows that all three spectra have peaks at ~0.11 – 0.12 eV. This is followed by other peaks at ~0.22 – 0.23 eV and possibly 0.33 – 0.34 eV, although the poor signal-to-noise ratio means that it is difficult to determine accurate peak positions. Typically, this information is used to construct a Birge-Sponer plot, from which the energy of the vibration can be determined.[136] However, this is not possible here given the limited number of peaks observed.

Considering the average spacing between the peaks observed, it is likely that these peaks do not come from molecular oxygen as a spacing of 0.18 eV would be expected for such a species. The observed spacing however is much closer to an O_2^- species. What is interesting is that these species are first observed in LVOF, where O-redox should in principle be inactive and second are observed at relatively low voltages (3 V). This suggests that these species form through processes other than O-redox as it is classically imagined. One possible explanation is that these species are caused by beam damage, but they may also be from intrinsic defects.[144]

6.3.5.2. ^{17}O solid-state NMR

Another method that has been reported in literature as a way of studying O-redox is to use ^{17}O NMR. As discussed in Chapter 2, House *et al* supposedly observe molecular oxygen forming on charging, although Bassey *et al* argue that this assignment is incorrect, as the reported chemical shift does not match what would be expected for molecular oxygen.[142,154] Despite this, it might be possible to see the ^{17}O signal appear as the vanadium is oxidised to V^{5+} before dying away as the oxide anions are oxidised and molecular oxygen potentially produced.

V_2O_5 was enriched with $^{17}O_2$ gas by heating at 600°C for 72 hours. To verify that this process does not alter the structure of the material PXRD patterns and ^{51}V NMR spectra were recorded for the enriched material as well as unenriched, natural abundance V_2O_5. This data is shown in Figures 6.26 and 6.27.

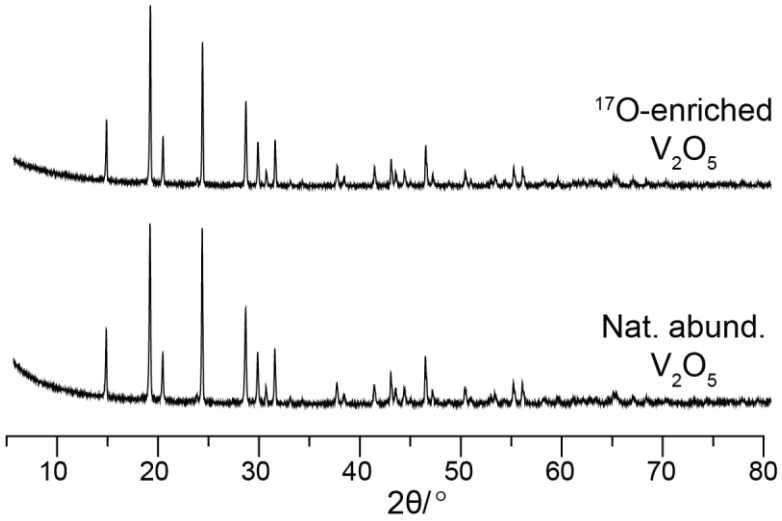

Figure 6.26: PXRD patterns recorded for ^{17}O-enriched V_2O_5 and natural abundance V_2O_5.

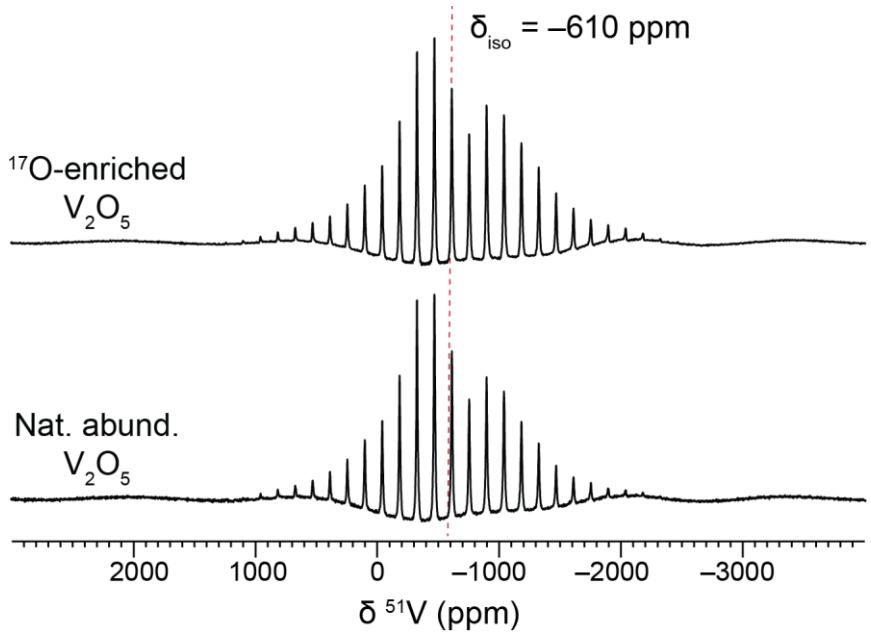

Figure 6.26: ^{51}V NMR spectra recorded for ^{17}O-enriched V_2O_5 and natural abundance V_2O_5. Spectra were acquired using a single pulse-acquire experiment and are the sum of 64 scans with a recycle delay of 3 s. The red line denotes the isotropic peak (–610 ppm), with all other peaks being spinning sidebands.

The PXRD patterns show good agreement with each other, as do the ^{51}V NMR spectra. This indicates that enrichment has not noticeably affected the long-range structure of the material as well as its local structure. ^{17}O NMR was then performed to verify that the material had been enriched. This is shown in Figure 6.28.

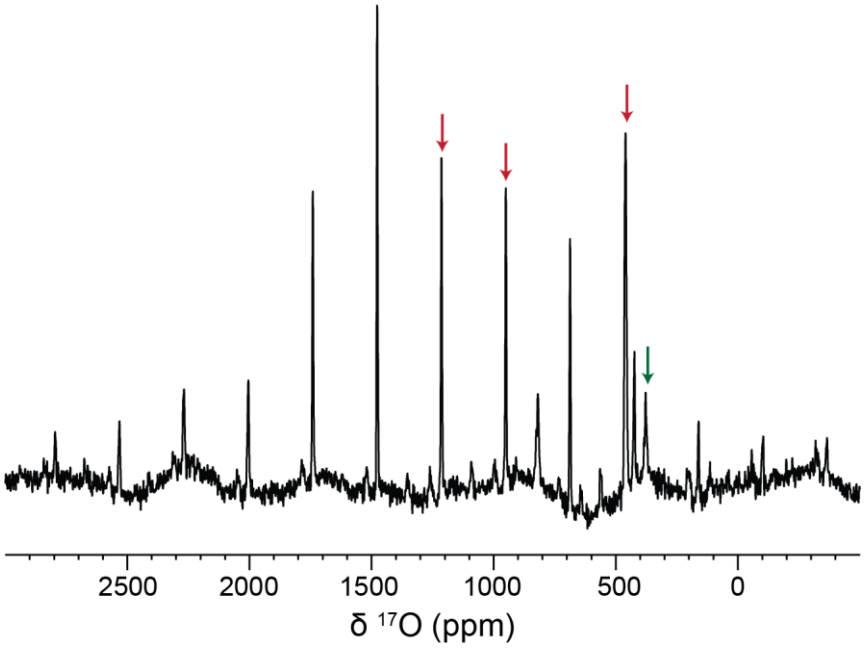

Figure 6.27: ^{17}O NMR spectrum for ^{17}O-enriched V_2O_5. The spectrum is the sum of 1024 scans with a recycle delay of 30 s. The red arrows denote the sites of V_2O_5 whilst the green arrow indicates the ZrO_2 peak. All other peaks are spinning sidebands.

A ^{17}O signal is observed for the enriched V_2O_5, with sites being observed at 460, 950 and 1210 ppm. This would be expected based on the crystal structure, as the unit cell contains three unique oxygen sites.[307] However, a peak is also observed at 380 ppm. This can be attributed to zirconia from the rotor, and the fact that it is visible means that the enrichment level is not very high.[178] Despite this, a cell was assembled and cycled to 4.6 V, to see if it is possible to observe a signal. However, no signal was observed (Figure 6.28) aside from a very weak peak at 380 ppm, which can once again be attributed to the rotor. This is likely due to the paramagnetism of the sample with not all the vanadium ions being fully oxidised. In addition, it may also be because the enrichment level is not high enough. V_2O_5 decomposes at 690°C, and so higher temperatures are not accessible.[308]

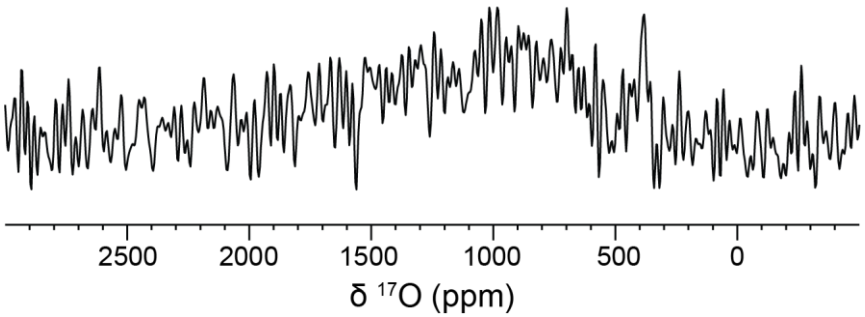

Figure 6.28: ^{17}O NMR spectrum for ^{17}O-enriched V_2O_5 charged to 4.6 V. The spectrum was acquired using a Hahn echo sequence and is the sum of 174080 scans separated by a recycle delay of 0.25 s.

6.3.5.3. Electron paramagnetic resonance spectroscopy

The final technique for characterising O-redox that will be considered in this chapter is EPR spectroscopy. This has been used by the group of Tarascon to highlight the formation of O_2^{n-} species.[309] Therefore, EPR spectra were recorded for $Li_3V_2O_5$ self-standing electrodes at different states of charge. These are shown in Figure 6.29.

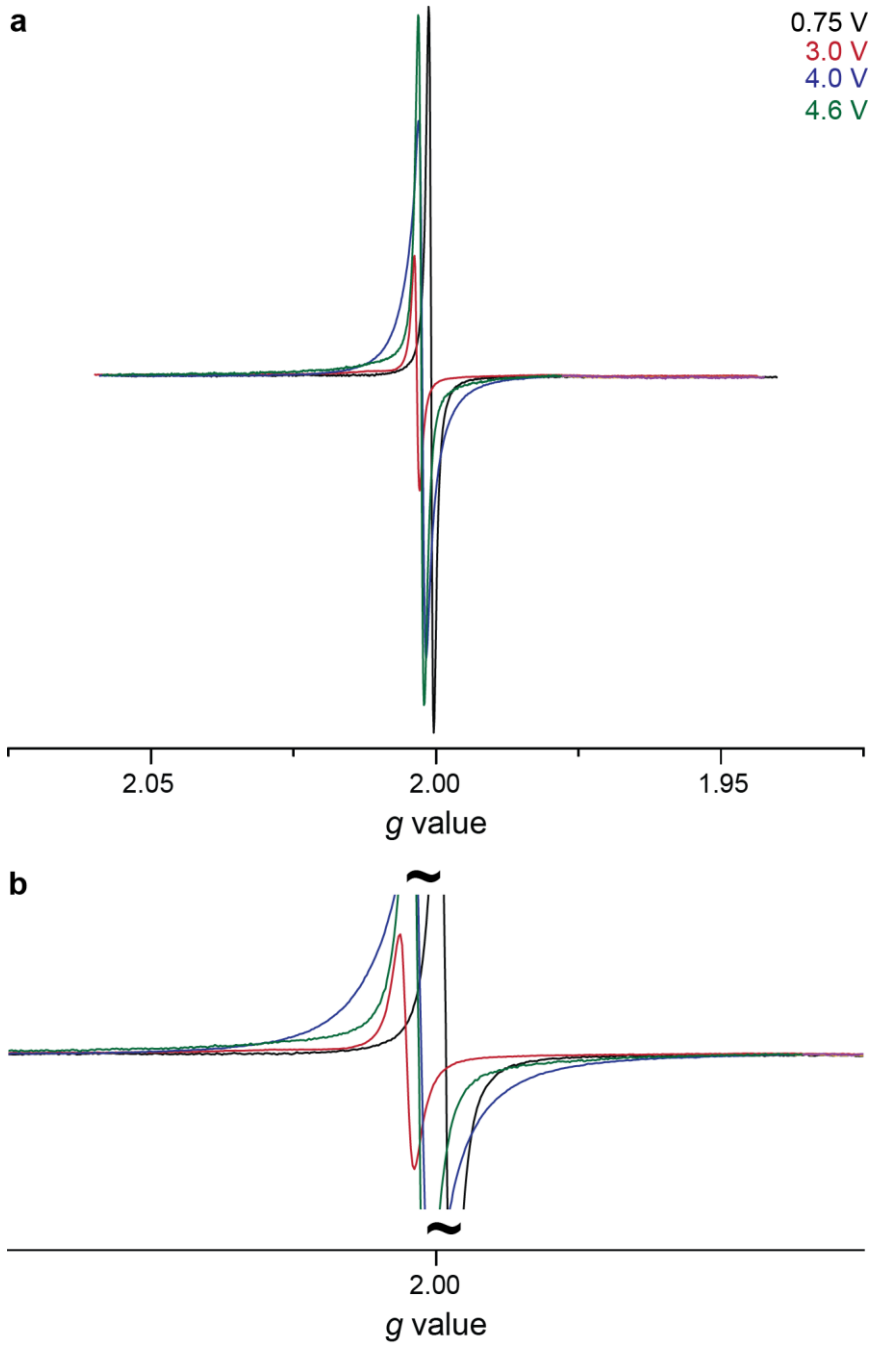

Figure 6.29: EPR spectra recorded for V_2O_5 at different states of charge. (b) shows an enlarged view of the region about $g = 2$

The EPR spectrum for the sample recorded at 0.75 V shows a signal centred at g = 2.001. On charging to 3 V, the intensity decreases and the signal shifts to g = 2.003. The peak then shifts slightly again to g = 2.002 when charged to 4 V and the intensity grows again. Charging to 4.6 V sees the intensity increase once again but the position does not shift. The changing g value of the peak suggests that the structure of the radical varies throughout cycling, or that multiple paramagnetic species appear throughout cycling.

Considering first the nature of the unpaired electron that is present at 0.75 V, the immediate assignment would be that this signal comes from vanadium ions in the DRX material. Both V^{3+} and V^{4+} are paramagnetic, although only V^{4+} is observable using this spectrometer (as V^{3+} is a non-Kramer's ion). This could explain why the signal intensity decreases on charging to 3 V, as vanadium ions start to be oxidised to V^{5+}, giving an observable ^{51}V NMR signal (Figure 6.15). However, g values for V^{4+} ions are often on the order of 1.93 – 1.98.[310,311] The observed g value of 2.001 therefore may be slightly too high for this signal to come from V^{4+} ions. This may seem counterintuitive, as the bulk of the material at this point will be V^{3+}/V^{4+}. However, these signals may still be present but are dominated by the signals observed that come from species with smaller g-anisotropies and therefore have much more intense lines. On the basis of g value, it can also be said that the other paramagnetic species formed at higher voltages also likely are not V^{4+} ions.

Based on the work described in Chapter 4, another possible source of radicals could be degradation of the PTFE binder. With this in mind, powder electrodes were prepared by mixing V_2O_5 with carbon black in a 2:1 ratio. Figure 6.30 shows the EPR spectra recorded for these cells. Samples were also prepared using only carbon black, to isolate any contributions coming specifically from carbon black (Figure 6.31)

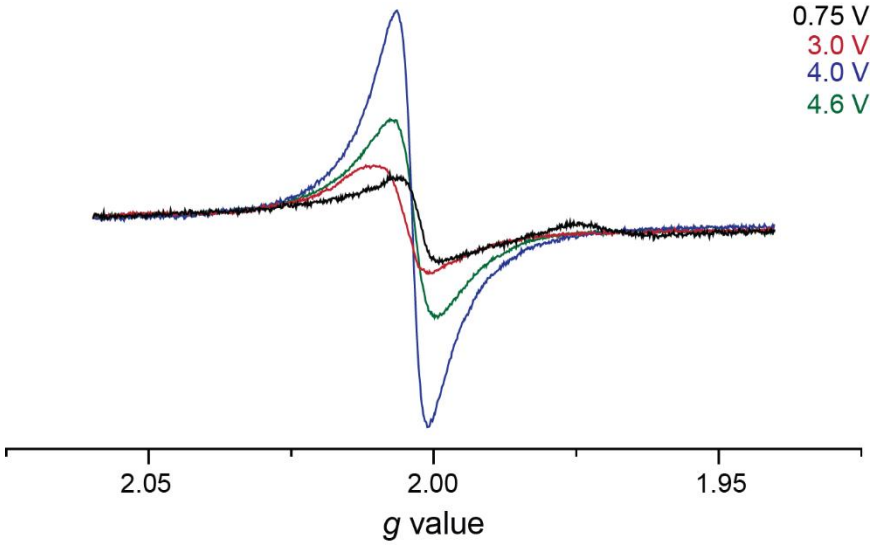

Figure 6.30: EPR spectra recorded for the V_2O_5/carbon black mixture at different states of charge.

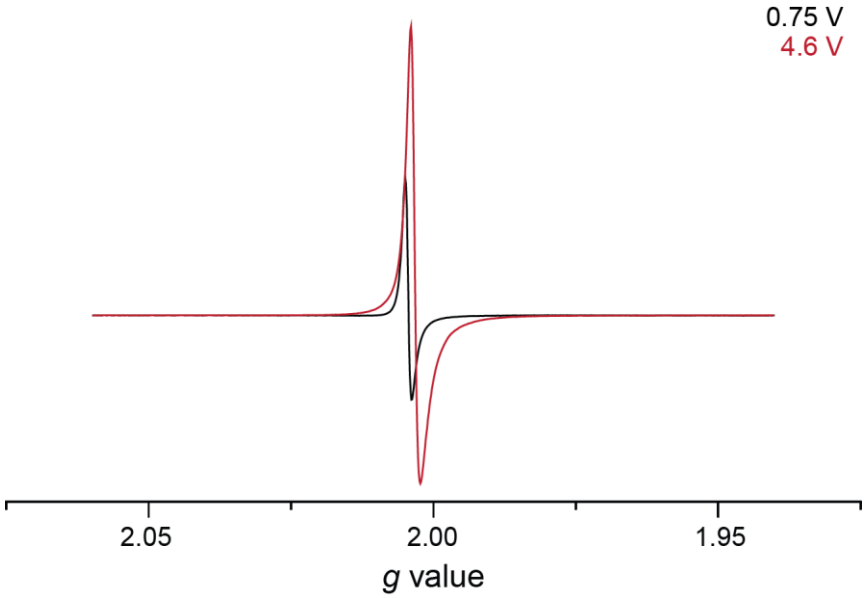

Figure 6.31: EPR spectra recorded for carbon black at different states of charge.

The spectrum recorded for the V_2O_5/carbon black mixture at 0.75 V shows two features at g = 2.002 and g = 1.974. These can be assigned to carbon-based radicals and V^{4+} ions based on their g values.[311,312] The intensity of these peaks is also significantly reduced from the signal observed for the full self-standing electrode, as can be seen from the reduced signal-to-noise and the fact that the V^{4+} peak is observable. This means that the intense feature seen in the spectrum for the self-standing electrode is likely primarily from the decomposition of PTFE. On charging to 3 V the signal shifts to g = 2.004 before shifting back to g = 2.003 at 4 and 4.6 V, which mirrors the shift observed for the self-standing electrode samples, although there are slight discrepancies in the g value measured. This

may be because there are no longer contributions from PTFE, which could cause the apparent position of the peak to shift right. The intensity of the signal measured also grows between 3 and 4 V, which suggests that new paramagnetic species are formed, this trend does not continue when charging to 4.6 V.

The spectrum recorded for carbon black discharged to 0.75 V shows a peak at g = 2.004. This is slightly different compared to the V_2O_5/carbon black mixture at the same state of charge (g = 2.002). The peaks are also asymmetric, with respect to the baseline. This means that the g-tensor for pure carbon is axial, rather than isotropic as in the case of V_2O_5 mixed with carbon. Furthermore, the spectrum recorded for the pristine carbon black is also much narrower (1 G vs 11 G). These differences suggest that the paramagnetic species are different, perhaps because of the phase transitions V_2O_5 undergoes, breaking up the carbon black particles. Grinding the two powders together could also reduce particle size.

The spectrum recorded for carbon black charged to 4.6 V has a g value of 2.003, meaning that it has shifted relative to the sample prepared at 0.75 V. In addition, the intensity of the peak grows. This suggests that the properties of carbon black change throughout cycling, can are likely the cause of the changes observed for the V_2O_5/carbon black mixture.

The RIXS spectra recorded for LVOF indicate the presence of oxidised oxygen species, despite O-redox being assumed to be inactive in this material. EPR spectra were therefore recorded for the pristine material, and LVOF mixed with carbon black at 3, and 4 V. These are shown in Figure 6.32.

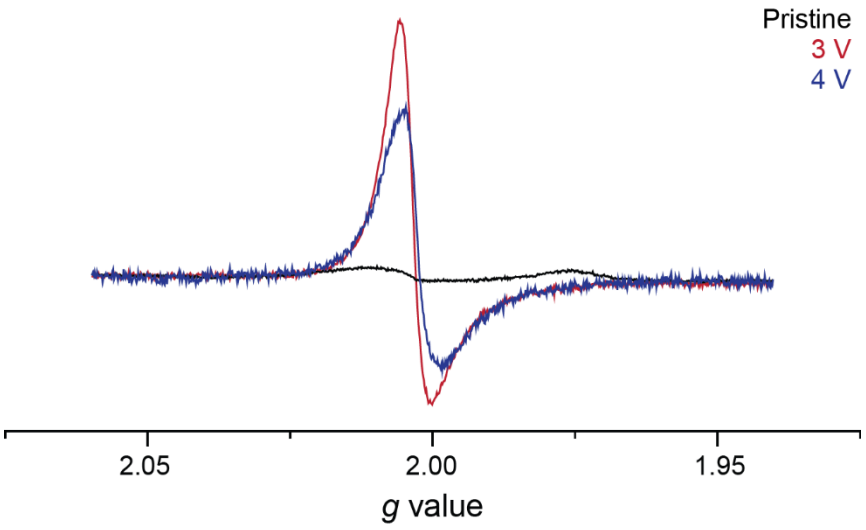

Figure 6.32: EPR spectra recorded for the LVOF/carbon black mixture at different states of charge.

The spectrum recorded for the pristine material shows two peaks at g = 2.003 and g = 1.974, which as with the discharged V_2O_5 sample, can be assigned to carbon-based radicals and V^{4+} ions respectively. Whilst low levels of V^{4+} ions would be expected due to oxidation of the precursor, carbon-based radicals should not be present in this material. This is likely background from the rotor or residual electrode inside the rotor from previous samples, based on the blank spectrum recorded (Figure 6.33).

The spectra recorded for LVOF charged to 3 and 4 V show peaks centred at g = 2.002, with axial symmetry, which can be attributed to carbon black, as already discussed for Figure 6.31. The fact that the symmetry of the peak is the same, unlike for the V_2O_5 sample suggests that the change in tensor symmetry is due to something related to V_2O_5 as already suggested. The increased peak width (9 G) is likely a consequence of grinding the active material powder with carbon black, as the width is more like what was seen for the V_2O_5 samples, rather than the pristine material.

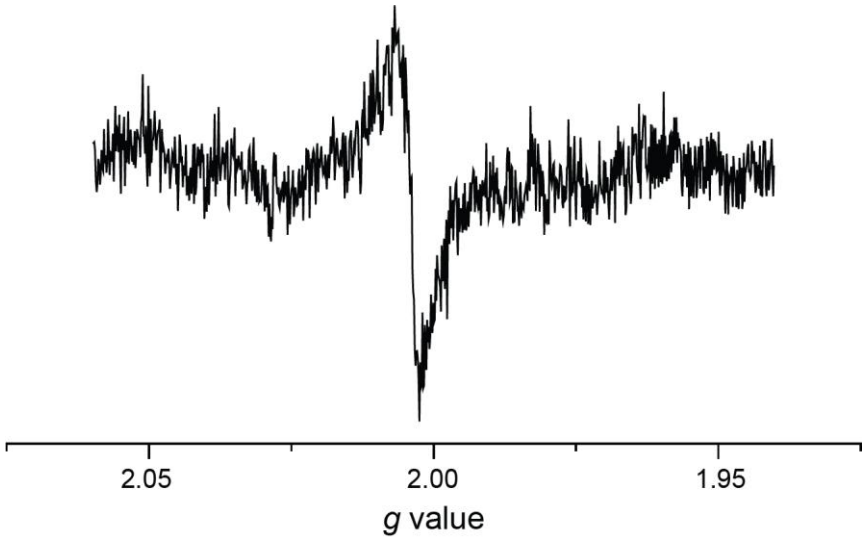

Figure 6.33: EPR spectrum recorded for KBr packed into a 2.5 mm rotor.

6.4. Discussion

The objective of the work in this chapter was to study the structural changes that occur in DRX materials when O-redox is active. For this purpose, $Li_3V_2O_5$ was chosen as it is redox-active, but the vanadium ions can be oxidised to V^{5+} (d^0) at high voltages. This makes this material more amenable to study by solid-state NMR, allowing the local structure to be more thoroughly investigated. Structural changes could then be correlated with any oxygen species formed, and compared to the behaviour of LVOF, where O-redox is in principle, inactive.

First, considering the electrochemical data collected, $Li_3V_2O_5$ has an additional plateau above 4 V, indicating a new process occurring at high voltages. One possible explanation is that this is due to electrolyte decomposition. However, a similar plateau is not observed for LVOF. This implies that this is due differences in the material, as the same electrolyte was used for both cells. Furthermore, work by Asl *et al*, shows that the phases that form prior to the DRX phase, do not exhibit this plateau even at high voltages.[279] This means that this is perhaps unique to the DRX phase. Given that this plateau is not present for LVOF, the next possible explanation is that this could indicate O-redox processes, hence why it appears at high voltages. This cannot be confirmed or excluded by the RIXS data, due to the poor data quality. A similar situation is true with the ^{17}O NMR. The EPR data does show signals at high voltages, but these signals can be attributed to the carbon black additive and the PTFE binder. This means that it is likely no EPR-observable oxygen species are present. However, it is difficult to fully exclude the possibility of such species being present, as the expected g value (2.007) overlaps with the peaks observed for carbon. Weak signals from oxygen species could therefore be dominated by other signals.

Another explanation is that the high voltage plateau is caused by a structural rearrangement that occurs at high voltages. The intensities of the ^7Li NMR spectra do not follow a trend with the sample prepared at 4 V showing greater amounts of lithium than the cells prepared at lower voltages. This could suggest that the material structure changes, moving the lithium ions away from paramagnetic vanadium ions, meaning that the signal intensity is higher. This is further supported by the PDF data which shows that the V-O distance expands between 4 and 4.6 V. As already mentioned, LVOF does not show this high voltage plateau. The capacities however for LVOF are much lower than those achieved for $Li_3V_2O_5$. This could mean that this structural rearrangement only occurs when

significant amounts of lithium are extracted from the structure, a condition that LVOF does not fulfil.

These two explanations for the high voltage plateau are not mutually exclusive as any rearrangement could be driven by the onset of O-redox or structural rearrangement could allow O-redox to become active. However, the results presented here there is no evidence of oxidised oxygen species from the data collected, although it is also not possible to exclude their presence.

It is also worth discussing the RIXS signals observed for LVOF. The signals observed suggest that oxidised oxygen species are present in LVOF after charging. This is unusual as O-redox should be limited or inactive in this material and it is observed at relatively low voltages (3 V). EPR however does not provide any evidence to support the presence of these species which means that the species observed by RIXS may be caused by the measurement itself causing reactive species to form.

6.5. Conclusions

The work presented in this chapter studied the structural transformations that occur in the model DRX material $Li_3V_2O_5$. This was prepared by the electrochemical lithitaition of V_2O_5, the formation of which follows the same mechanism as the chemically lithitated phases previously reported. On charging to above 4.6 V, this material shows an additional plateau, which may be due to the structure rearranging when significant amounts of lithium are extracted from the structure. It is possible that this could be due to or facilitated by O-redox, however no evidence of oxidised oxygen species was obtained from the results collected.

6.6. Future work

A key part of this work was observing oxidised oxygen species, but only limited evidence of such species was observed using RIXS. However, it is difficult to say that O-redox is not present as the species of interest may not have been observed due to experimental issues. Therefore, it would be useful to revisit some of the methods used and attempt other methods reported in literature. The ^{17}O enrichment of V_2O_5 was unsuccessful, however this could provide an interesting route to study these materials further. Any further enrichment by the method used here would likely be limited owing to the relatively low decomposition temperature of V_2O_5. Therefore, enrichment would need to be achieved by other means such as by oxidising V_2O_3 or VO_2, to form V_2O_5. This would likely require atmospheres with very high oxygen content to oxidise the lower oxides fully to V_2O_5.[313] DEMS could also be used to see if any molecular oxygen is released, although it might be difficult to determine whether these come from electrolyte decomposition or O-redox. *In situ* EPR experiments, like those performed by Sathiya *et al*, could also allow short-lived paramagnetic species to be observed, that may be lost during *ex situ* sample preparation.[309] However, these may still encounter the problem that EPR signals form the carbon additive used may dominate any species of interest. This could be mitigated to a degree by using other types of carbon that have less pronounced EPR signals. The data presented suggests that properties of the radical can be changed by preparing and cycling electrodes, which could suggest that different carbons have different EPR signatures. It would therefore be necessary to first investigate different carbon types, under the conditions to be used for the EPR measurements.

The *in situ* ^{51}V measurements performed in this chapter provide an interesting way to potentially study other materials, but it is not clear what the species in solution are. Therefore, the separator should be studied with ^{7}Li, ^{19}F and ^{31}P NMR to assist in identifying any species. Given that ^{51}V is spin-7/2, any J-coupling, particularly in the ^{19}F spectra collected should be readily apparent. It may also be interesting to study the first discharge process with *in situ* ^{7}Li NMR, to better understand the formation of the different $Li_xV_2O_5$ phases.

The ^{51}V spectra collected are very broad and so it is difficult to extract in-depth information from them. pj-MATPASS experiments were attempted but did not yield any further insight. However, repeating the experiments using much faster MAS (> 100 kHz) would massively improve the resolution compared to the 25 kHz MAS frequency used in this work. Furthermore, all of the vanadium spectra are acquired using a rotor-synchronised Hahn echo sequence. Faster MAS frequencies would reduce the delay required and reduce the amount of signal lost due to T_2 relaxation. The smaller rotor diameter required for these MAS frequencies (0.7 mm) would likely not pose an issue in terms of sample volume as most of the volume of a 2.5 mm rotor is taken up by KBr, with only several milligrams of electrode being present in the rotor. Even more routine speeds of 60 kHz would be beneficial. Lower magnetic field strengths could also help to reduce paramagnetic effects, although this may make acquiring spectra difficult given the low sample volumes and moderate sensitivity of ^{51}V.

7. Conclusions

This thesis explored the local structure of materials for lithium-ion batteries using a range of characterisation techniques, chief among them SSNMR. Chapter 4 focussed on protective surface coatings for high-voltage materials whilst Chapters 5 and 6 investigated the bulk structure of DRX materials.

Plasma polymerisation was investigated as an alternative way of preparing protective coatings. The coatings were characterised using XPS, EPR and NMR and initial investigations into their electrochemical performance were conducted. Whilst coatings were successfully deposited, plasma deposition was noted to result in the removal of surface species, and the formation of radicals in some substrates investigated. Precursor molecules were also found to adhere to the substrate surface. These observations explain previously reported EPR signals for coatings derived from the TEMPO radical and highlight that the deposition of plasma polymers is more nuanced than is often portrayed. No substantial effect on electrochemical behaviour was observed beyond the first cycle when the coatings were applied. However further investigation is needed into this, especially exploring other potential precursors

When using SSNMR to explore the bulk structure of paramagnetic electrode materials, such as DRXs, there are a number of experimental techniques that can be employed. However further insight can be gained by selecting appropriate model materials, that are diamagnetic models. Chapter 5 explored the structure of oxyfluoride DRXs using a scandium-based analogue. This allowed for in-depth characterisation using ^{6}Li, ^{19}F and ^{45}Sc NMR, as well as CASTEP calculations. From this a structural model was constructed, showing that LiF is, in part, incorporated into the DRX phase, rather than existing as an impurity. There is also evidence of direct bonding between transition metal cations and fluoride anions. This information was then used to understand the electrochemical behaviour of DRX materials. DRXs prepared by ball milling retain their DRX structure throughout cycling. In contrast, DRXs produced by electrochemical lithiation do not, with the coordination of the fluoride decreasing ions changing when the material is discharged, leading to the destruction of the DRX phase.

Diamagnetic analogue materials are not always appropriate, particularly when the processes of interest are driven by electrochemical activity such as O-redox. In such cases an

alternative approach is to choose a material that is diamagnetic at the state of charge of interest. Vanadium-based DRXs were studied as in principle, complete oxidation of the vanadium ions will render the material diamagnetic. However, it was not possible to fully delithitate the structure. Therefore, whilst new V^{5+} phases can be observed by ^{51}V NMR, indicating a structural transformation occurs at high voltages, it is difficult to fully elucidate the structure. However, the data collected shows promise and acquiring spectra using faster MAS may sufficiently address the paramagnetic broadening encountered. In addition, *in situ* ^{51}V NMR allows for the observation of vanadium species formed when vanadium ions dissolve out of the structure. This approach therefore may be of use to study other vanadium-based cathode materials.

The work presented in this thesis demonstrates ways that SSNMR can be combined with other techniques to provide information about surfaces and paramagnetic materials, that are often considered challenging. The structural insights presented may give some guidance to those preparing and studying similar materials.

References

1 UK House of Lords STSC, *Science and Technology Select Committee. Battery strategy goes flat : Net-zero target at risk*, 2021.

2 *Faraday Report - March 2020, Annual Gigafactory study: UK electric vehicle and battery production potential to 2040*, 2020.

3 B. Dunn, H. Kamath and J. M. Tarascon, *Science*, 2011, **334**, 928–935.

4 R. Borah, F. R. Hughson, J. Johnston and T. Nann, *Materials Today Advances*, 2020, **6**, 100046.

5 R. A. Huggins, *Advanced Batteries: Material Science Aspects*, Springer, 2009.

6 F. Wang, R. Robert, N. A. Chernova, N. Pereira, F. Omenya, F. Badway, X. Hua, M. Ruotolo, R. Zhang, L. Wu, V. Volkov, D. Su, B. Key, M. Stanley Whittingham, C. P. Grey, G. G. Amatucci, Y. Zhu and J. Graetz, *Journal of the American Chemical Society*, 2011, **133**, 18828–18836.

7 J. B. Goodenough and K. S. Park, *Journal of the American Chemical Society*, 2013, **135**, 1167–1176.

8 O. Ramstrom, *Scientific Background on the Nobel Prize in Chemistry 2019: Lithium-Ion Batteries*, 2019.

9 A. J. Bard and L. R. Faulkner, *Electrochemical Methods: Fundamentals and Applications*, John Wiley & Sons, 2001.

10 W. B. Jensen, *Journal of Chemical Education*, 2012, **89**, 1208–1209.

11 G. Fang, J. Zhou, A. Pan and S. Liang, *ACS Energy Letters*, 2018, **3**, 2480–2501.

12 Y. Ugata, C. Motoki, K. Dokko and N. Yabuuchi, *Journal of Solid State Electrochemistry*, 2024, **28**, 1387–1401.

13 J. H. Chang, C. Baur, J. M. Ateba Mba, D. Arčon, G. Mali, D. Alwast, R. J. Behm, M. Fichtner, T. Vegge and J. M. Garcia Lastra, *Journal of Materials Chemistry A*, 2020, **8**, 16551–16559.

14 E. Talaie, P. Bonnick, X. Sun, Q. Pang, X. Liang and L. F. Nazar, *Chemistry of Materials*, 2017, **29**, 90–105.

15 O. Pecher, J. Carretero-Gonzalez, K. J. Griffith and C. P. Grey, *Chemistry of Materials*, 2017, **29**, 213–242.

16 Y. Zhong, X. Yang, R. Guo, L. Zhai, X. Wang, F. Wu, C. Wu and Y. Bai, *Electrochemical Energy Reviews*, DOI:10.1007/s41918-024-00230-z.

17 L. Wang, L. Zhang, Q. Wang, W. Li, B. Wu, W. Jia, Y. Wang, J. Li and H. Li, *Energy Storage Materials*, 2018, **10**, 16–23.

18 B. Rowden and N. Garcia-Araez, *Energy Reports*, 2021, **7**, 97–103.

19 L. Zhang, C. Zhu, S. Yu, D. Ge and H. Zhou, *Journal of Energy Chemistry*, 2022, **66**, 260–294.

20 C. P. Sandhya, B. John and C. Gouri, *Ionics*, 2014, **20**, 601–620.

21 M. H. Hossain, M. A. Chowdhury, N. Hossain, M. A. Islam and M. H. Mobarak, *Chemical Engineering Journal Advances*, DOI:10.1016/j.ceja.2023.100569.

22 M. Krajewski, B. Hamankiewicz, M. Michalska, M. Andrzejczuk, L. Lipinska and A. Czerwinski, *RSC Advances*, 2017, **7**, 52151–52164.

23 E. J. Moon, J. K. Hong, S. K. Mohanty, M. Yang, K. Ihm, H. Lee and H. D. Yoo, *Journal of Power Sources*, DOI:10.1016/j.jpowsour.2023.232657.

24 X. Zuo, J. Zhu, P. Müller-Buschbaum and Y. J. Cheng, *Nano Energy*, 2017, **31**, 113–143.

25 A. L. Michan, G. Divitini, A. J. Pell, M. Leskes, C. Ducati and C. P. Grey, *Journal of the American Chemical Society*, 2016, **138**, 7918–7931.

26 G. F. I. Toki, M. K. Hossain, W. U. Rehman, R. Z. A. Manj, L. Wang and J. Yang, *Industrial Chemistry & Materials*, 2024, **2**, 226–269.

27 G. F. I. Toki, M. K. Hossain, W. U. Rehman, R. Z. A. Manj, L. Wang and J. Yang, *Ind. Chem. Mater.*, 2024, **2**, 226–269.

28 J. Jyoti, B. P. Singh and S. K. Tripathi, *Journal of Energy Storage*, DOI:10.1016/j.est.2021.103112.

29 A. Manthiram, *Nature Communications*, 2020, **11**, 1550.

30 Z. Xu, K. Song, X. Chang, L. Li, W. Zhang, Y. Xue, J. Zhang, D. Lin, Z. Liu, Q. Wang, Y. Yu and C. Yang, *Carbon Neutralization*, 2024, **3**, 832–856.

31 J. U. Choi, N. Voronina, Y. K. Sun and S. T. Myung, *Advanced Energy Materials*, DOI:10.1002/aenm.202002027.

32 T. Ohzuku and Y. Makimura, *Chemistry Letters*, 2001, 744–745.

33 A. R. Haworth, B. I. J. Johnston, L. Wheatcroft, S. L. McKinney, N. Tapia-Ruiz, S. G. Booth, A. J. Nedoma, S. A. Cussen and J. M. Griffin, *ACS Applied Materials and Interfaces*, 2024, **16**, 7171–7181.

34 U. H. Kim, D. W. Jun, K. J. Park, Q. Zhang, P. Kaghazchi, D. Aurbach, D. T. Major, G. Goobes, M. Dixit, N. Leifer, C. M. Wang, P. Yan, D. Ahn, K. H. Kim, C. S. Yoon and Y. K. Sun, *Energy and Environmental Science*, 2018, **11**, 1271–1279.

35 C. Tomon, S. Sarawutanukul, N. Phattharasupakun, S. Duangdangchote, P. Chomkhuntod, N. Joraleechanchai, P. Bunyanidhi and M. Sawangphruk, *Communications Chemistry*, DOI:10.1038/s42004-022-00670-y.

36 T. R. Somo, T. E. Mabokela, D. M. Teffu, T. K. Sekgobela, B. Ramogayana, M. J. Hato and K. D. Modibane, *Coatings*, 2021, **11**, 1–22.

37 G. H. Waller, P. D. Brooke, B. H. Rainwater, S. Y. Lai, R. Hu, Y. Ding, F. M. Alamgir, K. H. Sandhage and M. L. Liu, *Journal of Power Sources*, 2016, **306**, 162–170.

38 S. Choi, W. Feng and Y. Xia, *ACS Omega*, 2024, **9**, 18688–18708.

39 X. Zhu, A. Huang, I. Martens, N. Vostrov, Y. Sun, M. I. Richard, T. U. Schülli and L. Wang, *Advanced Materials*, DOI:10.1002/adma.202403482.

40 Y. Fang, J. Zhao, Y. Su, J. Dong, Y. Lu, N. Li, H. Wang, F. Wu and L. Chen, *Energy Material Advances*, DOI:10.34133/energymatadv.0115.

41 J. Hu, W. Huang, L. Yang and F. Pan, *Nanoscale*, 2020, **12**, 15036–15044.

42 V. Etacheri, R. Marom, R. Elazari, G. Salitra and D. Aurbach, *Energy and Environmental Science*, 2011, **4**, 3243–3262.

43 H. Wang, X. Li, F. Li, X. Liu, S. Yang and J. Ma, *Electrochemistry Communications*, 2021, **122**, 106870.

44 M. Gauthier, T. J. Carney, A. Grimaud, L. Giordano, N. Pour, H. H. Chang, D. P. Fenning, S. F. Lux, O. Paschos, C. Bauer, F. Maglia, S. Lupart, P. Lamp and Y. Shao-Horn, *Journal of Physical Chemistry Letters*, 2015, **6**, 4653–4672.

45 S. Haber and M. Leskes, *Advanced Materials*, DOI:10.1002/adma.201706496.

46 R. Fong, U. von Sacken and J. R. Dahn, *Journal of The Electrochemical Society*, 1990, **137**, 2009–2013.

47 J. Xiao, N. Adelstein, Y. Bi, W. Bian, J. Cabana, C. L. Cobb, Y. Cui, S. J. Dillon, M. M. Doeff, S. M. Islam, K. Leung, M. Li, F. Lin, J. Liu, H. Luo, A. C. Marschilok, Y. S. Meng, Y. Qi, R. Sahore, K. G. Sprenger, R. C. Tenent, M. F. Toney, W. Tong, L. F. Wan, C. Wang, S. E. Weitzner, B. Wu and Y. Xu, *Nature Energy*, 2024, **9**, 1463–1473.

48 S. Fang, D. Jackson, M. L. Dreibelbis, T. F. Kuech and R. J. Hamers, *Journal of Power Sources*, 2018, **373**, 184–192.

49 E. M. Erickson, W. Li, A. Dolocan and A. Manthiram, *ACS Applied Materials and Interfaces*, 2020, **12**, 16451–16461.

50 J. C. Hestenes, A. W. Ells, M. Navarro Goldaraz, I. V. Sergeyev, B. Itin and L. E. Marbella, *Frontiers in Chemistry*, 2020, **8**, 1–9.

51 J. Xu, *Nano-Micro Letters*, DOI:10.1007/s40820-022-00917-2.

52 R. Jung, M. Metzger, F. Maglia, C. Stinner and H. A. Gasteiger, *Journal of The Electrochemical Society*, 2017, **164**, A1361–A1377.

53 P. Hou, J. Yin, M. Ding, J. Huang and X. Xu, *Small*, 2017, **13**, 1–29.

54 N. Nitta, F. Wu, J. T. Lee and G. Yushin, *Materials Today*, 2015, **18**, 252–264.

55 J. C. Hestenes, R. May, J. T. Sadowski, N. Munich and L. E. Marbella, *Chemistry of Materials*, DOI:10.1021/acs.chemmater.1c03185.

56 U. Nisar, N. Muralidharan, R. Essehli, R. Amin and I. Belharouak, *Energy Storage Materials*, 2021, **38**, 309–328.

57 Y. Chen, W. Zhao, Q. Zhang, G. Yang, J. Zheng, W. Tang, Q. Xu, C. Lai, J. Yang and C. Peng, *Advanced Functional Materials*, 2020, **30**, 1–12.

58 J. Yang, X. Liu, Y. Wang, X. Zhou, L. Weng, Y. Liu, Y. Ren, C. Zhao, M. Dahbi, J. Alami, D. A. Ei-Hady, G. L. Xu, K. Amine and M. Shao, *Advanced Energy Materials*, DOI:10.1002/aenm.202101956.

59 Y. Li, K. Wang, J. Chen, W. Zhang, X. Luo, Z. Hu, Q. Zhang, L. Xing and W. Li, *ACS Applied Materials and Interfaces*, 2020, **12**, 28169–28178.

60 R. Schmidt, C. Liu, Z. Cui and A. Manthiram, *Journal of Power Sources*, DOI:10.1016/j.jpowsour.2024.235844.

61 Y. K. Han, J. Yoo and T. Yim, *Journal of Materials Chemistry A*, 2015, **3**, 10900–10909.

62 J. Qian, L. Liu, J. Yang, S. Li, X. Wang, H. L. Zhuang and Y. Lu, *Nature Communications*, DOI:10.1038/s41467-018-07296-6.

63 S. Wu, C. Li, J. Zhang, P. Wang, D. Zhao, Y. Quan, J. Sun, X. Cui and S. Li, *iScience*, DOI:10.1016/j.isci.2023.107052.

64 S. Haber, Rosy, A. Saha, O. Brontvein, R. Carmieli, A. Zohar, M. Noked and M. Leskes, *Journal of the American Chemical Society*, 2021, **143**, 4694–4704.

65 U. Nisar, R. Amin, R. Essehli, R. A. Shakoor, R. Kahraman, D. K. Kim, M. A. Khaleel and I. Belharouak, *Journal of Power Sources*, 2018, **396**, 774–781.

66 X. Zhang, I. Belharouak, L. Li, Y. Lei, J. W. Elam, A. Nie, X. Chen, R. S. Yassar and R. L. Axelbaum, *Advanced Energy Materials*, 2013, **3**, 1299–1307.

67 H. Ming, Y. Yan, J. Ming, J. Adkins, X. Li, Q. Zhou and J. Zheng, *Electrochimica Acta*, 2014, **120**, 390–397.

68 M. J. A. Leesmith, N. R. Halcovitch and X. Hua, *Journal of Materials Chemistry A*, 2023, **11**, 17027–17034.

69 H. Seng Chan, L. Bläubaum, D. Vijayshankar, F. Röder, C. Nowak, A. Weber, A. Kwade and U. Krewer, *Batteries and Supercaps*, DOI:10.1002/batt.202300203.

70 G. Štefanić, S. Krehula and I. Štefanić, *Dalton Transactions*, 2015, **44**, 18870–18881.

71 B. Ahmed, C. Xia and H. N. Alshareef, *Nano Today*, 2016, **11**, 250–271.

72 S. Liu, C. Zhang, Q. Su, L. Li, J. Su, T. Huang, Y. Chen and A. Yu, *Electrochimica Acta*, 2017, **224**, 171–177.

73 X. W. Gao, Y. F. Deng, D. Wexler, G. H. Chen, S. L. Chou, H. K. Liu, Z. C. Shi and J. Z. Wang, *Journal of Materials Chemistry A*, 2015, **3**, 404–411.

74 J. H. Cho, J. H. Park, M. H. Lee, H. K. Song and S. Y. Lee, *Energy and Environmental Science*, 2012, **5**, 7124–7131.

75 K. S. Kang, M. J. Seong, S. H. Oh, J. S. Yu and T. Yim, *Bulletin of the Korean Chemical Society*, 2020, **41**, 1107–1113.

76 Rosy, S. Haber, E. Evenstein, A. Saha, O. Brontvein, Y. Kratish, D. Bravo-Zhivotovskii, Y. Apeloig, M. Leskes and M. Noked, *Energy Storage Materials*, 2020, **33**, 268–275.

77 D. Thiry, S. Konstantinidis, J. Cornil and R. Snyders, *Thin Solid Films*, 2016, **606**, 19–44.

78 D. Beyer, W. Knoll, H. Ringsdorf, J. Wang, R. B. Timmons and P. Sluka, *Journal of Biomedical Materials Research*, 1997, **36**, 181–189.

79 A. R. Denes, E. B. Somers, A. C. L. Wong and F. Denes, *Journal of Applied Polymer Science*, 2001, **81**, 3425–3438.

80 R. Radjef, K. Jarvis, B. L. Fox and S. L. McArthur, *Plasma Processes and Polymers*, DOI:10.1002/ppap.202000017.

81 R. Múgica-Vidal, J. Mercadal-Guillén, F. Alba-Elías and E. Sainz-García, *Plasma Processes and Polymers*, 2021, **18**, 1–15.

82 A. Choukourov, H. Biederman, D. Slavinska, L. Hanley, A. Grinevich, H. Boldyryeva and A. Mackova, *Journal of Physical Chemistry B*, 2005, **109**, 23086–23095.

83 R. T. Chen, B. W. Muir, L. Thomsen, A. Tadich, B. C. C. Cowie, G. K. Such, A. Postma, K. M. McLean and F. Caruso, *Journal of Physical Chemistry B*, 2011, **115**, 6495–6502.

84 J. Friedrich, *Plasma Processes and Polymers*, 2011, **8**, 783–802.

85 E. Hulbert, *The Physical Review*, 1931, **37**, 1–8.

86 R. Snyders, D. Hegemann, D. Thiry, O. Zabeida, J. Klemberg-Sapieha and L. Martinu, *Plasma Sources Science and Technology*, DOI:10.1088/1361-6595/acdabc.

87 A. Michelmore, D. A. Steele, J. D. Whittle, J. W. Bradley and R. D. Short, *RSC Advances*, 2013, **3**, 13540–13557.

88 Frequency bands designated for industrial, scientific and medical (ISM) use, https://www.ofcom.org.uk/spectrum/frequencies/uk-fat, (accessed November 11, 2025).

89 S. J. P. McInnes, T. D. Michl, B. Delalat, S. A. Al-Bataineh, B. R. Coad, K. Vasilev, H. J. Griesser and N. H. Voelcker, *ACS Applied Materials and Interfaces*, 2016, **8**, 4467–4476.

90 A. Michelmore, J. D. Whittle, J. W. Bradley and R. D. Short, *Frontiers of Chemical Science and Engineering*, 2016, **10**, 441–458.

91 S. Saboohi, H. J. Griesser, B. R. Coad, R. D. Short and A. Michelmore, *Physical Chemistry Chemical Physics*, 2018, **20**, 7033–7042.

92 M. Lieberman and A. Lichtenberg, *PRINCIPLES OF PLASMA DISCHARGES AND MATERIALS PROCESSING*, John Wiley & Sons, 2005.

93 A. Milella, F. Palumbo, P. Favia, G. Cicala and R. D'Agostino, *Plasma Processes and Polymers*, 2004, **1**, 164–170.

94 M. Kuzuya, Y. Matsuno, T. Yamashiro and M. Tsuiki, *Electron Spin Resonance Study on Plasma-Induced Surface Radicals of Poly(Ethylene Naphthalate)*, 1997, vol. 2.

95 A. Michelmore, P. M. Bryant, D. A. Steele, K. Vasilev, J. W. Bradley and R. D. Short, *Langmuir*, 2011, **27**, 11943–11950.

96 M. J. Barnes, A. J. Robson, J. Naderi, R. D. Short and J. W. Bradley, *Biointerphases*, 2020, **15**, 061007.

97 M. Ji, A. Jagodar, E. Kovacevic, L. Benyahia and F. Poncin-Epaillard, *Materials Chemistry and Physics*, DOI:10.1016/j.matchemphys.2021.124621.

98 Z. Takehara, Z. Ogumi, Y. Uchimoto, K. Yasuda and H. Yoshida, *Journal of Power Sources*, 1993, **44**, 377–383.

99 T. Nakajima, V. Gupta, Y. Ohzawa, M. Koh, R. N. Singh, A. Tressaud and E. Durand, *Journal of Power Sources*, 2002, **104**, 108–114.

100 A. Song, J. H. Kim, H. Yong, Y. Rho, D. S. Song, E. Cho, M. J. Kim, K. B. Chung, H. S. Kim and S. J. Lee, *ACS Applied Nano Materials*, 2022, **5**, 14540–14550.

101 G. Homann, L. Stolz, J. Nair, I. C. Laskovic, M. Winter and J. Kasnatscheew, *Scientific Reports*, 2020, **10**, 2–10.

102 Z. Xue, D. He and X. Xie, *Journal of Materials Chemistry A*, 2015, **3**, 19218–19253.

103 K. S. Siow, S. Kumar and H. J. Griesser, *Plasma Processes and Polymers*, 2015, **12**, 8–24.

104 E. E. Johnston, J. D. Bryers and B. D. Ratner, *Langmuir*, 2005, **21**, 870–881.

105 R. R. Hendrixson, M. P. Mack, R. A. Palmer, A. Ottolenghi and R. G. Ghirardelli, *Toxicology and Applied Pharmacology*, 1978, **44**, 263–268.

106 H. D. Hazrati, J. D. Whittle and K. Vasilev, *Plasma Processes and Polymers*, 2014, **11**, 149–157.

107 T. Zhao, H. Mahandra, R. Marthi, X. Ji, W. Zhao, S. Chae, M. Traversy, W. Li, F. Yu, L. Li, Y. Choi, A. Ghahreman, Z. Zhao, C. Zhang, Y. Kang, Y. Lei and Y. Song, *Chemical Engineering Journal*, 2024, **485**, 149923.

108 M. Ma, F. Shao, P. Wen, K. Chen, J. Li, Y. Zhou, Y. Liu, M. Jia, M. Chen and X. Lin, *ACS Energy Letters*, 2021, **6**, 4255–4264.

109 M. C. Lukowiak, S. Wettmarshausen, G. Hidde, P. Landsberger, V. Boenke, K. Rodenacker, U. Braun, J. F. Friedrich, A. A. Gorbushina and R. Haag, *Polymer Chemistry*, 2015, **6**, 1350–1359.

110 M. Asadian, K. V. Chan, T. Egghe, Y. Onyshchenko, S. Grande, H. Declercq, P. Cools, R. Morent and N. De Geyter, *Applied Surface Science*, 2021, **563**, 150363.

111 K. S. Siow, *Plasma Processes and Polymers*, 2018, **15**, 1–19.

112 A. S. M. de Freitas, C. C. Maciel, J. S. Rodrigues, R. P. Ribeiro, A. O. Delgado-Silva and E. C. Rangel, *Vacuum*, DOI:10.1016/j.vacuum.2021.110556.

113 L. Zuri, M. S. Silverstein and M. Narkis, *Journal of Applied Polymer Science*, 1996, **62**, 2147–2154.

114 N. E. Blanchard, V. V. Naik, T. Geue, O. Kahle, D. Hegemann and M. Heuberger, *Langmuir*, 2015, **31**, 12944–12953.

115 C. J. Hall, T. Ponnusamy, P. J. Murphy, M. Lindberg, O. N. Antzutkin and H. J. Griesser, *ACS Applied Materials and Interfaces*, 2014, **6**, 8353–8362.

116 R. Chen, C. L. A. Leung and C. Huang, *Advanced Functional Materials*, DOI:10.1002/adfm.202308165.

117 R. J. Clément, Z. Lun and G. Ceder, *Energy and Environmental Science*, 2020, **13**, 345–373.

118 M. N. Obrovac, O. Mao and J. R. Dahn, *Solid State Ionics*, 1998, **112**, 9–19.

119 J. Lee, A. Urban, X. Li, D. Su, G. Hautier and G. Ceder, *Science*, 2014, **343**, 519–522.

120 J. Reed and G. Ceder, *Chem. Rev.*, 2004, **104**, 4513–4534.

121 M. Tabuchi, A. Nakashima, H. Shigemura, K. Ado, H. Kobayashi, H. Sakaebe, K. Tatsumi, H. Kageyama, T. Nakamura and R. Kanno, *J. Mater. Chem.*, 2003, **13**, 1747.

122 D. H. Seo, J. Lee, A. Urban, R. Malik, S. Kang and G. Ceder, *Nature Chemistry*, 2016, **8**, 692–697.

123 D. Chen, J. Ahn and G. Chen, *ACS Energy Lett.*, 2021, 1358–1376.

124 A. Urban, A. Abdellahi, S. Dacek, N. Artrith and G. Ceder, *Physical Review Letters*, DOI:10.1103/PhysRevLett.119.176402.

125 L. Li, B. Ouyang, Z. Lun, H. Huo, D. Chen, Y. Yue, C. Ophus, W. Tong, G. Chen, G. Ceder and C. Wang, *Nature Communications*, DOI:10.1038/s41467-023-43356-2.

126 A. Urban, J. Lee and G. Ceder, *Advanced Energy Materials*, DOI:10.1002/aenm.201400478.

127 A. G. Squires and D. O. Scanlon, *Journal of Materials Chemistry A*, 2023, **11**, 13765–13773.

128 X. Hua, T. Dean, S. A. Cussen and A. L. Goodwin, *JPhys Materials*, DOI:10.1088/2515-7639/acf5a5.

129 M. A. Jones, P. J. Reeves, I. D. Seymour, M. J. Cliffe, S. E. Dutton and C. P. Grey, *Chemical Communications*, 2019, **55**, 9027–9030.

130 N. J. Szymanski, Z. Lun, J. Liu, E. C. Self, C. J. Bartel, J. Nanda, B. Ouyang and G. Ceder, *Chemistry of Materials*, 2023, **35**, 4922–4934.

131 N. Mozhzhukhina, J. Kullgren, C. Baur, O. Gustafsson, W. R. Brant, M. Fichtner and D. Brandell, *Journal of Raman Spectroscopy*, 2020, **51**, 2095–2101.

132 V. C. Wu, H. A. Evans, R. Giovine, M. B. Preefer, J. Ong, E. Yoshida, P. E. Cabelguen and R. J. Clément, *Advanced Energy Materials*, DOI:10.1002/aenm.202203860.

133 Z. Lun, B. Ouyang, D. H. Kwon, Y. Ha, E. E. Foley, T. Y. Huang, Z. Cai, H. Kim, M. Balasubramanian, Y. Sun, J. Huang, Y. Tian, H. Kim, B. D. McCloskey, W. Yang, R. J. Clément, H. Ji and G. Ceder, *Nature Materials*, 2021, **20**, 214–221.

134 M. M. Rahman and F. Lin, *Matter*, 2021, **4**, 490–527.

135 Z. Yin, H. Zhu, Y. Huang, D. Luo, Y. Ren, S. Lan and Q. Liu, *Journal of Materials Chemistry A*, 2022, **10**, 19387–19411.

136 K. McColl, R. A. House, G. J. Rees, A. G. Squires, S. W. Coles, P. G. Bruce, B. J. Morgan and M. S. Islam, *Nature Communications*, 2022, **13**, 1–8.

137 M. J. Crafton, Y. Yue, T. Y. Huang, W. Tong and B. D. McCloskey, *Advanced Energy Materials*, DOI:10.1002/aenm.202001500.

138 Y. Yue, Y. Ha, T. Y. Huang, N. Li, L. Li, Q. Li, J. Feng, C. Wang, B. D. McCloskey, W. Yang and W. Tong, *ACS Nano*, 2021, **15**, 13360–13369.

139 W. Wang, Y. Shi, P. Li, R. Wang, F. Ye, X. Zhang, W. Li, Z. Wang, C. Xu, D. Xu, Q. Xu and X. Cui, *Energy Environ. Sci.*, 2024, **17**, 4283–4294.

140 M. J. W. Ogley, A. S. Menon, B. J. Johnston, G. Pandey, I. McClelland, X. Shi, S. Agrestini, V. Celorrio, G. E. Pérez, S. G. Booth, J. Cabana, S. A. Cussen and L. F. J. Piper, *ACS Energy Lett.*, 2024, **9**, 4607–4613.

141 R. A. House, L. Jin, U. Maitra, K. Tsuruta, J. W. Somerville, D. P. Förstermann, F. Massel, L. Duda, M. R. Roberts and P. G. Bruce, *Energy and Environmental Science*, 2018, **11**, 926–932.

142 R. A. House, G. J. Rees, M. A. Pérez-Osorio, J. J. Marie, E. Boivin, A. W. Robertson, A. Nag, M. Garcia-Fernandez, K. J. Zhou and P. G. Bruce, *Nature Energy*, 2020, **5**, 777–785.

143 M. Juelsholt, J. Chen, M. A. Pérez-Osorio, G. J. Rees, S. De Sousa Coutinho, H. E. Maynard-Casely, J. Liu, M. Everett, S. Agrestini, M. Garcia-Fernandez, K. J. Zhou, R. A. House and P. G. Bruce, *Energy and Environmental Science*, 2024, **17**, 2530–2540.

144 X. Gao, B. Li, K. Kummer, A. Geondzhian, D. A. Aksyonov, R. Dedryvère, D. Foix, G. Rousse, M. Ben Yahia, M.-L. Doublet, A. M. Abakumov and J.-M. Tarascon, *Nat. Mater.*, 2025, **24**, 743–752.

145 N. C. Mitchell, O. O. Thomas, B. G. Meyer, M. Garcia-Fernandez, K. Zhou, P. S. Grant, P. G. Bruce, R. Heap, R. Sayers and R. A. House, *Advanced Materials*, DOI:10.1002/adma.202419878.

146 M. Hirsbrunner, A. Mikheenkova, P. Törnblom, R. A. House, W. Zhang, T. C. Asmara, Y. Wei, T. Schmitt, H. Rensmo, S. Mukherjee, M. Hahlin and L. C. Duda, *Physical Chemistry Chemical Physics*, 2024, **26**, 19460–19468.

147 Y. shan Jiang, F. da Yu, W. Ke, L. Deng, Y. Xia, X. yu Li, L. fang Que, N. Zhang, L. Zhao and Z. bo Wang, *Advanced Functional Materials*, DOI:10.1002/adfm.202213615.

148 A. Abulikemu, T. Matsunaga, A. Watanabe, K. Yamamoto, T. Uchiyama, K. Nakanishi, S. Kawaguchi, K. Osaka and Y. Uchimoto, *Journal of Alloys and Compounds*, 2021, **853**, 156984.

149 J. Wu, Y. Yang and W. Yang, *Dalton Transactions*, 2020, **49**, 13519–13527.

150 X. Xu, L. Pi, J.-J. Marie, G. J. Rees, C. Gong, S. Pu, R. A. House, A. W. Robertson and P. G. Bruce, *Journal of The Electrochemical Society*, 2021, **168**, 080521.

151 M. Sathiya, G. Rousse, K. Ramesha, C. P. Laisa, H. Vezin, M. T. Sougrati, M. L. Doublet, D. Foix, D. Gonbeau, W. Walker, A. S. Prakash, M. Ben Hassine, L. Dupont and J. M. Tarascon, *Nature Materials*, 2013, **12**, 827–835.

152 E. McCalla, M. T. Sougrati, G. Rousse, E. J. Berg, A. Abakumov, N. Recham, K. Ramesha, M. Sathiya, R. Dominko, G. Van Tendeloo, P. Novák and J.-M. Tarascon, *J. Am. Chem. Soc.*, 2015, **137**, 4804–4814.

153 M. Sathiya, J. B. Leriche, E. Salager, D. Gourier, J. M. Tarascon and H. Vezin, *Nature Communications*, DOI:10.1038/ncomms7276.

154 E. N. Bassey, P. J. Reeves, I. D. Seymour and C. P. Grey, *J. Am. Chem. Soc.*, 2022, **144**, 18714–18729.

155 R. J. Clément, D. Kitchaev, J. Lee, and Gerbrand Ceder, *Chemistry of Materials*, 2018, **30**, 6945–6956.

156 Y. Yue, N. Li, Y. Ha, M. J. Crafton, B. D. McCloskey, W. Yang and W. Tong, *Advanced Functional Materials*, DOI:10.1002/adfm.202008696.

157 L. Li, J. Ahn, Y. Yue, W. Tong, G. Chen and C. Wang, *Advanced Materials*, DOI:10.1002/adma.202106256.

158 J. Ahn, Y. Ha, R. Satish, R. Giovine, L. Li, J. Liu, C. Wang, R. J. Clement, R. Kostecki, W. Yang and G. Chen, *Advanced Energy Materials*, DOI:10.1002/aenm.202200426.

159 M. J. Crafton, T. Y. Huang, Y. Yue, R. Giovine, V. C. Wu, C. Dun, J. J. Urban, R. J. Clément, W. Tong and B. D. McCloskey, *ACS Applied Materials and Interfaces*, 2023, **15**, 18747–18762.

160 L. Li, Z. Lun, D. Chen, Y. Yue, W. Tong, G. Chen, G. Ceder and C. Wang, *Advanced Functional Materials*, DOI:10.1002/adfm.202101888.

161 J. Ahn, D. Chen and G. Chen, *Advanced Energy Materials*, DOI:10.1002/aenm.202001671.

162 Y. Yue, Y. Ha, R. Giovine, R. Clément, W. Yang and W. Tong, *Chemistry of Materials*, 2022, **34**, 1524–1532.

163 K. P. Koirala, L. Jiang, S. Patil, P. Longo, Z. Liu, B. Freitag, J. Barthel, E. C. Self, Y. Du, L. Pullan, T. Tessner, L. J. Allen, W. Xu, W. Tong, J. Nanda and C. Wang, *ACS Energy Letters*, 2024, **9**, 10–16.

164 Y. Zhang, E. C. Self, B. P. Thapaliya, R. Giovine, H. M. Meyer, L. Li, Y. Yue, D. Chen, W. Tong, G. Chen, C. Wang, R. Clément, S. Dai and J. Nanda, *ACS Applied Materials and Interfaces*, 2021, **13**, 38221–38228.

165 R. Dominko, C. V.-A. Garrido, M. Bele, M. Kuezma, I. Arcon and M. Gaberscek, *Journal of Power Sources*, 2011, **196**, 6856–6862.

166 C. Wolverton and A. Zunger, *Physical Review B*, 1998, **57**, 2242–2252.

167 R. Chen, S. Ren, M. Knapp, D. Wang, R. Witter, M. Fichtner and H. Hahn, *Advanced Energy Materials*, DOI:10.1002/aenm.201401814.

168 D. A. Kitchaev, Z. Lun, W. D. Richards, H. Ji, R. J. Clément, M. Balasubramanian, D.-H. Kwon, K. Dai, J. K. Papp, T. Lei, B. D. McCloskey, W. Yang, J. Lee and G. Ceder, *Energy Environ. Sci.*, 2018, **11**, 2159–2171.

169 L. L. Driscoll, E. H. Driscoll, B. Dong, F. N. Sayed, J. N. Wilson, C. A. O'Keefe, D. J. Gardner, C. P. Grey, P. K. Allan, A. A. L. Michalchuk and P. R. Slater, *Energy and Environmental Science*, 2023, **16**, 5196–5209.

170 T. Tsuzuki, *Communications Chemistry*, DOI:10.1038/s42004-021-00582-3.

171 R. Schlem, C. F. Burmeister, P. Michalowski, S. Ohno, G. F. Dewald, A. Kwade and W. G. Zeier, *Advanced Energy Materials*, DOI:10.1002/aenm.202101022.

172 B. Ouyang, N. Artrith, Z. Lun, Z. Jadidi, D. A. Kitchaev, H. Ji, A. Urban and G. Ceder, *Advanced Energy Materials*, DOI:10.1002/aenm.201903240.

173 C. Delmas, S. Brèthes and M. Ménétrier, *o-Li,V205-a new electrode material for rechargeable lithium batteries**, 1991, vol. 34.

174 M. J. Duer, *Introduction to Solid-State NMR Spectroscopy*, Wiley India, 2010.

175 M. H. Levitt, *Spin Dynamics: Basics of Nuclear Magnetic Resonance*, John Wiley & Sons, 2008.

176 P. J. Hore, *Nuclear Magnetic Resonance*, Oxford University Press, 2015.

177 J. Keeler, *Understanding NMR Spectroscopy*, John Wiley & Sons, 2009.

178 K. J. D. MacKenzie and M. E. Smith, *Multinuclear Solid-State Nuclear Magnetic Resonance of Inorganic Materials*, Elsevier, 2002.

179 D. C. Apperley, R. K. Harris and P. Hodgkinson, *Solid State NMR: Basic Principles & Practice*, Momentum Press, 2012.

180 H. Bai, D. V. Abraimov, G. S. Boebinger, M. D. Bird, L. D. Cooley, I. R. Dixon, K. L. Kim, D. C. Larbalestier, W. S. Marshall, U. P. Trociewitz and H. W. Weijers, *IEEE Transactions on Applied Superconductivity*, DOI:10.1109/TASC.2020.2969642.

181 Y. Li, R. Chaklashiya, H. Takahashi, Y. Kawahara, K. Tagami, C. Tobar and S. Han, *Journal of Magnetic Resonance*, DOI:10.1016/j.jmr.2021.107090.

182 Y. Li, R. Chaklashiya, H. Takahashi, Y. Kawahara, K. Tagami, C. Tobar and S. Han, *Journal of Magnetic Resonance*, 2021, **333**, 107090.

183 L. Lätsch, C. J. Kaul, A. V. Yakimov, I. B. Müller, A. Hassan, B. Perrone, S. Aghazada, Z. J. Berkson, T. De Baerdemaeker, A. N. Parvulescu, K. Seidel, J. H. Teles and C. Copéret, *Journal of the American Chemical Society*, 2023, **145**, 15018–15023.

184 R. K. Harris, E. D. Becker, S. M. De Cabral Menezes, P. Granger, R. E. Hoffman and K. W. Zilm, *Magnetic Resonance in Chemistry*, 2008, **46**, 582–598.

185 P. Lazzeretti, *Progress in Nuclear Magnetic Resonance Spectroscopy*, 2000, **36**, 1–88.

186 P. K. Mandal and A. Majumdar, *Concepts in Magnetic Resonance Part A: Bridging Education and Research*, 2004, **20**, 1–23.

187 S. E. Ashbrook, D. M. Dawson and J. M. Griffin, in *Local Structural Characterisation*, John Wiley & Sons, 2014.

188 R. E. Wasylishen, S. E. Ashbrook and S. Wimperis, *NMR of Quadrupolar Nuclei in Solid Materials*, John Wiley & Sons, 2012.

189 Y. Nishiyama, G. Hou, V. Agarwal, Y. Su and A. Ramamoorthy, *Chemical Reviews*, 2023, **123**, 918–988.

190 R. Garg, B. DeZonia, A. L. Paterson and C. M. Rienstra, *Journal of Magnetic Resonance*, 2024, **365**, 107726.

191 A. E. Bennett, C. M. Rienstra, M. Auger, K. V. Lakshmi and R. G. Griffin, *The Journal of Chemical Physics*, 1995, **103**, 6951–6958.

192 I. I. Geru, in *Journal of Physics: Conference Series*, Institute of Physics Publishing, 2011, vol. 324.

193 A. Lesage, D. Sakellariou, S. Hediger, B. Eléna, P. Charmont, S. Steuernagel and L. Emsley, *Journal of Magnetic Resonance*, 2003, **163**, 105–113.

194 B. Rowlinson, E. Crublet, R. Kerfah and M. J. Plevin, *Biochemical Society Transactions*.

195 S. Odedra and S. Wimperis, *Journal of Magnetic Resonance*, 2012, **221**, 41–50.

196 C. P. Grey and A. J. Vega, *Journal of the American Chemical Society*, 1995, **117**, 8232–8242.

197 K. J. Griffith, M. A. Hope, P. J. Reeves, M. Anayee, Y. Gogotsi and C. P. Grey, *Journal of the American Chemical Society*, 2020, **142**, 18924–18935.

198 D. P. Lang, T. M. Alam and D. N. Bencoe, *Chemistry of Materials*, 2001, **13**, 420–428.

199 A. Abraham, R. Prins, J. A. van Bokhoven, E. R. H. van Eck and A. P. M. Kentgens, *Solid State Nuclear Magnetic Resonance*, 2009, **35**, 61–66.

200 A. E. Bennett, J. H. Ok, R. G. Griffin and S. Vega, *The Journal of Chemical Physics*, 1992, **96**, 8624–8627.

201 M. J. Duer, *Solid-State NMR Principles and Applications*, Blackwell Science, 2002.

202 M. Roos, V. S. Mandala and M. Hong, *Journal of Physical Chemistry B*, 2018, **122**, 9302–9313.

203 V. Chechik, E. Carter and D. Murphy, *Electron Paramagnetic Resonance*, Oxford University Press, 2016.

204 A. J. Pell, G. Pintacuda and C. P. Grey, *Progress in Nuclear Magnetic Resonance Spectroscopy*, 2019, **111**, 1–271.

205 I. Hung, L. Zhou, F. Pourpoint, C. P. Grey and Z. Gan, *Journal of the American Chemical Society*, 2012, **134**, 1898–1901.

206 J. Arai, Y. Okada, T. Sugiyama, M. Izuka, K. Gotoh and K. Takeda, *ECS Transactions*, 2014, **62**, 159–187.

207 P. M. Bayley, N. M. Trease and C. P. Grey, *Journal of the American Chemical Society*, 2016, **138**, 1955–1961.

208 R. Bhattacharyya, B. Key, H. Chen, A. S. Best, A. F. Hollenkamp and C. P. Grey, *Nature Materials*, 2010, **9**, 504–510.

209 I. Mohammad, M. A. Cambaz, A. Samoson, M. Fichtner and R. Witter, *Solid State Nuclear Magnetic Resonance*, 2024, **129**, 101914.

210 D. S. Sholl and J. A. Steckel, .

211 C. Bonhomme, C. Gervais, F. Babonneau and C. Coelho, .

212 O. Dmitrenko, S. Bai and C. Dybowski, .

213 S. S. Eaton and G. R. Eaton, *Anal. Chem.*, 1977, **49**, 1277–1278.

214 R. W. Hooper, B. A. Klein and V. K. Michaelis, *Chemistry of Materials*, 2020, **32**, 4425–4430.

215 M. A. Hope, D. M. Halat, P. C. M. M. Magusin, S. Paul, L. Peng and C. P. Grey, *Chemical Communications*, 2017, **53**, 2142–2145.

216 M. A. Hope, B. L. D. Rinkel, A. B. Gunnarsdóttir, K. Märker, S. Menkin, S. Paul, I. V. Sergeyev and C. P. Grey, *Nature Communications*, DOI:10.1038/s41467-020-16114-x.

217 S. Pylaeva, K. L. Ivanov, M. Baldus, D. Sebastiani and H. Elgabarty, *Journal of Physical Chemistry Letters*, 2017, **8**, 2137–2142.

218 B. Corzilius, *Physical Chemistry Chemical Physics*, 2016, **18**, 27190–27204.

219 T. Maly, G. T. Debelouchina, V. S. Bajaj, K. N. Hu, C. G. Joo, M. L. Mak-Jurkauskas, J. R. Sirigiri, P. C. A. Van Der Wel, J. Herzfeld, R. J. Temkin and R. G. Griffin, *Journal of Chemical Physics*, DOI:10.1063/1.2833582.

220 A. S. L. Thankamony, J. J. Wittmann, M. Kaushik and B. Corzilius, *Progress in Nuclear Magnetic Resonance Spectroscopy*, 2017, **102–103**, 120–195.

221 D. Jardón-Álvarez and M. Leskes, in *Comprehensive Inorganic Chemistry III (Third Edition)*, eds. J. Reedijk and K. R. Poeppelmeier, Elsevier, Oxford, 2023, pp. 366–397.

222 A. Harchol, G. Reuveni, V. Ri, B. Thomas, R. Carmieli, R. H. Herber, C. Kim and M. Leskes, *Journal of Physical Chemistry C*, 2020, **124**, 7082–7090.

223 A. J. Rossini, A. Zagdoun, M. Lelli, A. Lesage, C. Copéret and L. Emsley, *Accounts of Chemical Research*, 2013, **46**, 1942–1951.

224 K. N. Hu, H. H. Yu, T. M. Swager and R. G. Griffin, *Journal of the American Chemical Society*, 2004, **126**, 10844–10845.

225 C. Song, K. N. Hu, C. G. Joo, T. M. Swager and R. G. Griffin, *Journal of the American Chemical Society*, 2006, **128**, 11385–11390.

226 R. G. Griffin, T. M. Swager and R. J. Temkin, *Journal of Magnetic Resonance*, 2019, **306**, 128–133.

227 G. Stevanato, G. Casano, D. J. Kubicki, Y. Rao, L. E. Hofer, G. Menzildjian, H. Karoui, D. Siri, M. Cordova, M. Yulikov, G. Jeschke, M. Lelli, A. Lesage, O. Ouari and L. Emsley, *Journal of the American Chemical Society*, 2020, **142**, 16587–16599.

228 A. Lund, G. Casano, G. Menzildjian, M. Kaushik, G. Stevanato, M. Yulikov, R. Jabbour, D. Wisser, M. Renom-Carrasco, C. Thieuleux, F. Bernada, H. Karoui, D. Siri, M. Rosay, I. V. Sergeyev, D. Gajan, M. Lelli, L. Emsley, O. Ouari and A. Lesage, *Chemical Science*, 2020, **11**, 2810–2818.

229 A. R. West, *Basic Solid State Chemistry*, John Wiley & Sons, 1999.

230 O. H. Seeck, *X-ray diffraction : modern experimental techniques*, Pan Stanford Publishing, Boca Raton, Florida, 2015.

231 A. L. Patterson, *Physical Review*, 1939, **56**, 978–982.

232 T. Proffen, S. J. L. Billinge, T. Egami and D. Louca, *Z. Kristallogr.*, 2003, **218**, 132–143.

233 S. J. L. Billinge, *Philosophical Transactions A*, DOI:10.1098/rsta.2018.0413.

234 S. J. L. Billinge and M. G. Kanatzidis, *Chemical Communications*, 2004, **4**, 749–760.

235 J. Bosse, J. Gu, J. Choi, V. Roddatis, Y. B. Zhuang, N. A. Kani, A. Hartl, M. Garcia-Fernandez, K. J. Zhou, A. Nicolaou, T. Lippert, J. Cheng and A. R. Akbashev, *Journal of the American Chemical Society*, 2024, **146**, 23989–23997.

236 F. M. F. de Groot, M. W. Haverkort, H. Elnaggar, A. Juhin, K. J. Zhou and P. Glatzel, *Nature Reviews Methods Primers*, DOI:10.1038/s43586-024-00322-6.

237 J. Dvorak, I. Jarrige, V. Bisogni, S. Coburn and W. Leonhardt, *Review of Scientific Instruments*, DOI:10.1063/1.4964847.

238 F. A. Stevie and C. L. Donley, *Journal of Vacuum Science & Technology A*, 2020, **38**, 063204.

239 P. Atkins and J. de Paula, *Atkins' Physical Chemistry*, 2014.

240 E. Markevich, G. Salitra and D. Aurbach, *ACS Energy Letters*, 2017, **2**, 1337–1345.

241 Y. Wu, X. Liu, L. Wang, X. Feng, D. Ren, Y. Li, X. Rui, Y. Wang, X. Han, G. L. Xu, H. Wang, L. Lu, X. He, K. Amine and M. Ouyang, *Energy Storage Materials*, 2021, **37**, 77–86.

242 T. D. Michl, J. Barz, C. Giles, M. Haupt, J. H. Henze, J. Mayer, K. Futrega, M. R. Doran, C. Oehr, K. Vasilev, B. R. Coad and H. J. Griesser, *ACS Applied Nano Materials*, 2018, **1**, 6587–6595.

243 S. D. Lin, Y. B. Yohannes, B.-J. Hwang and N.-L. Wu, *ECS Transactions*, 2020, **97**, 135–142.

244 M. Leskes, G. Kim, T. Liu, A. L. Michan, F. Aussenac, P. Dorffer, S. Paul and C. P. Grey, *Journal of Physical Chemistry Letters*, 2017, **8**, 1078–1085.

245 A. Michelmore, P. Gross-Kosche, S. A. Al-Bataineh, J. D. Whittle and R. D. Short, *Langmuir*, 2013, **29**, 2595–2601.

246 D. T. Daniel, S. Mitra, R. A. Eichel, D. Diddens and J. Granwehr, *Journal of Chemical Theory and Computation*, 2024, **20**, 2592–2604.

247 X. Yang, M. Jiang, X. Gao, D. Bao, Q. Sun, N. Holmes, H. Duan, S. Mukherjee, K. Adair, C. Zhao, J. Liang, W. Li, J. Li, Y. Liu, H. Huang, L. Zhang, S. Lu, Q. Lu, R. Li, C. V. Singh and X. Sun, *Energy and Environmental Science*, 2020, **13**, 1318–1325.

248 A. A. Savina and A. M. Abakumov, *Heliyon*, DOI:10.1016/j.heliyon.2023.e21881.

249 Z. Zhao, D. Xiao, K. Chen, R. Wang, L. Liang, Z. Liu, I. Hung, Z. Gan and G. Hou, *ACS Central Science*, 2022, **8**, 796–803.

250 N. R. Babij, E. O. McCusker, G. T. Whiteker, B. Canturk, N. Choy, L. C. Creemer, C. V. D. Amicis, N. M. Hewlett, P. L. Johnson, J. A. Knobelsdorf, F. Li, B. A. Lorsbach, B. M. Nugent, S. J. Ryan, M. R. Smith and Q. Yang, *Organic Process Research and Development*, 2016, **20**, 661–667.

251 T. D. Michl, D. T. T. Tran, K. Böttle, H. F. Kuckling, A. Zhalgasbaikyzy, B. Ivanovská, A. A. Cavallaro, M. A. Araque Toledo, P. J. Sherman, S. A. Al-Bataineh and K. Vasilev, *Biointerphases*, DOI:10.1116/6.0000259.

252 T. D. Michl, D. T. T. Tran, H. F. Kuckling, A. Zhalgasbaikyzy, B. Ivanovská, L. E. González García, R. M. Visalakshan and K. Vasilev, *RSC Advances*, 2020, **10**, 7368–7376.

253 K. Böttle, K. Vasilev and T. D. Michl, *Antibiotics*, DOI:10.3390/antibiotics10040362.

254 Y. Wang, X. Ma, A. J. Robson, R. D. Short and J. W. Bradley, *Plasma Processes and Polymers*, DOI:10.1002/ppap.70035.

255 U. Roland, F. Holzer, A. Pöppl and F.-D. Kopinke, *Applied Catalysis B: Environmental*, 2005, **58**, 227–234.

256 A. Oshima, H. Horiuchi, A. Nakamura, S. Kobayashi, A. Terui, A. Mino, R. Shimura and M. Washio, *Scientific Reports*, DOI:10.1038/s41598-021-90462-6.

257 N. J. Szymanski, Y. Zeng, T. Bennett, S. Patil, J. K. Keum, E. C. Self, J. Bai, Z. Cai, R. Giovine, B. Ouyang, F. Wang, C. J. Bartel, R. J. Clément, W. Tong, J. Nanda and G. Ceder, *Chemistry of Materials*, 2022, **34**, 7015–7028.

258 J.-M. Ateba Mba Jože Moškon Elena Tchernychova Sorour Semsari Parapari Francisco Ruiz Zepeda Victoria Bracamonte Miran Gaberščček Robert Dominko Ref Ares, *LiRichFCC Novel Cathode Materials for Lithium Ion Batteries National Institute of Chemistry Title: D3.3: Porous electrode model development and verification*, 2020.

259 E. K. Dempsey and J. Cumby, *Chemical Communications*, 2024, **60**, 2548–2551.

260 O. B. Lapina, D. F. Khabibulin, K. V. Romanenko, Z. Gan, M. G. Zuev, V. N. Krasil'nikov and V. E. Fedorov, *Solid State Nuclear Magnetic Resonance*, 2005, **28**, 204–224.

261 Database of Ionic Radii, http://abulafia.mt.ic.ac.uk/shannon/ptable.php.

262 The Materials Project: Materials Explorer: LiF mp-1138, https://next-gen.materialsproject.org/materials/mp-1138.

263 The Materials Project: Materials Explorer: Sc2O3 mp-755313, https://next-gen.materialsproject.org/materials/mp-755313.

264 The Materials Project: Materials Explorer: Al2O3 mp-1143, https://next-gen.materialsproject.org/materials/mp-1143/.

265 The Materials Project: Materials Explorer: Y2O3 mp-2652, https://next-gen.materialsproject.org/materials/mp-2652/.

266 A. Sadoc, M. Biswal, M. Body, C. Legein, F. Boucher, D. Massiot and F. Fayon, *Solid State Nuclear Magnetic Resonance*, 2014, **59–60**, 1–7.

267 A. Sadoc, M. Body, C. Legein, M. Biswal, F. Fayon, X. Rocquefelte and F. Boucher, *Physical Chemistry Chemical Physics*, 2011, **13**, 18539–18550.

268 D. Wu, R. Shen, R. Yang, W. Ji, M. Jiang, W. Ding and L. Peng, *Scientific Reports*, DOI:10.1038/srep44697.

269 N. Kim, C. H. Hsieh and J. F. Stebbins, *Chemistry of Materials*, 2006, **18**, 3855–3859.

270 T. Bräuniger, A. J. Hofmann, I. L. Moudrakovski, C. Hoch and W. Schnick, *Solid State Sciences*, 2016, **51**, 1–7.

271 A. Y. H. Lo, V. Sudarsan, S. Sivakumar, F. van Veggel and R. W. Schurko, *J. Am. Chem. Soc.*, 2007, **129**, 4687–4700.

272 A. Rakhmatullin, F. Ek S ˇ Imko, D. Zanghi, Z. Netriová, I. B. Polovov, A. Dimiev, K. V. Maksimtsev, C. Bessada and M. Korenko, *Rare Metals*, DOI:10.1007/s12598.

273 N. Dupré, J. Gaubicher, D. Guyomard and C. P. Grey, *Chemistry of Materials*, 2004, **16**, 2725–2733.

274 A. A. Shubin, D. F. Khabibulin and O. B. Lapina, *Catalysis Today*, 2009, **142**, 220–226.

275 O. B. Lapina, D. F. Khabibulin, A. A. Shubin and V. V. Terskikh, *Progress in Nuclear Magnetic Resonance Spectroscopy*, 2008, **53**, 128–191.

276 F. Pourpoint, X. Hua, D. S. Middlemiss, P. Adamson, D. Wang, P. G. Bruce and C. P. Grey, *Chemistry of Materials*, 2012, **24**, 2880–2893.

277 J. Skibsted, N. C. Nielsen, H. Bildsoe and H. J. Jakobsen, *J. Am. Chem. Soc.*, 1993, **115**, 7351–7362.

278 A. Pendashteh, B. Orayech, H. Suhard, M. Jauregui, J. Ajuria, B. Silván, S. Clarke, F. Bonilla and D. Saurel, *Energy Storage Materials*, 2022, **46**, 417–430.

279 N. M. Asl, J. H. Kim, W. C. Lee, Z. Liu, P. Lu and Y. Kim, *Electrochimica Acta*, 2013, **105**, 403–411.

280 C. P. Grey and N. Dupré, *Chemical Reviews*, 2004, **104**, 4493–4512.

281 X. Wang, Y. C. Lin, H. Zhou, F. Omenya, I. H. Chu, K. Karki, S. Sallis, J. Rana, L. F. J. Piper, N. A. Chernova, S. P. Ong and M. S. Whittingham, *ACS Applied Energy Materials*, 2018, **1**, 4514–4521.

282 R. Chen, E. Maawad, M. Knapp, S. Ren, P. Beran, R. Witter and R. Hempelmann, *RSC Advances*, 2016, **6**, 65112–65118.

283 J. Dabachi, M. Body, C. Galven, F. Boucher and C. Legein, *Inorganic Chemistry*, 2017, **56**, 5219–5232.

284 J. V. Hanna, K. J. Pike, T. Charpentier, T. F. Kemp, M. E. Smith, B. E. G. Lucier, R. W. Schurko and L. S. Cahill, *Chemistry - A European Journal*, 2010, **16**, 3222–3239.

285 X. Zhi and A. R. West, *Chemistry of Materials*, 2023, **35**, 6790–6798.

286 C. Leger, S. Bach, P. Soudan and J.-P. Pereira-Ramos, *Journal of The Electrochemical Society*, 2005, **152**, A236.

287 X. Lan, L. Wang, L. Yu, Y. Li and X. Hu, *ACS Materials Letters*, 2021, **3**, 1394–1401.

288 X. Guo, C. Chen and S. P. Ong, *Chemistry of Materials*, 2023, **35**, 1537–1546.

289 C. K. Christensen, D. R. Sørensen, J. Hvam and D. B. Ravnsbæk, *Chemistry of Materials*, 2019, **31**, 512–520.

290 P. E. Stallworth, F. S. Johnson, S. G. Greenbaum, S. Passerini, J. Flowers and W. Smyrl, *Journal of Applied Physics*, 2002, **92**, 3839–3852.

291 X. Rocquefelte, F. Boucher, P. Gressier and G. Ouvrard, *Chemistry of Materials*, 2003, **15**, 1812–1819.

292 Z. Ren, S. Yu, T. Yao, T. Xu, J. He and L. Shen, *Journal of Materials Chemistry A*, 2022, **11**, 621–629.

293 J. Hu, S. Zhong and T. Yan, *Journal of Power Sources*, DOI:10.1016/j.jpowsour.2021.230342.

294 N. Spinner, L. Zhang and W. E. Mustain, *Journal of Materials Chemistry A*, 2014, **2**, 1627–1630.

295 Z. Wang, S. Yuan, X. Tang, H. Wang, M. Zhang, F. Liu, N. Yao and Y. Ma, *Energy Storage Materials*, 2023, **54**, 284–293.

296 J. Si, R. Ma, Y. Wu, Y. Dong and K. Yao, *Journal of Materials Science*, 2022, **57**, 8154–8166.

297 I. R. Ibrahim, K. A. Matori, I. Ismail, Z. Awang, S. N. A. Rusly, R. Nazlan, F. Mohd Idris, M. M. Muhammad Zulkimi, N. H. Abdullah, M. S. Mustaffa, F. N. Shafiee and M. Ertugrul, *Scientific Reports*, 2020, **10**, 3135.

298 J. Hirschinger, T. Mongrelet, C. Marichal, P. Granger, J.-M. Savariault, E. Deramond and J. Galy, *J. Phys. Chem*, 1993, **97**, 10301–10311.

299 P. E. Stallworth, F. S. Johnson, S. G. Greenbaum, S. Passerini, J. Flowers, W. Smyrl and J. J. Fontanella, *Solid State Ionics*, 2002, **146**, 43–54.

300 J. Terwort, F. Berkemeier and G. Schmitz, *Journal of Power Sources*, 2016, **336**, 172–178.

301 M. Vijayakumar, S. Selvasekarapandian, K. Nakamura, T. Kanashiro and R. Kesavamoorthy, *Solid State Ionics*, 2004, **167**, 41–47.

302 K. A. See, M. A. Lumley, G. D. Stucky, C. P. Grey and R. Seshadri, *Journal of The Electrochemical Society*, 2017, **164**, A327–A333.

303 Z. Jadidi, J. H. Yang, T. Chen, L. Barroso-Luque and G. Ceder, *Journal of Materials Chemistry A*, 2023, **11**, 17728–17736.

304 F. Mattelaer, K. Geryl, G. Rampelberg, J. Dendooven and C. Detavernier, *ACS Applied Materials and Interfaces*, 2017, **9**, 13121–13131.

305 R. Siegel, N. Dupré, M. Quarton and J. Hirschinger, *Magnetic Reson in Chemistry*, 2004, **42**, 1022–1026.

306 S. Ren, R. Chen, E. Maawad, O. Dolotko, A. A. Guda, V. Shapovalov, D. Wang, H. Hahn and M. Fichtner, *Advanced Science*, DOI:10.1002/advs.201500128.

307 The Materials Project: Materials Explorer: V2O5 mp-25279, https://next-gen.materialsproject.org/materials/mp-25279.

308 S. Liu, W. Xue and L. Wang, *Metals*, DOI:10.3390/met11081301.

309 M. Sathiya, J.-B. Leriche, E. Salager, D. Gourier, J.-M. Tarascon and H. Vezin, *Nat Commun*, DOI:10.1038/ncomms7276.

310 S. Hants, J. Wang, Y. Xutl, Y. Liu and J. Weit, *Journal of Condensed Matter Physics*, 1992, **4**, 6009–6014.

311 Y. NejatyJahromy, S. C. Roy, R. Glaum and O. Schiemann, *Applied Magnetic Resonance*, 2021, **52**, 169–175.

312 E. Saab, E. Abi-Aad, M. N. Bokova, E. A. Zhilinskaya and A. Aboukaïs, *Carbon*, 2007, **45**, 561–567.

313 P. Hu, P. Hu, T. D. Vu, M. Li, S. Wang, Y. Ke, X. Zeng, L. Mai and Y. Long, *Chem. Rev.*, 2023, **123**, 4353–4415.